RESPONSE OF REINFORCED CONCRETE COLUMNS SUBJECTED TO IMPACT LOADING

by

Paul Imbeau

A thesis submitted to
the Faculty of Graduate and Postdoctoral Studies
in partial fulfilment of the requirements
for the degree of
Master of Applied Sciences
in Civil Engineering

Department of Civil Engineering
Faculty of Engineering
University of Ottawa

Abstract

Reinforced Concrete (RC) bridge piers, RC columns along exterior of buildings or those located in parking garages are designed to support large compressive axial loads but are vulnerable to transverse out-of-plane loadings, such as those arising from impacts or explosions. To address a lack of understanding regarding blast and impact response of RC members and the need for retrofit techniques to address deficiencies in existing structures, a multi-disciplinary team including various institutes of the National Research Council and the University of Ottawa has initiated work towards developing a fibre reinforced polymer composite protection system for RC columns subjected to extreme shocks. This thesis will focus on the impact program of the aforementioned project.

An extensive literature review was conducted to gain a better understanding of: impact loading and associated dynamic effects; experimental testing of RC members subjected to impact; experimental testing of axially loaded members; and retrofit methods for the protection of RC under impact loading. Five half-scale RC columns were constructed and tested using a drop-weight impact machine and two additional specimens were tested under static loading. Deflections, strain distributions within the columns, impact loads and reaction loads were measured during the testing of the built RC members. Comparisons of experimental datum were established between members with differing levels of axial load and between a retrofitted and a non-retrofitted member. Single-degree-of-freedom analysis was used to obtain the predicted response of certain columns under impact loading allowing for comparisons with experimental data.

Acknowledgements

I would like to thank my supervisors, Husham Almansour and Dan Palermo, for their guidance, experience and wisdom. Special thanks to Bruce Baldock, Dennis Krys, Jim Margeson and Roger Smith for their valuable expertise and attentive work during laboratory testing and analysis at the National Research Council.

I wish to express my gratitude towards the Fonds de Recherche du Québec en Nature et Technologies, the National Research Council and the University of Ottawa for providing me with financial assistance during my studies.

I must also thank my family and friends for their love and support over the course of this endeavour.

Table of Contents

List of Figures

List of Tables

Notations

Acronyms

ASTM	- American Society for Testing and Materials / American Standard Test Method
CFRP	- Carbon fibre reinforced polymer
EAM	- Energy absorbing material
FE	- Finite element
FRP	- Fibre reinforced polymer
LCPC	- Laboratoire Central des Ponts et Chaussées
MOR	- Modulus of rupture
NRC	- National Research Council
RC	- Reinforced Concrete
SHPB	- Split Hopkinson pressure bar
SAP	- Super absorbent polymer

Symbols

c	- Damping constant
k	- Stiffness
F	- External force
F_D	- Damping force
F_I	- Inertia force
F_S	- Spring force
f'_c	- Peak concrete stress
f_u	- Ultimate steel stress
f_y	- Yield steel stress
G_F	- Fracture energy
h	- Specimen cross-section height
h	- Initial distance between two plates (Stefan effect)
$\dot{h}$	- Velocity of separation of two plates (Stefan effect)
i_S	- Positive specific incident impulse
i_S^-	- Negative specific incident impulse
k*	- Equivalent stiffness of system
L	- Length of specimen
M	- Mass of system

m^*	- Equivalent mass of system
$\bar{m}$	- Mass per unit length
P_{max}	- Peak load
P_r	- Normally reflected peak pressure
P_{SO}	- Peak incident pressure
P_{SO}^-	- Peak negative incident pressure
t	- Time
t_A	- Time of shock front arrival
t_d	- Time of positive load duration
t_d^-	- Time of negative load duration
t_m	- Time to maximum member response
V	- Volume of liquid (Stefan effect)
w/c	- Water to cement ratio in concrete
x	- Displacement
$\dot{x}$	- Velocity
$\ddot{x}$	- Acceleration
ε'_c	- Strain at peak compressive strength
η	- Viscosity
ρ	- Longitudinal reinforcement ratio
$\dot{\sigma}$	- Stress rate
$\psi(x)$	- Shape function

Chapter 1: Introduction

1.1 General

Traditionally, reinforced concrete (RC) columns were designed to withstand only gravity loads. With time and improving analytical tools, seismic activity was included in design as well. Recently, the vulnerability of columns to transverse out-of-plane loadings arising from extreme shocks, such as impacts and explosions, has garnered increasing attention. While guidelines are emerging for the design and retrofit of structures to withstand blast loading, there exist no guidelines to account for out-of-plane transverse loading arising from accidental or malicious impact loading. Unlike blast loads which generally lead to a globalized member response, impact loads also cause localized damage near the contact surface which is difficult to account for in modeling and design. Impact loading can arise from: traffic colliding with bridge piers or parking garage columns; over height vehicular collisions where passing trucks damage girder elements beneath overpasses; ships colliding with dock facilities or with infrastructure during tsunamis; and large debris projected during explosions.

1.2 Objective

The first objective of this research project was to develop and implement a testing protocol at the NRC for the experimental testing of RC columns subjected to drop-weight impact loading. Once this was achieved, the second objective was to study the response of beams, columns and retrofitted specimens when subjected to a consistent impact of 70.6 kg at a velocity of 7 m/s, representing the capacity of the testing apparatus. This was completed as part of a multi-institute project focusing on the development of an innovative advanced composites system for the protection of critical concrete infrastructure against extreme shocks. The design of the tested specimens was similar to that of RC columns tested under simulated blast load at the University of Ottawa's shock tube. This allowed for a comparison between similar specimens when subjected to impulsive loads of different nature, namely, impact and blast. Static tests were also performed to obtain baseline resistance curves to be used in single-degree-of-freedom modeling and to compare concrete cracking patterns in these specimens with specimens subjected to impact.

1.3 Scope

The current research project introduced a number of testing procedures that are thought to be improvements of impact testing methodologies encountered in the literature. The supports used

during testing provided boundary conditions consistent with the theoretical idealization of a pin and a roller in addition to having built-in load cells capable of measuring both tensile (uplift) and compressive forces, a first for impact testing. Axial load levels were recorded accurately by a load cell, permitting the evaluation of any losses or gains during an impact event. Test specimens were instrumented with up to twenty strain gauges, located on lateral and longitudinal reinforcing steel and on the concrete surface to measure strain distribution within a specimen under impact. Laser displacement sensors were used to accurately measure deflections under impulsive loading. Finally, a high speed (minimum 2000 frames per second) video recording of each impact test was recorded allowing for observations to be made regarding crack development of specimens under impact.

The following forms the complete scope of the current investigation:

- Review of previous research pertaining to impact testing of RC
- Design, construction and instrumentation of seven half-scale RC specimens
- Retrofitting of two half-scale RC specimens
- Design and implementation of axial loading system
- Drop-weight impact testing of five half-scale RC members
- Static three-point bending testing of two half-scale RC members
- Evaluation of test data and presentation of test results
- Application of statically obtained resistance curves and measured impact loads to the SDOF modeling of two tested specimens
- Testing of preliminary normal strength concrete cylinders wrapped with different configurations of carbon fibre reinforced polymer (Appendix B)

1.4 Thesis Outline

This thesis is divided into six chapters and two appendices. Chapter 1 is an introduction that presents the objectives and scope of the project. Chapter 2 is a review of research on understanding impulsive loading and strain rate effects, experimental impact testing of RC beams and columns, methods currently available to protect existing RC structures from impact, and SDOF modeling of impulsive phenomena. Chapter 3 details the experimental program including the construction of specimens, the material properties of the specimens, the development of instrumented supports and axial loading system, and the instrumentation used during experimental tests. Chapter 4 presents the data recorded during testing of specimens subjected to drop-weight

impacts and to quasi-static loading. Chapter 5 discusses the data that was obtained from these tests as well as from SDOF modeling. Chapter 6 provides conclusions drawn during the project and suggests areas for future research. Appendix A presents additional plots of data obtained during testing as well as a summary of strain data for each test specimen and Appendix B discusses the compressive testing of normal strength concrete cylinders wrapped with varying configurations of FRP.

Chapter 2: Literature Review

2.1 Introduction

This chapter presents an overview of research conducted towards the understanding of the behaviour of reinforced concrete (RC) under impact loading and the development of protection systems to limit impact damage in RC. Section 2.2 presents differences between blast and impact loading. Section 2.3 addresses strain rate sensitivity, the phenomenon of apparent increased material strength with increased rate of loading. Instances where strain rate sensitivity was observed will be discussed as well as existing theories to explain such behaviour. Section 2.4 discusses experimental setups that have been used for the application of axial load, and for the testing of RC under drop-weight and pendulum type impacts. Section 2.5 discusses the protection of RC against impact loads by sacrificial built-up systems, energy absorbing bumpers and FRP technology. Finally, Section 2.6 provides a brief overview of single-degree-of-freedom modeling for impulsive loading.

2.2 Impact Compared to Blast Loading

As blast and impact loads have similar characteristics, a retrofit or a design principle that can improve structural response under one of these types of loads is most likely beneficial in improving performance of the structure under the other load type. It is thus important to understand and distinguish the differences and similarities between these types of loads.

A load can be characterized based on its duration compared to the natural frequency of the impacted member. Krauthammer et al. (1990) define three general cases for relative relationships between the load function and the structural response as shown in Figure 2-1. In the impulsive domain, the load is over before the structure reaches its maximum response. In the quasi-static domain, the structure reaches its maximum deflection well before the load is over. Meanwhile, in the dynamic domain, the maximum deflection is reached near the end of the loading. Typically, both impact and blast are considered impulsive loads as the loading occurs very rapidly and prior to the structure fully responding.

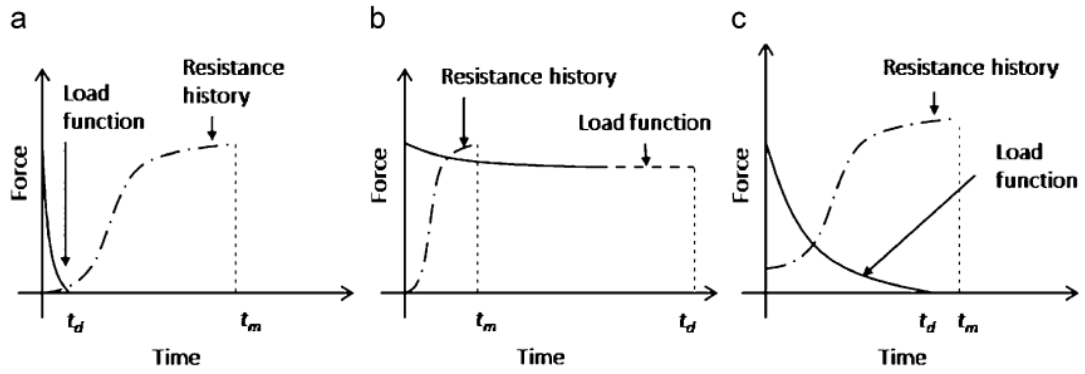

Figure 2-1: Typical response domains: (a) Impulse; (b) Quasi-static; and (c) Dynamic (Krauthammer et al., 1990)

2.2.1 Blast Loading

An explosion is defined as a large scale and sudden release of energy. When an explosive detonates, an exothermic chemical reaction known as oxidation occurs. Heat or energy is produced because the molecules of the final (burned) substances possess less internal energy than the molecules of the initial (unburned) substance.

The detonation of a condensed high explosive generates hot gasses under pressure up to 300 kilo bar and temperatures in the range of 3000 – 4000 °C. The hot gas expands, forcing out the volume it occupies. As a consequence, a layer of compressed air (blast wave) forms in front of this gas volume containing most of the energy released by the explosion (Ngo et al., 2007). The blast wave instantaneously increases to a pressure above the ambient atmospheric pressure. This is referred to as the side-on overpressure that decays as the shock wave expands outward from the explosion source. After a short time, the pressure behind the front may drop to below atmospheric pressure values creating a negative phase vacuum in which air is sucked in.

Figure 2-2 shows a typical blast pressure profile. At time t_A, the time of arrival of the shock front after detonation, a near-instantaneous increase in ambient pressure (overpressure) occurs due to the highly compressed air of the shock front; this pressure is called the peak incident (or side-on) pressure, P_{so}. The positive pressure decays back to ambient pressure over the period known as the positive phase duration, t_d. The pressure further decays past ambient pressure during the longer negative phase duration t_d^- down to a maximum negative pressure, P_{so}^-. As the shock wave expands outwards, its supersonic propagation velocity and incident overpressure decrease and its wavelength and positive phase duration increase; this is due to spherical divergence, as well as

dispersive effects. The peak positive overpressure near the explosion can be several orders of magnitude greater than the atmospheric pressure but occurs over only milliseconds.

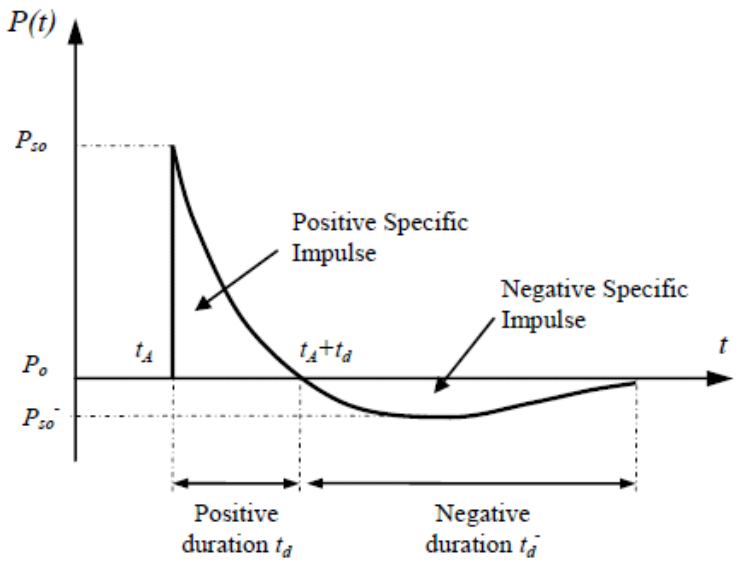

Figure 2-2: Blast wave pressure - Time history (Ngo et al., 2007)

The area under the pressure-time pulse in the positive phase is referred to as the positive specific incident impulse, i_s (MPa*ms). Similarly, the area under the negative phase is called the negative specific incident impulse, i_s^-. For designers, i_s is more important when considering rigid structures but when dealing with elastic structures, one must consider both the positive and negative impulses as the negative phase could create negative moments in members being analyzed.

Also, if the shock front impinges a reflecting surface, the incident pressure is amplified because the shock wave's propagation through the air is suddenly arrested and then redirected by the surface. The resulting normally reflected peak pressure P_r is two to approximately 13 times larger than the peak incident pressure, P_{so}. The value of P_r depends on P_{so} and the angle of incidence; tables are available that give P_r in relation to these two factors.

The primary blast loading parameters for design are usually incident or reflected peak (shock) pressures and their corresponding impulses. For initial design, it is usually adequate to represent the actual blast pressure-time pulse shown above in Figure 2-2 with a linearly-decaying triangular pulse as shown in Figure 2-3. Notice the absence of the negative phase since it will not typically affect design. The area under the triangle is, by definition, the positive impulse i, therefore the fictitious pulse duration t_d is computed from the peak pressure P_{SO} and the impulse:

$$t_d = \frac{2*i}{P_{so}} \quad [2.1]$$

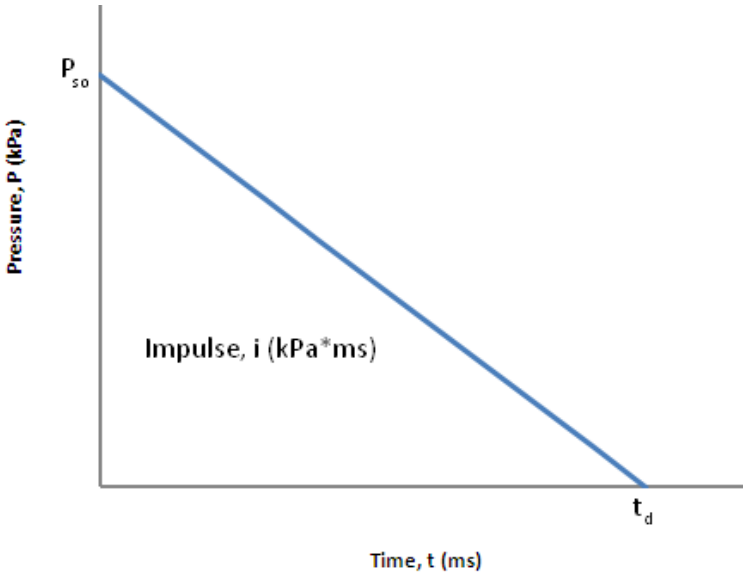

Figure 2-3: Idealized pressure-time relationship for blast shock (Uddin, 2010)

2.2.2 Impact Loading

Unlike blast loading where one can normalize a given blast load with equivalent mass of TNT and stand-off distance to obtain a representative pressure-time history using given formulae and graphs, there exists no universal approximation method for predicting impact forces.

Many factors combine to determine the type of impact forces and the associated member response. Some impacts produce deformations in a small zone surrounding the point of impact while others involve deformations of the entire structure. In some cases, a major portion of the impact energy is transferred to the structure and in other cases most of the energy is resituated to the impacting device (drop-weight, vehicle, projectile, etc.). For some problems, the indentation absorbs a significant portion of the impact energy so that it must be modeled adequately in the analysis while in other cases the effects of indentation are negligible. Sorting out these different types of behaviour is necessary for the interpretation of experimental results and for the selection of an appropriate mathematical model (Abrate, 1998).

When conducting experimental testing with impact loading, the force that the impactor imparts onto the test specimen must be measured. This is challenging since the imparted force is not simply the product of mass of the impactor and its acceleration. Other salient parameters include

localized damage, inertial loads resulting from the acceleration of the structure, resonance between the structure and the impacting device, and boundary conditions. Section 2.4 discusses observations and recommendations made by researchers studying the impact of RC. It should be noted that in the instances where impact forces were measured, there was no trend that could be observed regarding the shape of the impact force-time history.

2.3 Strain Rate Sensitivity

Typical impact tests result in strain rates ranging from 10^{-1} to 10^{2} s^{-1} (Figure 2-4). [Note: Quasi-static loading is typically about 10^{-5} s^{-1}]. It is important to understand how this elevated loading rate will affect the response of the structure as a whole and the materials that constitute the structure. It has been well documented that materials and structures display apparent strength gain during dynamic and impulsive testing when compared to quasi-static experiments. This apparent change in material behaviour related to changes in rate of loading is called strain rate sensitivity.

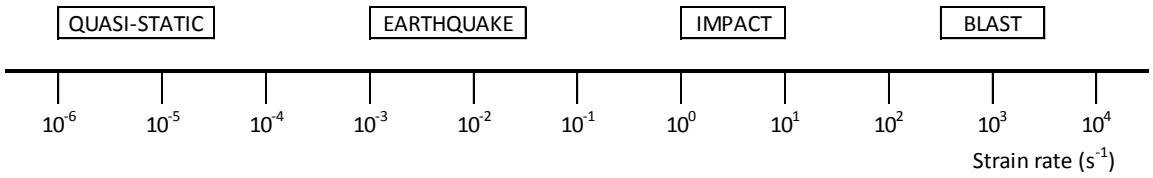

Figure 2-4: Strain rates associated with different types of loading (Ngo et al., 2007)

The fundamental cause of this gain in strength in dynamic and impulsive testing regimes is still uncertain and there exists no consensus within the scientific community to explain it. The following section will present research that displays the strength gain of mortar, concrete and high strength concrete when loaded at high rates. However, most of the investigations provide results without explaining the observed behaviour. In Section 2.3.2, two theories are presented to explain the strain-rate effect.

2.3.1 Instances of Strain Rate Sensitivity

W. Suaris and S. P. Shah, 1983

Suaris and Shah (1983) conducted tests on concrete and fibre reinforced concrete beams in a drop-weight, instrumented impact testing machine to quantify the constitutive properties of concrete over a wide range of strain rates. Preliminary tests revealed that dynamic peak loads were 9 times higher than equivalent static loads. The average values of modulus of rupture (MOR) for mortar

and concrete calculated from the peak load assuming linear behaviour for various strain rates were obtained. When the strain rate was increased from quasi-static (0.67×10^{-6} s^{-1}) to dynamic (0.27 s^{-1}), the flexural strength of mortar and concrete specimens increased by 67 % and 46 %, respectively.

Figure 2-5 compares the strain rate sensitivity for different types of loading cases as obtained from Suaris and Shah (1983). These results are given without much context; it is thus difficult to determine their applicability. It would seem that compression loading is relatively insensitive to strain rate while tension loading is quite sensitive. Conversely, Grote et al. (2001) demonstrated with tests conducted at strain rates 3 or 4 orders of magnitude greater than those measured by Suaris and Shah that concrete in compression is indeed quite sensitive to strain rate as shown in Figure 2-9 where there is approximately a three-fold increase in concrete compressive strength with an increase in strain rate from 290 s^{-1} to 1500 s^{-1}.

Suaris and Shah stated that the strength gain does not reflect material sensitivity to strain rate but rather inertial effects within the concrete beam. This hypothesis was supported by the fact that the peak loads varied almost linearly with impact velocity and that these peak loads were insensitive to any addition of fibre to the concrete mix. It was determined that the use of a rubber pad in the tup-specimen impact zone could significantly reduce these inertial effects. The researchers also indicated that matrix cracking is a major process responsible for strain-rate sensitivity.

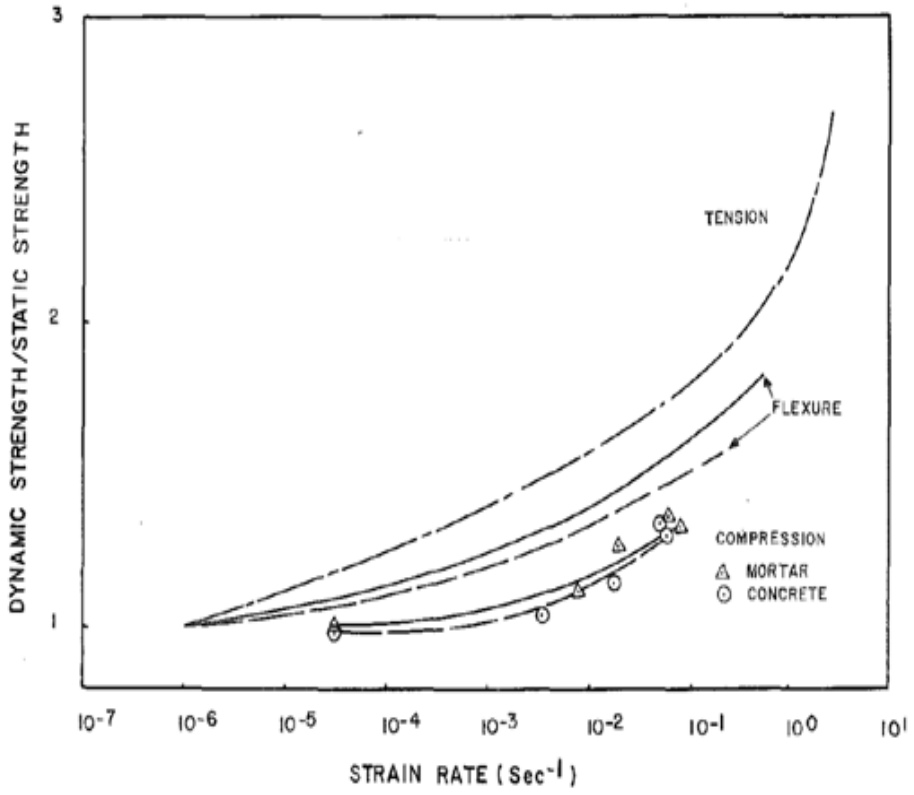

Figure 2-5: Comparison of the strain-rate sensitivity in tension, flexure and compression (Suaris et al., 1983)

Miyamoto A, King M and Fujii M, 1989

Miyamoto et al. (1989) studied the behaviour of RC beams under impulsive loading both experimentally and analytically. The analytical portion of the study was carried out using the non-linear dynamic finite element method. The results of the analyses were accurate when compared to those obtained experimentally from static and drop-weight impact tests on RC beams. Of note, their work demonstrated that the deviation from static response becomes more pronounced as loading rate is increased and primarily takes the form of an increase in stiffness and load-carrying capacity, followed by a decrease in ductility (Figure 2-6). For dynamic loading (impacts in this study), there is a smooth transition from elasticity to plasticity without sudden drops in stiffness, but in the case of static loading, a sudden drop in stiffness occurs with the appearance of cracks and the response curve inflects approaching failure.

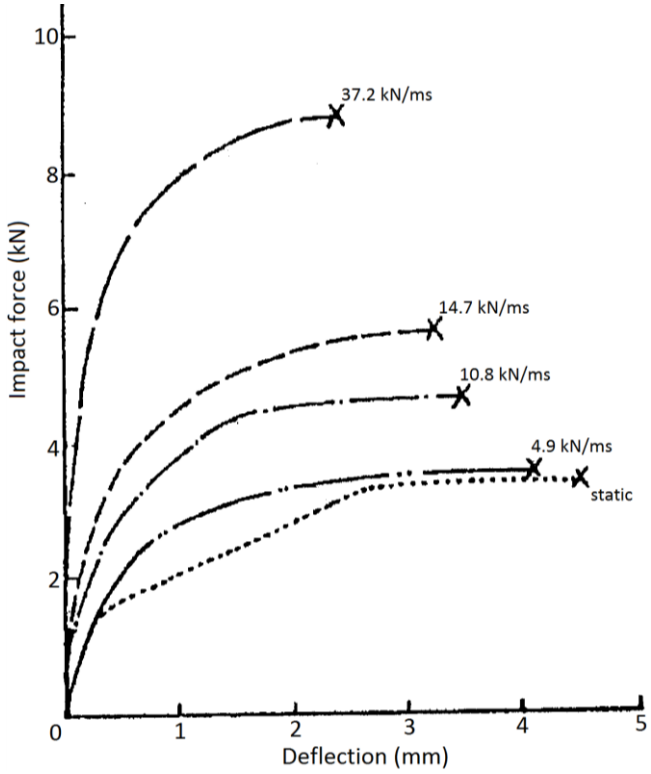

Figure 2-6: Impact force-midspan displacement functions for various loading rates (Miyamoto et al., 1989)

Ngo T, Mendis P, Gupta A and Ramsay J, 2007

A decrease in ductility with elevating strain rates cannot be assumed to be always the case. Research by Ngo et al. (2007) in which moment-curvature diagrams were obtained for a column cross-section for different strain rates clearly indicates that increasing strain rate will dramatically increase the ductility of the column (Figure 2-7). It is very difficult to comment on the difference in results regarding ductility enhancements with increasing strain rates as some results are obtained experimentally (using various test configurations) while others are obtained analytically (using differing modeling assumptions). The authors noted that due to the increased gain of flexural strength compared to shear strength when strain rates increase, there may be a shift from ductile flexural failure to a more brittle shear failure mode.

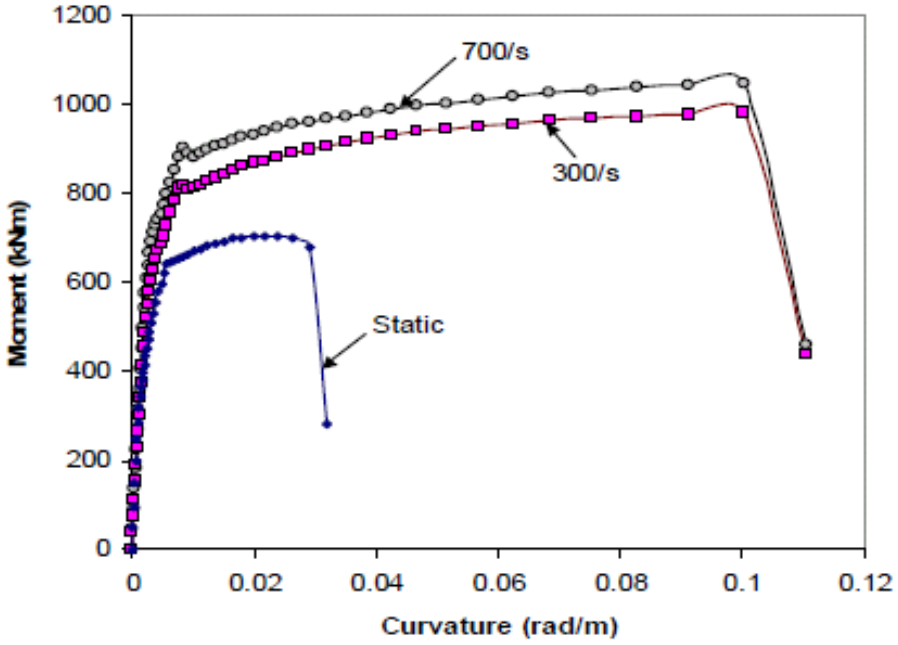

Figure 2-7: Moment-curvature curves for a cross-section of a column at different strain rates (Ngo et al., 2007)

Grote DL, Park SW and Zhou M, 2001

Experimental studies have been conducted demonstrating the existence of strain-rate sensitivity in concrete and cement mortar. Grote et al. (2001) produced experimental data for extreme conditions using plate impact and split Hopkinson pressure bar (SHPB) experiments to generate strain rates over the range of $10^2 – 10^4$ s^{-1} and pressures of up to 1.5 GPa. The applicability of the results with regards to impact loading is questionable as the strain rates and stresses are beyond the generally accepted realm when discussing impacts. Quasi-static experiments were also conducted. The testing was performed on concrete and pure mortar; pure mortar having the same composition as the mortar phases in the concrete. During quasi-static testing, the compressive strength of the mortar, obtained following ASTM standard C39-96 for unconfined uniaxial pressure tests, was found to be higher than the compressive strength of the concrete. This was attributed to micro-cracks that develop along the matrix-aggregate interface and that subsequently transform into macro-cracks with increasing load.

Some very indicative curves by Grote et al. (2001) depict strain-rate sensitivity of mortar in Figure 2-8 and Figure 2-9. The figures illustrate that the maximum compressive stress of mortar at strain rates of 1500 s^{-1} is nearly 3.5 times that observed at a strain rate of 290 s^{-1} (160 vs 45 MPa). Also, for strain rates below 100 s^{-1}, strain rate does not seem to affect the compressive strength of mortar, but beyond this value there is a sharp and sudden rise in associated

compressive strength demonstrating strain rate sensitivity. Also noticeable is the slight increase in strain at failure with increasing strain rate (Figure 2-9).

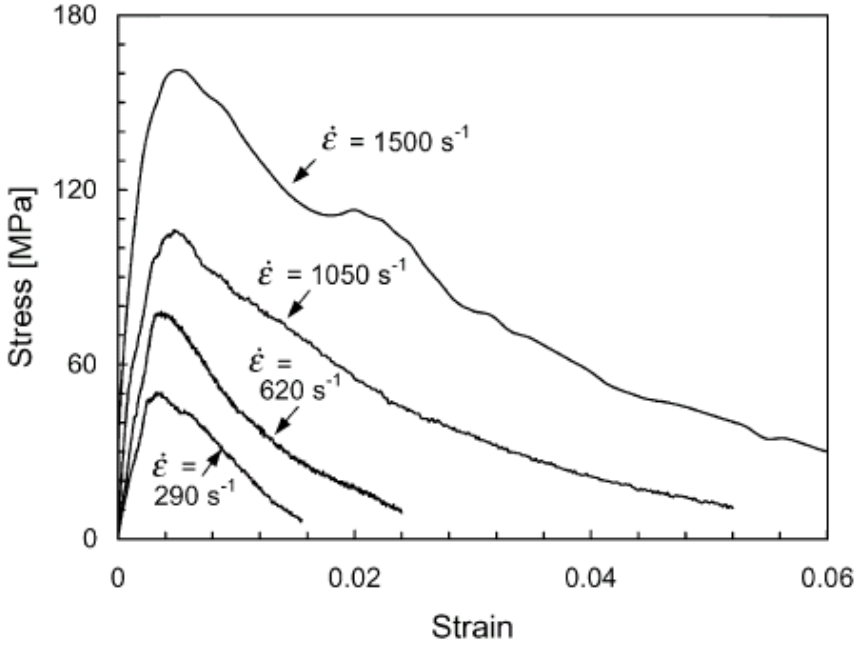

Figure 2-8: Stress-strain behaviour of mortar at different strain rates (Grote et al., 2001)

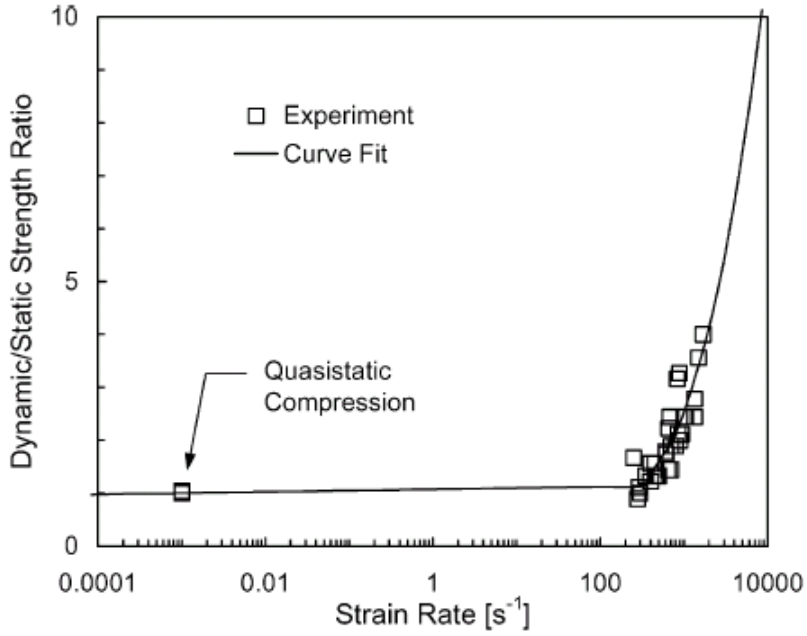

Figure 2-9: Strain-rate dependence of the compressive strength of mortar (normalized with respect to the quasi-static strength) (Grote et al., 2001)

Zhang XX, Ruiz G, Yu RC and Tarifa M, 2009

To gain insight into the loading rate effect on the fracture properties of high strength concrete (HSC), Zhang et al. (2009) performed dynamic three-point bending tests on notched beams using both a hydraulic testing machine and a drop-weight impact instrument. The loading point-displacement rate varied from 10^{-4} to 10^{3} mm/s, while the average concrete compressive strength, f'_c, was 127 MPa. The results clearly indicate that there exists strain rate dependence in HSC as demonstrated in Figure 2-10. At low loading rates, the trend is moderate but beyond a certain loading rate threshold, the tendency is much sharper. The researchers also presented empirical formulae to predict this behaviour.

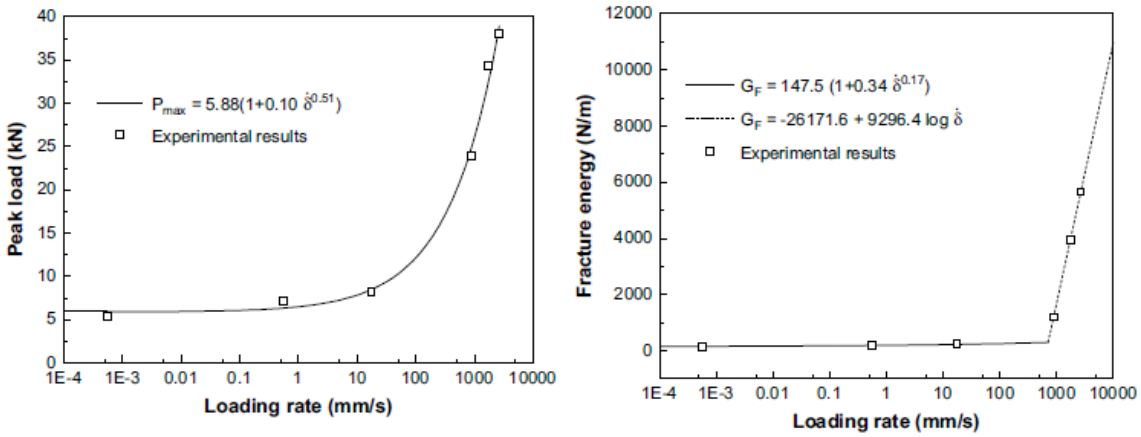

Figure 2-10: Loading rate dependence of the peak load (left) and the fracture energy (right) (Zhang et al., 2009)

Additionally, in the course of their research into the development of a constitutive law to describe the strain-rate-dependant compression behaviour of concrete, Zheng et al. (1999) stated that it is not sufficient to regard the maximum of the strain rate only to describe dynamic material behaviour. Stress history should be related to strain history, meaning that for two identical conditions, if the peak strain rate is the same but the strain history is different, the strength gain will not necessarily match. Also, while stiffness remains practically the same for static or dynamic conditions, the compressive strength of concrete can experience significant gains when specimens are loaded dynamically. More so, the model proposed by Zhang et al. is adequate in predicting stress-strain relations for concrete loaded dynamically using an extended Split Hopkinson Bar (SHB) method.

2.3.2 Explanation of Strain Rate Effect

Rossi, 1997

Except for Suaris and Shah (1983) who attributed dynamic strength gain to inertial forces and matrix cracking, explanations for the results above are limited, though a few researchers have attempted to explain the strain-rate effect more thoroughly. Namely, Rossi (1997), while working for the Laboratoire Central des Ponts et Chaussées (LCPC), attributed the increase in material strength to viscous phenomena due to the presence of free water in the nanopores of concrete hydrates, for strain rates equal to or less than 1 s^{-1}. For strain rates above 1 s^{-1}, the increase in strength was attributed to inertial forces acting on specimens under dynamic loading.

First, consider the pore water explanation for lower strain rates. The Stefan effect plays a large role in explaining the strength gain, it can be summarized as follows: When a thin film of viscous liquid is trapped between two perfectly plane plates that are separated at a displacement rate *h*, the liquid exerts a return force on the plates that is proportional to the velocity of separation. The mechanism is reflected by the following equation:

$$F = \frac{3\eta V^2}{2\pi h^5} \cdot \dot{h} \qquad [2.2]$$

where F is the return force, η is the viscosity of the liquid, h is the initial distance between the two plates, $\dot{h}$ is the velocity of separation of the two plates and V is the volume of the liquid.

Rossi further explains that if it is assumed that the presence of free water in the concrete pores underlies a mechanism similar to the Stefan effect when the solid matrix (here regarded as a network of plates) is subjected to tensile strains. It could thus be understood that loading rate effects are large in wet concretes and very small in dry concretes (Figure 2-11). However, it has been shown that the maximum tensile strength and modulus of elasticity gains are independent of w/c ratio (Figure 2-12). Thus, knowing that the diameter of micropores is independent of w/c ratio, it can be assumed that the micropores of the hydrates play an important role when discussing strain rate effects.

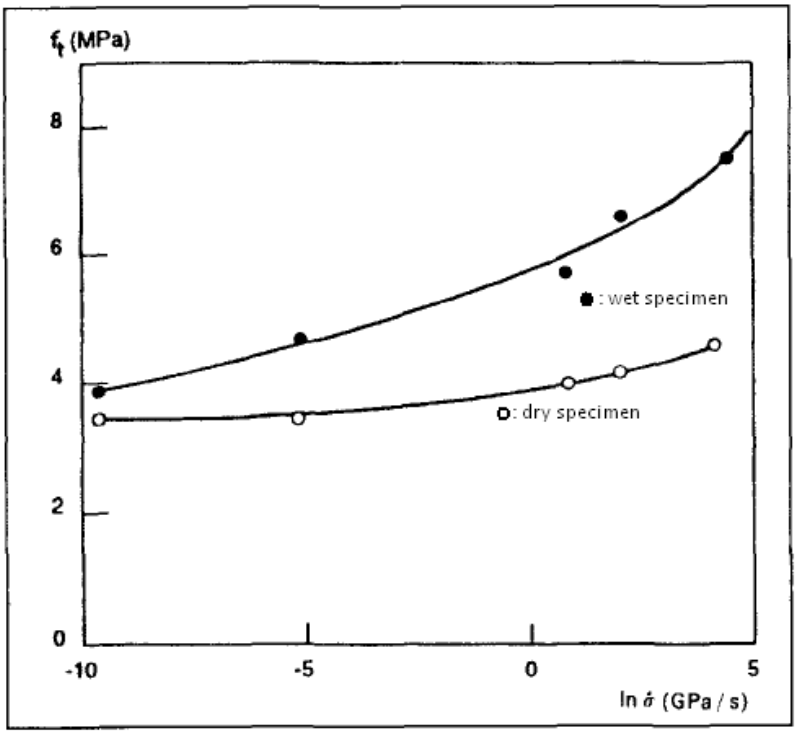

Figure 2-11: Influence of the presence of free water on the strain rate effects in concrete, Rossi (1997)

It should be noted that the Stefan effect has more influence on the peak load than on the modulus of elasticity. For Young's modulus, aggregates play an important role but are not subjected to the Stefan effect.

Rossi also stated that at strain rates approximately below 1 s^{-1}, viscous effects account for the increase in material strength. This mechanism opposes microcracking localization (material level) and macrocrack propagation (structural level). Meanwhile, at strain rates greater than 10 s^{-1}, the forces of inertia account for the gain in strength.

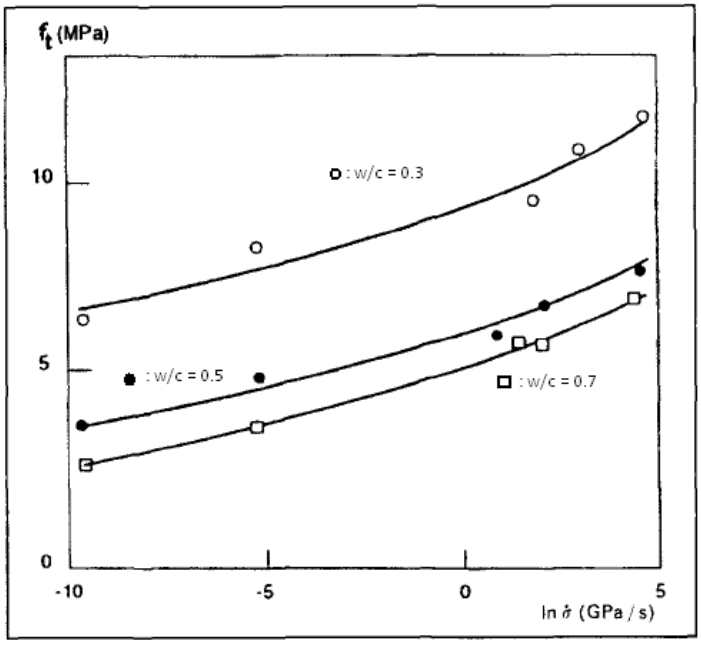

Figure 2-12: Influence of w/c on the strain rate effect in concrete, Rossi (1997)

Cotsovos and Pavlovic, 2008, 2008 and 2010

To explain the strength increase of materials when loaded dynamically, Cotsovos and Pavlovic (2008) presented a two-part study that constituted a major departure from recent thinking regarding material modeling of concrete under high rates of strain. A simplified FE model was employed to investigate the effect of loading rate on the behaviour of prismatic concrete elements under high rates of uniaxial compressive loading in an effort to identify the fundamental causes of experimentally observed apparent strength increase of specimens when a threshold range of loading rates is surpassed. The authors found that it is inertial effects that cause the strength gain.

Past and current empirical models that account for the different behaviour of concrete at higher strain rates are incorporated in FE packages such as LS-DYNA, ABAQUS, ADINA, etc. aimed at accurately predicting the behaviour of RC subjected to extreme loading conditions. These empirical models are referred to as phenomenological since they are based on theories capable of providing a close fit to experimental data without taking into consideration the causes of the behaviour. These models share a number of fundamental assumptions: strain softening, stress-path dependency and load rate sensitivity. The validity of these assumptions was investigated by Cotsovos and Pavlovic (2008). They employed a FE model to reproduce the experimental data, while simultaneously aiming to provide a fundamental explanation for the sudden increase in concrete strength and the overall change in specimen behaviour as a limiting rate of loading is

surpassed. The proposed material model is fully defined by only one parameter, concrete strength, f'_c, and places special emphasis on the response of concrete to triaxial stress conditions.

Cotsovos and Pavlovic (2008) investigated a large number of studies involving strain-rate sensitivities in concrete and found that while a trend exists (Figure 2-13), namely that increased rate of loading leads to increased strength, stiffness and ultimate strain, very large scatter is present making it very challenging to form a universal law on the subject.

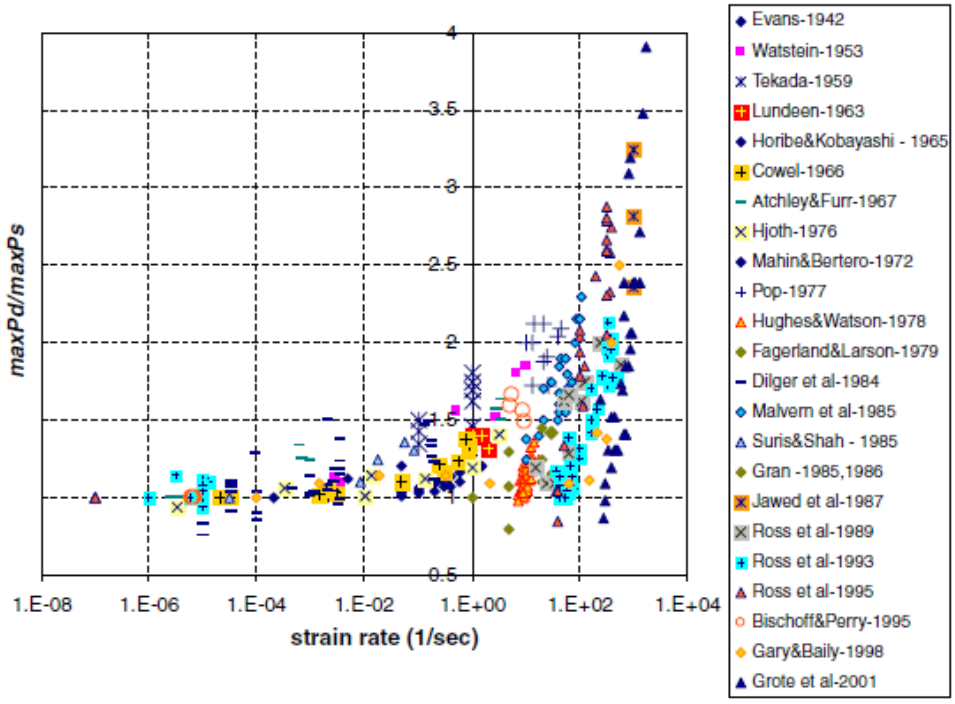

Figure 2-13: Variation of load-carrying capacity with strain rate for concrete in uniaxial compression (Cotsovos and Pavlovic, 2008)

As mentioned, rather than attributing the strength gains to strain rate sensitivity, the authors advance the hypothesis that the entirety of the increased performance at higher rates of loading is due to inertial effects in the specimen. A schematic of the inertial forces acting on a beam impacted at mid-span that the authors claim are responsible for the strength gain in concrete when strain rate is increased is shown in Figure 2-14. For the dynamic case of this diagram, it is important to observe the larger shear forces acting at midspan and the increased length of the negative bending zone near the supports when compared to the static case.

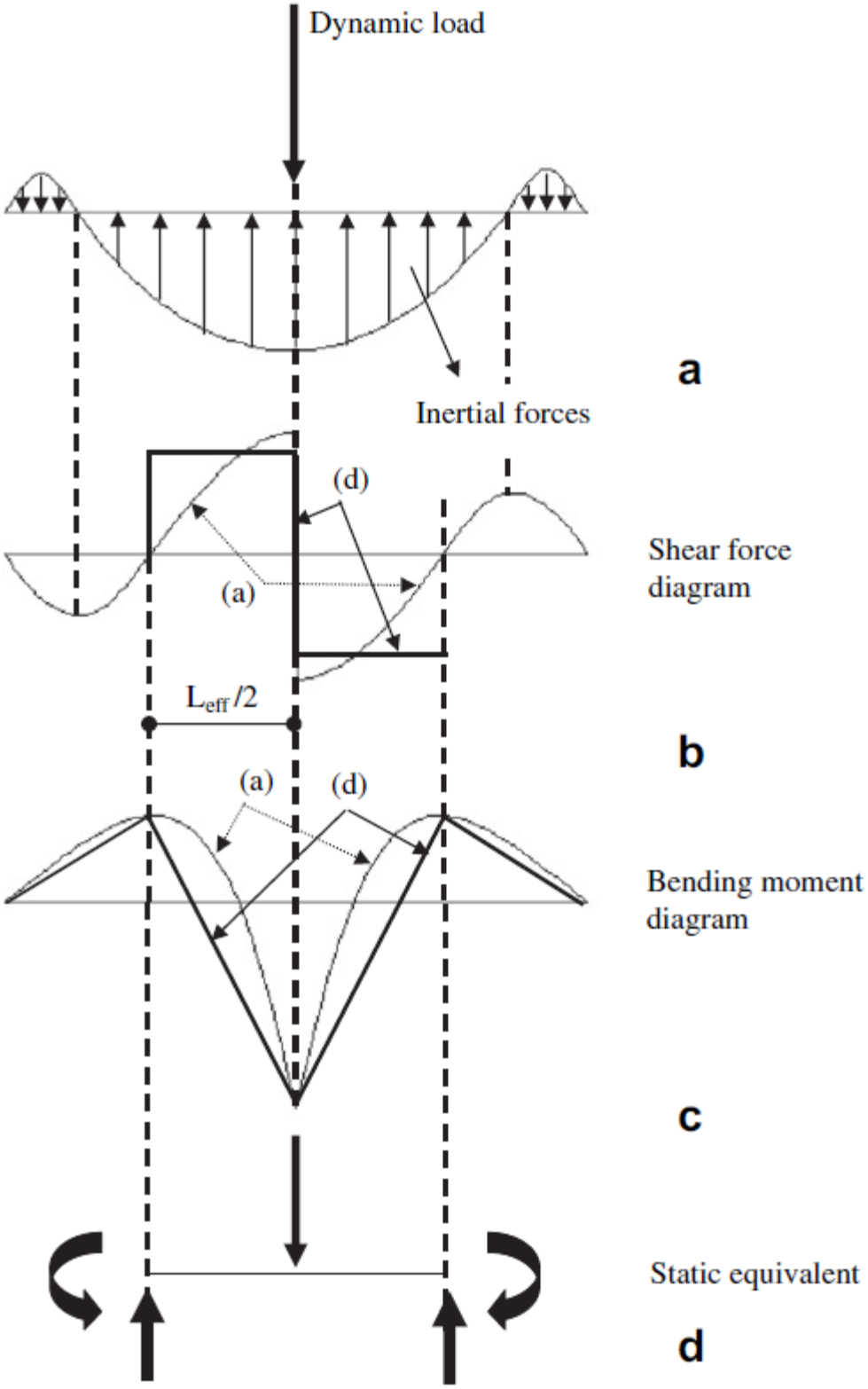

Figure 2-14: Internal actions (b and c) developing under the actual high rate loading (a) and its simplified static equivalent (d) (Cotsovos, 2010)

An explanation of the proposed FE model can be found in Cotsovos and Pavlovic, 2008. The model was in good agreement with the very large number of experiments used for comparison purposes as illustrated in Figure 2-15. According to the researchers, their hypothesis was verified since the change in behaviour in concrete prismatic elements when subjected to high rates of compressive loading could be attributed mainly to the effects of inertia in both the axial and the transversal direction. The inertia loads reduce both the rate of cracking of the specimen and its effective height, factors which lead to an increase in load-carrying capacity.

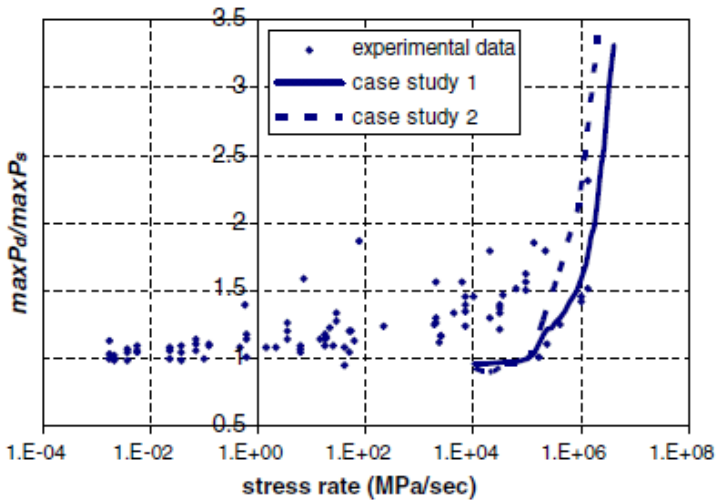

Figure 2-15: Comparison of numerical (two studies) and experimental results describing the variation of load-carrying capacity with the applied stress rate for concrete in uniaxial compression (Cotsovos and Pavlovic, 2008)

Furthermore, it was stated that concrete specimens under dynamic loading cannot be used to describe concrete behaviour since, in contrast to static loading, they do not constitute a material unit from which average material properties may be obtained. Under dynamic tests, concrete specimens must be viewed as *structures* due to mass inertial effects and implied boundary conditions. Thus, using dynamic tests on concrete specimens to develop constitutive material models is questionable.

In the second part of Cotsovos and Pavlovic's 2008 study, the new FE model was used to quantify the importance and effects of parameters such as f'_c, testing method, shape and size of specimens, concrete density and moisture content, etc. when conducting tests on concrete at high rates of loading. Based on data obtained from the numerical parametric investigations, it was concluded that the individual effect of the variation of f'_c, the specimen dimensions, loading conditions or material density only partially account for the magnitude of the scatter that characterizes the available experimental data. The scatter could be explained by considering the different loading

setups and strain rate definitions that researchers have used in the past century on research conducted with regards to concrete material properties at high rates of loading. To truly analyze the material properties of concrete under high rates of strain, it is recommended to use the split-Hopkinson pressure bar (SHPB) test with short specimens.

Additionally, Cotsovos et al. (2010) stated that it is very difficult to obtain experimental results that fall within an acceptable standard deviation. Most experimental results exhibit very large scatter. Figure 2-16 shows the results obtained from high rate impact tests on a RC beam performed by Hughes et al. (1982).

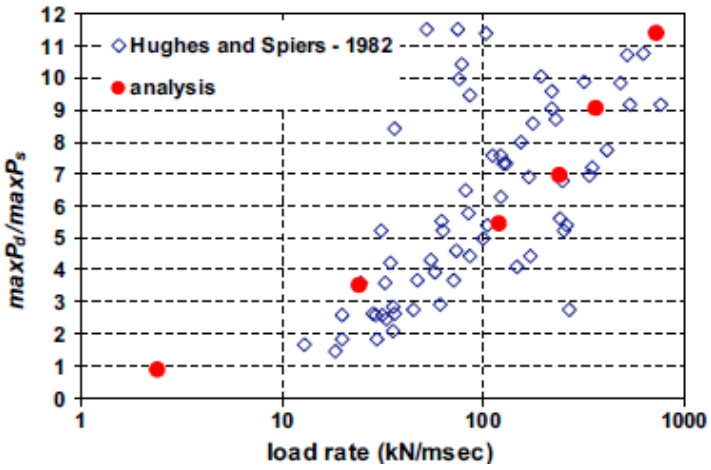

Figure 2-16: Experimental and numerical data expressing the variation of load-carrying capacity of the RC beams with the applied loading rate (max Pd = capacity under dynamic loading; max Ps = capacity under static loading) (Hughes et al., 1982)

The figure demonstrates that the spread of load carrying capacity values for a given loading rate is larger than the mean value for a given loading rate. This scatter could be caused by the number of parameters relating to the experimental setup or the specimen details (shape and mass of striker or tup, beam dimensions, type of pad used, boundary conditions, type and specifications of reinforcement, grade of concrete, etc.).

However, Cotsovos et al. (2010) stated the scatter reflects the inability of the experimental techniques adopted to closely correlate the measured response of the actual physical state and strength characteristics of the specimen. Also, the applied load, P(t), is usually expressed from the expression:

$$P(t) = m * a(t) \qquad [2.3]$$

where *m* is the impactor mass and *a(t)* is the measured value of the impactor's deceleration after contact with the specimen, with load carrying capacity defined as the maximum value of *P(t)*. However, deceleration continues well after the true load carrying capacity is attained, with max *P(t)* often corresponding to a physical state of the specimen characterized by concrete disintegration and low residual load carrying capacity, the latter provided by other mechanisms than beam action such as catenary action of the reinforcement (Cotsovos et al., 2010).

It is important to note that Cotsovos et al. (2008) acknowledged that the modification of effective material properties when dealing with dynamic problems is a practical method for design. It remains that during dynamic impact loading tests, stress waves occur within the material causing the development of high stress concentrations in localized regions of the specimens, leading to localized tensile failure and cracking. Thus, the behaviour of RC elements under high loading rates is a complicated, non-linear wave-propagation dynamic analysis problem (Cotsovos et al., 2008).

2.4 Experimental Observations in Drop Weight Impact Testing and Axial Load Applications

Banthia N, 1987

Banthia experimentally tested over 350 concrete specimens under impact load to develop a repeatable impact testing procedure and better understand the response of concrete to impact. Plain concrete, fibre reinforced concrete and conventionally reinforced concrete specimens were tested, the vast majority of which had 960 mm clear spans with 100 mm x 125 mm cross sections. The impact mass was selected to be approximately eight times the specimen mass to ensure specimen failure under a single blow. While Banthia aimed to develop a comprehensive impact testing method, no lateral deflection data was recorded for any of the tests. The recorded data included the tup load, the support reactions and acceleration data from three accelerometers. The displacements could be obtained analytically by double integration of the accelerations, but this could not be validated experimentally. The author concluded that due to specimen inertial effects, the impact load between the hammer and the beam was not the true bending load; the true bending load was based on the difference between the effective inertial load acting at midspan and the impact force. This actual stressing load on the specimen was as low as 15% of the recorded tup load. It was also established that the use of stirrups increased the impact resistance compared to reinforced concrete beams without transverse steel reinforcement.

Louw J, Maritz G and Loedolff M, 1992

Louw et al. (1992) studied the response of 28 RC cantilever columns under axial load subjected to a soft (similar to a vehicle) horizontal impact load at mid-height. Static tests were also performed for comparison purposes. The duration time from contact to peak impact load was between 20 and 100 ms and the measured strain rates in the column varied between 10^{-3} to 10^{-2} s^{-1} with impact velocities around 7 m/s. Figure 2-17 depicts the test setup for this study.

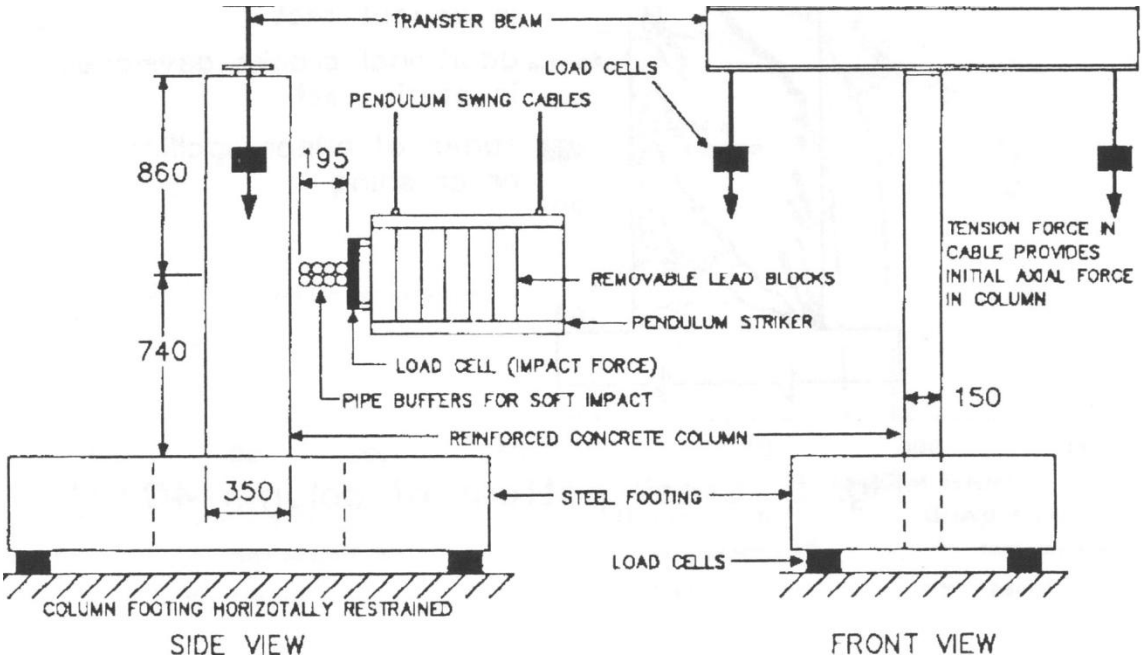

Figure 2-17: Test setup for experimental program of Louw et al., 1992

An important observation made by the researchers was the increase in axial load under both dynamic and static loading. This increase was attributed to the lengthening along the centroidal axis of the column due to flexural cracks that "move" the neutral axis away from the centroidal axis. This lengthening exceeds the downward displacement caused by the flexural loading and is restrained by the flexural stiffness of the horizontal transfer beam on top of the column resulting in increased axial load. The authors speculated that this increase in axial load does not affect the ultimate strength of the column. The ratios of maximum dynamic to static responses for the column were obtained for shear, moment and reaction.

For columns whose only difference was concrete strength, a 93 % increase in concrete strength resulted in about 33 % increase in impact strength of the column and a 17 % increase in static strength. As for the influence of shear reinforcement, reducing the stirrup spacing in a column

from 250 to 100 mm resulted in a 100% increase in ultimate impact strength. Also worth mentioning, this paper is the first encountered were the modified compression field theory (MCFT) was used to predict the strength of RC elements under impact loads.

Remennikov and Kaewunruen, 2006

The experimental behaviour of quarter-scale reinforced concrete columns designed to Australian Standard AS3600 under static and impact loads was investigated. Contrary to most impact tests on columns, the specimens tested were fixed-fixed; conditions provided by concrete block footings that were cast monolithically with the columns. The applied axial load was ~25% of the nominal axial capacity of the specimens which was chosen to represent realistic service loads on a column. The only variables for tests were the type of longitudinal steel reinforcement (No. 10 or No. 12 bars) and the impact drop height. It was observed that all specimens failed suddenly in shear near mid-span with limited flexural cracks. Figure 2-18 shows the concrete block footings that provided the fixed-fixed end support conditions as well as a typical brittle shear mode failure that occurred from an impact of 160 kg falling from 1.5 m. Based on findings from other studies, the authors of this study attributed the increase of modulus of elasticity, strength and toughness of concrete material under impact loading to the development of cracks through rather than around granular aggregate.

Figure 2-18: Impact test setup showing block footings and shear failure of specimen (Remennikov and Kaewunruen, 2006)

S. Saatci, 2007

Saatci conducted an experimental drop-weight testing program on eight RC beams to corroborate a two-dimensional nonlinear finite element analysis program that was modified to include dynamic loading conditions. The beams were 250 mm in width, 410 mm in height and 4880 mm in length, were simply supported with a clear span of 3000 mm and had a 940 mm overhang at each end. All beams had the same longitudinal reinforcement configuration (ρ = 1.6%) with the shear reinforcement varying from 0 to 0.3%. Special supports that permitted rotational freedom were fitted in order to prevent any uplift from occurring at the supports. The specimen was clamped down from the top onto a hinge by No 30 bars that were secured to spherical bearings that permitted rotation of the setup at each end (Figure 2-19).

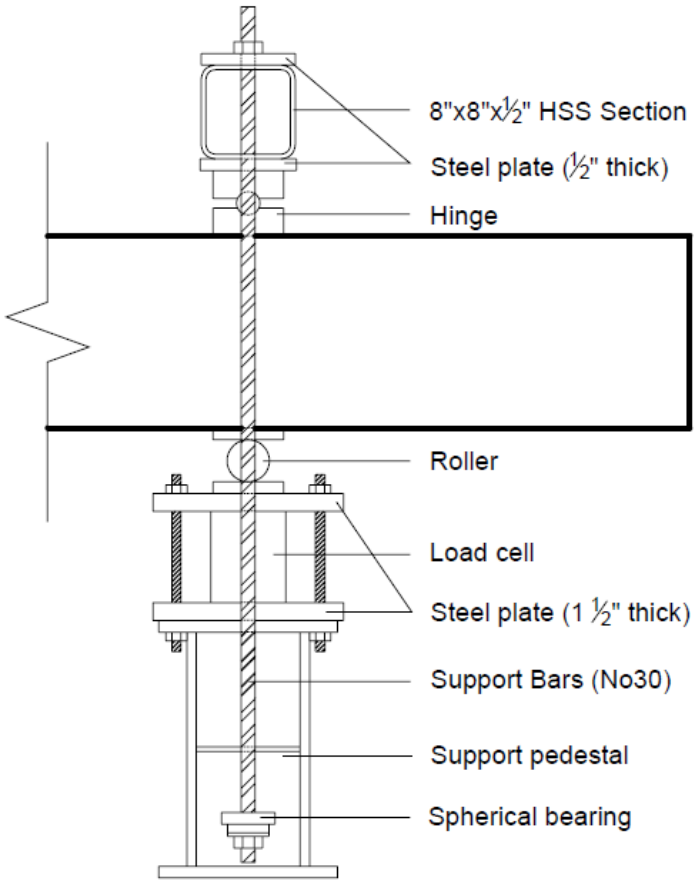

Figure 2-19: Side view of specimen support (Saatci, 2007)

Some important observations were made in the experimental portion of this study.

1) During experimental impacts, linear variable differential transformers (LVDTs) and linear motion position transducers (potentiometers) were used to measure displacements along the

specimens. It was observed that the potentiometers generated significantly less noise than the LVDTs and, as a result, the use of LVDTs was abandoned halfway through the testing regimen.

2) It was observed that if the drop-weight mass was allowed to directly impact the RC specimen, significant local damage occurred. To prevent this local damage and promote a more global response of the specimen, a 50 mm thick steel plate was placed on top of the specimen.

3) A sampling rate of 2.4 kHz for displacement data, strain data and load cell data measurements was deemed sufficient to accurately capture specimen response under impact. This value would seem low compared to other research where, generally, the sampling rate is minimally 100 kHz. The 2.4 kHz sampling rate was determined to be insufficient to capture accurate accelerations due to high frequency vibrations in the specimen and drop weight following impact.

4) The specimens did not behave in the manner of a SDOF system since the beam overhangs and the formation of shear plugs introduce complexities that cannot be accounted for by a simple SDOF system.

5) In the initial stages of response, the specimens experienced the same shear force but significantly smaller moments than it would under static loading, thus becoming shear-critical, forming diagonal shear cracks and shear plugs.

6) The dynamic energy dissipation capacity of the specimens was significantly higher than their static energy dissipation capacity.

Cotsovos D, Zeris C and Stathopoulos N, 2008

By examining the deflected shape of simply supported concrete beams subjected to impact loads at their midspan that were tested by Miyamoto et al. (1989), Cotsovos et al. concluded that the deflected shape displays a slope discontinuity point when the loading rate increases, Figure 2-20.

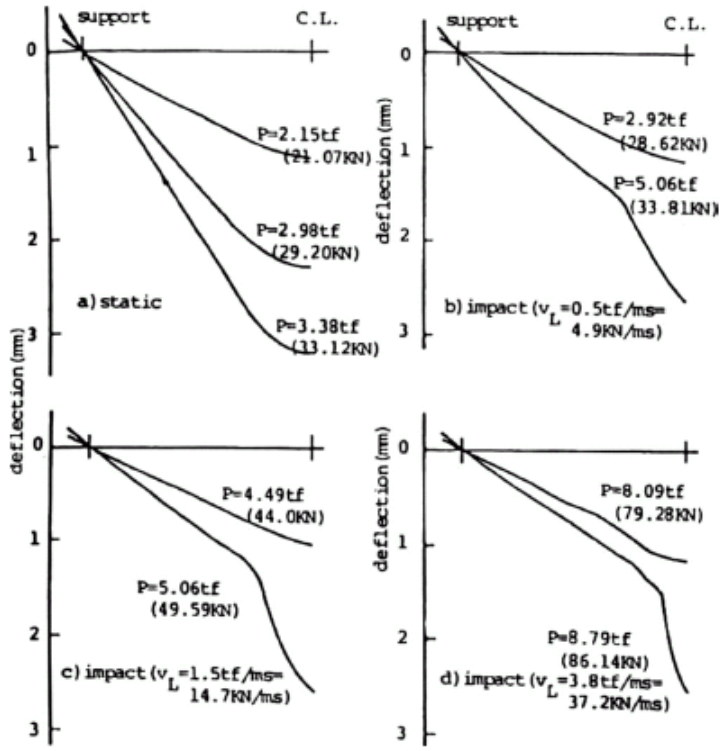

Figure 2-20: Deflected shape predicted by analysis for RC beams under transverse load applied at midspan for various rates (Miyamoto et al., 1989)

Cotsovos et al. (2008) refer to the section of the beam about the center line between these two discontinuity points as L_{eff}. As illustrated in Figure 2-20, L_{eff} is the zone in which, as the loading rate increases, the deflections measured increase at a much higher rate than outside this zone. Also, as loading rate increases, the length of L_{eff} decreases, showing that damage becomes more localized as loading rate increases. Observing cracking patterns under dynamic loading further corroborates this behaviour. Furthermore, this slope discontinuity would appear to indicate the exact location of the beginning of the shear plug observed by, amongst others, Saatci (2007).

Data obtained also indicated that the higher the loading rate, the higher the difference between the applied load and the support reaction. It may thus be assumed that the stress wave generated by the impact at mid-span is unable to reach the supports due to two reasons: Firstly, due to the short duration of the loading procedure which can be less than the time required for the wave to reach the supports; and secondly, due to damage associated with cracking of the concrete and yielding of the steel which would absorb part of the energy transmitted and bound the response. This localized response, which has been verified analytically and experimentally, cannot be accounted for with traditional SDOF modeling and is completely different than response at low rates of

loading. Because of the above mentioned reasons, the external load does not affect the entire member, only L_{eff}, which acts as a beam fixed at both ends and whose span decreases as the loading rate increases. It is this decrease in the length of L_{eff} which is responsible for the increase in overall stiffness and strength of the beam. A formula is given for finding the peak dynamic load as well as L_{eff} depending on the rate of applied loading, wave speed, and flexural moment at onset of cracking. It was concluded that an increase of load carrying capacity associated with increased loading rate reflects the change in the manner that the structural element responds to the applied load rather than to an increase in the flexural capacity.

Fujikake K, Li B and Soeun S, 2009

Fujikake et al. performed drop hammer impact tests on twelve RC beams expected to fail in flexure. The influence of drop height and the amount of longitudinal reinforcement were the principle parameters investigated. The specimens tested had a 1400 mm span with cross sectional dimensions of 150 mm x 250 mm. The drop weight impactor had a mass of 400 kg and was instrumented with a dynamic load cell to measure the impact force-time history. Data was recorded at a rate of 100 kHz. Specially designed end supports were used. While no specific detail was given about these supports, it appears that their use was meant to allow end rotations while preventing uplift of the specimen under impact (Figure 2-21).

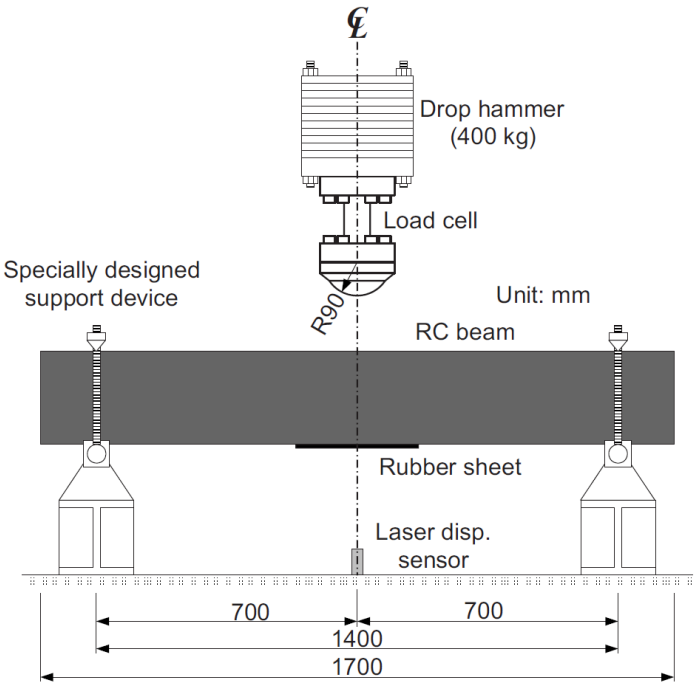

Figure 2-21: Drop hammer test setup (Fujikake, 2009)

Non-linear analysis was performed to predict the flexural capacity of the beams and an analytical model was also developed to determine the maximum midspan deflection of RC beams subjected to impact loads at midspan. The experimental results were used to validate the analytical data. It was noted during the experimental phase that for a RC beam with an under-reinforced section, increasing the amount of tensile reinforcement can cause local failure near the impact loading point. It was also concluded that increasing compression zone longitudinal reinforcement tends to decrease the risk of localized failure.

Khalighi, 2009

Khalighi tested reinforced concrete beams strengthened with FRP under impact. The impactor had a mass of 591 kg and could be dropped from heights up to 2.5 m while data was recorded at a rate of 100 kHz. The specimen that produced the best results was a beam with 550 mm x 150 mm x 150 mm dimensions with a deep notch cut into the tension side to prevent the development of any concrete tensile forces. An important observation was made during impact tests: if the specimens are not prevented from vertical movement at the supports, contact between the supports and the specimen will be lost resulting in unreliable experimental results. To prevent this uplift, steel yokes were used at either support as shown in Figure 2-22. The designed supports performed well to prevent uplift of the beams during impact while maintaining rotational freedom at the support.

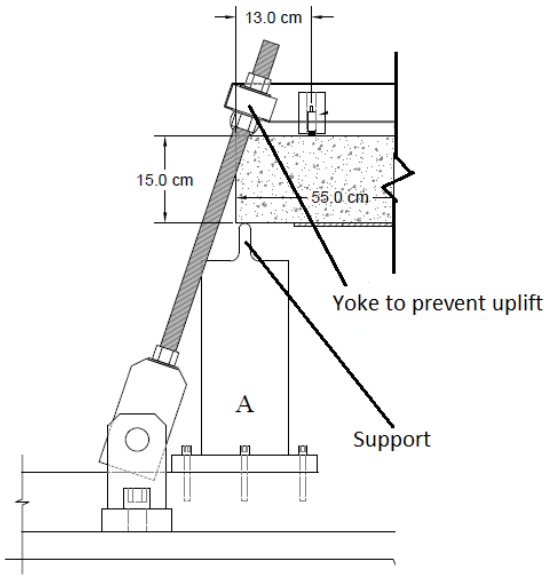

Figure 2-22: Sketch showing half of the final testing setup used for impact testing (Khalighi, 2009)

Bisby L and Ranger M, 2010

The researchers conducted experiments on circular FRP confined RC columns of realistic slenderness under eccentric axial load to address a lack of experimental data pertaining to the mechanics of FRP confined columns in the presence of stress gradients and the development of P-M interaction diagrams for confined RC columns. Fourteen pin-ended, small scale circular RC columns were tested to failure under monotonic, eccentric axial compressive load. Two parameters were varied among the tested columns: the presence of FRP confinement in the form of a single carbon fibre hoop wrap; and the eccentricity of the axial load which varied from 0 to 40 mm. Of interest to this thesis is the manner in which the axial load was applied to the specimens as illustrated in Figure 2-23.

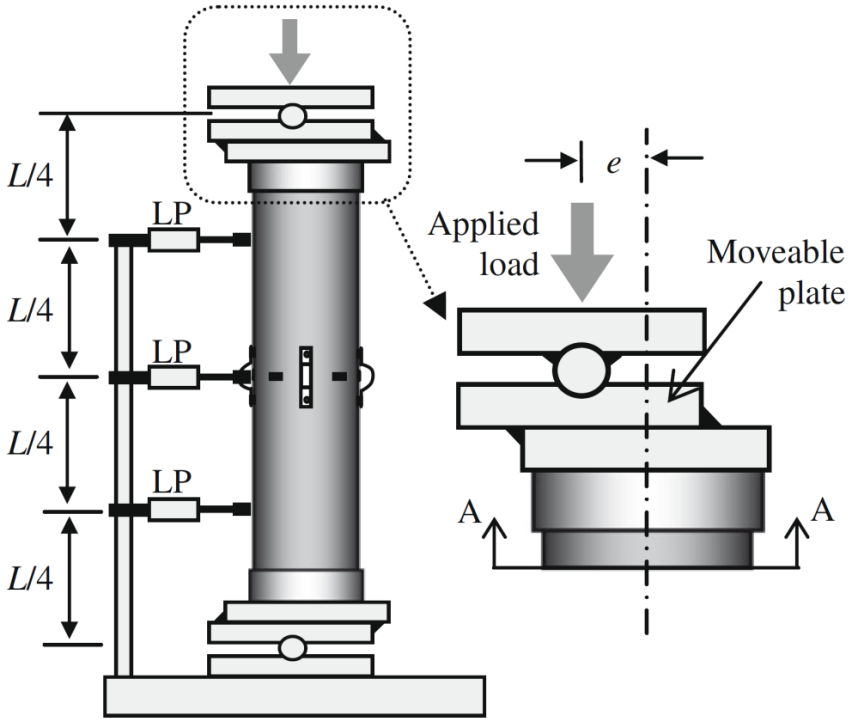

Figure 2-23: Instrumentation and test setup for column specimens (Bisby and Ranger, 2010)

The tests were performed in a 1000 kN servo-hydraulic testing frame. To create the pinned end support conditions for the specimens, steel collars and quick-set mortar were used to rigidly fix the column ends to thick steel plates. Steel rollers that were nested in precision machined semi-circular grooves in opposing end plates were used to adjust the eccentricity of the axial load. Outer hinge plates to which the steel rollers were welded were bolted into the loading head and test table of the testing machine to force bending in a predetermined direction. Bisby and Ranger concluded that: FRP confinement of eccentrically loaded columns significantly increased peak

load while decreasing lateral displacements at peak load; reductions in capacity due to load eccentricity are more pronounced for FRP confined columns than for unconfined columns; and the strain gradient caused by eccentric loading produces uneven confinement of the column cross-sections, with maximum hoop strains at the extreme compression fibre.

Ozbolt J and Sharma A, 2011

Experiments that were reported in literature were numerically simulated using three dimensional finite element methods by the researchers. The impact was not modeled as the collision of two bodies; instead, the load point displacement was incremented until the maximum value and at the rate reported. The results obtained from the analysis were in close agreement with the experimental values for the static and dynamic reactions, the crack patterns and the failure modes. The impacts reported on were considered blunt impacts with velocities of approximately 1 m/s. An important conclusion reached was that the amount of shear reinforcement can significantly affect crack patterns and the formations of shear plugs, the punching out of the member face opposite impact.

Like Saatci (2007), Ozbolt and Sharma observed the formation of severe diagonal cracks, originating from the impact point and propagating downward with an angle of approximately 45°. Flexural cracks extending from the top surface of the members near the supports were also apparent in the model. Failure in the specimens was attributed to shear forces not reaching the supports due to insufficient strength between the shear plug and the supports. The authors provide incremental crack patterns for different displacement levels that suggest the formation of vertical flexural cracks in the bottom of the specimen at 25% of peak displacement with the formation of shear plug cracks beginning at 50% of peak displacement.

2.5 Retrofits to Protect Reinforced Concrete Elements from Impact Loads

Some research has been conducted to evaluate the impact performance and effectiveness of different impact protection retrofits. The simplest method to mitigate impact damage is through the use and implementation of sacrificial barriers or protective built-up systems. The main function of these protection systems is to prevent the extreme load from reaching the protected element or to significantly decrease/absorb the energy of the impact. Examples of sacrificial barriers or protective built-up systems are guardrails or blast walls, Figure 2-24.

Figure 2-24: Examples of sacrificial barriers: guardrail (left) and blast wall (right)

While the effectiveness of sacrificial barriers is undisputed, their implementation is not always possible. Indeed, if clearance around a structural element such as a column or wall is limited, there may not be enough space to install the system or to allow workers to operate the required machinery. Additionally, occupant access or sightlines to the structure may be hindered by the use of sacrificial barriers. This is why active protection systems that interact directly with the load and the structure must be investigated.

2.5.1 Overheight Impact Protection by Use of Energy Absorbing Bumpers

A common structural problem in existing reinforced concrete (RC) highway overpasses is damage to girder elements caused by the passing of trucks exceeding allowable height clearances beneath bridges. These types of impacts are called overheight collisions. Commonly, for RC girders, the impact causes the cover concrete to spall off, exposing reinforcing steel which contributes to the acceleration of corrosion, reducing load carrying capacity and/or the service life of the structure as shown in Figure 2-25.

Figure 2-25: Damage to concrete and steel bridge girders resulting from overheight vehicular impacts (Sharma et al., 2008)

Beyond prohibiting access to and rerouting overheight trucks from bridges, one method of mitigating damage due to overheight impact is to apply an energy absorber to the lower lip of bridges to deflect and absorb impact forces. Yang and Qiao (2010) concluded that the core of protective structural design lies in the capacity to absorb energy (or decelerate the projectile) while maintaining the stress/deflection/force transferred to the protected structures below prescribed limits that initiate damage or failure to the protected structures. This converted kinetic energy can be reversible such as the pressure energy in compressible fluids and the elastic strain energy in solids, or irreversible resembling plastic deformation energy (Alghamdi, 2000).

H. Sharma, S. Hurlebaus, and P. Gardon, 2008

Sharma et al. (2008) proposed an energy absorbing system or bumper consisting of a stiff guard that distributes the impact energy over a large area and an energy absorbing material (EAM) that dissipates the impact energy (Figure 2-26).

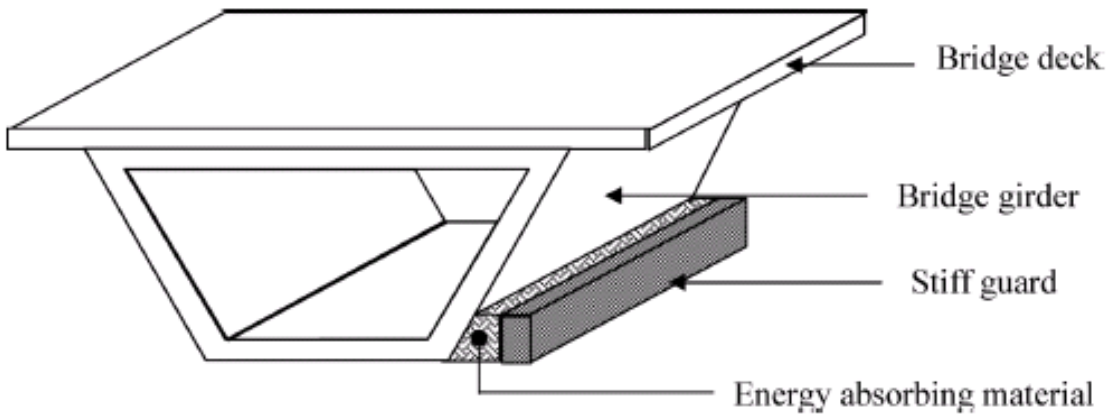

Figure 2-26: Sketch of proposed bumper for bridge girder (Sharma et al., 2008)

This investigation consisted of impacting a scaled concrete beam (representing a bridge girder) retrofitted with varying types of bumpers with solid steel balls. Four different bumpers were tested: each containing a 3.175 mm layer of stiff guard with modulus of elasticity of 200 GPa with differing types of 50 mm thick high-density flexible polyurethane foam acting as the EAM. The specific material used as stiff guard was not specified. Double-sided duct tape was used to attach the stiff guard and the EAM and to connect the bumper to the concrete beam. The experimental results demonstrated the efficiency of the proposed bridge bumper. When comparing the retrofitted girder to the bare original girder, the maximum tensile stress was reduced 73% (from 1.76 to 0.46 MPa), the maximum compressive stress was reduced 98% (from 17.0 to 0.43 MPa)

and the maximum contact force was reduced 96% (from 7.77 to 0.31 kN). The results were validated using the finite element software LS-DYNA. Furthermore, the authors also scaled the results and were thus able to suggest a suitable bridge bumper system for protecting actual concrete bridge girders.

While the system investigated was very effective at decreasing stresses observed during and after impact, a major concern arises regarding its on-field implementation. The system would appear to be relatively heavy, adding eccentric dead loads to the structure. Designers would need to analyze the retrofitted structure to ensure that global performance was not affected by the retrofit. If the analysis reveals that the structure is not able to safely accommodate the bumper, an additional retrofit would be necessary to implement the system or other alternatives would have to be explored.

M. Yang and P. Qiao, 2010

In collaboration with the Ohio Department of Transportation, Qiao et al. (2008) developed, designed, analyzed, fabricated, tested and field-installed a double-layer aluminum honeycomb I-Lam (Impact-Laminate) sandwich system to protect girders from overheight vehicle impacts. The I-Lam system consists of two thin face sheets that sandwich two 4 in. (102 mm) thick honeycomb layers with crushing strength of 90 and 210 psi (0.62 MPa and 1.45 MPa), respectively. Numerous numerical simulations using the commercially available finite element sofware LS-DYNA were performed upon which the authors provided recommended thickness of the I-Lam system to adequately protect a concrete girder from varying hypothetical impacts. The bond between a concrete beam (girder) and the collision protection system provided by an epoxy paste anchoring adhesive was evaluated. Also, the crushing of the I-Lam core was studied by experimentally measuring the deformations and strain fields during the crushing process.

As part of their research, Qiao et al. (2008) conducted three full scale impact tests on RC beams: two retrofitted with the I-Lam and one control. A 12 in. (305 mm) cubic wooden projectile was used as the impactor with an impacting speed of approximately 72 km/h. Based on qualitative observations and comparisons of the RC beams with and without the I-Lam protection system (Figure 2-27), the researchers stated that the I-Lam panels are capable of protecting the substrate material from severe damage and are capable of absorbing the impact energy by crushing of the core materials.

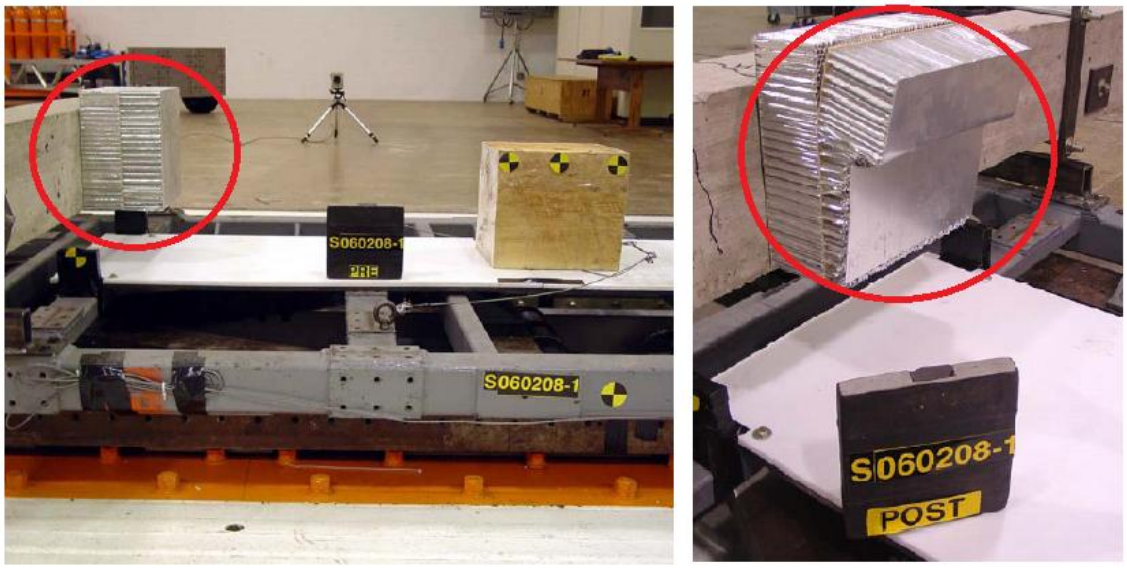

Figure 2-27: I-Lam girder protection system (circled) before (left) and after (right) being impacted by a wooden cube (Qiao et al., 2008)

The protection system was implemented on a concrete bridge in Delaware, U.S. in the fall of 2006 (Figure 2-28). Additionally, the researchers also developed and tested a smart impact detection system capable of measuring the level of damage in a concrete girder using piezoceramic (PZT) transducers. The system also has the capability of photographing the offending (impacting) vehicle. A step-by-step construction method for field implementation of the I-Lam system was ultimately proposed.

Figure 2-28: Field installation of I-Lam panels on concrete bridge (DEL-23-12.99) in Delaware, U.S. (Qiao et al., 2008)

The protection system devised by Qiao et al. (2008) presents certain flaws. It is rather cumbersome and would be difficult to implement in tight spaces or in locations that require architectural aspects and aesthetics to be respected. The system would also likely benefit from a stiff guard such as the one used by Sharma et al. (2008) to distribute the concentrated impact loads over a wider area and reduce damage to the system itself. Like most existing bumper systems, once the system has been impacted, it must be replaced to ensure ongoing protection.

2.5.2 Impact Protection by Use of FRP

Significant research has been conducted to investigate the use of composites in protecting concrete from impact forces. Composite materials are formed by the combination of two or more materials to achieve superior physical and chemical properties. Fibre Reinforced Polymers (FRPs) are a type of composite that has emerged in civil engineering applications. The main components of the composite are the fibre and the matrix.

The fibres provide most of the strength and stiffness while the matrix holds the fibres together providing load transfer from the retrofitted structure to the composite (Uddin et al., 2005). There are many types of fibres available to designers and manufacturers of composites: glass fibres which are inexpensive and versatile; carbon fibres which are lightweight and very resistant but more expensive; and aramid fibres, such as Kevlar, which display high energy absorption at failure but are sensitive to creep, moisture and UV light.

The matrix can fall into one of two categories: thermoset or thermoplastic. In a thermosetting resin, the matrix permanently cures or hardens (sets) into a given shape through the application of heat. A polymerization (chemical linking to create long molecular chains) reaction produces the hardening, and the cured material becomes substantially infusible and insoluble (ISIS Canada, 2008). Meanwhile, a thermoplastic resin will soften or melt with the application of heat and will harden upon cooling. The process can be repeated nearly indefinitely.

The use of externally bonded composite materials such as FRP for the strengthening and retrofitting of existing or new structures has been adopted in construction practice. This is due to the light weight, high strength, good durability, high fatigue endurance, competitive cost, low thermal coefficient in fibre direction, and ease of installation of available composite materials. A number of methods exist for external strengthening of columns using composites. Wrapping is the most common and consists of unidirectional fibre sheets or woven fabric sheets impregnated

with polymer resins and wrapped around the column with the fibres principally oriented in the hoop direction. Filament winding is similar to wrapping except that it utilizes continuous fibre strands instead of sheets. Pre-fabricated shell jacketings are built off-site and are usually in the shape of a half-circle or half-rectangle so that they can be opened and placed around deficient columns.

2.5.2.1 Thermoset FRP Impact Testing

D. Jerome and C. Ross, 1997

Jerome and Ross (1997) experimentally investigated the dynamic behaviour of beams externally strengthened with varying amounts of FRP on the bottom or tension side subjected to drop-weight impact at the midspan. The beams were small in dimension (7.62 cm x 7.62 cm x 76.2 cm), thus no reinforcing steel was provided. The beams with composite wrap on the side faces and bottom (tension) side were also tested. It was consistently observed that the average static peak capacity was less than the dynamic peak capacity. This was attributed to strain-rate effects in the concrete. Also, for beams retrofitted with composites, the dynamic energies were consistently less than the static energies. The addition of external CFRP significantly stiffened the beam, enhancing the beam's brittle behaviour when loaded dynamically. The mechanism by which the beams failed dynamically was similar to that for the static case; shear failure of the concrete at approximately one-quarter of the span from the midspan followed by delamination and peeling of the CFRP. It was concluded that significant gains in terms of load and displacement capacity were achieved by application of the retrofit.

M. Erki and U. Meier, 1999

Erki and Meier (1999) investigated concrete beams subjected to impact loads that were retrofitted with CFRP laminates. The results were compared to previous studies where concrete beams were retrofitted with steel plates. A novel approach to induce impact forces was utilized: the impact was produced by raising one end of the beam and dropping it from a certain height. While not representative of any real impact scenarios, the tests provided valuable results regarding retrofit detailing. The loading-induced rates of strain ranged from 0.057 s^{-1} to 0.8 s^{-1}. The amount of CFRP used in the retrofit was such that the total tensile strength provided by the CFRP (200 kN) was approximately equal to that of the steel plates in the previous retrofit scheme (207.5 kN). During testing, energy was first absorbed by a damper located at the point of impact and then by the beams, through concrete cracking and reinforcement yielding. For the beams retrofitted with steel plates, further energy was absorbed by yielding of the plates and by debonding. For the

CFRP strengthened beams, the bonded CFRP laminates absorbed energy through the formation of longitudinal cracks in the epoxy layer and by tension failure of the CFRP laminate. It was observed during the explosive failure of the CFRP in tension that many small and jagged fragments of the CFRP projected a significant distance from the beam. The failure was attributed to both debonding and tensile failure: one of the two plies of CFRP would debond, overloading the second, which would fail in tension. It was concluded that the RC beams externally strengthened for flexure with CFRP laminates performed well under impact loading although energy absorption was less than the beams externally strengthened with steel plates. It was recommended that additional anchoring of the CFRP would increase the impact performance of the beams. Additionally, the midspan deflections for the beams were predicted using an equation of motion with satisfactory results.

T. Tang and H. Saadatmanesh, 2003

Tang and Saadatmanesh (2003) conducted experiments to study the effects of impact on concrete beams strengthened with FRP laminates. In all, twenty-seven beams were tested but only five beams were steel reinforced (two No.3 bars): two strengthened with Kevlar laminates; two strengthened with carbon laminates; and one control specimen. The retrofit materials were applied to both the top and bottom of the reinforced concrete beams because of the decaying cyclic vibrations caused by impact loading and the associated compression-tension stress cycles that the top and bottom of the specimens would experience. It was demonstrated that the composite laminates significantly increased the flexural cracking strength, shear failure strength and peak failure load of the beam, and decreased deflections. However, the strength related to diagonal cracking was not significantly affected. Also, vibrations in the beam due to inertial effects were sufficient to cause strains resulting in cracking of the concrete and significant deflections.

J. Kirby and S. Orton, 2011

To further explore the strength reduction of CFRP retrofits applied to concrete that have been damaged by transverse impact, the researchers impacted seventy-nine CFRP coupons and tested their residual tensile strength. The CFRP system coupons were applied to the concrete using the traditional wet-layup method with the difference that a sheet of plastic was inserted between the concrete substrate and the CFRP coupon in order to avoid damaging the coupon when removing it from the concrete surface (Figure 2-29). The impact force was imposed by a drop weight impactor with a total striker mass of only 9.1 kg with dropping heights between 0.46 and 2.74

meters. Three levels of damage were observed and qualified: fibre indentation (4% drop in control strength); epoxy matrix damage with whitish areas visible (37% drop in control strength); and fibre breakage (77% drop in control strength). An impact pressure threshold of 21 MPa was observed as the limit for which impacts below that value caused no strength reduction in the samples.

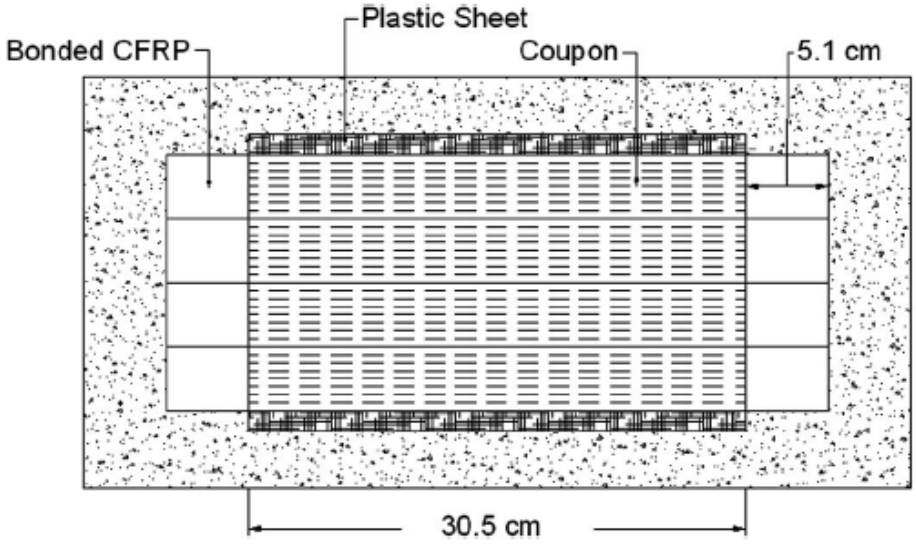

Figure 2-29: CFRP application schematic (Kirby and Orton, 2011)

2.5.2.2 Thermoplastic FRP Impact Protection

Thermoplastics are relatively new materials that have evolved from conventional thermoset composites. They consist of two elements: a thermoplastic matrix and a reinforcing fibre. One reason that they are not as widely used as thermoset composites is that until recently, the processing and moulding of thermoplastics was difficult. In addition, there is concern within the industry as to the sensitivity of this type of composite to heat: thermoplastics can be softened by increases in temperature. It was demonstrated that glass reinforced thermoplastic tested at 204°C experienced considerable weakening: the longitudinal and transverse strengths were lowered by 85% and 37% of their original values, respectively (Milke et al., 1993). A concern is whether thermoplastic FRPs used to retrofit columns to resist impact loads resulting from vehicles or explosive debris would be subjected to similar high temperatures. It is probable that impact generated loads could occur in conjunction with a heightening of temperature. However, thermoplastic composites offer many advantages over thermoset composites: they have a nearly unlimited shelf life, unlike thermoset FRPs that are unstable in their prepregnated form; they do

not require a chemical process to cure; they are less brittle; damage is more easily observed; and they offer better impact resistance.

D. Dixon, 1990

Dixon (1990) conducted research on thermoplastics for the aerospace industry. Flat plate impact tests using a helium-driven gas gun were conducted to better understand the spalling failure of flat carbon fibre reinforced poly ether ether ketone (PEEK) thermoplastic specimens. The rate of loading varied from 36 m/s (no delamination) to an impact velocity of 520 m/s (specimen disintegration). It was concluded from the tests that spall failure in CFRPEEK begins in the matrix rich zone between plies and is brittle. When complete spall separation occurs the spall surface is rough, showing subsurface damage and extensive fibre breakage. It was also observed through electron micrography that crack initiation begins in the matrix.

N. Uddin, N. Farhat, U. Vaidya and J. Serrano-Perez, 2005

Uddin et al. (2005) conducted research investigating the reduction in vulnerability of RC columns by retrofitting with a polypropylene (PP) thermoplastic FRP developed for construction purposes. Tests were done to characterize the bond between concrete and PP to develop and implement a method for retrofitting concrete cylinders with glass-reinforced PP (glass/PP) confining jackets. The intent was to determine the energy absorption capacity and ballistic limit and, finally, to replicate ballistic impact results using a FE numerical model. The design and manufacture of the glass/PP composite was completed jointly by researchers at the University of Alabama in Birmingham and the Southern Research Institute (SRI). The result was a thermoplastic composite material produced in pultruded continuous form. It was determined that the bond between the concrete cylinder substrate and the thermoplastic tape was sufficient since the jacket fitted tightly around the cylinder providing adequate confinement during impact events. Stress-strain relationships obtained for the retrofitted cylinders indicate that the thermoplastic jacket increases the ductility response (peak strain was nearly 15 times greater for the retrofitted specimen) without affecting peak load. The authors were also able to accurately model the perforation of concrete plates subjected to missile impacts ranging in speeds from 60 m/s to 121 m/s.

N. Uddin, J. Purdue and U. Vaidya, 2008

Uddin et al. (2005) conducted research investigating the reduction in vulnerability of RC columns by retrofitting with a polypropylene (PP) thermoplastic FRP developed for construction purposes. Tests were performed to characterize the bond between concrete and PP to develop and

implement a method for retrofitting concrete cylinders with glass-reinforced PP (glass/PP) confining jackets. The intent was to determine the energy absorption capacity and ballistic limit and, finally, to replicate ballistic impact results using a FE numerical model. The design and manufacture of the glass/PP composite was completed jointly by researchers at the University of Alabama in Birmingham and the Southern Research Institute (SRI). The result was a thermoplastic composite material produced in pultruded continuous form. It was determined that the bond between the concrete cylinder substrate and the thermoplastic tape was sufficient since the jacket fitted tightly around the cylinder providing adequate confinement during impact events. Stress-strain relationships obtained for the retrofitted cylinders indicated that the thermoplastic jacket increased the ductility (peak strain was nearly 15 times greater for the retrofitted specimen) without affecting peak load. The authors were also able to accurately model the perforation of concrete plates subjected to missile impacts ranging in speeds from 60 m/s to 121 m/s.

2.6 Single-Degree-of-Freedom (SDOF) Modeling of Impacts

Single-degree-of-freedom (SDOF) modeling has shown satisfactory performance at predicting the midspan displacement-time history for structural members subjected to dynamic and impulsive loading (Biggs, 1964). The key concept is that if the dynamic midspan displacement of the member with a distributed mass and resistance is known, the displacement at any point along the member can also be known by assuming that the dynamic deflected shape follows that of the equivalent static system. The response of a system subjected to external loads varying with time is based on treating the dynamic forces developing within the system as a static problem. The following equation of motion holds true for any point in time, t_i:

$$F_I(t_i) + F_D(t_i) + F_S(t_i) = F(t_i) \quad [2.4]$$

where, the inertia force, F_I, the damping force, F_D and the spring force, F_S are given by:

$$F_I = M \cdot \ddot{x} \quad [2.5]$$

$$F_D = c \cdot \dot{x} \quad [2.6]$$

$$F_S = k \cdot x \quad [2.7]$$

where F is the applied external force, M is the mass of the system, c is the damping constant, k is the stiffness, $\ddot{x}$ is the acceleration, $\dot{x}$ is the velocity and x is the displacement. The response of members to impact loads is transient and decays rapidly after the load has ceased to act. From an

engineering standpoint, it is the maximum response of the structure and the associated stresses that are of interest, not the vibratory period afterwards. Because of the short duration of response, damping does not have a significant influence and can reasonably be ignored in the analysis (Humar, 2005).

Since the force-displacement relationship of a RC member subjected to a midspan load is non-linear, a closed-form solution for the dynamic response of the column to a midspan impact cannot be obtained. Instead, step-by-step numerical integration techniques must be used to predict the dynamic response. The response is evaluated at successive increments of time, Δt, where, at the beginning of each interval, the condition of dynamic equilibrium is established. The response at the next time increment is evaluated approximately on the basis that the coefficients of mass, damping and stiffness follow a given trend for that short interval of time. The nonlinear characteristics of these coefficients are considered in the analysis by revaluating these coefficients at the beginning of each time increment. The response is then obtained using the displacement and velocity calculated at the end of the time interval as the initial conditions for the next time step (Paz, 1991).

Thus, all that is required for the implementation of a SDOF model is: a static resistance curve providing the midspan relationship between applied load and deflection; an external forcing function that stimulates the studied member; and an equivalent mass for the system that accounts for boundary conditions, distributed mass of the system and assumed deflected shape (usually taken as the first mode of vibration). The equivalent mass, m^*, is easily evaluated using the following integration:

$$m^* = \int_0^L \bar{m}\{\psi(x)\}^2 dx \qquad [2.8]$$

where, $\bar{m}$ is the mass per unit length of the specimen, L is the length of the specimen and $\psi(x)$ is the shape function. The equivalent mass, m^*, of a simply supported beam or column is thus found to be:

$$m^* = \frac{17}{35}\bar{m}L \qquad [2.9]$$

Taking into account this equivalent mass, m^*, which replaces M in the equation of motion; the midspan stiffness of the structure obtained from the static resistance curve; the external forcing function; and neglecting damping, the equation of motion becomes:

$$F_i(t_i) + F_S(t_i) = F(t_i) \qquad [2.10]$$

The corresponding idealized free-body diagram is given in Figure 2-30:

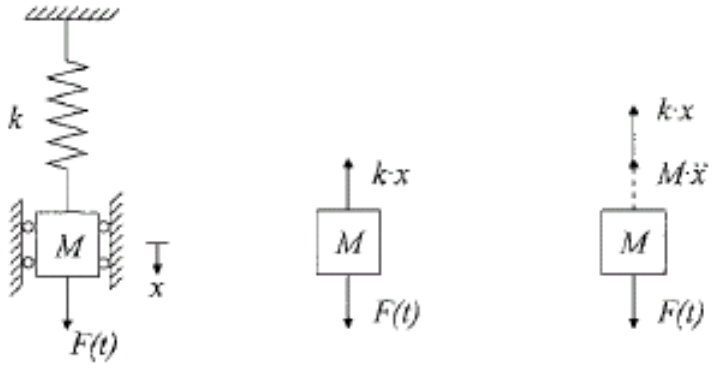

Figure 2-30: SDOF system in dynamic equilibrium

While all of the above theoretically holds true, the accurate prediction of the impact response of RC members by SDOF procedures is not always possible. Saatci (2007) stated that SDOF modeling cannot account for complexities such as shear plug formation and the presence of overhangs outside of the supports that seem to lag behind the predicted response and display a "whip effect" eventually surpassing the predicted displacements. While not completely capturing the full behaviour of impacted structures, it seems that SDOF modeling can still be used to approximately estimate member response to impact loading.

2.7 Summary

While much effort has been invested towards investigating dynamic phenomena and methods of protecting RC against impact loads, more work is needed in this field. The relative novelty of impact research, the material and structural response caused by the extremely rapid application of impact loading and the high cost of full-scale impact testing are reasons to justify the lack of knowledge. The literature review conducted herein raises further questions relating to impact testing and identifies some experimental procedures that could be improved upon.

While some researchers have observed the uplift of impacted specimens from supports and corrected for it by using some form of a rotational clamp, the negative reaction forces that result from restricting the uplift have never been measured. Furthermore, a link between experimental impact tup loads and both the inertia forces within the impacted specimen and the positive reaction loads that occur after impact has been identified but no comment on losses of tup load as the force wave travels through a specimen is offered. In the same vein, a correlation between the observed damage in an impacted specimen and the recorded tup and reaction loads has not been presented. Also, while some research has been conducted to quantify the difference in strength between specimens tested statically and under impact, there has been no attempt to observe differences in failure modes and crack propagation for such specimens. Additionally, the development of a shear plug in RC specimens tested under impact has been observed but an explanation into the shear plug's role in specimen failure and the influence that it may have on strain patterns has not been given. Another major variable that has not been deeply investigated is the application of axial load on a RC member subjected to impact. It would be important to quantify how applying axial load to an impacted member affects the member resistance to impact.

As such, there are still voids of knowledge that can be addressed with further experimental testing of RC members subjected to impact. What follows is a description of experimental procedures that are thought to be advancements in the field of impact testing, a presentation of recorded experimental data and an analysis and explanation into the observed phenomena.

Chapter 3: Experimental Program

3.1 Introduction

This section details the process of setting up an impact test protocol at the National Research Council's structural laboratory in Ottawa, Ontario. It describes the design and construction of impact and quasi-static test specimens, the fabrication of supports, the fabrication and use of an external post-tensioning axial loading system, the use of an instrumented drop-weight impact tower, the use of a hydraulic actuator for the static testing of certain specimens and the instrumentation methods and data acquisition systems used to record impact and quasi-static phenomena.

3.2 Description of Test Specimens

3.2.1 Specimen Design

This research project is part of a joint effort by National Research Council Canada (NRC), Department of Defence, Department of Foreign Affairs and International Trade, Transport Canada, BASF Canada and the University of Ottawa. The Institute for Research in Construction (IRC) of the NRC is leading this project in collaboration with the Industrial Materials Institute (IMI) and the Institute for Aerospace Research (IAR). The major objective of this project is to develop an innovative advanced composite protection system for concrete structures against extreme shocks (mainly blast and impact). The specimens discussed herein form a companion study to those tested under simulated blast loads at the University of Ottawa using a shock tube by Lloyd (2010) and Kadhom (in progress). The control specimens were detailed to optimize damage potential under simulated blasts and drop-weight impacts while allowing for reasonable and measurable damage of the retrofitted specimens.

All specimens discussed herein were 150 mm x 150 mm in cross-section and 2438 mm long, with 10 mm clear concrete cover. Four No.10 bars were used as longitudinal reinforcement (Figure 3-1), resulting in a reinforcing ratio, ρ, of 1.78%. The only variable between specimens was the spacing of lateral stirrups. Five specimens had a stirrup spacing of 100 mm which falls below the maximum permitted spacing of ties for compression members (150 mm) specified by the Canadian Standards Association (CSA) Standard A23.3-04 Design of Concrete Structures Clause 7.6.5.2. Two preliminary test specimens were casted with closer stirrup spacing: one had a spacing of 37.5 mm (h/4), which represents the maximum spacing according to Clause 21.3.3.2

(special provision for seismic design) of CSA A23.3-04; the second had a stirrup spacing of 75 mm.

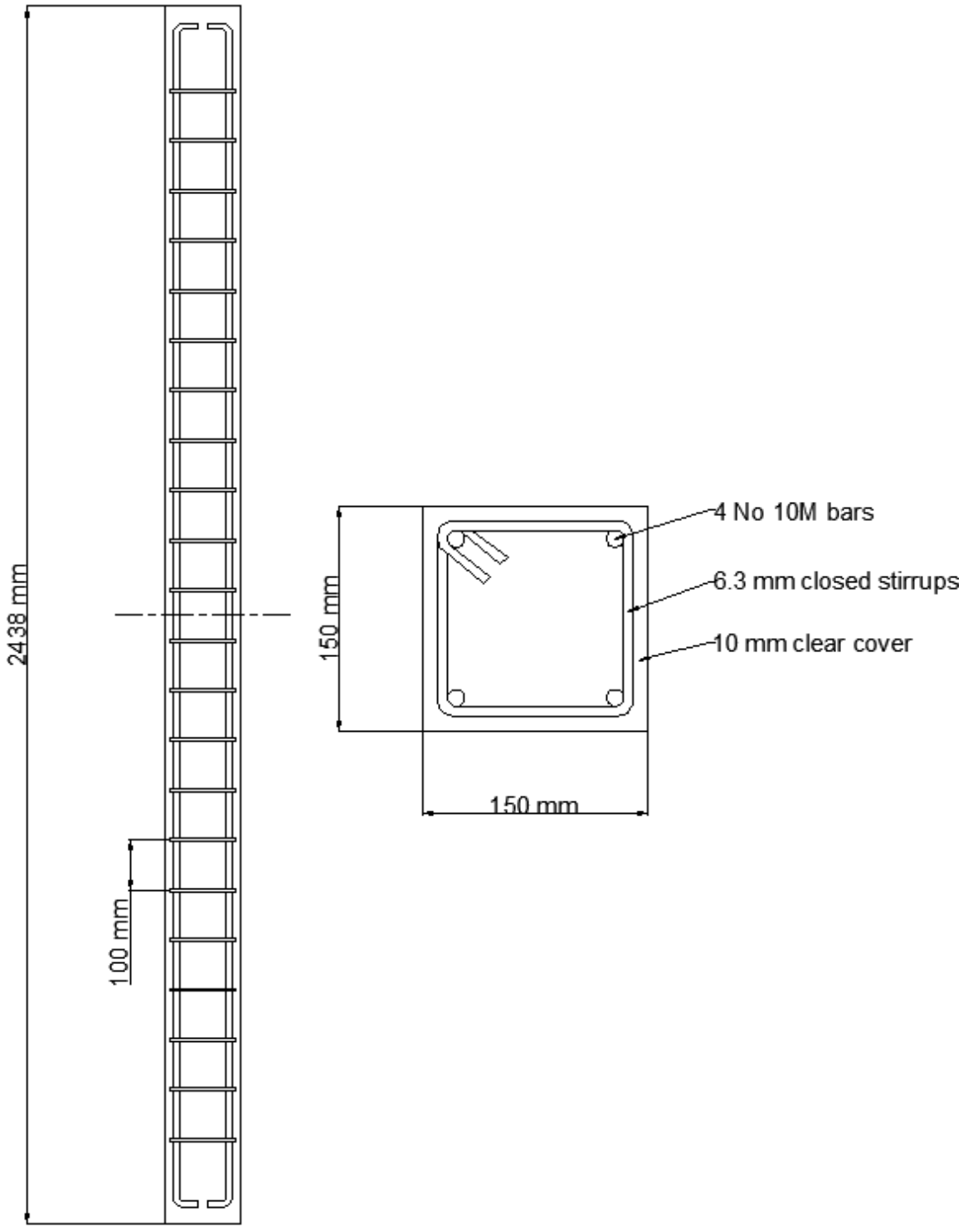

Figure 3-1: Specimen design

3.2.2 Specimen Construction

3.2.2.1 Formwork Construction

The first step in the construction of the specimens was building the formwork. The formwork was built using ¾ in. (19 mm) thick plywood. To avoid the development of stress concentrations in the fibre reinforced polymer (FRP) at the corner of the specimens for the retrofitted columns, the corners were rounded. Two options were studied: modifying the formwork to round the corners before casting, or grinding the column corners with a diamond disk grinder after casting to achieve the desired corner radius.

While numerous methods were investigated to round the corners in the formwork (pre-casting), the most feasible approach was the addition of a large bead of latex caulking to the bottom corners of the forms. The bead of caulking was smoothed into a curved shape using a metal spatula as illustrated in Figure 3-2. After formwork stripping, it was necessary to further round the corners with a diamond disk grinder. For this reason, it is recommended to leave formwork unmodified and round the corners of the specimen after casing. This was confirmed by other workers in the lab who prepared their specimens uniquely by grinding and achieving satisfactory results.

Figure 3-2: Application of latex caulking beads to bottom corners of formwork

3.2.2.2 Instrumentation and Assembly of Steel Reinforcement Cages

The assembly of the steel reinforcement cages used in the construction of the reinforced concrete specimens was completed in six steps. These steps were: bending the stirrups, instrumenting the longitudinal rebar and the stirrups with strain gauges, tying the cages, running the lead wires from the strain gauges along the reinforcement to the exit point near the column ends, and testing the installed strain gauges. The stirrups were 130 mm square (outside dimensions) to allow for 10 mm clear concrete cover. Stirrups were made by cutting 580 mm lengths of 6.3 mm diameter steel wire and then bending the wire lengths using a steel bending gig fabricated at the University of Ottawa machine shop. Each stirrup required five individual bends. Figure 3-3 shows the fabricated bending gig and bending lever arm with the completed stirrup.

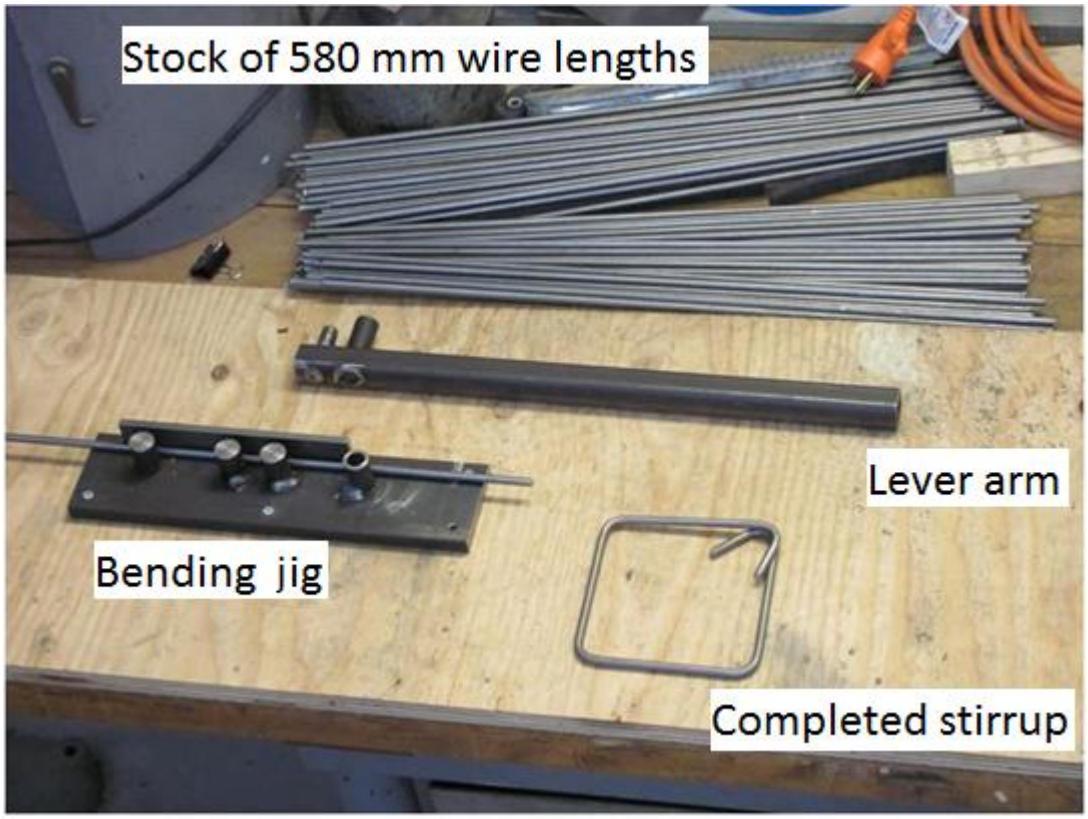

Figure 3-3: Stirrup bending gig, lever arm and completed stirrup

Before assembly of the steel reinforcing cages, strain gauges had to be installed on two of the four longitudinal reinforcing bars and certain stirrups. Each steel reinforcement cage had sixteen strain gauges: six strain gauges on a compression zone rebar, six strain gauges on the opposite tension zone rebar and four strain gauges on the shear resisting legs of the two stirrups near the support regions.

Each instrumented stirrup (two per column) had two strain gauges: one at the center of each shear resisting leg perpendicular to the bending plane. Note that on either end of the columns, a 250 mm long zone was determined to be the support region. No instrumentation is located within this distance, although stirrups were present.

All strain gauges used were Vishay general purpose linear pattern strain gauges designation C2A-XX-250LW-350, a widely used general purpose gauge (Figure 3-4) with a gauge length of 6.35 mm. The gauges were bonded to the rebar and stirrups using Vishay Micro-Measurements Certified M-Bond 200 adhesive, which is a modified alkyl cyanoacrylate compound. The procedure outlined in Vishay's Instruction Bulletin B-127-14 was closely followed to ensure proper adhesion of strain gauges. The steps were:

1) Grind off the ribs on a small section of rebar (this step was not necessary for stirrup strain gauges as the stirrup wire was smooth);

2) File the grinded section with 3 progressively finer files (this step was not necessary for stirrup strain gauges);

3) Clean the filed area with CSM degreaser;

4) Apply M-Prep Conditioner A;

5) Apply M-Prep Neutralizer 5A;

6) Position gauge in desired location and apply M-Bond 200 catalyst;

7) Apply M-Bond 200 adhesive and affix the strain gauge by applying pressure to installation assembly.

Figure 3-4: Strain gauge bonded to stirrup leg

Once the gauge was properly glued to the rebar/stirrup, the assembly was protected using Vishay's M-Coat F Protective Coating Kit, carefully following the procedure of Vishay's Instruction Bulletin B-134-4 (Figure 3-5). The protection steps were:

1) Apply a piece of M-Coat FT Teflon tape over the gauge assembly;

2) Apply a patch of M-Coat FB butyl rubber sealant;

3) Cover the entire patch with M-Coat FA aluminum tape;

4) Seal all tape edges with M-Coat B, a rubber cement compound.

Figure 3-5 shows the finalized and installed protection system for a stirrup.

Figure 3-5: Protected and finalized stirrup strain gauge assembly

Once the reinforcing steel was instrumented and the gauges were protected and tested for proper functioning, assembly of reinforcement cages could begin. The stirrups were attached to the longitudinal rebars with steel twist ties and placed symmetrically about the center line of the rebars to the end of the specimen to ensure that stirrups extended into the support zone.

The functioning of the strain gauges was monitored before and after cage assembly to ensure that gauges worked properly prior to casting. After strain gauge installation and protection on a length of rebar (six gauges) or on a stirrup (two gauges), the gauges were individually checked using a Gauge Installation Tester. The verification was to ensure that:

1) The nominal resistance of the gauges was adequate (350±5 Ω);

2) The deviation of gauge resistance from nominal was adequate (±0.5%);
3) The insulation resistance between the gauge and the steel rebar/stirrup was sufficiently high (MΩ reading maxed).

This procedure was repeated once the cages were assembled with the wires running along the length of the cage and exiting near one end. If all gauges performed satisfactorily, the finished instrumented reinforcement cage was placed in the formwork, ready for casting. If any gauge was found to be defective, it was replaced as necessary.

3.2.2.3 Casting of Concrete

The casting of the specimens took place on June 13th 2011. In an attempt to facilitate the grinding of specimen corners after formwork stripping, the top edges of all specimens were finished with a curved curbing trowel. This added step during finishing did not have the desired effect as the top corners of the columns still required a significant amount of grinding in order to achieve a smooth circular corner. It was established that for future casts, this step be abandoned. The specimens were kept under wet burlap for the first seven days, after which formwork was stripped and the specimens were cured under wet burlap for an additional seven days.

3.2.2.4 Instrumentation of Concrete Surface

Once concrete was properly cured, strain gauges were applied to specific locations on the concrete surface. The strain gauges used were Vishay general purpose linear pattern strain gauges (designation N2A-XX-20CBW-120). These strain gauges were installed and protected using the same procedure as those outlined for the steel strain gauges, although surface preparation did differ. To prepare the concrete surface for gauge installation, a very thin film of rapid drying epoxy was first applied to the surface to fill voids on the surface and ensure a uniform surface for proper gauge bonding. The cured epoxy film was then sanded and degreased. Concrete surface strain gauge application could then proceed. Unlike the gauges used on the steel cages, the concrete surface strain gauges did not include wires. The wires were soldered post-installation. Lastly, to provide mechanical protection and reduce the risk of damage during FRP installation, the gauges were protected with M-Coat FB butyl rubber sealant (Figure 3-6).

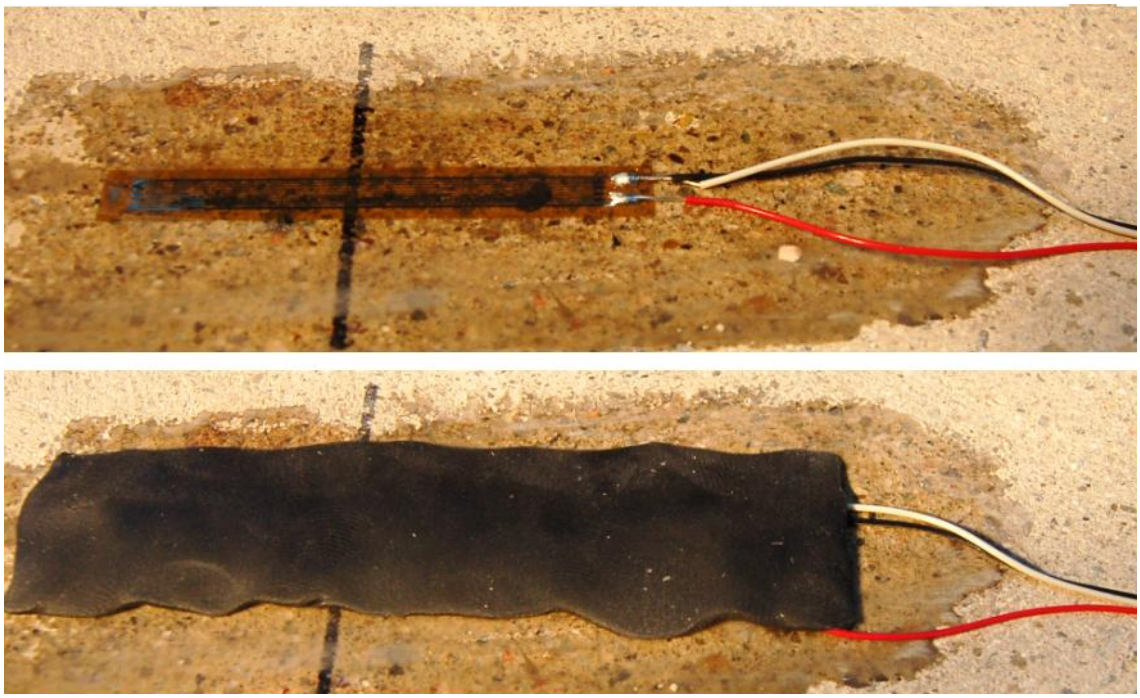

Figure 3-6: Concrete surface strain gauge before and after butyl rubber application

3.2.3 Retrofitting of Specimens

Before application of the FRP to the columns and after grinding the specimen corners to a circular shape, minor patchwork was necessary. To repair the damaged/defective spots along the top edges of the specimens that surfaced during the rounding of the corners, a mortar mix was prepared in the lab to patch these locations. This minor repair was required to ensure that no jagged edges that could potentially affect the performance of the retrofit remained. The prepared mix had w/c ratio of 0.45. Super absorbent polymer (SAP) was added to make the mix more sticky and gel-like while a small amount of super plasticizer was added to improve workability. Figure 3-7 shows a defective portion of a column before and after the repair.

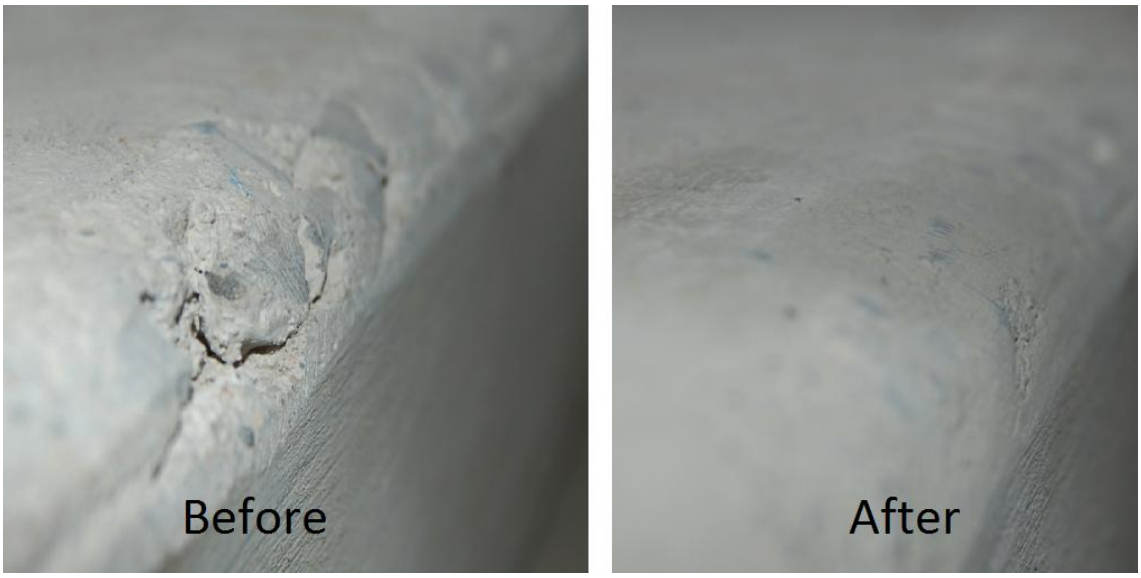

Figure 3-7: Damaged column edge before and after patchwork repair

Of the seven specimens tested, two were identically retrofitted. The application of the retrofit to the specimens was through hand lay-up using a 3:1 (epoxy:hardener) ratio. The retrofit included four layers of unidirectional (UD) FRP. The first two layers were applied on all four faces of the specimens with the fibres running in the longitudinal direction of the specimen, while the other two layers were applied in the hoop direction to provide added confinement (Figure 3-8). The overlap of FRP sheets was always at least 50 mm.

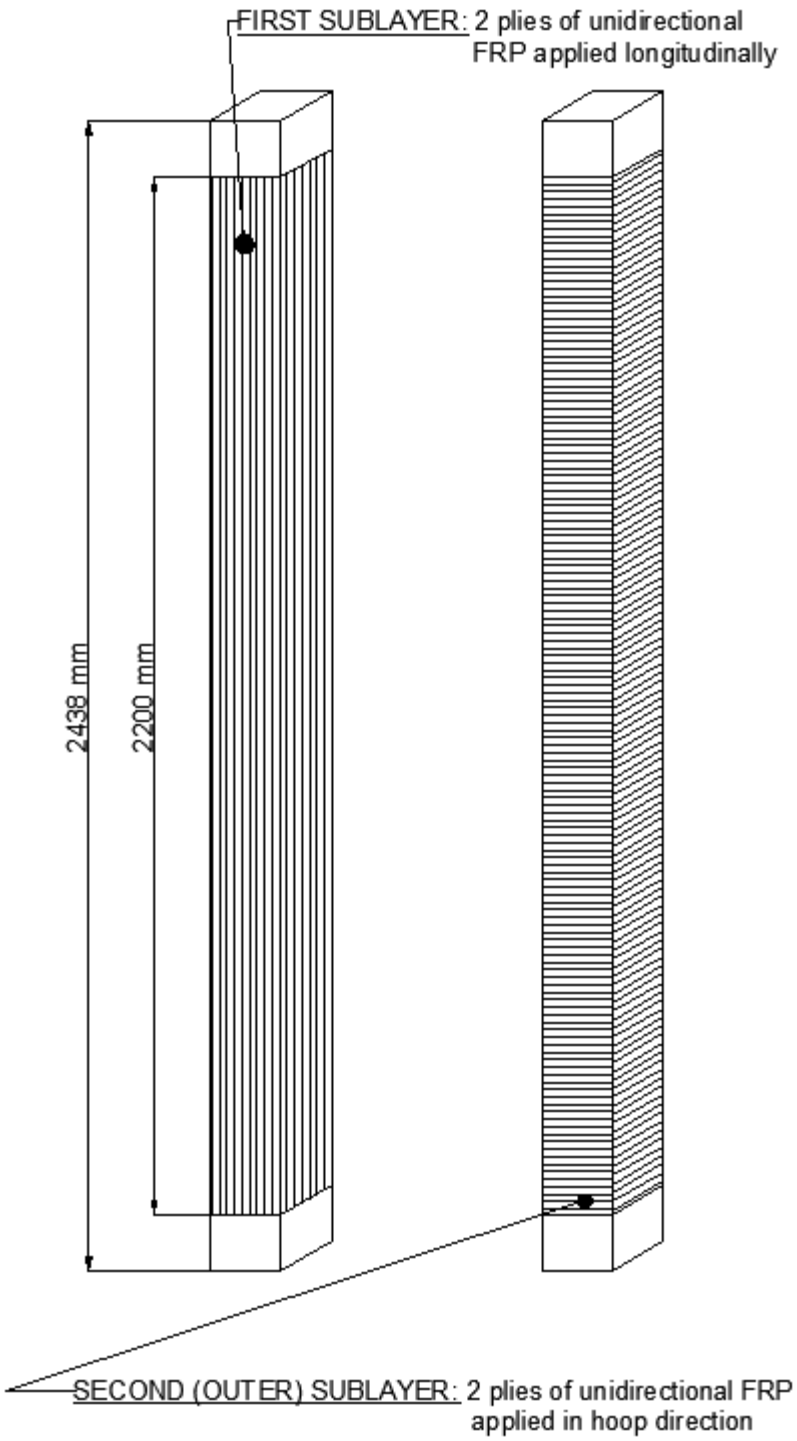

Figure 3-8: Retrofit configuration for specimens Imp-5 and QS-2

3.2.4 Material Properties

3.2.4.1 Concrete Properties

The concrete used for specimen construction was ordered from a local ready mix company. The only specifications given were a target compressive strength of 25 MPa and a 10 mm coarse aggregate size. The mix had adequate workability and placed well, but was difficult to finish after the first hour. It required considerable vibration to consolidate, however, no segregation was observed and very slight surface water (bleeding) appeared. Table 3-1 shows the mix properties of the concrete.

Table 3-1: Concrete properties

Slump (mm)	100
Density (kg/m3)	2390
Compressive Strength, f'_c (MPa)	42.7
Strain at Peak Compressive Strength, ε'_c (mm/mm)	0.0029
Splitting Tensile Strength (MPa)	3.2
Static Modulus of Elasticity (MPa)	32000
Poisson's Ratio	0.24

The compressive strength was obtained by following ASTM standard C39, 141 days after casting, on the first day of testing. The tensile splitting strength was obtained by following ASTM standard C496 and the static modulus of elasticity and Poisson's ratio were obtained by following ASTM standard C469. Test results were determined from the average of at least three cylinders.

Figure 3-9 provides a typical stress-strain curve from compressive tests performed 287 days after casting. Even though a preload of 5 kN was applied during compressive cylinder tests to eliminate the influence of localized cylinder damage on stress-strain curves, an S-shape in the early loading phase was still visible. As a result, the strain at peak stress, ε'_c, was higher than expected. The value of 0.0026 mm/mm that is reported was obtained by neglecting the initial soft response and applying the initial stiffness from the onset of loading instead.

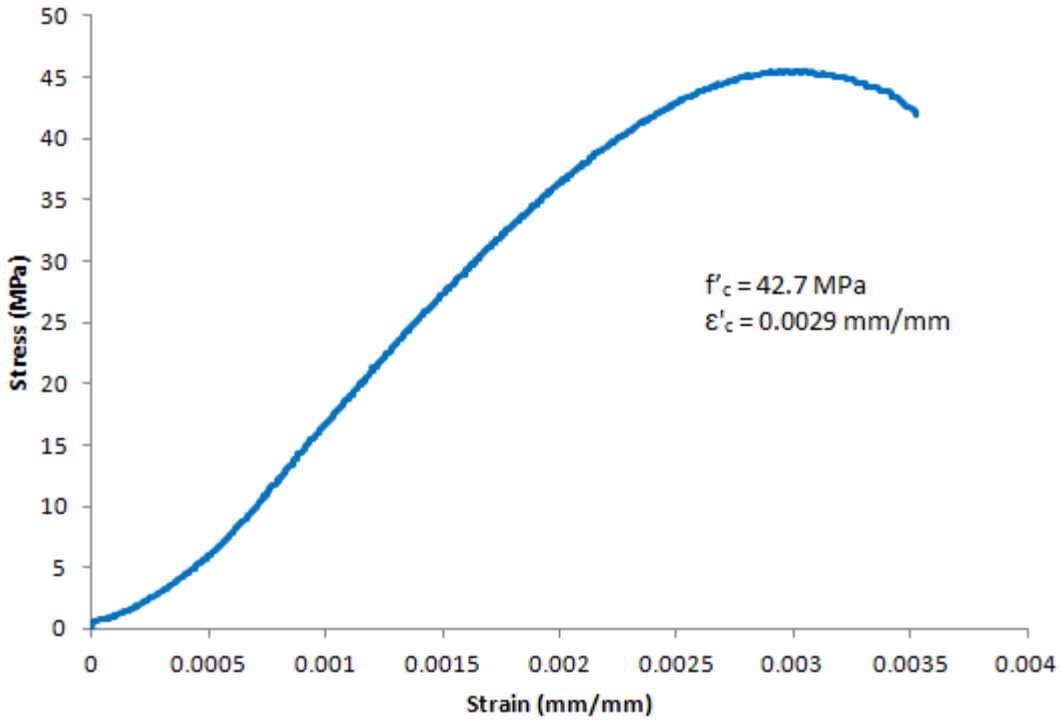

Figure 3-9: Typical stress-strain curve for concrete and associated material properties

3.2.4.2 Steel Properties

Coupon tests on 500 mm lengths of steel rebar and transverse wire were performed using an MTS material testing frame. Figure 3-10 and Figure 3-11 show the stress-strain relationships, average modulus of elasticity, average yield stress and strain, and average ultimate stress and strain for the longitudinal and transverse steel, respectively. For the longitudinal steel, the yield stress was taken as the average value of the plateau that develops prior to strain hardening. For the transverse steel, yield stresses and strains were obtained by applying a 0.2% strain offset interception to the obtained stress-strain curves as they did not exhibit a defined yield plateau. Note that the discontinuity that occurs in the stress-strain curve for the transverse steel is due to the fact that strain was recorded using an extensometer up to 50 000 microstrain and beyond that the strain was a function of cross-head displacement. The discontinuity occurs when the strain data from the two methods is merged but does not affect the validity of results.

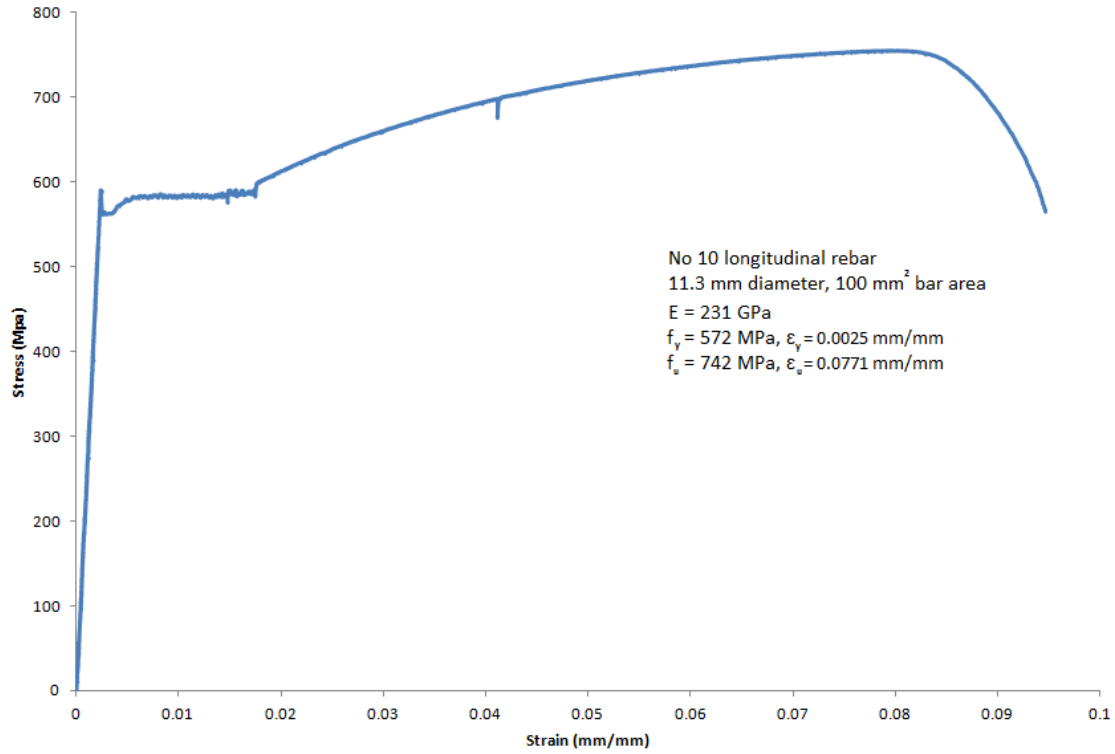

Figure 3-10: Typical stress-strain curve for longitudinal rebar and associated material properties

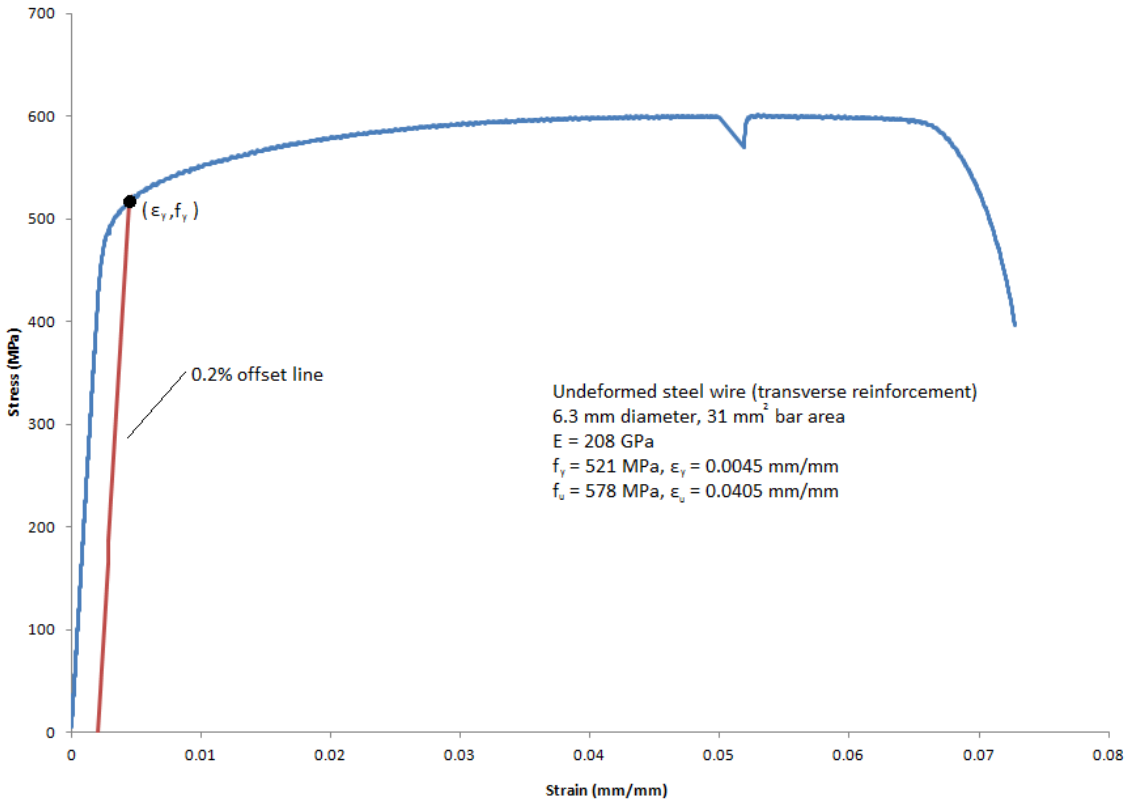

Figure 3-11: Typical stress-strain curve for transverse reinforcement and associated properties

3.2.4.3 FRP Properties

The unidirectional FRP used for the retrofitting of the RC column specimens was provided by JB Martin and had an areal weight of 305 g/m^3. The matrix consisted of Probuild MM55538 epoxy resin and Probuild MM55729 hardener in a 3:1 (epoxy:hardener) ratio. Tensile tests were performed on 25 mm wide and 250 mm long specimens according to ASTM D3039 standard. A cross-head speed of 2 mm was used to perform all tests. Tabs were bonded to the specimens to avoid failure at the grips. Deformation was recorded using 50 mm extensometer. Two stacking sequences were studied for the unidirectional FRP: a unidirectional configuration, $[0]_4$, with four layers of the fabric oriented in the same direction; and a cross-ply configuration, $[0/90]_{4S}$, with two layers in each orthogonal direction (it is this configuration that was applied to retrofitted specimens). The tensile properties for these two configurations are provided in Table 3-2 while Figure 3-12 provides a typical stress-strain curve for the FRP coupons.

Table 3-2: Material properties of FRP composite

Stacking Sequence	Total Thickness (mm)	Tensile Modulus (GPa)	Ultimate Tensile Strength (MPa)	Strain at Ultimate Tensile Strength (%)	Fibre Areal Weight (g/m^2)	Fibre Weight Content (%)
$[0]_4$	1.6	77.0	1237	1.9	1220	40
$[0/90]_{4S}$	1.6	37.2	596	0.9	1220	40

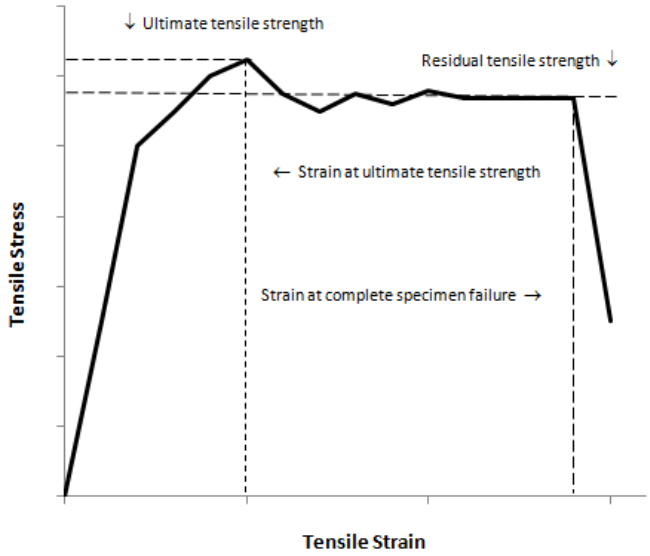

Figure 3-12: Schematic representation of a tensile stress-strain curve for tested FRP coupons

3.3 Experimental Program

Seven half-scale reinforced concrete test specimens designed according to CSA A23.3-04 standards were constructed and tested as part of this research project. Three of the specimens with stirrup spacing of 37.5, 75 and 100 mm were initially impacted as part of a preliminary study to observe the performance of the impact setup and axial loading system. Thereafter, four specimens with a stirrup spacing of 100 mm were tested without axial load to complement the data from preliminary impacts and to be part of a comparative study to differentiate the impact and static behaviour of retrofitted and control specimens. The clear span for these final four specimens was increased to 2200 mm, from 2000 mm, to maximize damage levels in the specimens and to reduce the length of the overhang, permitting more accurate SDOF modeling. Table 3-3 provides an overview of testing conditions for each specimen.

Table 3-3: Test Specimen Overview

Specimen Name	Loading Type	Stirrup Spacing (mm)	Clear Span (mm)	Axial Load (kN)	Retrofitted
Imp-1	Impact	37.5	2000	283	No
Imp-2	Impact	75	2000	0	No
Imp-3	Impact	100	2000	100	No
Imp-4	Impact	100	2200	0	No
Imp-5	Impact	100	2200	0	Yes
QS-1	Static	100	2200	0	No
QS-2	Static	100	2200	0	Yes

3.4 Specimen Supports

Custom roller and pin supports that were designed and fabricated by the NRC were used in the current study. The support design and detailing can be found in a government report by Almansour, Smith and Margeson (2012).

It was observed during exploratory impact tests on simply supported RC beams that the specimen would experience uplift from the simple supports immediately following the impact event. Not only is this release from the supports not representative of real structural behaviour, it also tended to shift the specimen both laterally and longitudinally from its original position. This behaviour has been confirmed in literature and has usually been addressed by clamping the specimen to the

simple supports while allowing for some rotations. Thus, to properly test RC columns under drop weight impact, new supports were designed and built. An improvement on the rotational clamp used in some form by Saatci (2007), Fujikake (2009) and Khalighi (2009) is presented herein.

The aim of the newly designed and fabricated pin-roller end supports for RC members tested under impact was to prevent uplift and lateral movements while allowing for longitudinal elongation/contraction due to axial load if present. At the pin support (Figure 3-13), the specimen was fully clamped (preventing movement in the x and y directions) but was still able to rotate using a hinge that was designed to allow for up to 15 degrees of rotation in either direction (positive or negative bending) with minimal friction during impact induced specimen deflections.

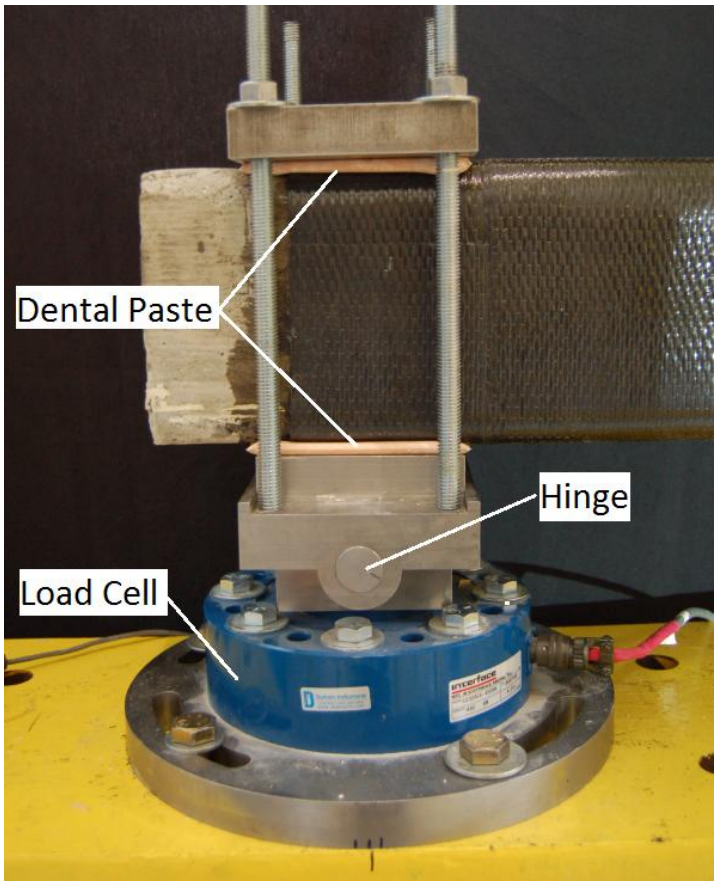

Figure 3-13: Pin Support

At the roller support, the specimen was also clamped with a hinge, but rollers were installed on the top and bottom of the specimen to allow movement in the longitudinal direction (Figure 3-14). Friction was considered negligible in these rollers as they were greased as required before every test.

Both the pin and the roller support were rigidly fixed to a 450 kN Interface load cell to measure the support reactions during the tests. These load cells were calibrated to within one percent accuracy using the MTS compression frame in the lab. Also, to ensure an even load distribution between the supports and the specimen, dental paste was inserted between the top and bottom support contact plates and the specimen before every test.

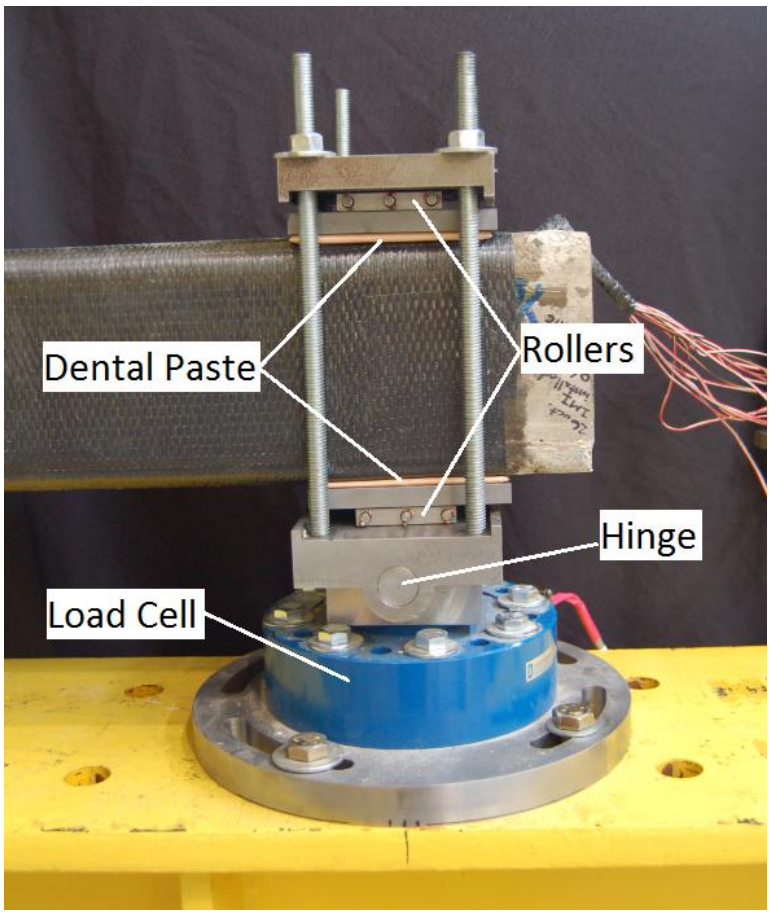

Figure 3-14: Roller Support

The support/load cell assemblies were bolted to a customized frame built from W310 x 158 steel sections. Two of these built-up testing stages were constructed: one beneath the impactor and one beneath the static actuator. The pin and roller supports were moved between the two stages depending whether an impact or static test was to be performed. The main purpose of these frames was to elevate the specimen and its supports to the required height for testing. The built-up testing stage had a very large mass compared to that of the specimens to be tested and a very high rigidity to minimize its response during tests. The dynamic support frame was modified with two slots cut using a plasma torch at midspan to accommodate two laser displacement sensors

placed at midspan to measure specimen deflection during impact tests. Figure 3-15 shows the dynamic testing stage.

3.5 Load Application

3.5.1 Impact Load Application

Dynamic impact loads for this testing program were applied by a customized CEAST 9350 drop tower (Figure 3-15). The main features of this system are: additional spring loaded energy system that can accelerate the striker beyond gravitational acceleration; an instrumented tup that measures the force-time history of the impact; and a tup antirebound system that catches the tup to prevent any secondary impacts. Additionally, this system is equipped with an independent data acquisition system, named DAS16000, that records the impact force-time history at a frequency of 2 000 000 Hz. The "16000" in the name refers to the maximum number of data points that can be recorded for a given impact, the maximum length of an impact force-time history recording captured by the DAS16000 is thus 8 ms. Impacts were controlled remotely through a computer which also recorded the force-time history of the event at a frequency of two million times per second with a total recording capacity of sixteen thousand data points (8 ms is the length of the recording at maximum frequency).

Figure 3-15: Ceast 9350 drop-weight impact tower with test specimen supported by custom supports installed on built-up frame

The tup used to impose the impact loads had a semi-cylindrical shape with a radius of 25.4 mm and a length of 177.8 mm. The width of the tup was larger than the width of the specimen to ensure a uniform impact load on the specimen.

The drop tower was also equipped with a photoelectric flag mechanism that can be used to trigger the recordings of external equipment such as data acquisition systems and high speed cameras. As the tup and its attached weight carriage fall towards the specimen after release, they pass through a "gate" creating a measurable voltage spike (Figure 3-16). Knowing the dimensions of the flag and the times at which the voltage output spikes and subsequently drops, the velocity of the striker can be calculated to verify the programmed drop speed.

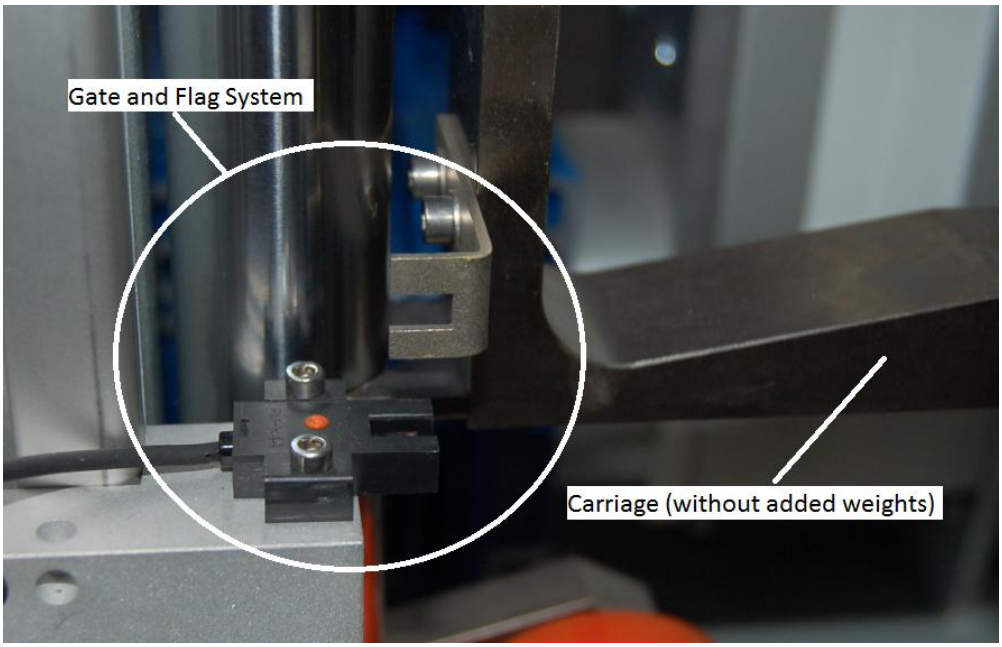

Figure 3-16: Drop Tower Trigger System

3.5.2 Static Load Application

Static loads were applied by a 500 kN MTS servo-hydraulic actuator. A solid steel cylinder was cut through its length and inserted between the actuator's loading plate and the specimen to replicate as closely as possible the impact tup. Static loading was imposed through displacement control at a rate of 1 mm/min.

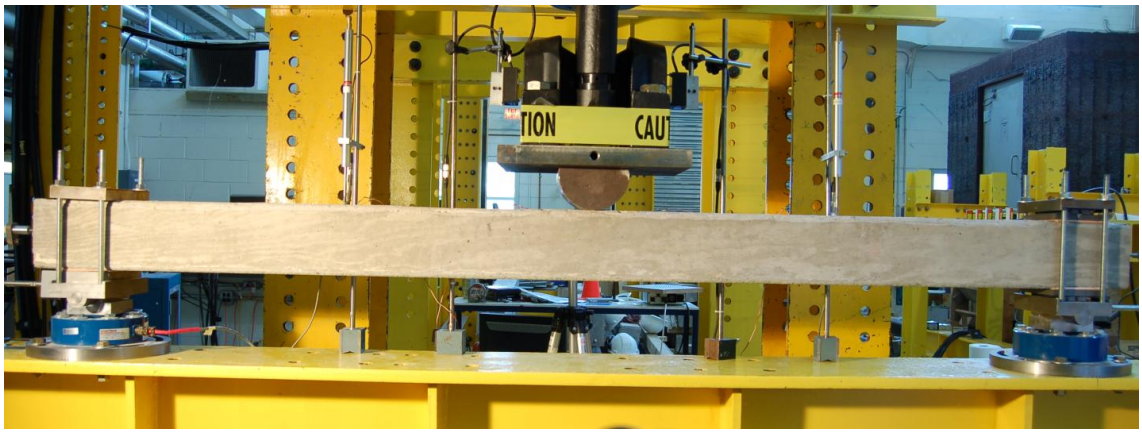

Figure 3-17: Static testing stage: Hydraulic actuator with tup replicator inserted between specimen and piston applying quasi-static load

3.6 Axial Loading System

An axial loading system was designed and fabricated for the experimental testing of columns under impact load. Requirements of the axial loading system were:

1) Axial load capacity of 1000 kN;
2) Adaptable to both the static and impact testing in the laboratory;
3) Ability to maintain a constant axial load during an impact event;
4) Ability to control the rate of axial loading;
5) Ability to track variations in the axial load during dynamic testing;
6) Minimal impact on the specimen boundary conditions.

3.6.1 First Prototype

A first prototype system that addressed the above criteria was designed and tested. It consisted of an external post-tensioning setup utilizing two hydraulic jacks. Axial load levels in the specimen were controlled by loading a 60 ton (534 kN) master jack in the MTS material testing frame. The master jack was connected in a hydraulic circuit to a motorized hydraulic pump and to a 50 ton (445 kN) slave jack which applied the axial load to the specimen as shown in Figure 3-18. By controlling the force exerted on the master jack by the MTS testing frame through its control station, the axial force applied to the specimens by the slave jack could be accurately monitored at all times. More importantly, the axial load applied to the specimen could be gradually increased through programming rather than increased in steps. The latter would have been the case had the hydraulic pump been used since the pump has very rudimentary pressure control. During axial load application to the specimen, the hydraulic pump was not used. Its purpose in the circuit was

to move both jack pistons during test setup and to act as a reservoir for hydraulic oil between tests.

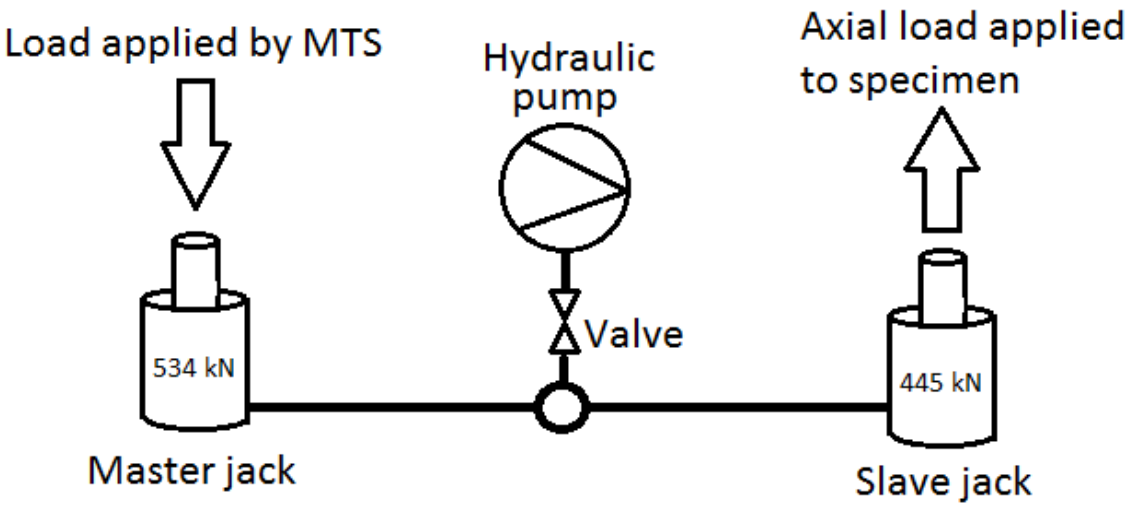

Figure 3-18: Diagram of hydraulic component of prototype axial loading system

The first axial loading system that was designed (Figure 3-19) was installed on a preliminary control column that was intended to be tested under a static lateral load. The slave jack was bolted to a support plate through which four post-tensioning rods passed. A customized tilt saddle was fitted to the end of the slave jack piston. The purpose of the tilt saddle was to allow for specimen end rotations and to release moment loading on the specimen and on the slave jack during specimen deflection. An intermediate transfer plate that was held in place by friction was placed between the tilt saddle and the specimen to distribute the load to the specimen section (Figure 3-20). At the opposite end of the specimen (East), a 450 kN load cell was fitted between another intermediate transfer plate and a second end plate through which the post-tensioning rods passed. The properties of each post-tensioning rod used in the system were: 28 mm nominal diameter; 445 kN minimum ultimate strength; 334 kN minimum yield strength; and 5.06 kg/m. Oversized fasteners were used to secure the end plates at each end of the setup.

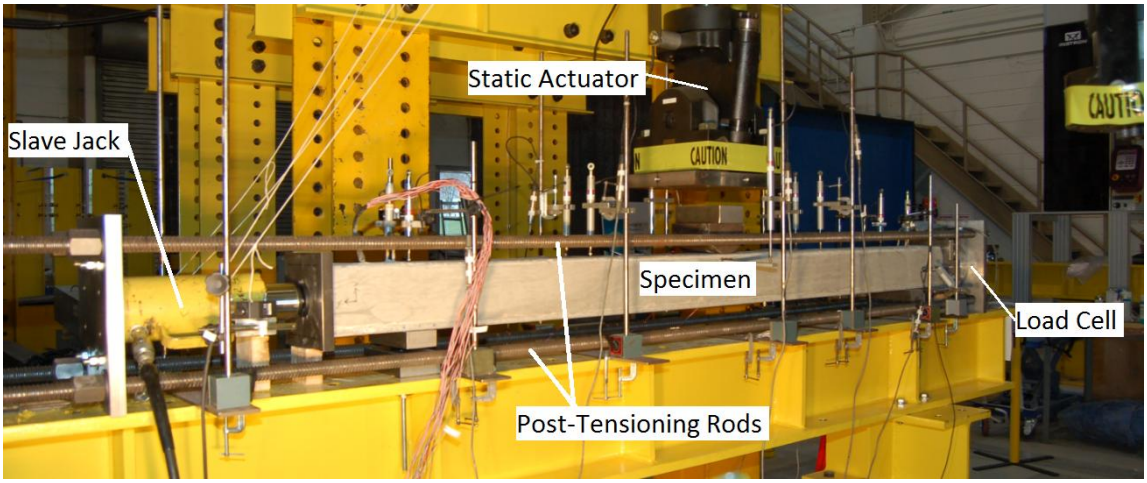

Figure 3-19: Prototype axial loading system installed on static testing stage

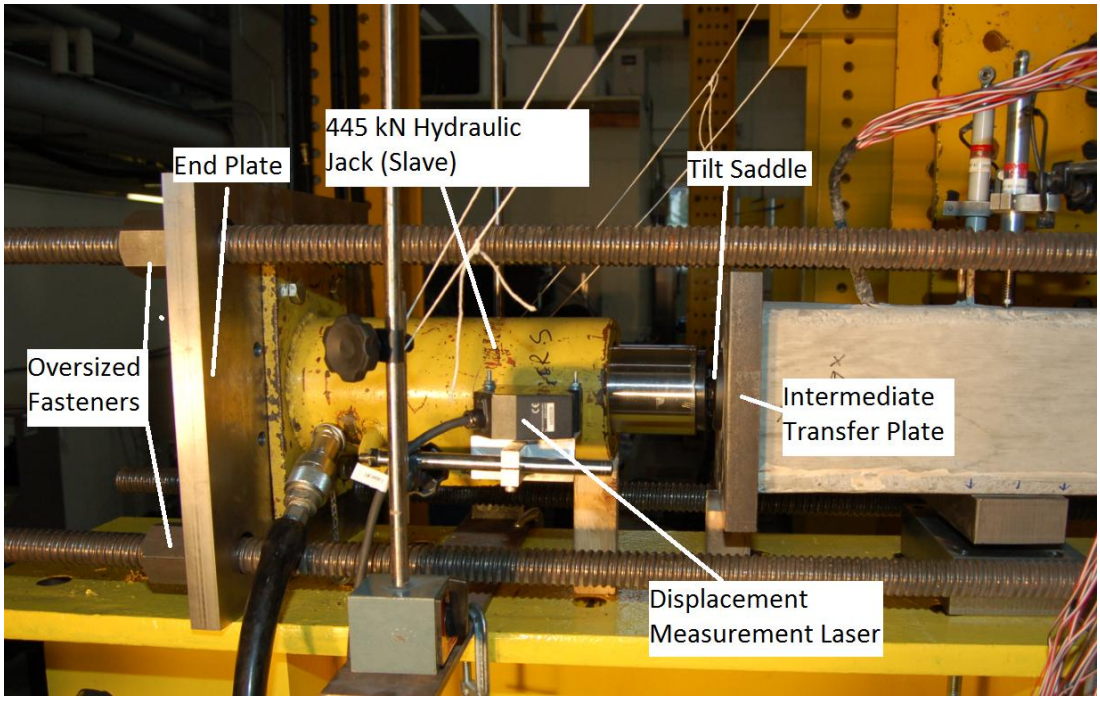

Figure 3-20: Slave jack end of prototype axial loading system with test specimen

During preliminary tests of the axial loading system, some problems were encountered. The first concern was a lack of control regarding the minimization of eccentricity of the axial load. Since there were no built-in means to ensure concentricity of the slave jack, the intermediate transfer plate and the specimen, rudimentary alignments were necessary using string and measuring tapes, however it was challenging to ensure precision beyond ±5 mm.

Also, the connection between the tilt saddle and the slave jack piston could potentially fail. The tilt saddle was held in place by one-10 mm bolt that was screwed into a custom threaded hole in

the slave jack piston. The connection was designed based on only compression; any eccentricity of the axial force would induce shear forces in the bolt that could cause failure. Failure of this bolt combined with an eccentricity of the slave jack piston in relation to the specimen's neutral axis could cause the entire setup to buckle.

Another area of concern was the lack of stability offered by the simple supports used during the prototype test (Figure 3-21). These supports were bolted to the testing frame but provided only frictional contact with the specimen with no clamping or restraint. During external post-tensioning operations, it is not uncommon to observe minimal specimen shifting as the member settles to equilibrium under the added tension forces in the steel post-tensioning rods. Unlike the newly designed supports that were used for all subsequent testing, the simple supports did not prevent the specimen from shifting laterally or upwards during application of axial loads. This lack of stability could further accentuate eccentricities in the system, causing failure of the axial loading system.

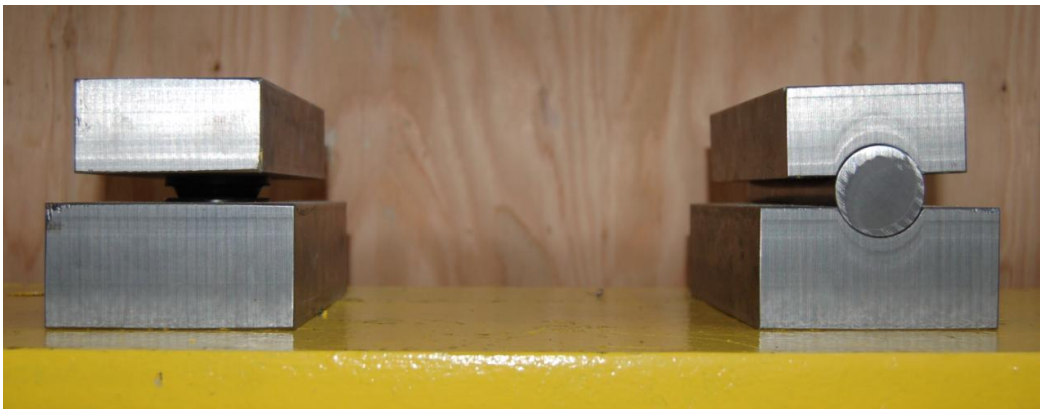

Figure 3-21: Simple supports used in conjunction with prototype axial loading system

The lack of eccentricity control, the tilt saddle that was not designed to account for these eccentricities and simple supports that did not stabilize the RC beam adequately all had the potential to destabilize the system. Furthermore, the program controlling the MTS load application had no built-in failure detection that would shut off the system in case of slippage or specimen failure. For these reasons, the first prototype axial loading system was abandoned in favour of an improved design.

3.6.2 Second Prototype

The new system (Figure 3-22 and Figure 3-23) incorporated numerous modifications while maintaining the concept of slave and master jacks as part of an external post-tensioning setup. In this system, four 267 kN hollow cylinder hydraulic jacks were used to directly tension the four post-tensioning bars, adding stability and improving load distribution on the specimen cross-section.

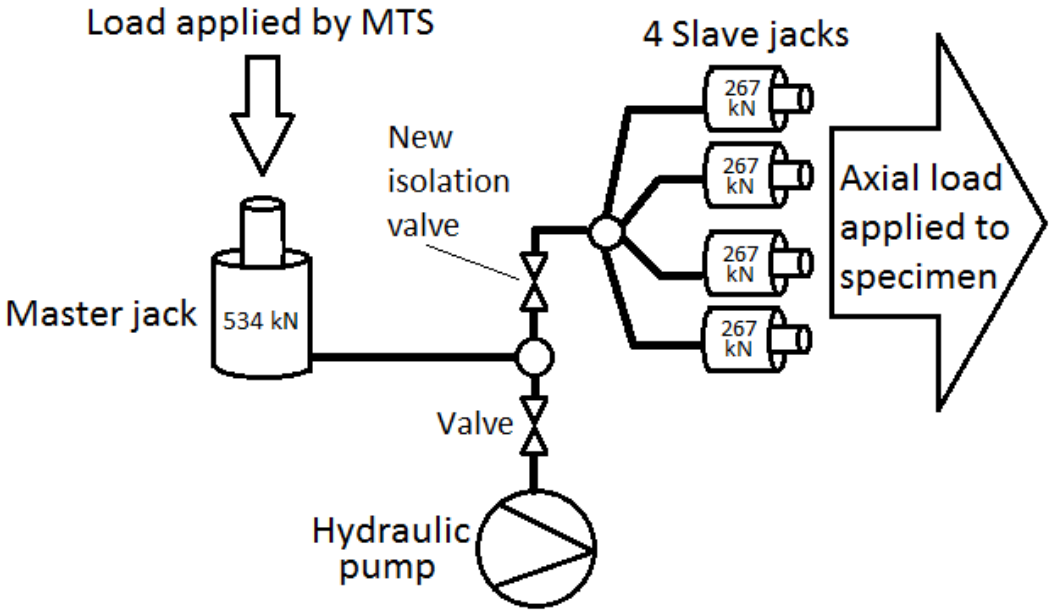

Figure 3-22: Diagram of hydraulic component of improved axial loading system

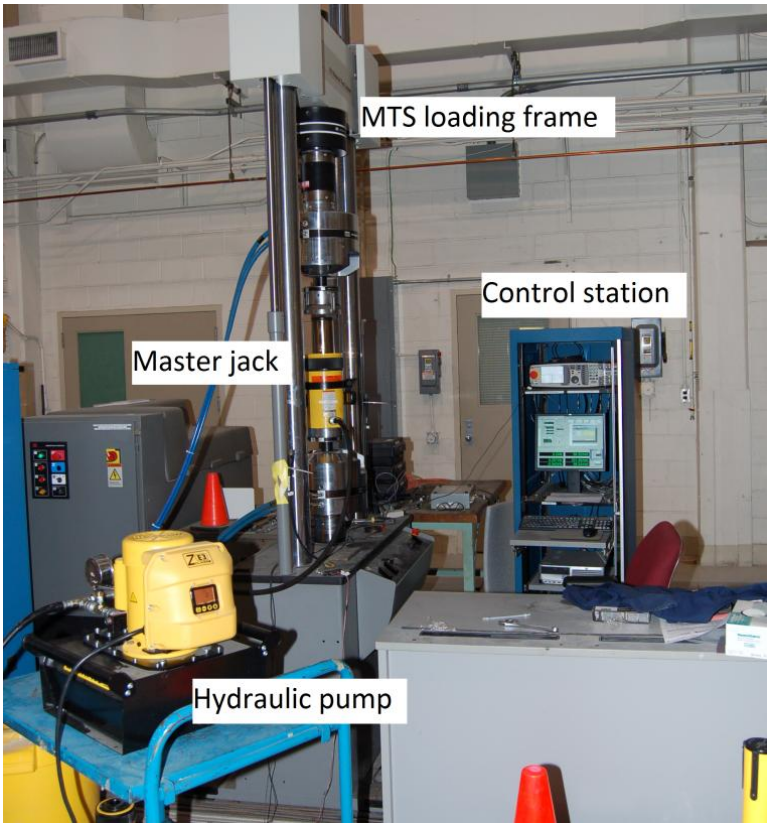

Figure 3-23: Master jack, loading frame, hydraulic pump and control station used in hydraulic component of improved axial loading system

To further increase specimen stability and improve load distribution, 25 mm thick steel flanges were added to the intermediate transfer plates (Figure 3-24). The added flanges nestled the specimen and added support to its four sides. Also, a roller was fitted between the intermediate and end plates near the roller support to allow specimen in-plane bending. To avoid variations in axial load levels due to the MTS frame, an isolation valve was added near the four slave jacks. This valve was closed prior to impact testing to isolate the hydraulic oil near the slave jacks and, ideally, to maintain axial load on the specimen during impact testing. The customized supports would always be used in conjunction with the axial loading system to provide necessary support in the vertical and lateral planes.

Relative to the first prototype system, the hydraulic system was further improved by adding a force transducer to provide real time system pressure readings during testing, and the program controlling the MTS loading was modified to include an emergency shut off if sudden drops in load resistance were encountered during testing.

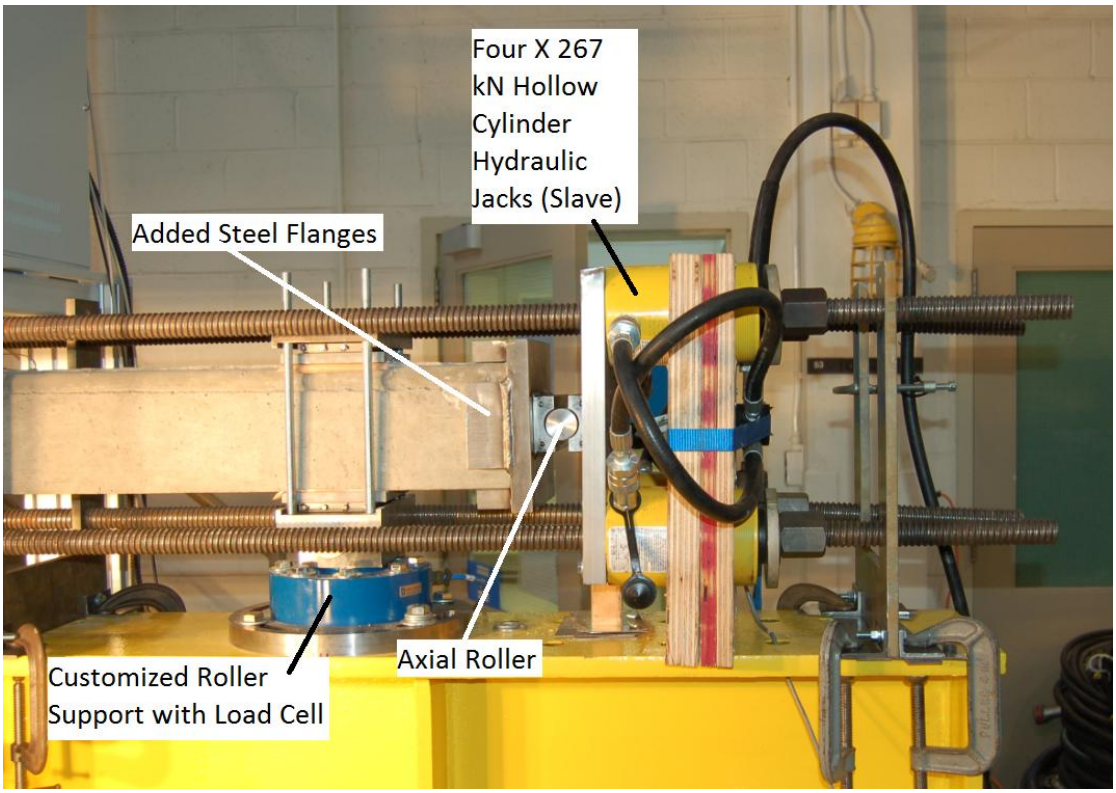

Figure 3-24: Improved axial loading system

3.7 Test Instrumentation

3.7.1 Data Acquisition Systems

3.7.1.1 Impact Tests

For all impact tests, an HBM Gen2i high speed portable data recorder was used. This unit had a maximum recording frequency of 1 MHz per channel: four voltage channels and four strain channels. The four voltage channels were assigned as follows to record: the load output from the impact tower; the trigger signals from the impact tower; and the displacements from the two displacement lasers located at midspan. The four strain channels were assigned to capture: the pin support reaction, the roller support reaction, the axial load (when applicable); and one strain gauge. When no axial load was applied to the specimen, the channel assigned to record axial load was used to record a second strain gauge at high speed.

To monitor the other strain channels during an impact test, an HBM MGCplus data acquisition system was used. The maximum recording frequency of this unit is 9600 Hz with a capacity of sixteen channels. Thus, of the twenty total strain gauges installed on a specimen, eighteen could be monitored during a beam test with no axial load (sixteen with the MGCplus and two with the

Gen2i) and seventeen could be monitored during a column impact test (sixteen with the MGCplus and one with the Gen2i). In addition to these sixteen strain channels recorded, the impact load was also recorded by the MGCplus unit in order to align the time stamps from both data acquisition units.

3.7.1.2 Static Tests

For both static tests, the HBM MGCplus data acquisition system was used to record data at a frequency of 50 Hz with no limitations on the number of recordable channels. Thus, in addition to all strain channels being recorded, the static load level from the actuator, the displacement of the actuator, the displacement levels of two lasers placed at midspan (to verify the actuator displacement), and the axial deformation at each support from two LVDTs were also recorded.

3.7.2 Strain Gauges

With the exception Imp-1 and Imp-2 (only concrete surface strain gauges), each tested specimen was instrumented with twenty strain gauges: six located on one compression rebar, six located on the opposite tension zone rebar, four on the shear resisting legs of two support region stirrups and four located on the concrete compression face (Figure 3-25). Each strain gauge was assigned a label that indicates: whether it was located on a tension rebar, on a compression rebar, on a stirrup, or on the compression face of the specimen; and the distance of the strain gauge from the specimen midspan (a negative distance is assigned when measuring between the midspan and the pin support). Figure 3-26 provides a schematic of the strain gauges used on the test specimens.

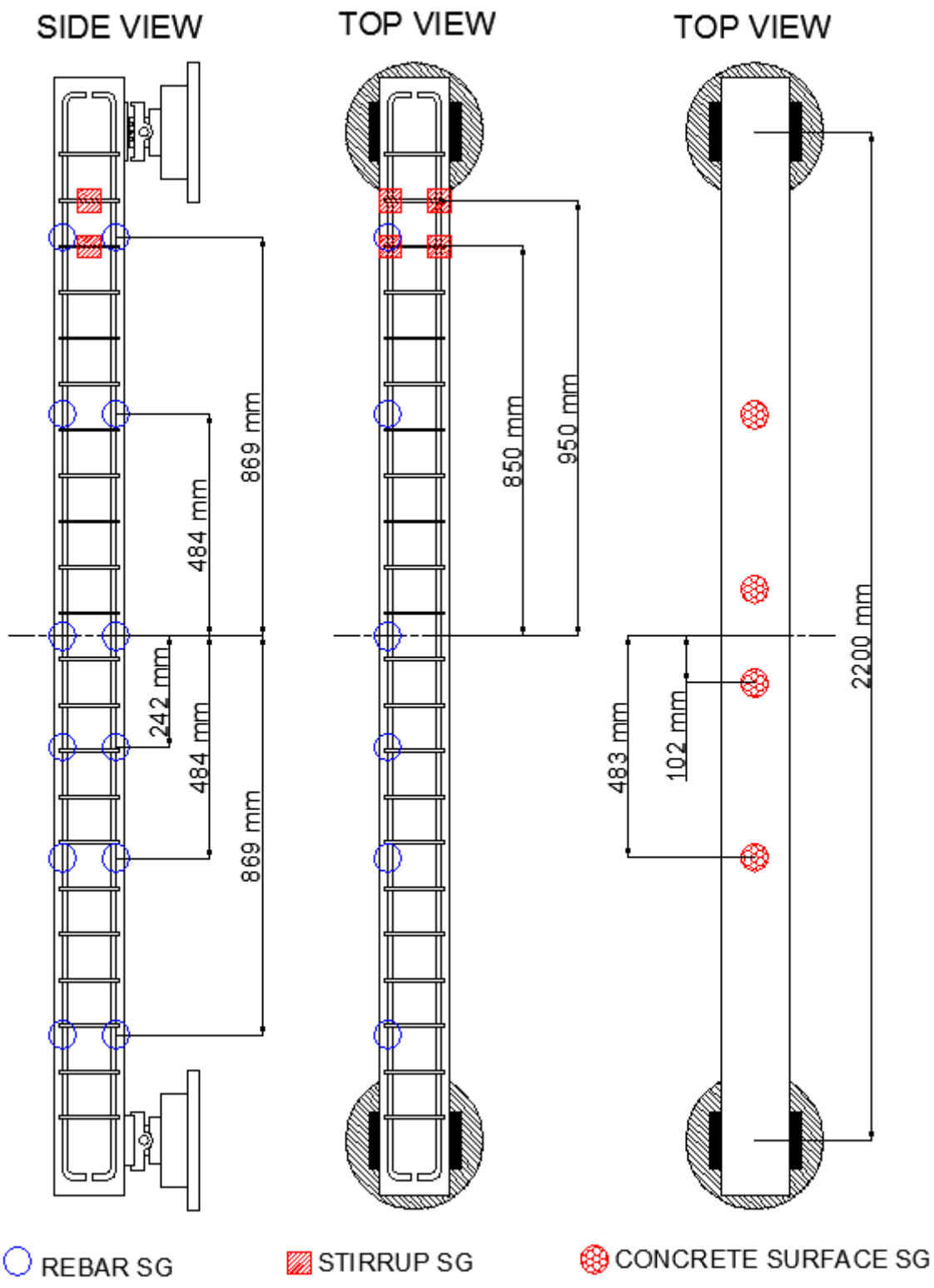

Figure 3-25: Strain gauge locations for Imp-3, Imp-4, Imp-5, QS-1 and QS-2

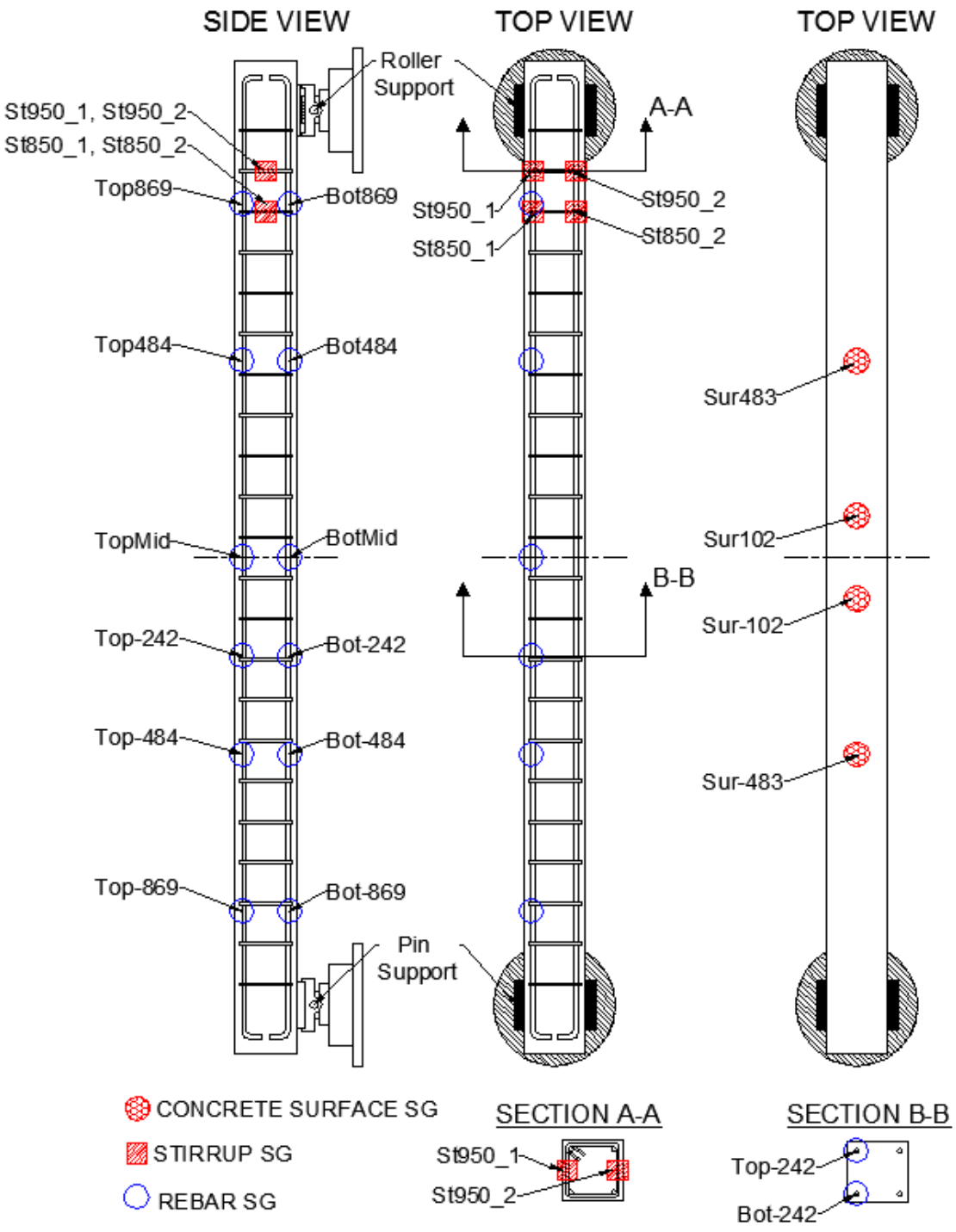

Figure 3-26: Strain gauge identification scheme

3.7.3 Displacement Measurements

3.7.3.1 Impact Tests

For the impact tests, midspan deflections were measured by two laser displacement sensors, each located 37.5 mm from the longitudinal centerline of the specimen. The lasers were bolted to the web of the testing frame with two slots plasma cut into the upper flange to allow for the laser beams to pass as shown in Figure 3-27. This also served to protect the lasers from large debris.

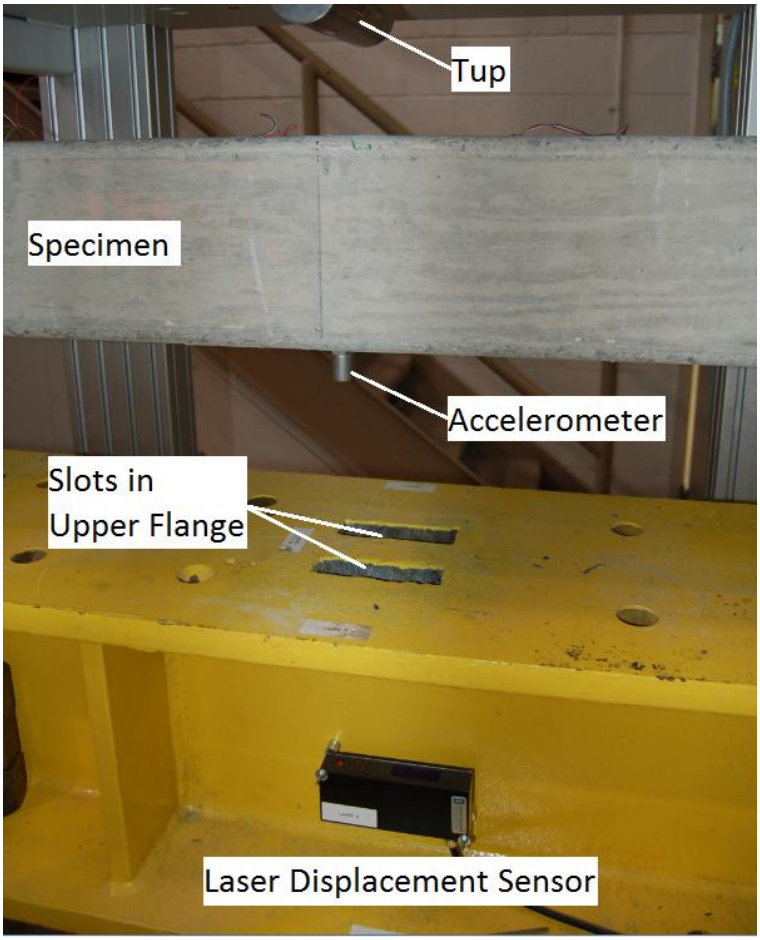

Figure 3-27: Location of laser displacement sensors for impact tests

3.7.3.2 Static Tests

For static tests, the midspan displacement was measured in two different ways: first, by the actuator's control software which tracks the cross head position; and second, by two laser displacement sensors, each aimed at the rigid steel transfer plate connected to the actuator (Figure 3-28).

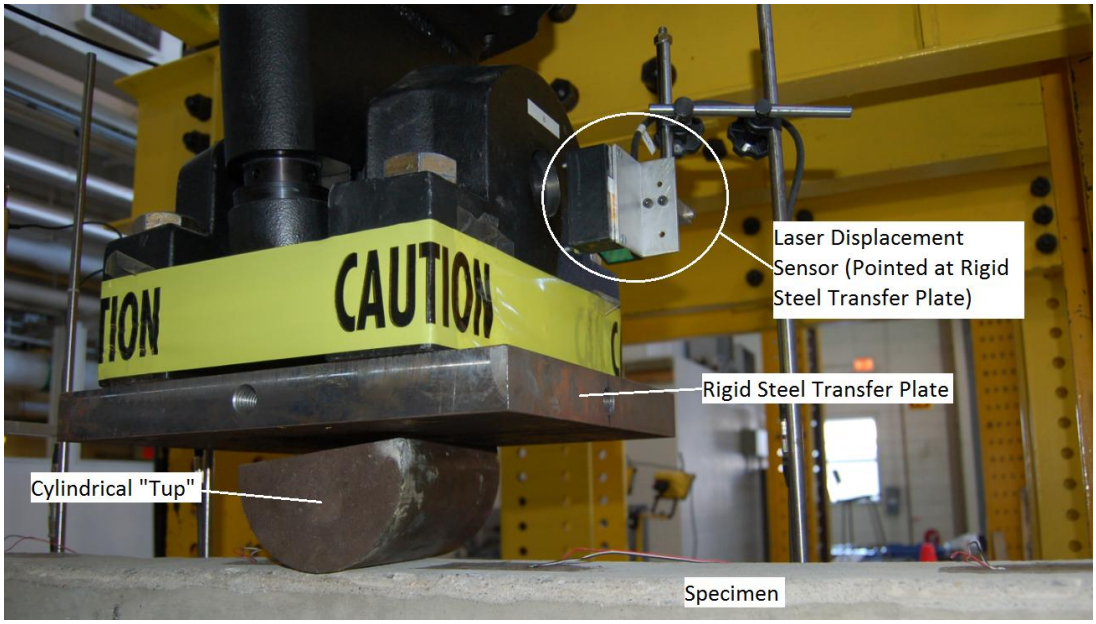

Figure 3-28: One of two midspan laser displacement sensors for specimen midspan deflection

Axial displacement levels were also recorded for static tests by two LVDTs attached to stands with magnetized bases. These bases were connected to the lower portion of each support, allowing the LVDTs to rotate with the specimen and measure only axial displacement (Figure 3-29).

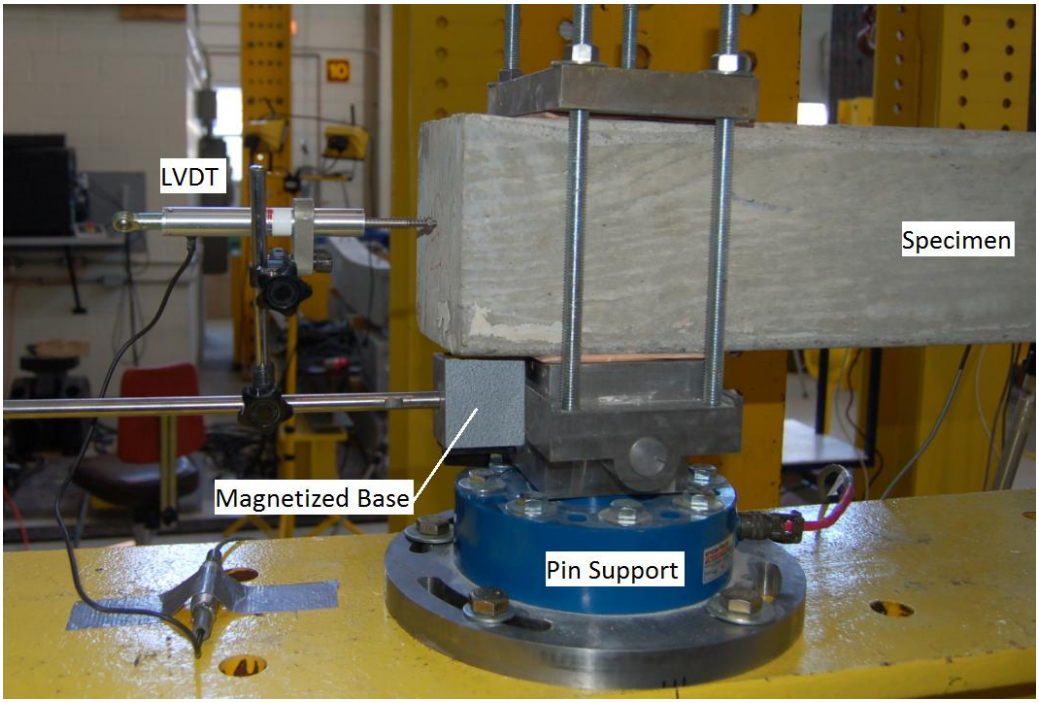

Figure 3-29: LVDT to capture axial deformation at pin support during a static test

3.7.4 Reaction Loads, Axial Loads and Tup Loads

For the impact and static tests, which shared the same supports, the reaction forces were captured by two identical Sensotec 450 kN load cells integrated into the roller and the pin support. The axial load level was captured by a 1335 kN Sensotec load cell integrated into the axial loading system. These three load cells were calibrated prior to testing.

The impact force-time history was continually recorded by the DAS16000 unit connected to the impact tower. The voltage signal from the load cell integrated into the tup was also recorded by both data acquisition systems to verify the readings and, also, to align the time stamps when using two different data acquisition systems to record data.

3.7.5 High Speed Camera

All impact tests were filmed using a FastecHispec 4 color high speed camera. During an impact test, the purpose of these recordings was to observe the performance of the steel striker head, to observe crack development, to observe crushing of the concrete due to both the localized impact and the global bending of the specimen, and to document each test.

The high speed film was recorded on a loop and was triggered by a photoelectric cell in the CEAST impact tower. On average, each recording had a speed of 2000 frames per second with a resolution of 800 by 800 pixels.

3.7.6 Accelerometer

An accelerometer was bonded to the underside of specimen Imp-4 at midspan. Unfortunately, the development of a large crack at midspan immediately after the impact affected the bond, causing the accelerometer to detach from the specimen. Furthermore, the signal that was collected prior to the accelerometer detaching was saturated due to accelerations exceeding the tolerances of the instrument. Thus, the use of an accelerometer was abandoned for the final impact test on Imp-5 and no acceleration results are presented or discussed in the following chapters.

Chapter 4: Experimental Results

4.1 Introduction

The following chapter presents observations and data recorded during the impact and static testing of specimens at the structural laboratory of the NRC in Ottawa, Ontario. For the five specimens tested under impact (Imp-1 to Imp-5), a figure showing the midspan deflection, the total reaction load, the tup load and the axial load (if present) versus time is given. While the focus of these figures is on the peak response of the specimens, residual values are shown as well. Also, typical strain-time histories are given but the strain gauges differ between specimens depending on which strain gauges were functional and whether the recorded strain-time histories were deemed important for the discussion. Additionally, Section 4.3 presents a summary of the impact tests performed. For the two specimens tested statically (QS-1 and QS-2), load-deflection and typical load-strain graphs are presented.

Appendix A presents data that was considered repetitive or unsuitable for discussion. Strain-time histories (for impacted specimens), load-strain relations (for static tests) and a summary of peak and residual strain values are given.

4.2 Impact Tests

4.2.1 Imp-1

The first specimen was impacted as a column on November 23, 2011. Prior to impacting the specimen, the axial load was slowly and gradually increased to 282 kN over one hour and twenty minutes. When the desired axial load was reached, the MTS control program maintained a constant applied load on the master hydraulic jack, thus the axial load applied to the specimen remained constant as well. Figure 4-1shows Imp-1 prior to impact.

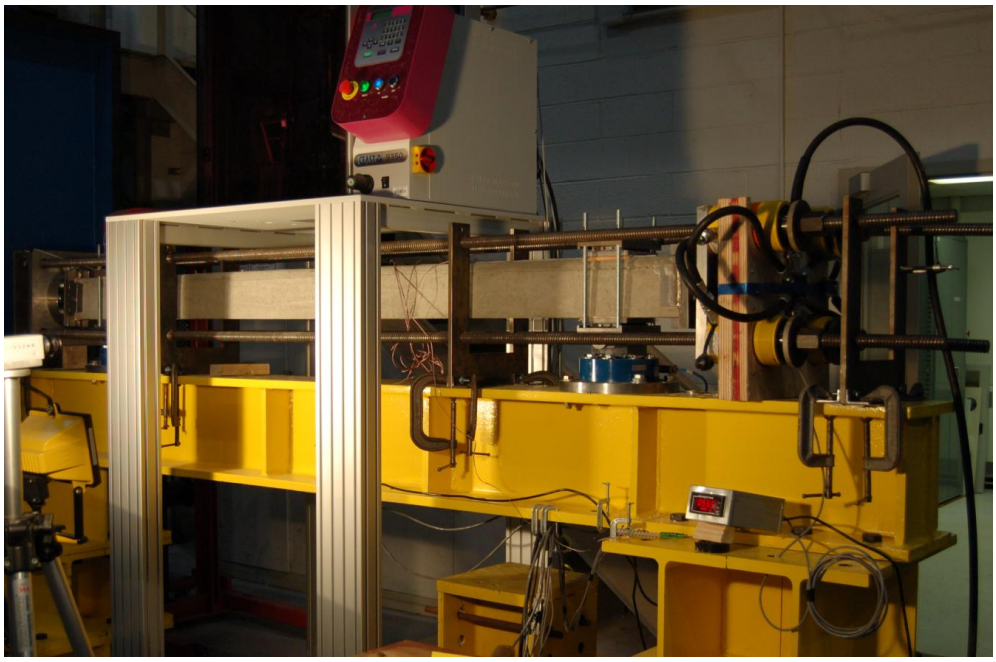

Figure 4-1: Imp-1 prior to impact

The peak deflection that was reached under impact for this specimen was 21.5 mm with a residual deflection of 4.0 mm that was unnoticeable when viewed from a distance. Peak total reaction and tup loads occurred well before peak midspan deflection was reached. Surprisingly, the peak total reaction force exceeded the tup load as illustrated in Figure 4-2. This may be attributable to the axial load system transferring significant amounts of load into the reactions, possibly also explaining the spike in axial load that occurs. This will be discussed further in Chapter 5.

The only strain data recorded for this impact test was from Sur102. Due to improper limit settings in the data acquisition software the maximum strain values that could be recorded were -2000 μm/m (-2400 μm/m after offset due to axial load). This was corrected for subsequent tests. The residual concrete strain, with axial load present, was -1200 μm/m (from a pre-impact value of -400 μm/m).

Very little permanent damage was sustained during the impact. Slight concrete spalling and crushing were apparent near the impact zone (Figure 4-3), and minor residual cracks ($\leq$ 0.1 mm) were observable in the tension zone (Figure 4-4). Maximum crack thicknesses that were reached during the impact could not be measured meaning that only residual cracks can be commented on.

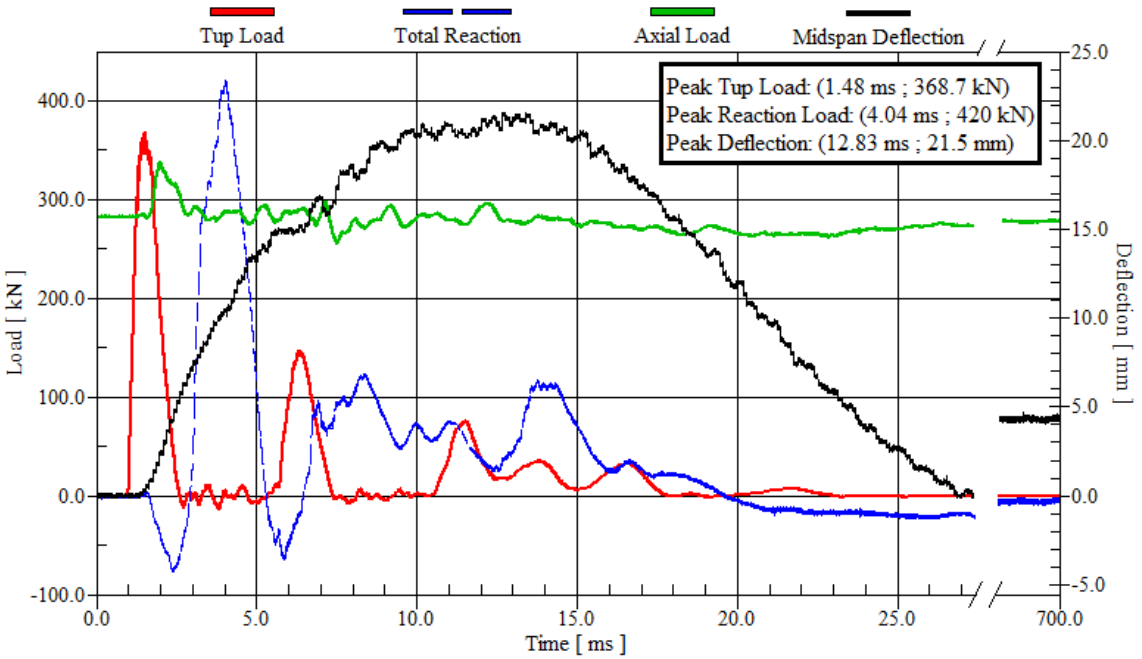

Figure 4-2: Peak Response for Imp-1

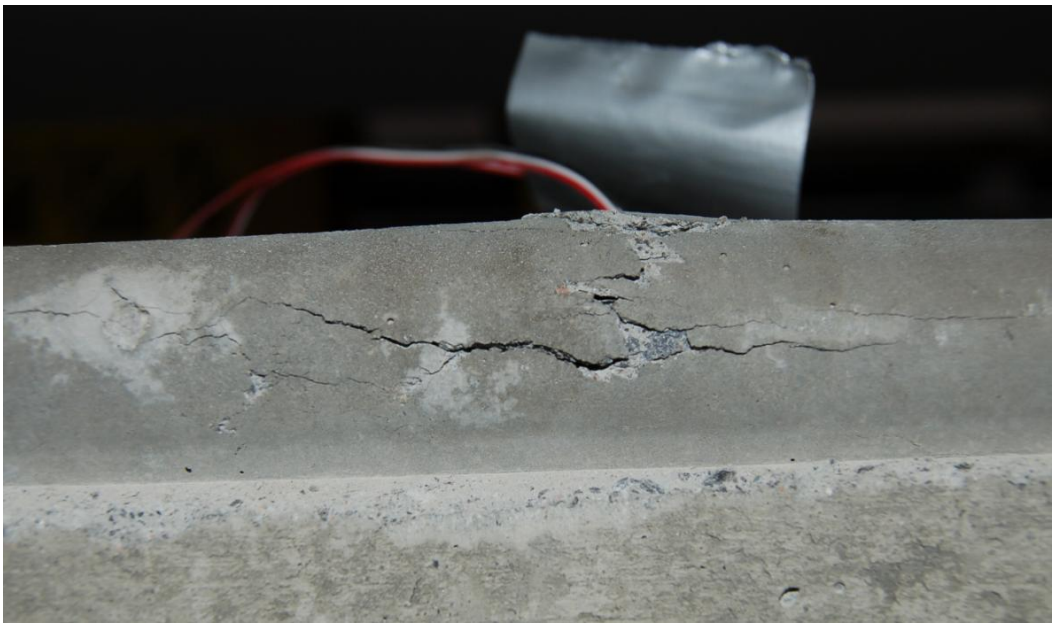

Figure 4-3: Compression zone damage in Imp-1 (side view)

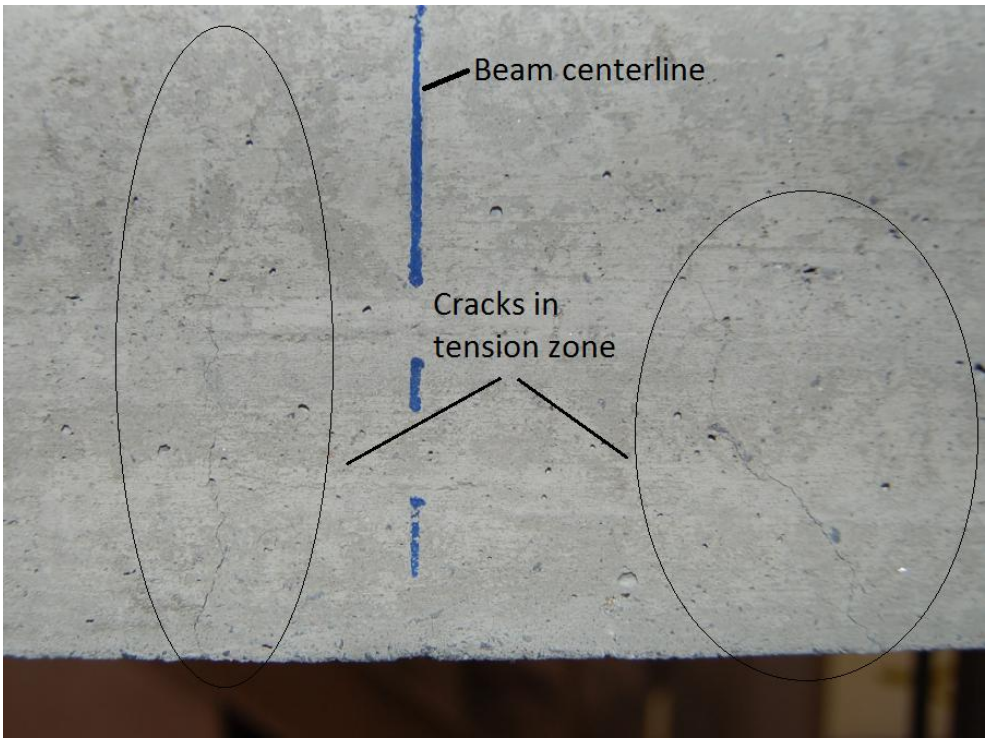

Figure 4-4: Tension zone cracking in Imp-1

Note that for Imp-1, the midspan deflection variation during the application of axial load and the concrete surface strain-time history are given in Appendix A.

4.2.2 Imp-2

The second impact test took place on December 5, 2011. For this test, no axial load was applied to the specimen. The same eight recording channels as those used for specimen Imp-1 were available and used; the only difference being that strain values from a second strain gauge, Sur483, were recorded (in place of the axial load level). No trigger signals were acquired for this test meaning that the verification of the impact velocity was not possible. Also, no pictures were taken of the specimen prior to testing.

As expected, this specimen suffered much more damage than Imp-1 due to the removal of the axial load and larger stirrup spacing (75 mm compared to 37.5 mm for Imp-1). Peak midspan displacement reached 47.4 mm with no negative bending rebound due to permanent plastic deformations. Residual deflection was 30.2 mm. Again, the majority of tup and reaction loads occur well before peak deflection of the specimen. The response of the reaction loads was very different than that for Imp-1 with a much lower peak value and no significant uplift forces after

the positive spike (Figure 4-5). However, both specimens did experience significant uplift forces at the supports prior to peak total reaction load being reached. These forces explain why specimens subjected to impact uplift from the supports if they are not clamped down. An explanation into their occurrence is given in Chapter 5.

Since the specimen was under no axial loads prior to impact, the initial concrete surface strains before impact where zero. For Sur102, the peak strain was -1650 μm/m with a residual strain of -400 μm/m. For Sur483, the residual strain value was -150 μm/m. The peak strain for this gauge was more difficult to evaluate due to the high frequency noise in the response, but the value was in the -800 μm/m range (Figure 4-6). The increased strain measured for Sur102 is normal as this gauge was closer to the impact (102 mm from midspan) than Sur483 (483 mm from midspan).

The cracking pattern for this specimen showed vertical cracks extending from the impact point down to specimen midheight and the apparent formation of a shear plug in the lower third of the specimen as depicted in Figure 4-7. Crack sizes were not measured for this specimen. Note that the lower edge in Imp-2 is rounded and indented due to the prototype formwork modifications.

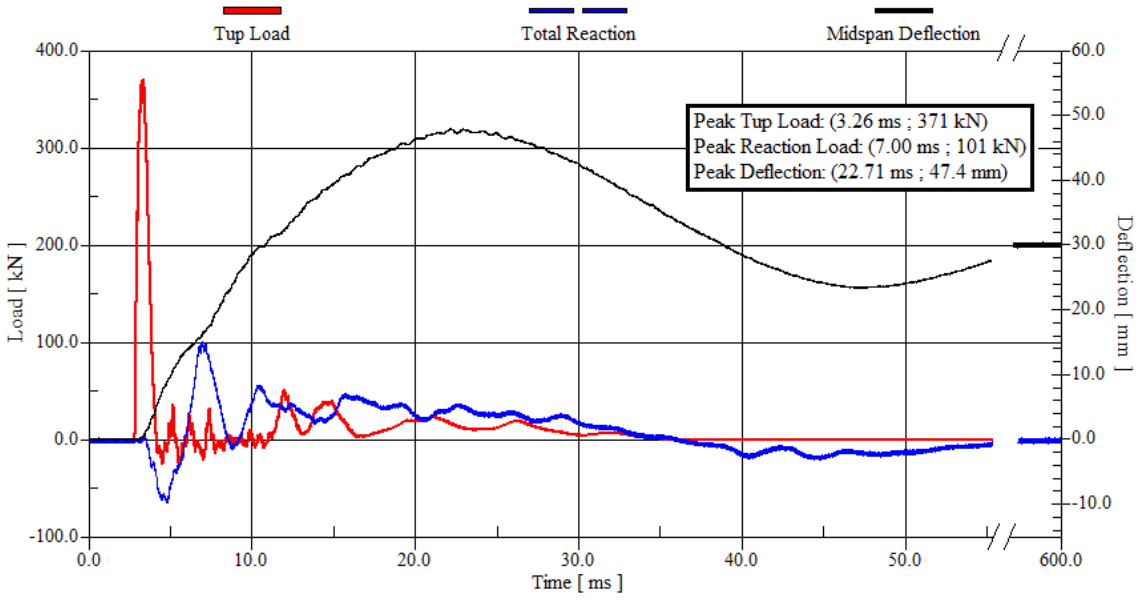

Figure 4-5: Peak Response for Imp-2

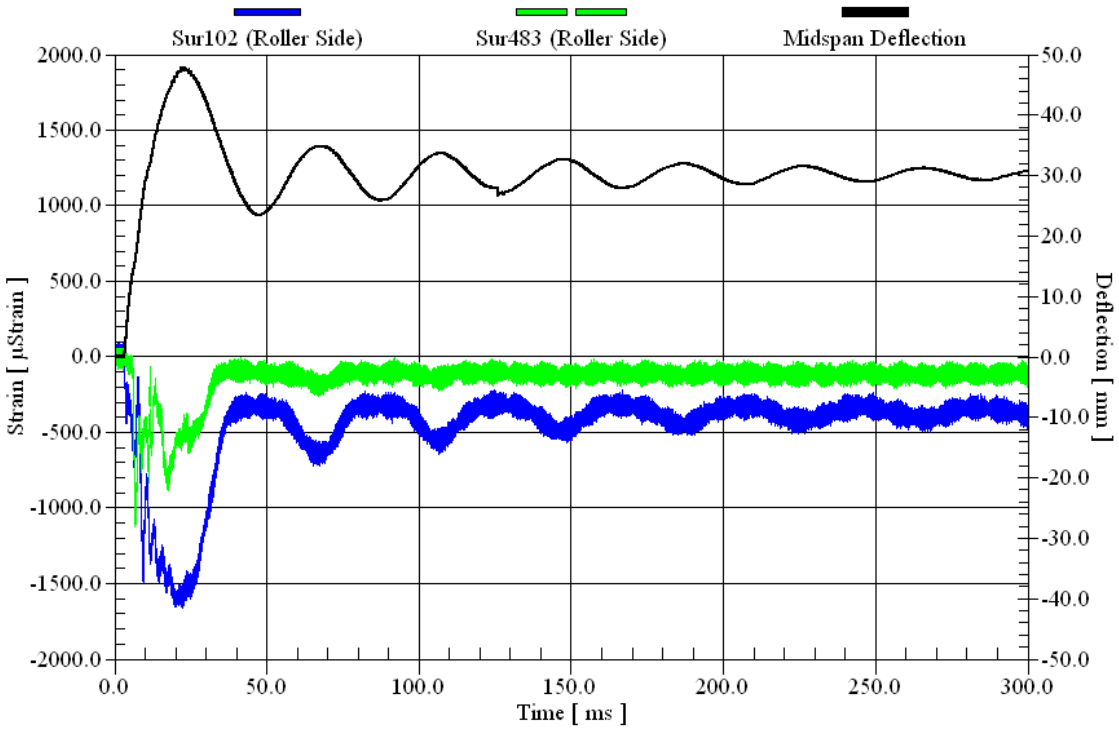

Figure 4-6: Concrete surface strain-time history for Imp-2

Figure 4-7: Midspan zone damage in Imp-2 (lower edge rounded and indented for this specimen due to prototype formwork modifications)

4.2.3 Imp-3

This specimen was impact tested on February 16, 2012 under an axial load of 100 kN. The same axial loading system that was used for Imp-1 was used again for Imp-3, with the only difference that an isolation valve was added near the slave jacks. This valve was closed, prior to impact, when the desired axial load was reached. Figure 4-8 shows Imp-3 prior to impact.

Figure 4-8: Imp-3 prior to impact

This was the first impact test performed where data was recorded by two separate data acquisition systems. To align the time stamps from both systems, the time of peak impact load from each recording was aligned. While the post-peak impact load record from the MGCplus (9600 Hz) compares very favourably with that from the Gen2i (1 000 000 Hz), it is apparent that the slower rate of acquisition is insufficient to accurately capture peak response values as the peak tup load recorded from the MGCplus is 12% lower (325 kN vs 369 kN) than that of the Gen2i (Figure 4-9).

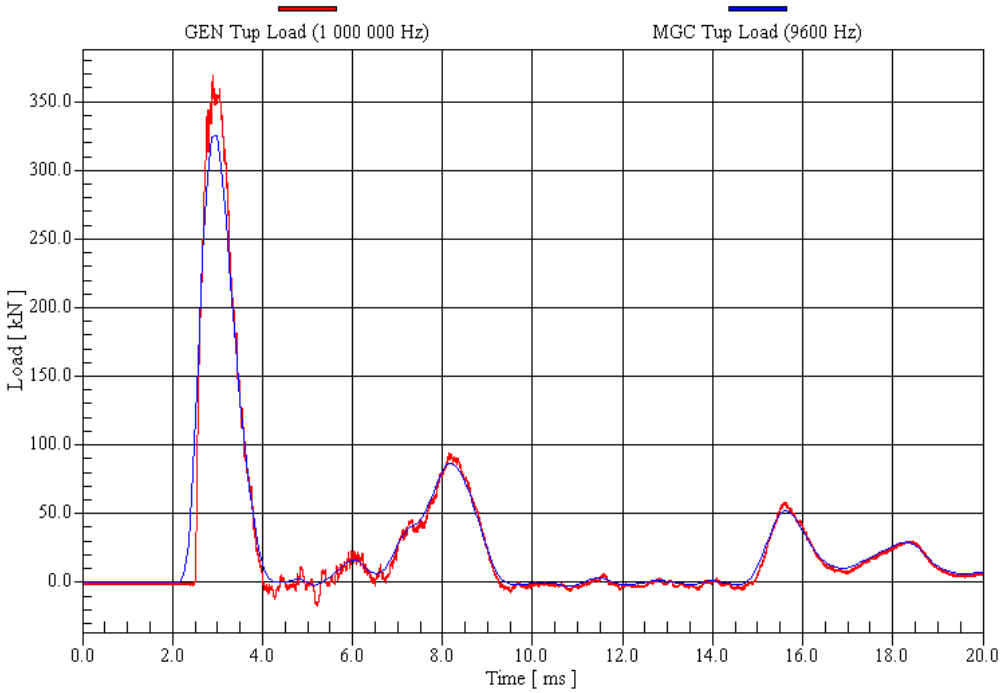

Figure 4-9: Tup load comparison for Imp-3

As for specimen Imp-1 which also had an axial load, the peak reaction load is surprisingly high with uplift forces causing oscillations in the peak response and uplift forces occurring before and after the peak positive spike. Also, a sudden spike in axial load levels can be observed following the impact (Figure 4-10). This will be discussed in Section 5.3. It can be seen that decreasing the axial load on similar columns, from 283 kN to 100 kN, caused an increase in midspan deflection (from 21.5 mm to 29.9 mm) while reducing the peak total reaction load (from 420 kN to 386 kN). Following impact, the axial load stabilized at a value of 110 kN (and not the pre-impact value of 100 kN), due to compressing of the fixed amount of hydraulic oil between the slave jacks and the closed isolation valve. The residual deflection was 6.7 mm, slightly larger than the value of 4.0 mm registered by Imp-1.

Strain readings from this test were captured accurately. Of particular interest are the strain readings from the compression rebar, which experienced tensile strains reaching 5200 μm/m. This will be further discussed in Chapter 5. The signal from the midspan tension rebar strain gauge (BotMid) was lost before peak deflection and is thus of little analytical value. Concrete surface strains were captured for gauges Sur-102 and Sur102. For these gauges, peak compressive strain on the roller supported side reached -2800 μm/m, 25% larger than on the pin supported side, Figure 4-11. Again, localized concrete damage can explain this discrepancy.

This specimen had stirrup spacing roughly 2.7 times larger than that of Imp-1 with an axial load 2.8 times smaller. As such, the observed damage was more significant. Very minimal concrete spalling occurred at the impact surface with fine shear cracks extending from this zone to the bottom of the specimen as depicted in Figure 4-12. Crack widths were not measured for this test.

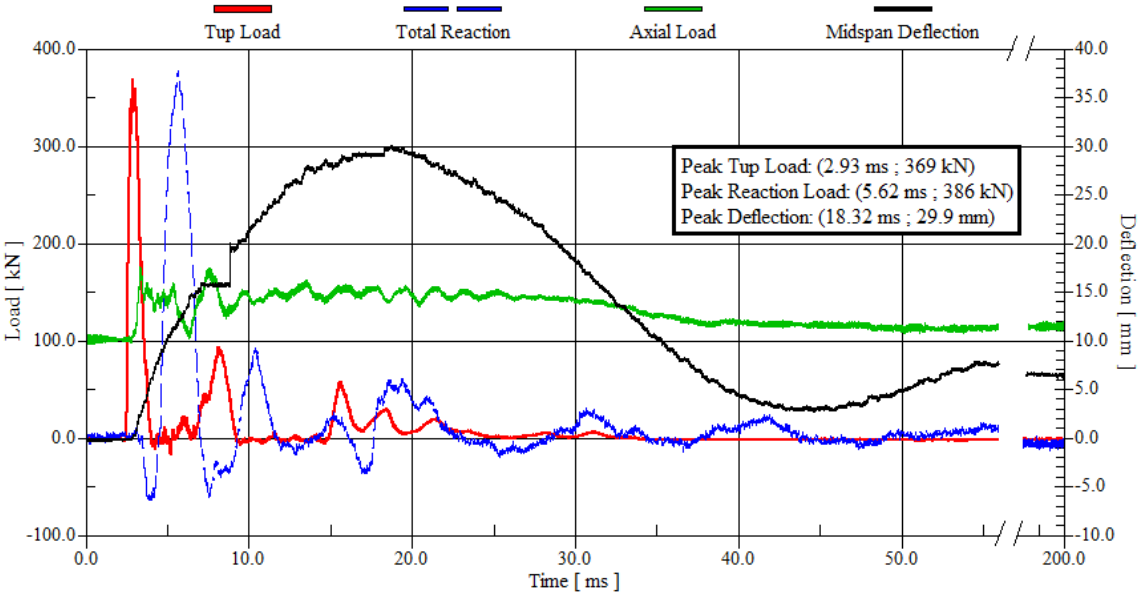

Figure 4-10: Peak response for Imp-3

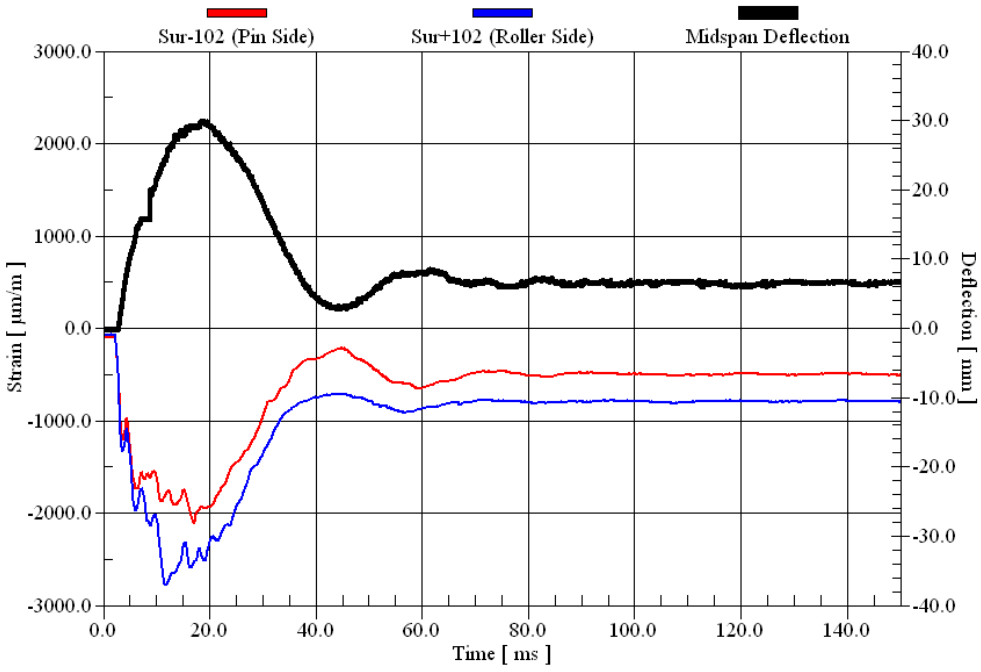

Figure 4-11: Concrete surface strain-time history for Imp-3

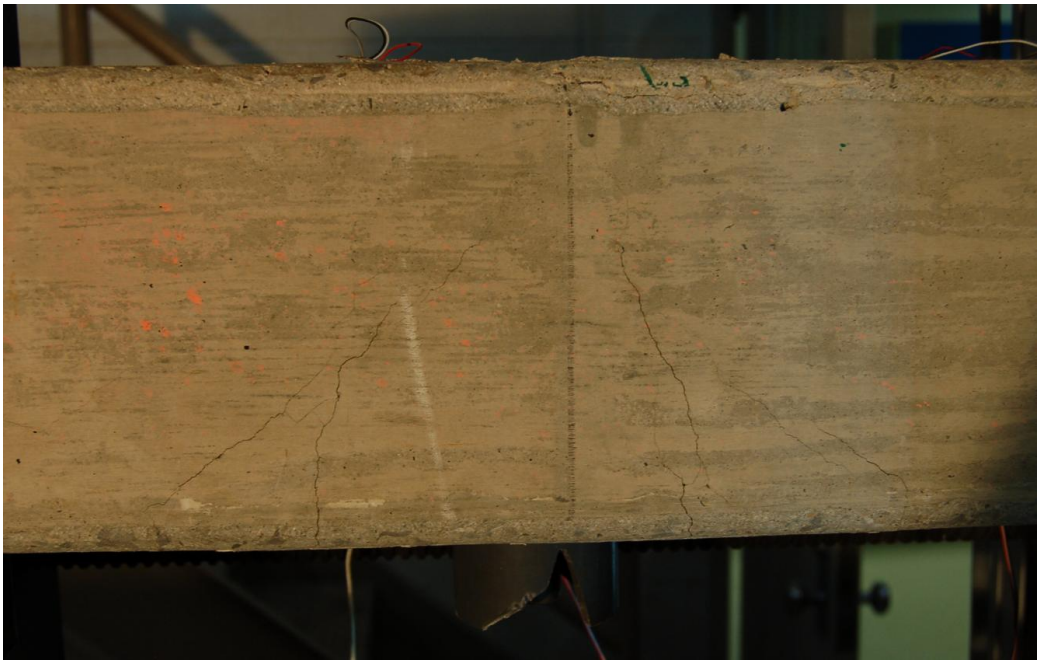

Figure 4-12: Impact zone damage for Imp-3

Note that for Imp-3, the average stirrup strain-time history is given in Appendix A.

4.2.4 Imp-4

This impact test took place on February 22, 2012. To increase damage levels and reduce the effect of the overhangs, the span was increased from 2000 to 2200 mm. This longer span was maintained for subsequent impact and static tests (specimens Imp-5, QS-1 and QS-2). Both data acquisition systems were used for this test with the time signature being synchronized by aligning the peak impact load from each recorder. An accelerometer was fastened with epoxy to the underside of the specimen at midspan for this test. However, the accelerometer detached from the specimen immediately after impact due to a large crack opening across the underside of the beam. As such, the obtained recording will not be discussed. No picture was taken of the specimen prior to the impact test.

Peak deflections for Imp-4 occurred well after peak reaction and tup forces and reached 57.3 mm with a residual value of 37.3 mm as provided in Figure 4-13. With this test, a pattern emerged regarding the total reaction loads for specimens with and without axial load. For specimens without axial load (Imp-2 and Imp-4), the peak total reaction is a fraction (roughly 30%) of the peak tup load. Meanwhile, for specimens with axial load (Imp-1 and Imp-3), the peak total reactions surpass the peak tup load by about 10%. The peak tup load was consistently around 350

kN. The large difference between the observations for specimens with and without axial load requires careful analysis and an evaluation of the test apparatus to ensure that the axial loading system is not the cause of the observed behaviour.

Nearly all strain gauge data followed a similar pattern to that of midspan deflection during oscillation of the specimen after peak deflection, with peak strains reached simultaneously with peak deflections (Figure 4-14). However, very large noise levels combined with the 9600 Hz recording frequency make the values reached during the first 20 ms of the response, prior to peak deflection, difficult to interpret. As for Imp-3, tensile strains reaching 3000 μm/m were recorded in the compression rebar.

Maintaining the same impact mass and velocity while increasing the span resulted in appreciable increase in damage compared with Imp-2. Larger and more numerous shear plug cracks, with residual widths of up to 1.7 mm, were observable, as depicted in Figure 4-15.

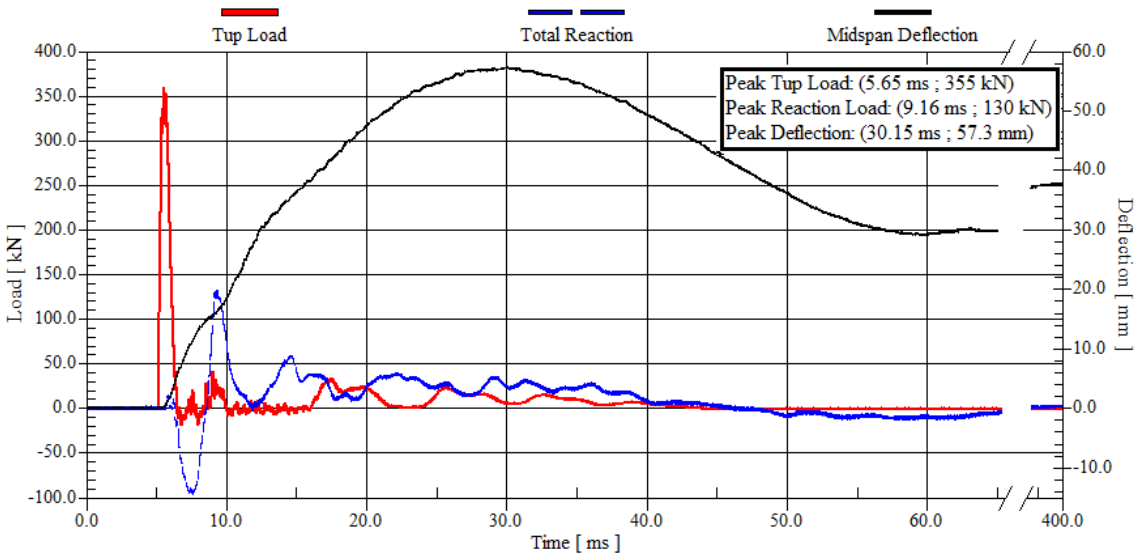

Figure 4-13: Peak response for Imp-4

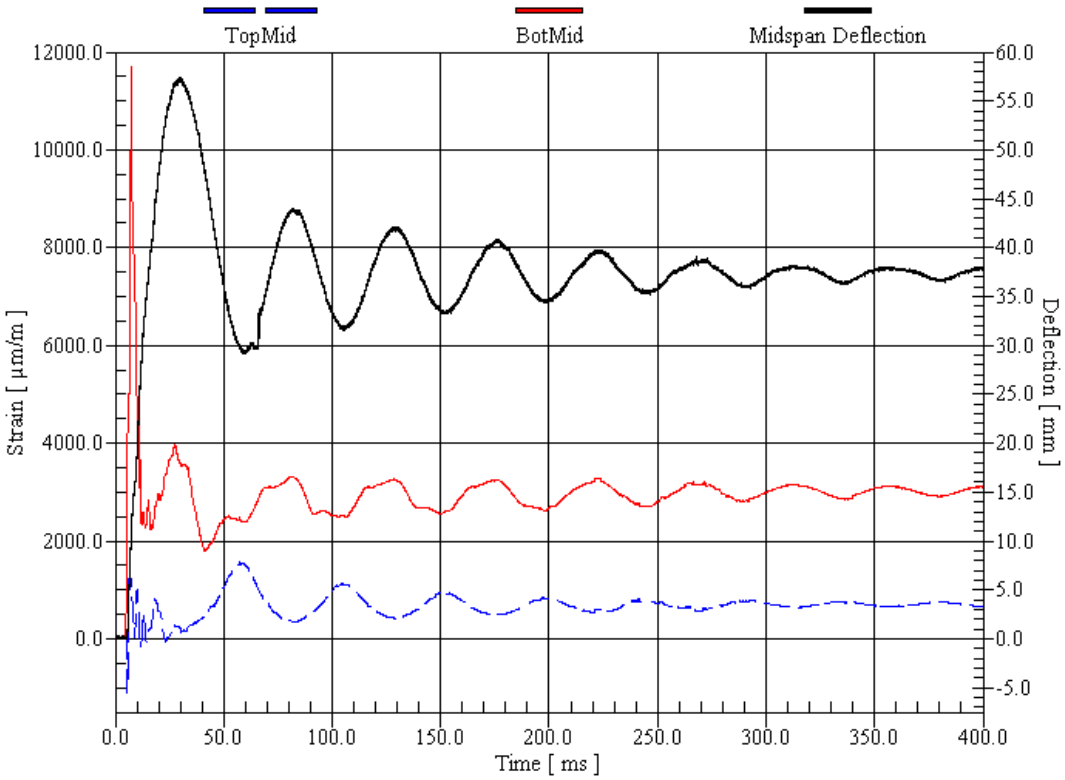

Figure 4-14: Strain-time history in midspan section for Imp-4

Figure 4-15: Impact zone damage for Imp-4

Note that for Imp-4, the compression rebar, tension rebar and stirrup strain-time histories are given in Appendix A. A comparison between the recorded tup load from each data acquisition system is provided as well as a screenshot from the SDOF modeling software.

4.2.5 Imp-5

This specimen was tested on February 27, 2012. A thin layer of epoxy resin was added to the contact surface between the tup and the specimen to ensure distribution of the impact load across the specimen surface. Figure 4-16 shows Imp-5 prior to testing. Unfortunately, all computerized systems used during the initial impact of this specimen experienced a power surge that extended throughout the NRC structural lab; therefore, the data recorded was not reliable. The surge caused the software that remotely controls the drop tower to "freeze" immediately prior to the impact event being triggered. As such, the computer had to be restarted. When the software was reinitialized, it caused the sudden and unexpected firing of the impact load. The Gen2i was triggered but it only recorded data from the reaction loads and one of the midspan lasers. This data did not present any irregularities. The MGCplus, meanwhile, recorded continuously during the surge, but the strain data was questionable given the unusual response as shown in Figure 4-17. All strain measurements from this first impact present extreme noise levels that render the data very difficult to interpret. Because of the uncontrolled impact, the irregular strain data and the lower than expected residual damage levels, this specimen was impacted a second time. The data from this impact is presented as well.

Figure 4-16: Imp-5 prior to impact

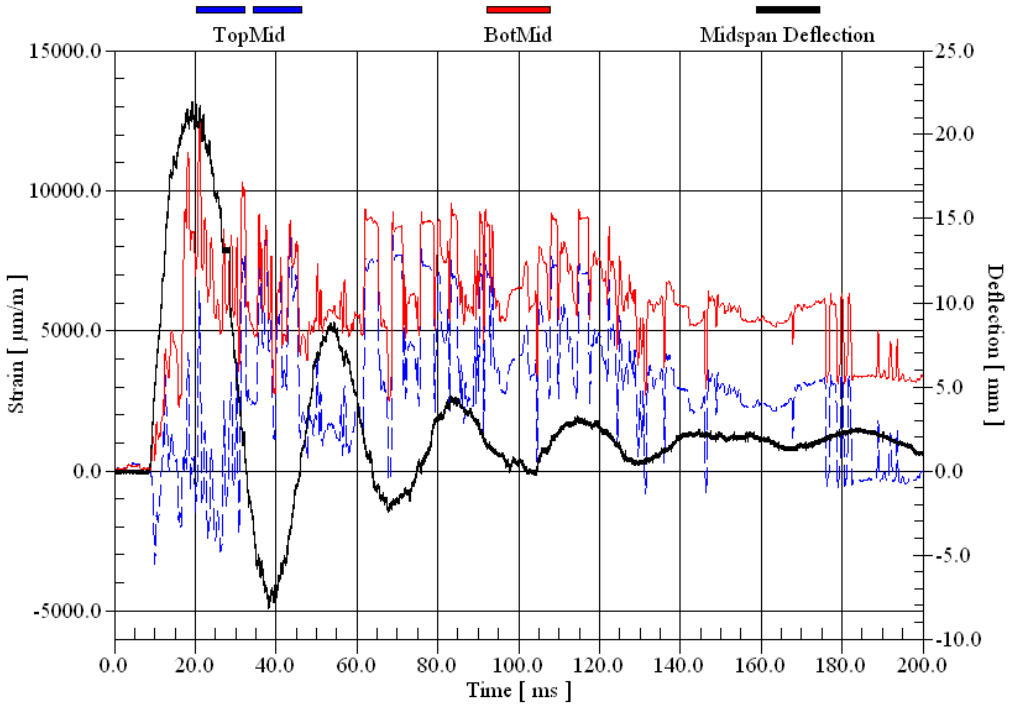

Figure 4-17: Irregular strain-time history in midspan section for the 1st impact of Imp-5

4.2.5.1 1st impact

Peak deflection was 21.4 mm with a residual value of 2.0 mm (Figure 4-18). Peak total reaction load was 255 kN, falling between those observed for the axially loaded specimens and those

without axial load. This peak positive total reaction load is higher than that observed for Imp-2 and Imp-4 (without axial load) but lower than that observed for Imp-1 and Imp-3 (with axial load). The second reaction load spike reached 180 kN for this test, higher than the secondary peaks observed previously. No visible damage to the FRP retrofit was visible following the first impact. Strain-time history plots are not reported here as they presented extreme irregularities. They are given instead in Appendix A.

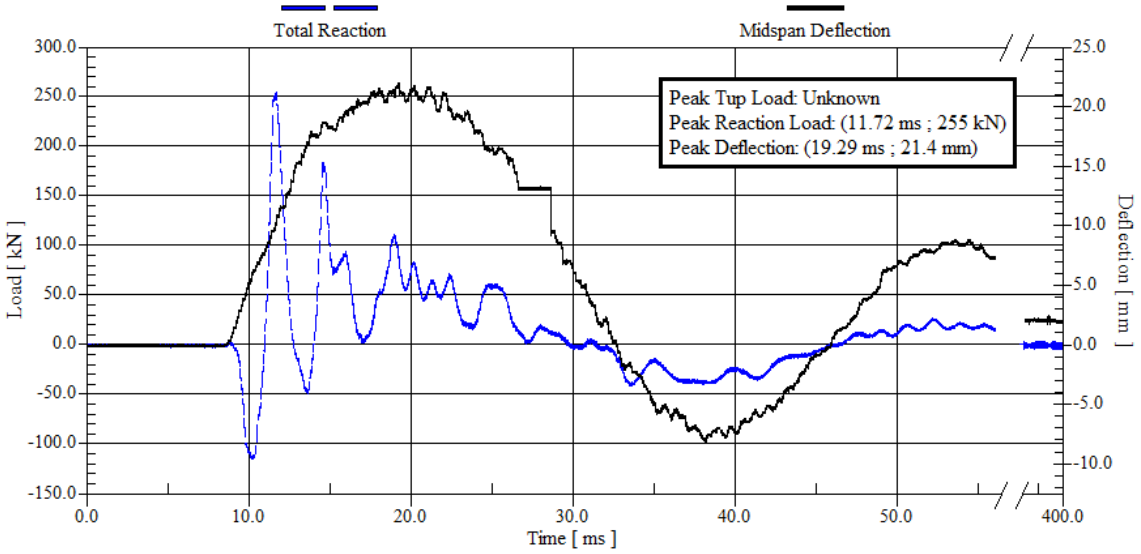

Figure 4-18: Peak response for the first impact of Imp-5

4.2.5.2 2nd impact

For this impact, tup load values were successfully recorded from the Gen2i and MGCplus data acquisition systems as well as from the DAS16000. These values compared very well in the post-peak region. However, as expected, the MGCplus sampling rate of 9600 Hz was insufficient to fully capture peak load As for the 1st impact on this specimen, strain values presented extreme noise levels that post-process refining could not correct and were judged erroneous. They are presented in Appendix A.

Peak deflection during this impact event reached 28.9 mm with a residual value of only 2.1 mm. The same residual deflection value for both impacts indicates that the specimen responds elastically to the second impact. It was thus surprising that the peak deflection during the second impact was 35% higher. A verification of the trigger signal for the first and second impact indicated that, while the second impact achieved the programmed velocity of 7 m/s, the velocity for the first impact may have been as low as 6 m/s (15% lower). The trigger signal for all impacts

can be found in Appendix A. The drop in velocity can be attributed to the power surge and the unexpected firing of the impactor. The variation in impact velocity explains the higher peak deflection for the second impact.

Again, the peak reaction load surpassed the tup load with the peak total reaction load being 28% larger (360 kN versus 282 kN) as shown in Figure 4-19. The reaction load response is very close to that of the first impact but with greater values (41% for the peak). Furthermore, the tup load presents a double peak for this test. This can be attributed to localized damage in the epoxy that may have shattered during the first peak.

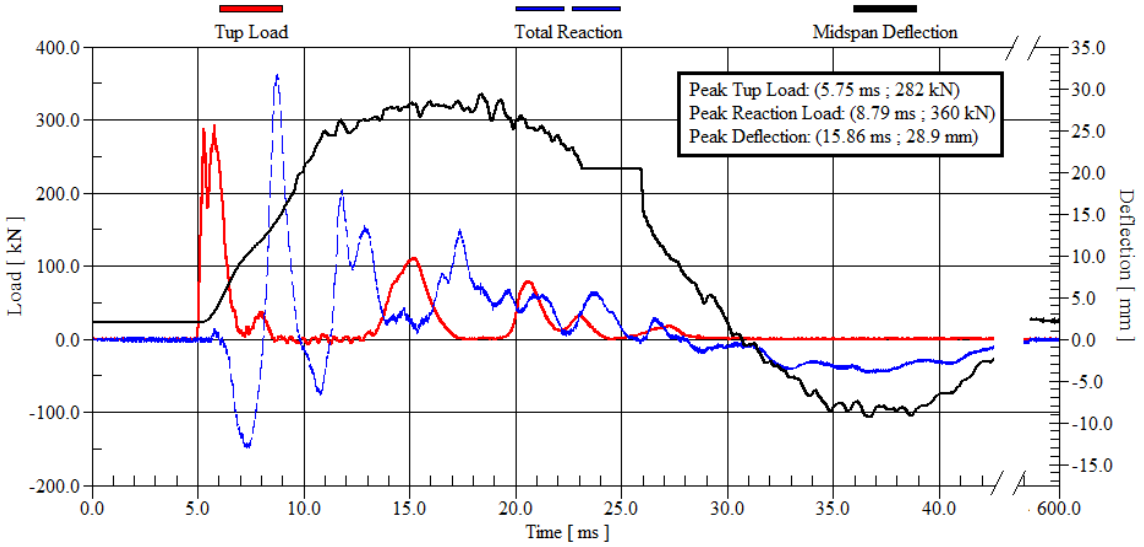

Figure 4-19: Peak response for the second impact of Imp-5

Note that for both impacts on Imp-5, the tension rebar and stirrup strain-time histories as well as a screenshot from the SDOF software are given in Appendix A.

4.3 Summary of Impact Tests

Table 4-1 provides a summary of the response for the impacted specimens. Peak tup load, Peak reaction uplift load, peak reaction load, peak deflection, the time to peak deflection (taken as the difference between time of peak deflection and time of peak tup load) and residual deflection values are given.

The peak tup load for specimens Imp-1, Imp-2, Imp-3 and Imp-4 are very consistent, falling between 355 kN and 371 kN. However, the peak tup load that was measured for the second

impact on Imp-5 is significantly lower, registering 282 kN. This is probably due to the double peak that was observed for the tup load of Imp-5 (Figure 4-19), which resulted in two successive peaks of lower load. Uplift forces were significantly higher for the retrofitted specimen (average of 133 kN for both impacts on Imp-5 versus an average of 75 kN for Imp-1, Imp-2, Imp-3 and Imp-4). For unretrofitted specimens, peak reaction loads were much greater for specimens with axial load than for those without (403 kN versus 116 kN). Both the presence of axial load and the addition of retrofitting FRP resulted in lower peak and residual deflections and quicker deflection response times.

Table 4-1: Response summary of impacted specimens

Specimen	Axial Load (kN)	Peak Tup Load (kN)	Peak Reaction Uplift Load (kN)	Peak Reaction Load (kN)	Peak Deflection (mm)	Time to Peak Deflection (ms)	Residual Deflection (mm)
Imp-1	282	369	-76	420	21.5	11.35	4.0
Imp-2	0	371	-66	101	47.4	19.45	30.2
Imp-3	100	369	-61	386	29.9	15.39	6.7
Imp-4	0	355	-96	130	57.3	24.5	37.3
Imp-5 1st impact	0	-	-115	255	21.4	-	2.0
Imp-5 2nd impact	0	282	-151	360	28.9	10.11	2.1

4.4 Static Tests

4.4.1 QS-1

This specimen was tested statically on March 7, 2012. The loading was displacement controlled and terminated when the midspan deflection reached the same level as that reached by specimen Imp-4 under impact (57.3 mm). The values from displacement lasers, and not the internal readings from the actuator, were used determine midspan deflection. The specimen began to

yield at a load of 19.7 kN before reaching an ultimate load of 22.9 kN at a peak deflection of 56.9 mm (Figure 4-21). Residual midspan deflection was 43.3 mm. Figure 4-20 shows QS-1 prior to testing.

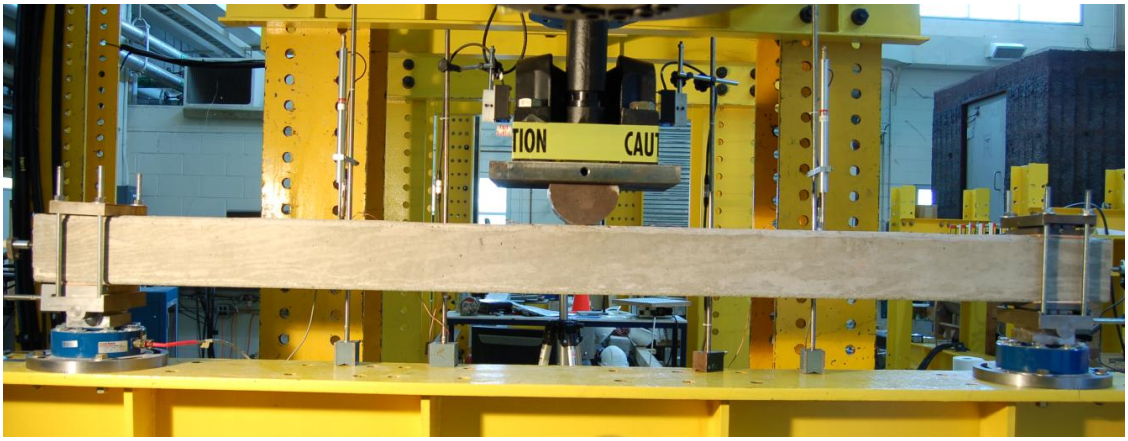

Figure 4-20: QS-1 prior to load application

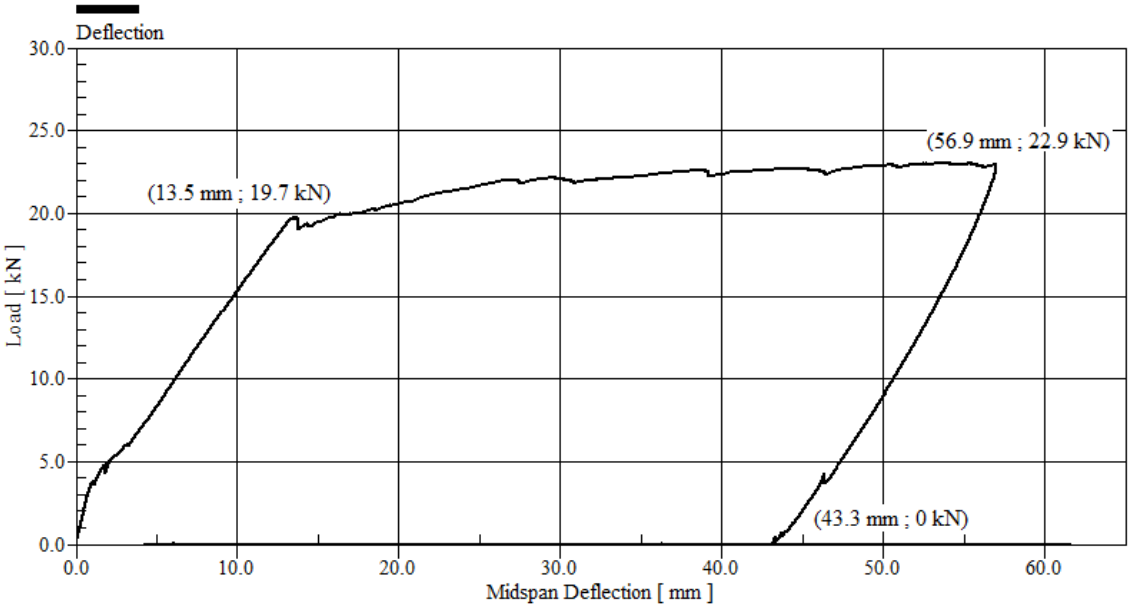

Figure 4-21: Load-deflection for QS-1

Figure 4-22 provides the compression rebar load-strain while Figure 4-23 provides the tension rebar load-strain. A curve identified as "average" indicates that the average strain for coupled strain gauges, strain gauges located at the same distance from midspan, was taken. For example, "Top484 (average)" is the average load-strain from gauges Top-484 and Top484. The average value is reported when strains from coupled gauges are very close in value. Strain on the tension and compression rebars at midspan (gauges TopMid and BotMid) could not be properly evaluated

due to signal irregularities when peak load was approached. As expected, the peak strains for the compression rebar were negative (between 0 and -400 μm/m) and well below the yield strain, ε_y, of ±2500 μm/m. However, the residual strains were positive (between 0 and 250 μm/m). This anomaly cannot be explained without further testing. For the strains on the tension rebar, the larger the distance from midspan, the smaller the peak strain. All gauges operational strain gauges on the tension rebar had residual strains that fell between 400 and 600 μm/m.

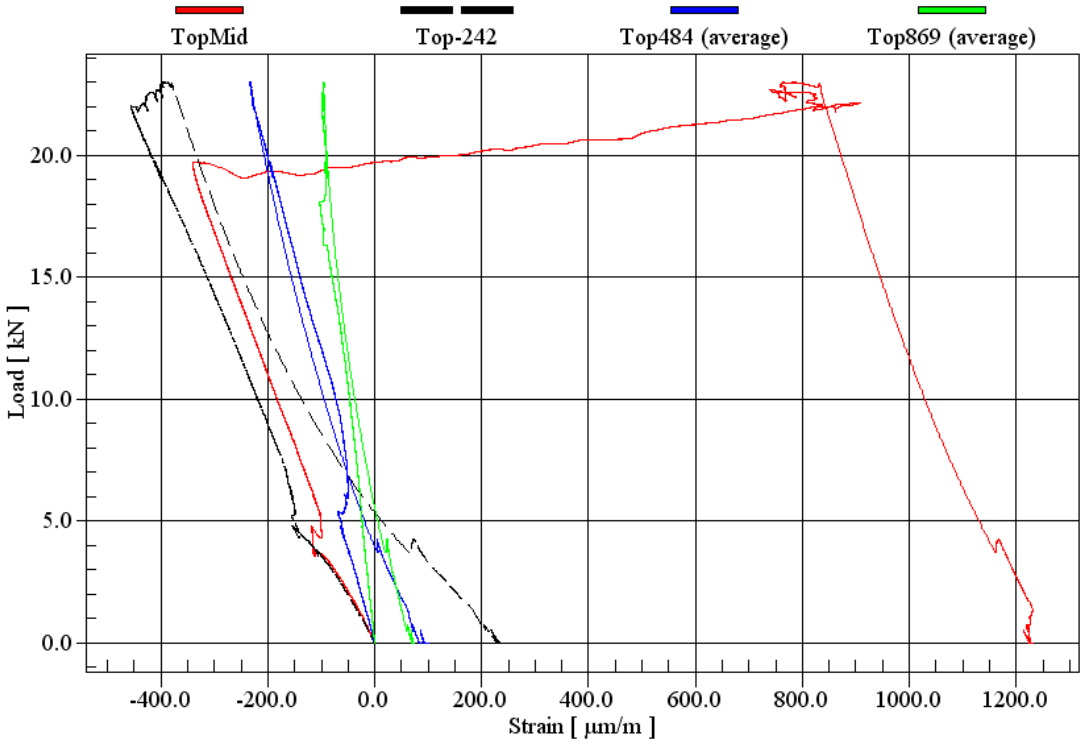

Figure 4-22: Compression rebar load-strain for QS-1

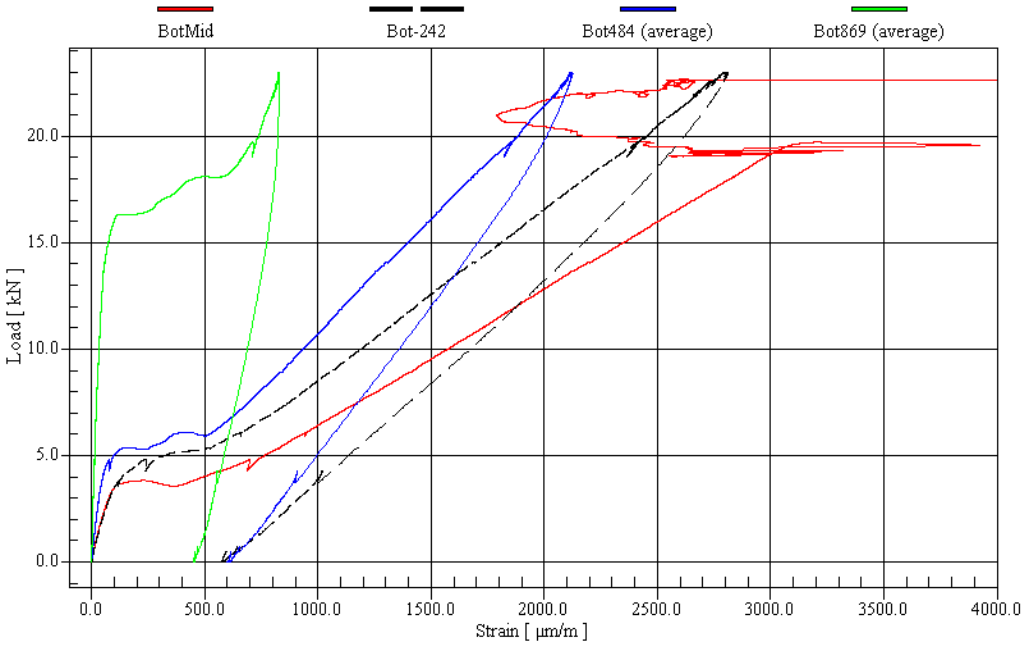

Figure 4-23: Tension rebar load-strain for QS-1

While this specimen reached the same peak deflection as that of specimen Imp-4, the residual crack pattern was not the same, as shown in Figure 4-24. Cracks were more numerous with the widest measuring 1.3 mm at midspan. No shear plug cracking could be identified. The specimen had visibly failed with some minor concrete crushing attributable to bearing failure occurring and a large residual midspan deflection of 43.3 mm. A comparison between the observed damage in specimens Imp-4 and QS-1 is offered in Section 5.8.

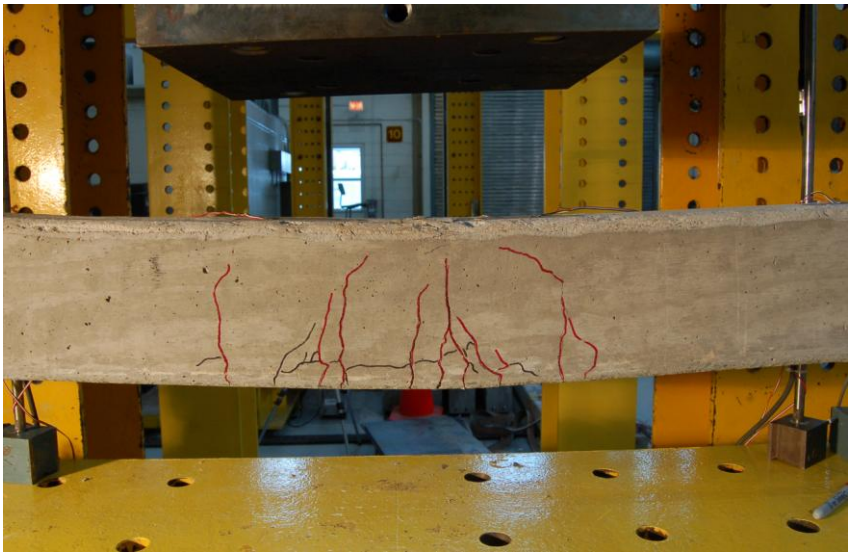

Figure 4-24: Impact zone damage for QS-1

4.4.2 QS-2

The specimen was tested statically on March 12, 2012. Figure 4-25 shows the specimen prior to testing. Two successive displacement-controlled static load cycles were applied: the first up to peak deflection experienced by specimen Imp-5 under the first impact (21.4 mm); and the second to peak deflection sustained by Imp-5 under the second impact (28.9 mm). The peak displacement values attained by QS-2 vary slightly from these values due to deflection measurements recorded by the laser displacement sensors being used for plotting data rather than the position of the actuator stroke. Peak deflection for the first loading cycle was reached at a load of 50.5 kN while the load reached during the second cycle was 63.4 kN (Figure 4-26). The residual deflection following both loading cycles of 7 mm was not visually evident.

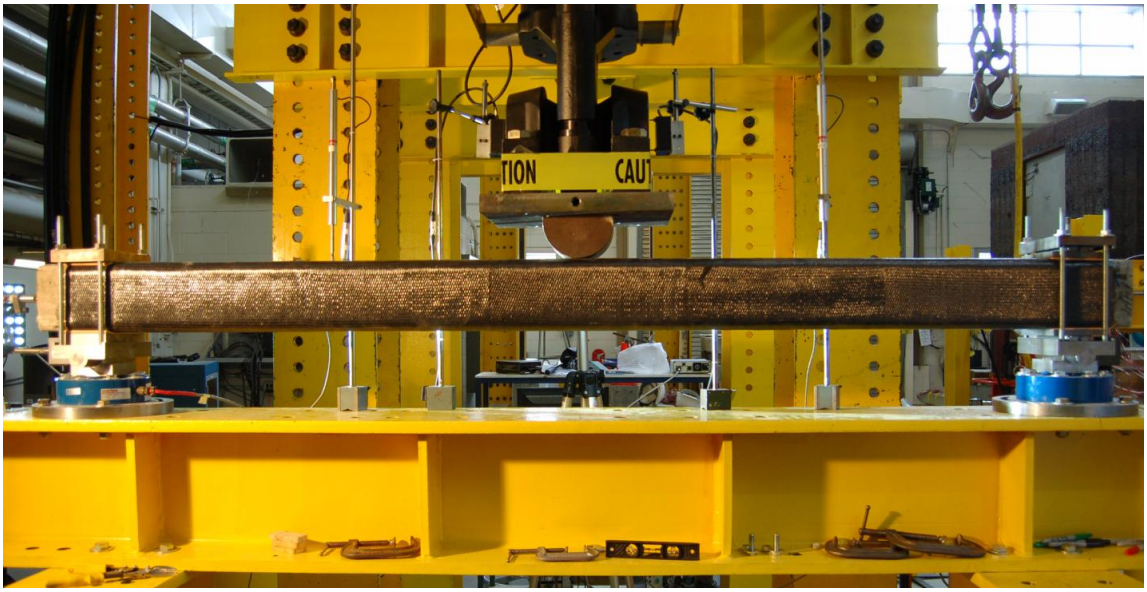

Figure 4-25: QS-2 prior to load application

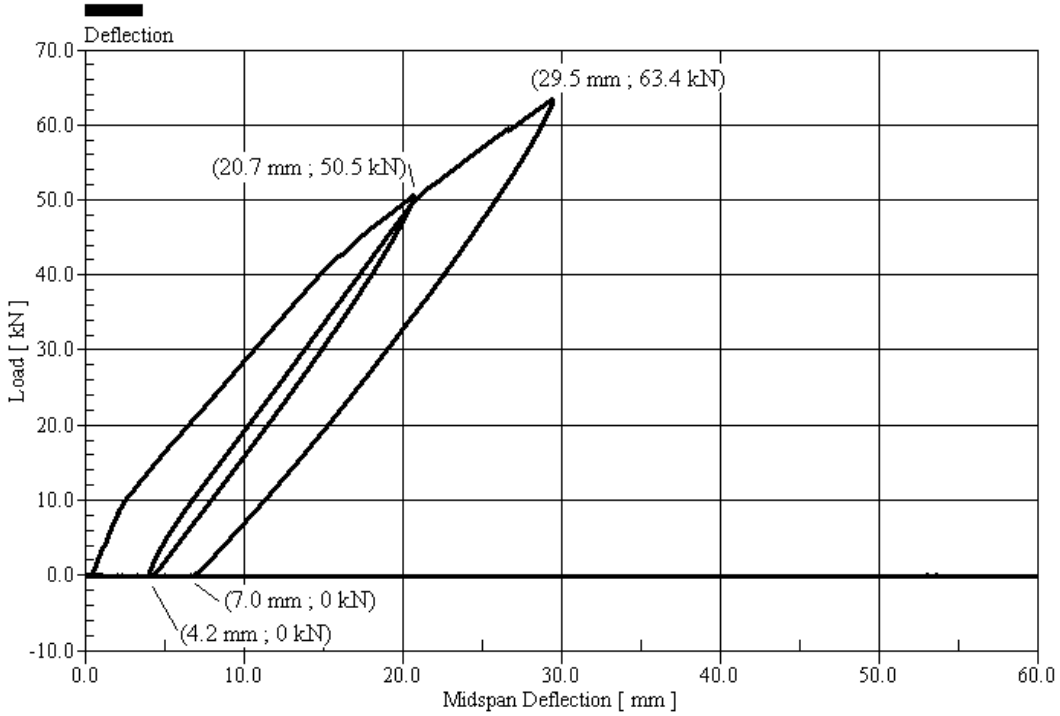

Figure 4-26: Load-deflection for QS-2

Compression rebar strain values followed a predictable pattern with residual deformations falling between -100 μm/m and 100 μm/m (Figure 4-27). The peak strain for Top-242 (-1175 μm/m) is almost equal to the peak strain on the compression rebar at midspan, (-1220 μm/m) even though it is located 242 mm from midspan. On the tension rebar, the average residual strain for gauges located 484 and 869 mm from midspan were below 400 μm/m (Figure 4-28). Meanwhile strain at gauge Bot-242 was elastic during the first loading cycle but large plastic deformations (nearly 16 000 μm/m) were reached during the second cycle. Strain data from middle of the tension rebar cannot be relied upon as it presents bizarre behaviour before the peak load is reached in the first loading cycle.

Some audible crackling and popping attributable to damage in the epoxy resin matrix occurred during the loading of the specimen but no visible damage could be observed following the removal of the load. Figure 4-29 shows the specimen at peak deflection.

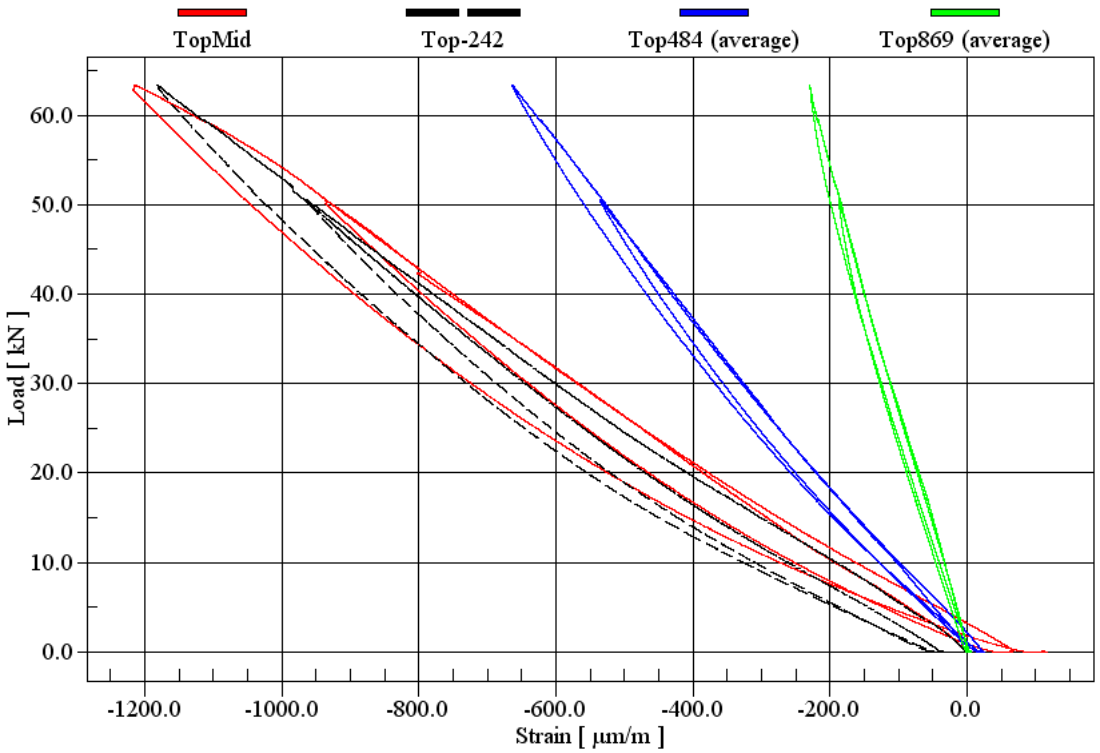

Figure 4-27: Compression rebar load-strain for QS-2

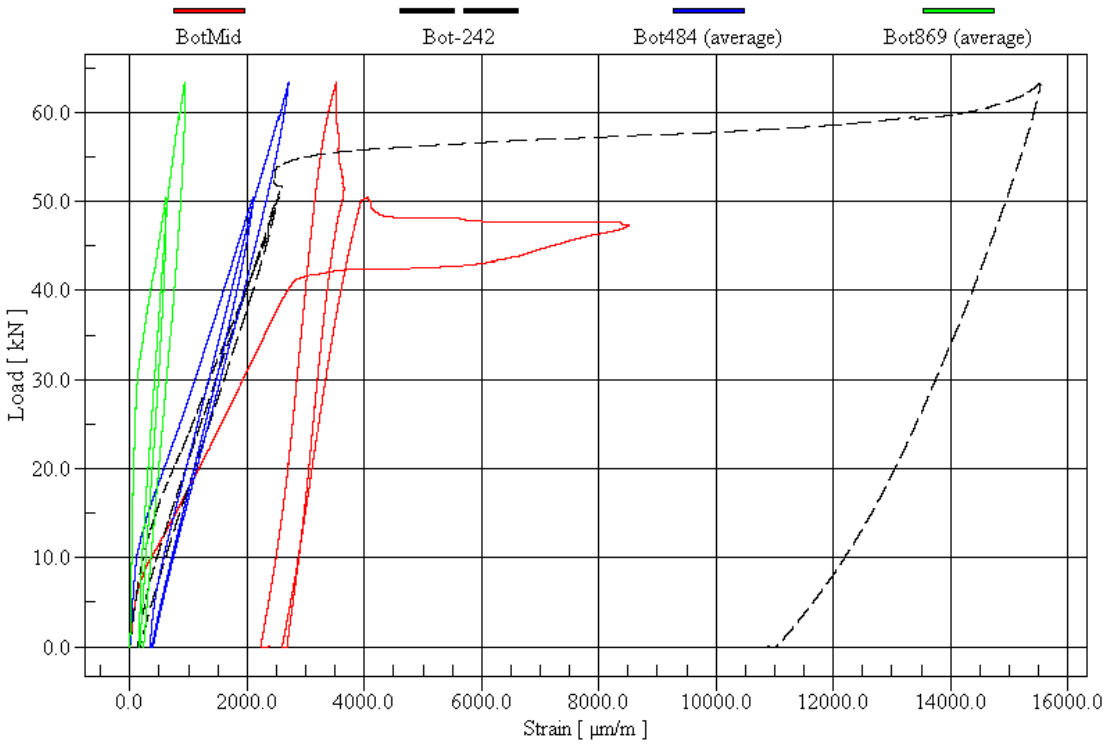

Figure 4-28: Tension rebar load-strain for QS-2

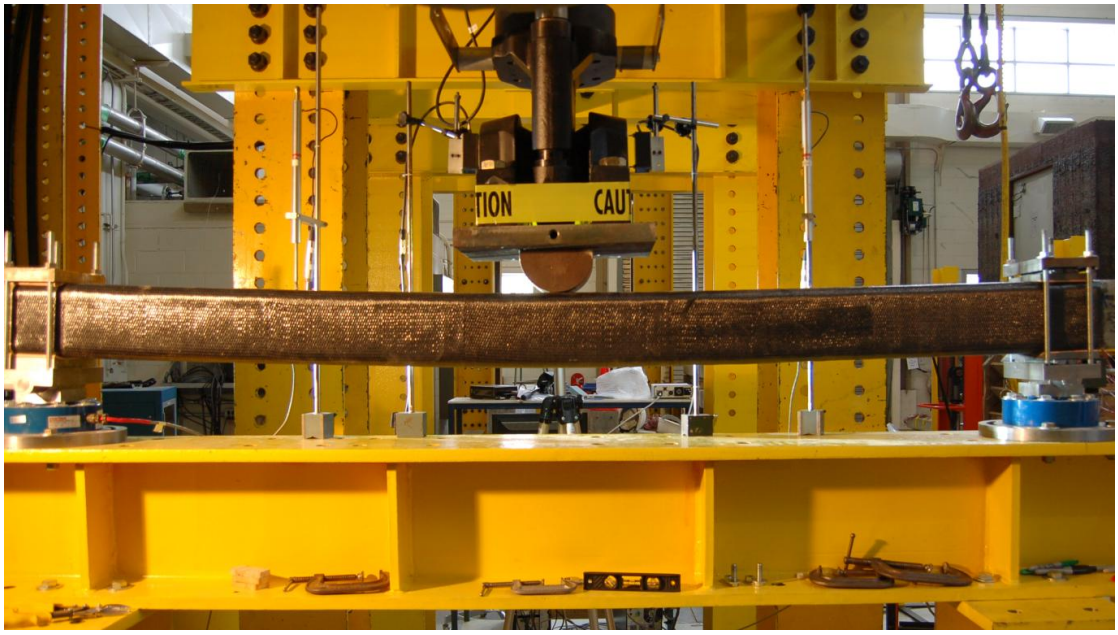

Figure 4-29: QS-2 at peak deflection (29.5 mm) during static testing

Note that for QS-1 and QS-2, the load-stirrup, load-concrete surface and load-midspan strain relationships are given in Appendix A.

Chapter 5: Discussion of Results

5.1 Introduction

While Chapter 4 presented the results, Chapter 5 will offer explanations into observed behaviour and present comparisons between different specimens. First, a SDOF model is used to validate the tup loads measured experimentally. Then, the influence that the custom supports, the axial loading system and the retrofit have on the response of the columns is investigated. Afterwards, the strain patterns observed in the compression zone rebars of specimens Imp-3 and Imp-4 are discussed. Also, the performance of the retrofit with repeated loading, both dynamic and static, is addressed. A comparison is made between the crack mapping observed for specimens Imp-4 and QS-1. Finally, strain rates that were observed for specimens under impact are commented on.

5.2 Tup Load Investigation by SDOF Model

The load cell in the Ceast 9350 drop-weight impact tower and associated data acquisition system (DAS16000) that were used for testing provided the tup load-time history for each impact test. However, due to a programming limitation, this force output would plateau at a value of 182 kN before descending back to zero (green curve in Figure 5-1). To address this, the raw voltage signal from the load cell integrated into the tup was recorded for a low velocity impact test and a calibration was achieved to match that voltage signal to the recorded force output. Thus, using the obtained calibration, the peak force values that occurred during the plateau phase could be interpolated. For each test, the impact force-time history for the output from the impact tower (DAS16000) and the calculated value from the raw voltage measurement for both the GEN2i and MGC data acquisition systems could be compared (Figure 5-1). The initial rise and descent of the load are well captured by both data acquisition systems but it is evident that the MGC (blue curve) is not able to capture very high frequency responses that the GEN2i (red curve) is capable of reading.

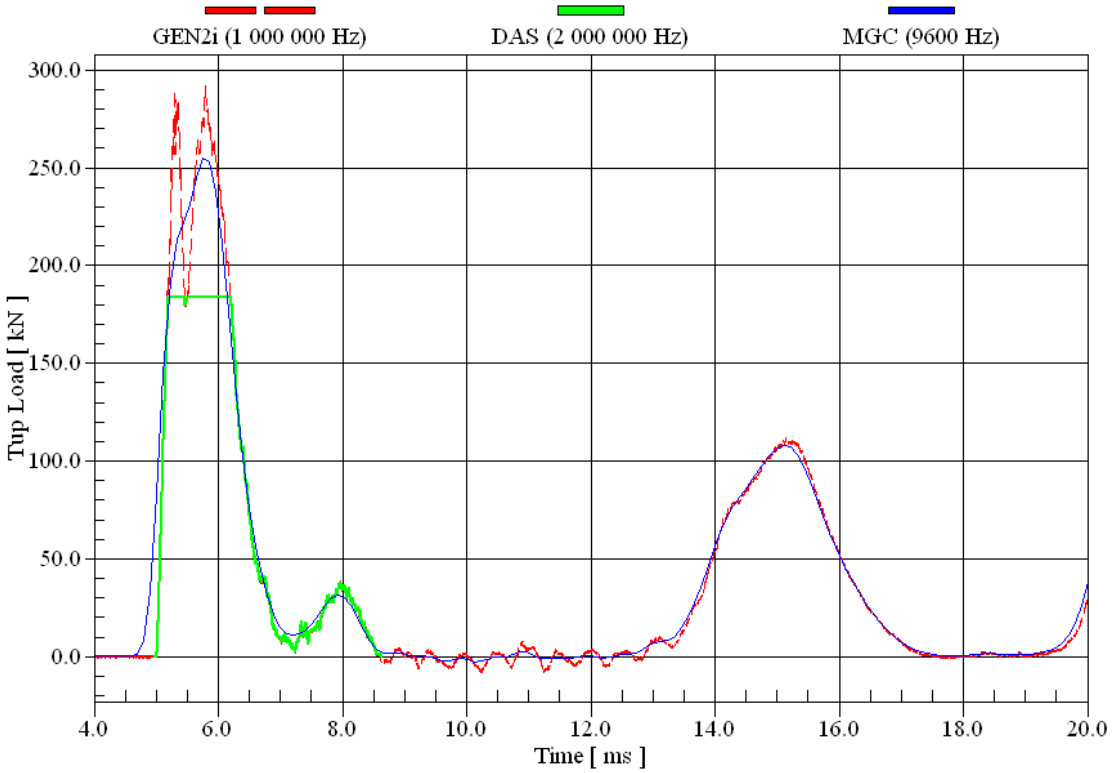

Figure 5-1: Tup load comparison for 2nd impact on Imp-5

Knowing the impact force-time history is of utmost importance when analyzing the response of structures subjected to impact loading. Thus, to verify the calculated tup load-time history, a computer program that calculates single degree-of-freedom (SDOF) displacement-time histories was used. This software, developed by Jacques (2011), presents a user-friendly interface that allows the user to enter the resistance characteristics of the analyzed member, its mass, mass factors (as expressed by Biggs, 1964) and an external forcing function to obtain the predicted response of the member. The single-degree-of-freedom is taken as the midspan displacement for all members. The objective was to use this software to predict the peak midspan deflection and corresponding time of occurrence knowing the forcing function (tup load-time history), the static resistance characteristics of the column, and the mass.

The theoretical impact response of column Imp-4 was predicted using the measured tup load for that test. This specimen was chosen because its static force-deflection relationship was obtained experimentally through specimen QS-1 (QS-1 and Imp-4 were tested in exactly the same manner with the exception of the midspan loading which was static and dynamic, respectively). An idealization of the measured force-time history for Imp-4 was used as the forcing function, while an idealization of the force-deflection values of QS-1 was used as the resistance curve (Figure 5-2

and Figure 5-3). The idealized force-time history has the shape of a trapezoid with a rise lasting only 0.27 ms, followed by a plateau of 340 kN (maintained for 0.23 ms) before a descent back to zero taking 0.84 ms. The entire loading takes place in 1.34 ms. Meanwhile the idealized resistance curve follows an elasto-plastic bilinear shape with an initial stiffness of 1.63 kN/mm that reaches a maximum resistance of 22 kN where the specimen is assumed to be fully plastic. The SDOF prediction of the response is shown in Figure 5-4.

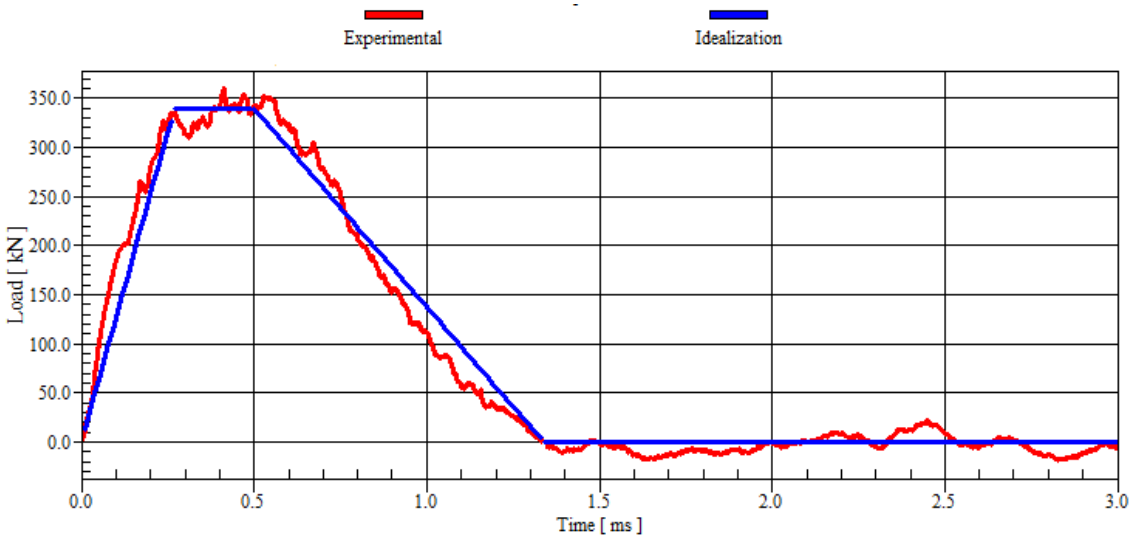

Figure 5-2: Idealized tup load for Imp-4

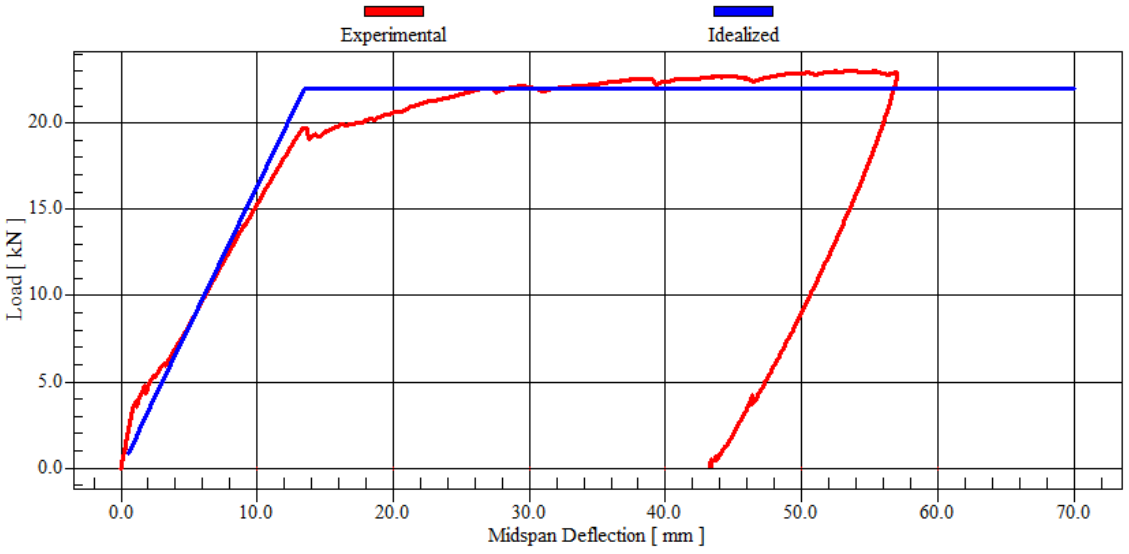

Figure 5-3: Idealized resistance curve for QS-1 and Imp-4

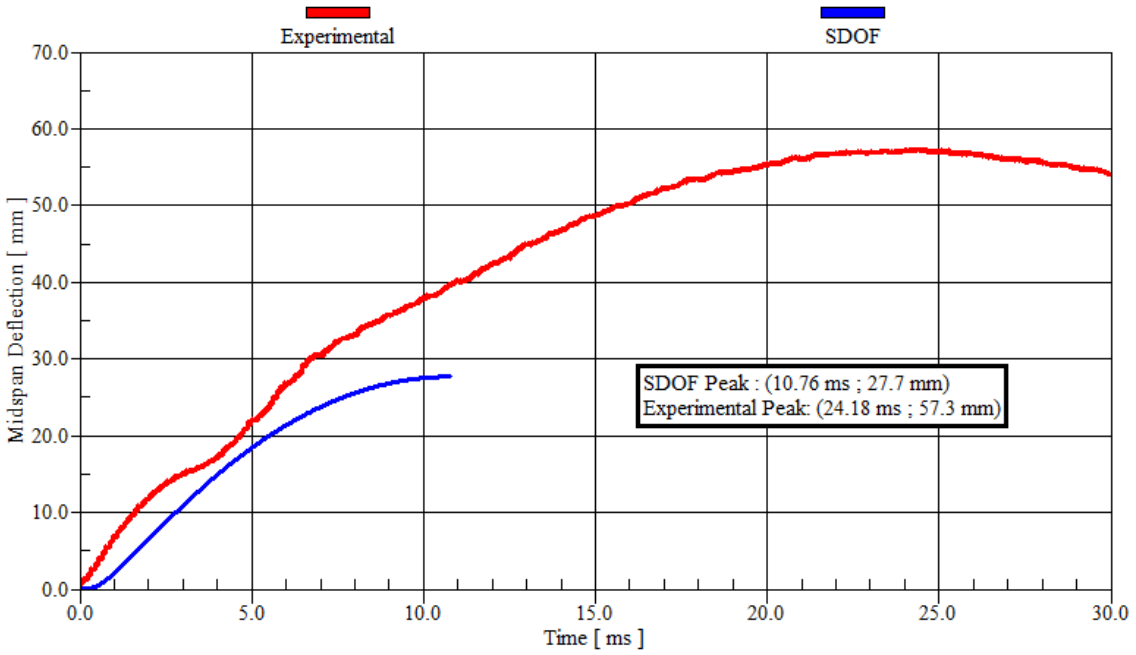

Figure 5-4: Deflection-time history for Imp-4

Visibly, the SDOF prediction underestimated the peak displacement and corresponding rise time for the response of Imp-4. The experimental peak deflection is 107% greater than the predicted value and occurs much later than the predicted time (24.2 ms versus 10.8 ms). This can lead to either of two assumptions: SDOF modeling is inadequate to properly capture the response of inelastic RC members to impact; or there was an error in either the amplitudes of the forcing function or the experimentally obtained resistance curve. While SDOF modeling cannot completely capture the complexities of impact phenomena, it has been shown to give an adequate approximation of peak response (Saatci, 2007). Thus, a second analysis was performed as a verification of the established SDOF model.

The same procedure outlined above was used to obtain the predicted deflection-time response for the second impact test on Imp-5. This test was chosen because the tup load was successfully recorded and because the static resistance curve obtained for QS-2 allowed for the idealization of the impact properties of the specimen (Figure 5-5 and Figure 5-6). The approximated resistance of the specimen for the second impact was taken as a linear function passing through the point of peak static deflection obtained experimentally having a slope (stiffness) of 2.50 kN/mm. The idealized tup load-time history is more complex than that of Imp-4 with the initial peak broken into two successive peaks of 280 kN and 287 kN followed by two smaller spikes in load of 112 kN and 79 kN. The residual deflection from the 1st impact/1st cycle of loading was ignored for

the application of the SDOF model. Unlike for specimen Imp-4, the SDOF predicts the deflection-time history of the second impact of Imp-5 with sufficient accuracy as depicted in Figure 5-7. The experimental peak deflection is only 6% greater than the predicted value while its occurrence is underestimated by 3.04 ms (8.46 ms and 11.50 ms for predicted and experimental values, respectively).

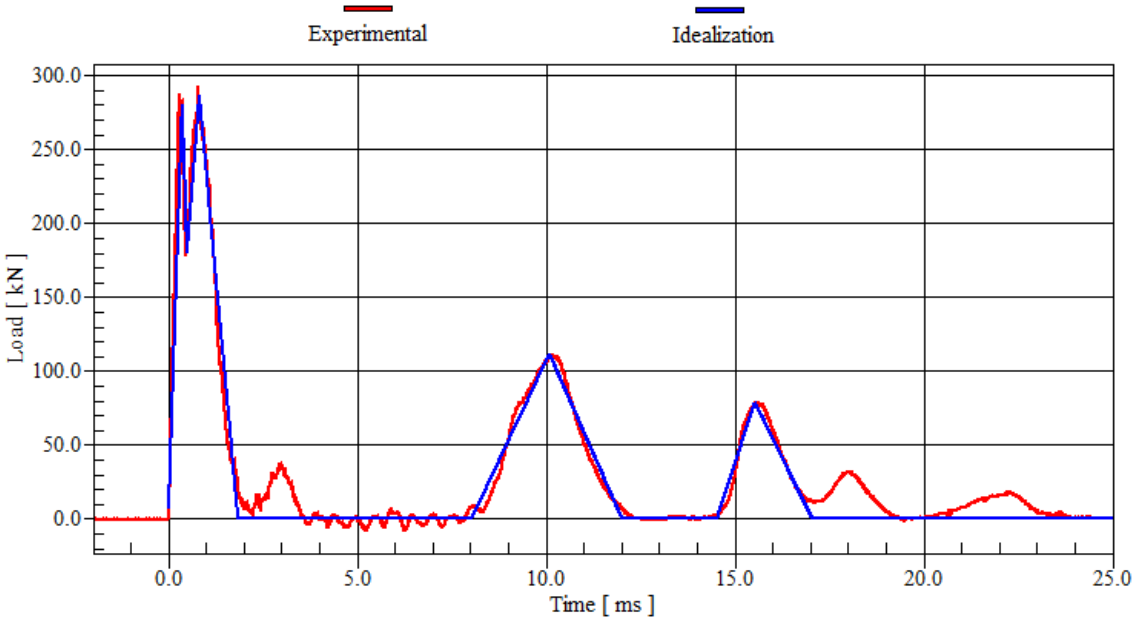

Figure 5-5: Idealized tup load for second impact on Imp-5

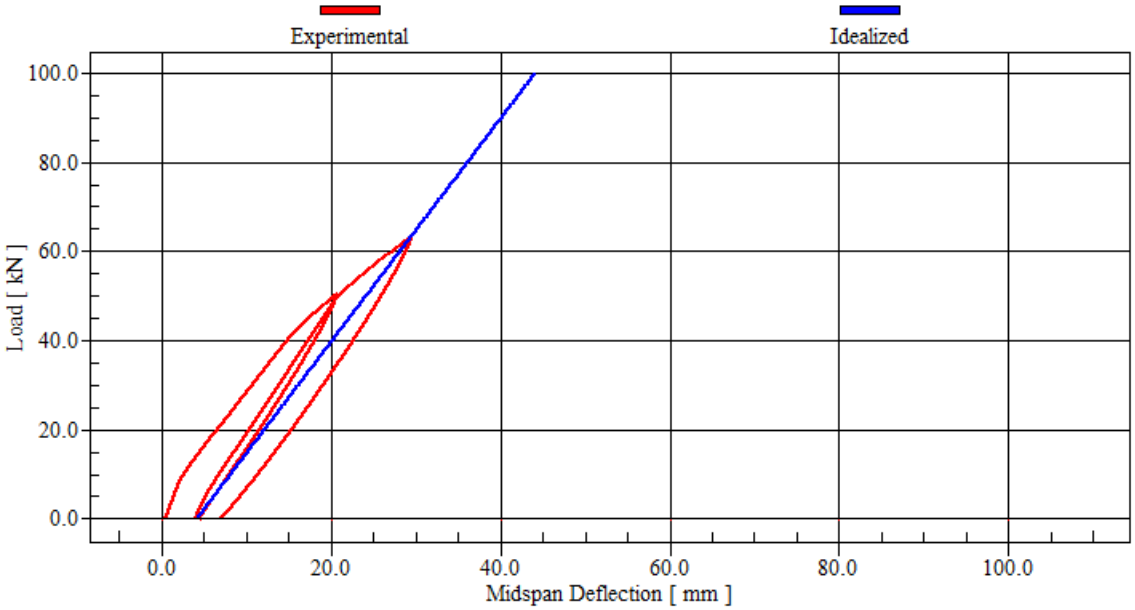

Figure 5-6: Idealized resistance curve for 2nd loading cycle of QS-2 and Imp-5

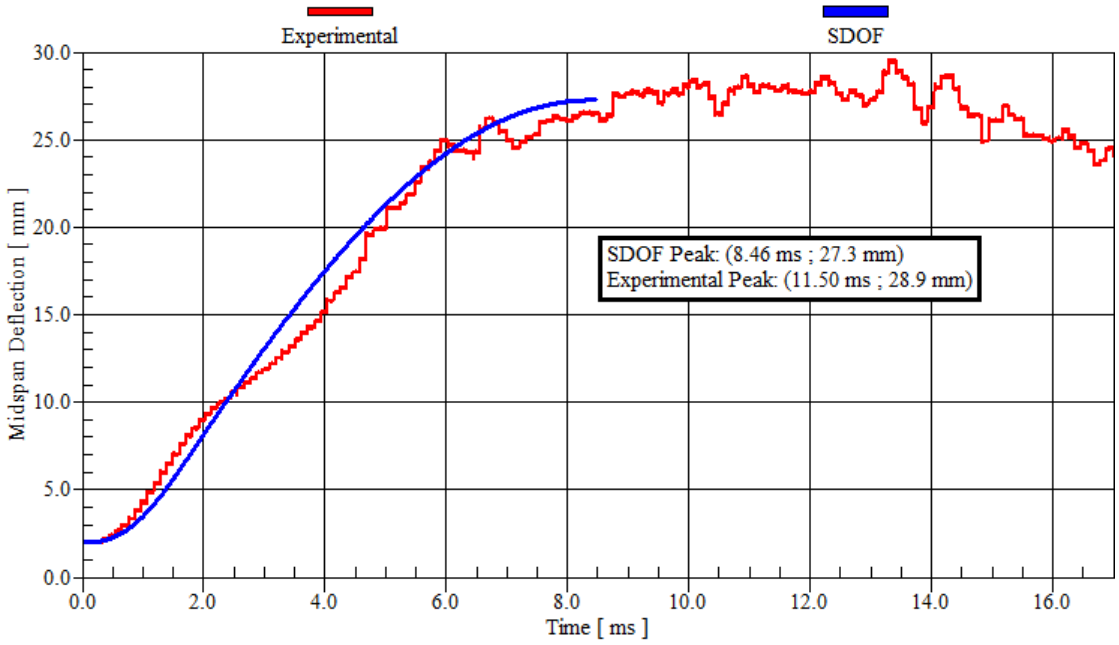

Figure 5-7: Deflection-time for 2nd impact of Imp-5

The discrepancies in accuracy of SDOF modeling for the impact on the unretrofitted specimen (Imp-4) and for the second impact on the retrofitted specimen (Imp-5), while unexpected, can be partly explained by the formation a shear plug in specimen Imp-4, which increases the measured midspan deflection. This behaviour cannot be captured by SDOF modeling. Also, it was obvious from test results that the impact on Imp-4 caused plastic deformations while the equivalent impact on Imp-5 resulted in primarily elastic behaviour. It is speculated that if a member with distributed mass and stiffness, subjected to impact, experiences plastic deformations during its deflection cycles, that the 1st mode of bending might be overshadowed by more complex modes of vibrations that cannot be accounted for with SDOF modeling. This might explain why SDOF analysis performed poorly in predicting the response of Imp-4.

The above analysis is not sufficient to determine the validity of the calibrated tup load-time history. While the SDOF results for the second impact on Imp-5 are excellent, the poor prediction given by SDOF analysis for Imp-4 makes it challenging to state conclusively the success of the performed calibration. Additional impact tests on elastic systems would have been ideal to allow for a more straightforward prediction of expected response using SDOF modeling with obtained tup load-time histories.

5.3 Effect of Pin and Roller Supports

All specimens discussed herein were supported on custom-built supports that replicated the theoretical cases of a pin and a roller end conditions. No literature was available that discussed how this particular support type could affect measured experimental values at either end of tested specimens.

First, to evaluate the performance of the supports, the axial displacements near the pin and roller supports were measured for both quasi-static tests (QS-1 and QS-2). Both tests demonstrated that zero axial displacement occurred at the pin support, validating the design. Meanwhile, the roller support performed properly, allowing elongation of the specimen with increasing lateral load. Interestingly, axial displacements followed a very similar trend to that of the midspan deflections for the same specimen. For the unretroffited specimen (QS-1), axial displacement at the roller support was linear up to cracking at which point the axial elongation at the roller support was 5.1 mm at a load of 19.7 kN. Then, the cracks generated a lengthening of the specimen up to 17.6 mm with no significant increase in applied load (Figure 5-8). For the retrofitted specimen, axial displacement at the roller support increased proportionally to load, with minimal residual displacement at the end of the first and second loading cycles (1.6 mm and 2.6 mm, respectively), as shown in Figure 5-9. While these axial displacements were not accurately measured for any of the impact tests, the same behaviour is assumed, namely that zero displacement occurs at the pin support and that the specimen is free to displace longitudinally at the roller support.

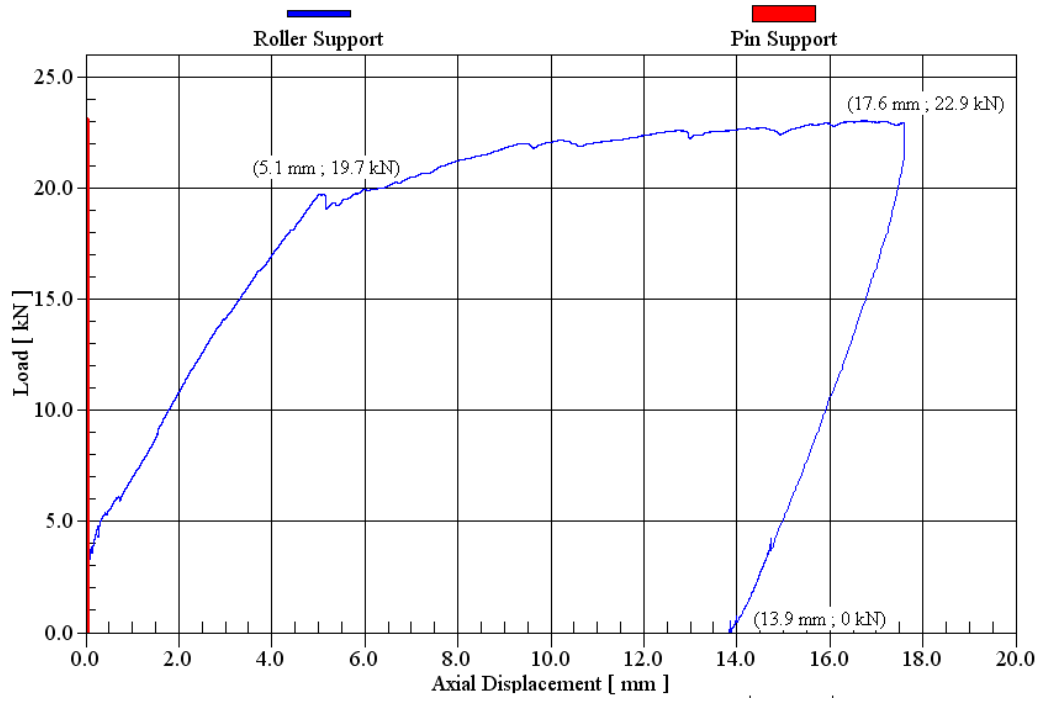

Figure 5-8: Axial displacement at supports for QS-1

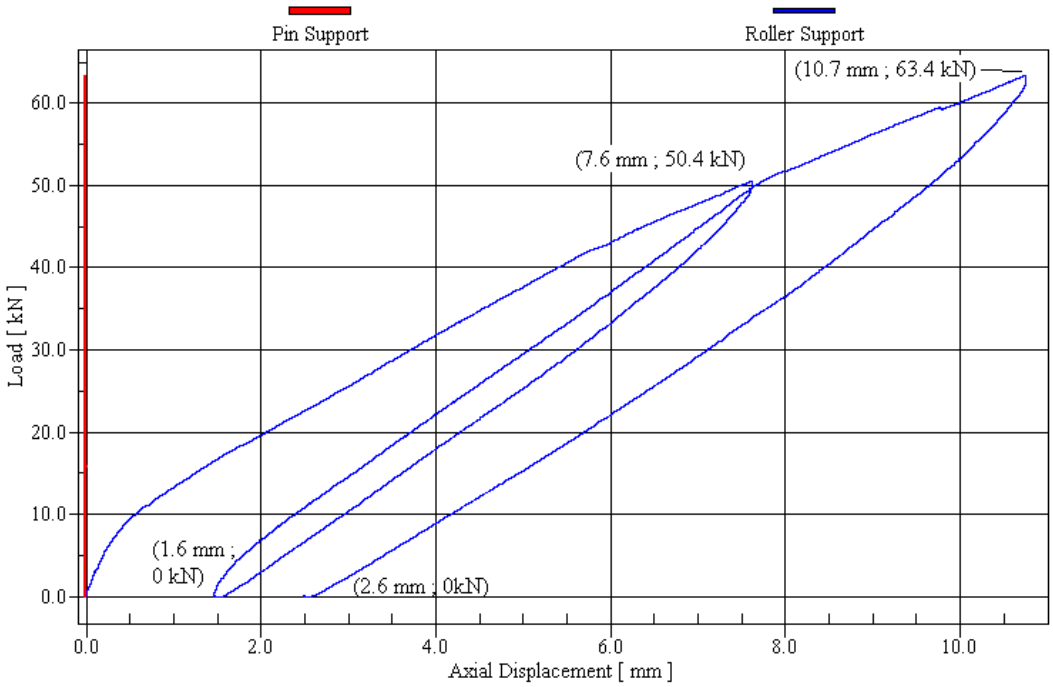

Figure 5-9: Axial displacement at supports for QS-2

Given that the supports behaved according to design, an investigation into the influence the pin and roller supports had on measured strain values was conducted since all specimens were instrumented with strain gauges placed symmetrically about the midspan. It was hypothesised

before testing that the roller support might relieve strain in the specimen near that support while increasing tensile strains in the specimen half nearest to the pin support. Some strain gauge pairs were not included in the analysis as a result of one or both symmetric gauges forming a pair not working.

For the static tests, no conclusive evidence was found to show that the different support configurations at each end of the specimen had any influence on strain patterns within the longitudinal steel. For symmetric gauges, the peak strain consistently fell within 150 μm/m of its counterpart strain gauge (Figure 5-10 and Figure 5-11). Without further test results, this slight difference can only be attributed to non-homogenous material and to slightly unsymmetrical placement of the gauges. Unexpectedly, very large differences were observed from strain gauges placed on the concrete surface, 102 mm from midspan (Sur-102 and Sur102) for specimen QS-1. Peak compressive strain for Sur102 on the roller side reached -4000 μm/m, while the value for its counterpart (Sur-102) on the pin side was 33% lower, -2670 μm/m (Figure 5-10). It is possible that localized concrete crushing near one of the gauges caused the discrepancy but additional static test data is required to confirm this unsymmetrical behaviour at the concrete surface.

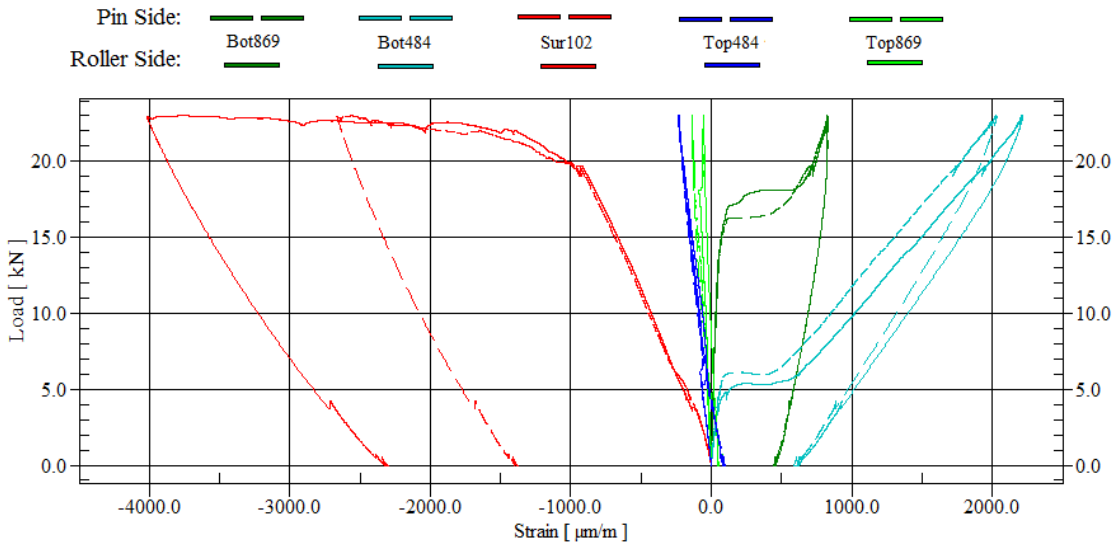

Figure 5-10: Comparative load-strain for QS-1

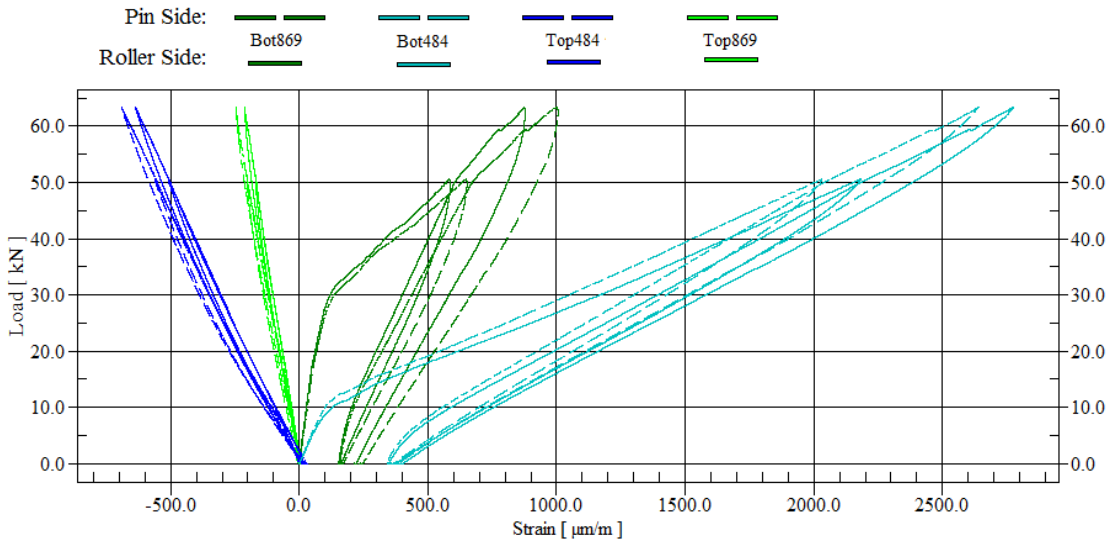

Figure 5-11: Comparative load-strain for QS-2

For the impact tests, strain-time data was plotted for the specimens for which quality strain data was acquired (Imp-3 and Imp-4). Only gauges situated on the compression rebar could be compared for Imp-3 due to the malfunctioning of gauges located elsewhere in the specimen. The only major observation to be made regarding the gauges in Imp-3 is that those located on the pin side experienced considerably more tension than their counterpart on the roller side. That these gauges, situated on the compression rebar, experienced tension was not expected since their position in the cross-section, in addition to the axial loading applied, would indicate predominance for compressive strains in their response. This tension-dominated response will be discussed further in Section 5.6.

The response of symmetric gauges for Imp-4 is very consistent between coupled gauges with the exception, of the concrete surface strain gauges. For this test, the pin side gauge (Sur-102) experienced a 75% greater peak compressive strain than its counterpart, Sur102 (Figure 5-13). This could be attributed to a shift of localized damage towards the pin side more than to the influence of the support conditions.

For both of these impact tests, it is important to observe that peak strain in longitudinal rebar generally occurred well before peak midspan deflection, contrary to observed strain response during static tests. Whether this was due to shock wave propagation or to excitations of different mode shapes remains to be determined. The presence of a roller support at one end of the specimen seems to have some influence on strain symmetry about the midspan especially for the

specimen loaded axially. Additional strain data closer to the respective supports would help for future analysis.

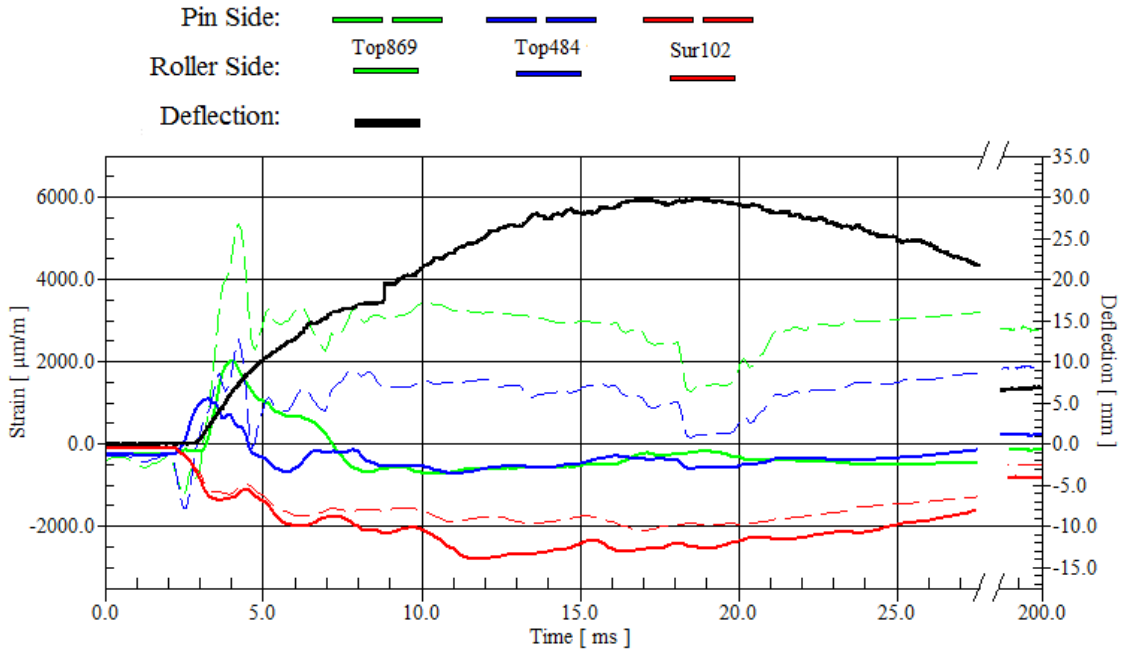

Figure 5-12: Comparative strain-time history for Imp-3

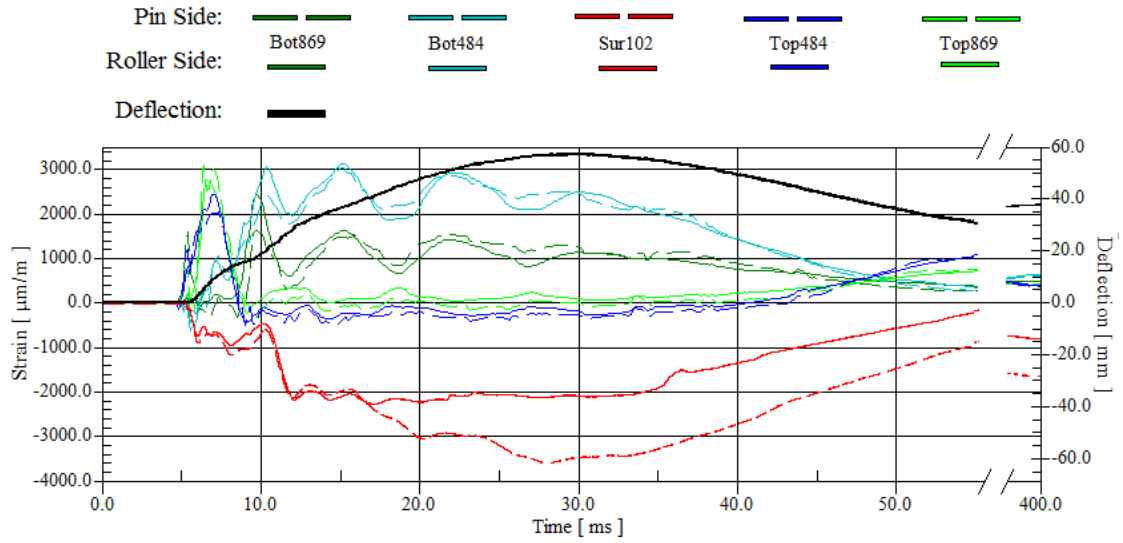

Figure 5-13: Comparative strain-time history for Imp-4

5.4 Axial Load

5.4.1 Axial Loading System Performance

A custom-built axial loading system was used to apply axial load to test specimens Imp-1 and Imp-3. Its performance will be discussed in this section. For Imp-1, the quasi-static application of axial force resulted in non-negligible reaction loads at the supports. This can be seen in Figure 5-14 which shows the individual reaction forces and the strain at strain gauge Sur102 with increasing axial load. This would seem to indicate that a portion of the axial load is transferred into the supports instead of into the column, increasing the measured reaction forces, as was observed for specimens Imp-1 and Imp-3. Strain measured on the concrete surface at Sur102 did not increase linearly but this is to be expected for a strain gauge on the outer surface of the specimen. Deflection in the bending plane, meanwhile, was minimal for the entirety of the axial loading phase (see Appendix A).

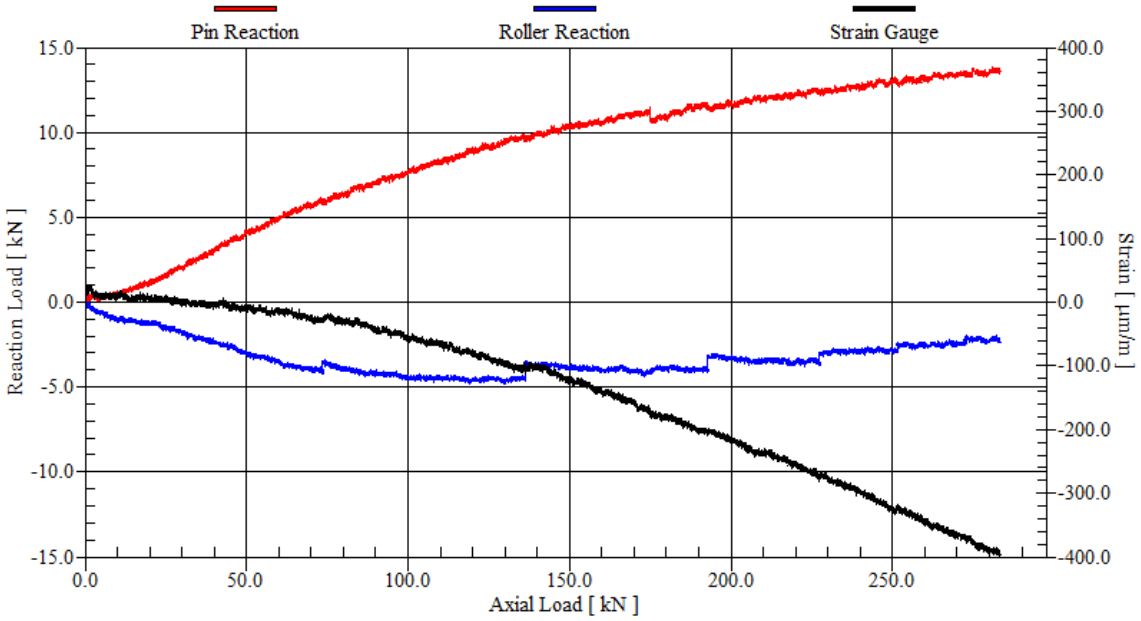

Figure 5-14: Reaction loads and strain during quasi-static axial load application for Imp-1

For Imp-1, the axial load was kept constant at 283 kN prior to impact. The aim was to obtain 300 kN but the load conversion factor between the MTS and the master jacks was not exact, resulting in a slightly lower load. There was a sudden rise in axial load to 337 kN only 0.54 ms after the peak impact force was reached. Eight hundred milliseconds after this rise, the axial load level stabilized back to 280 kN (Figure 5-15). The support reaction measurements demonstrated that the axial loading system transferred a portion of the applied load into the supports after the axial

load stabilized following the impact: the roller support (nearest the slave jacks) stabilized at a load of 5 kN, while the pin support reaction stabilized at -10 kN (upwards).

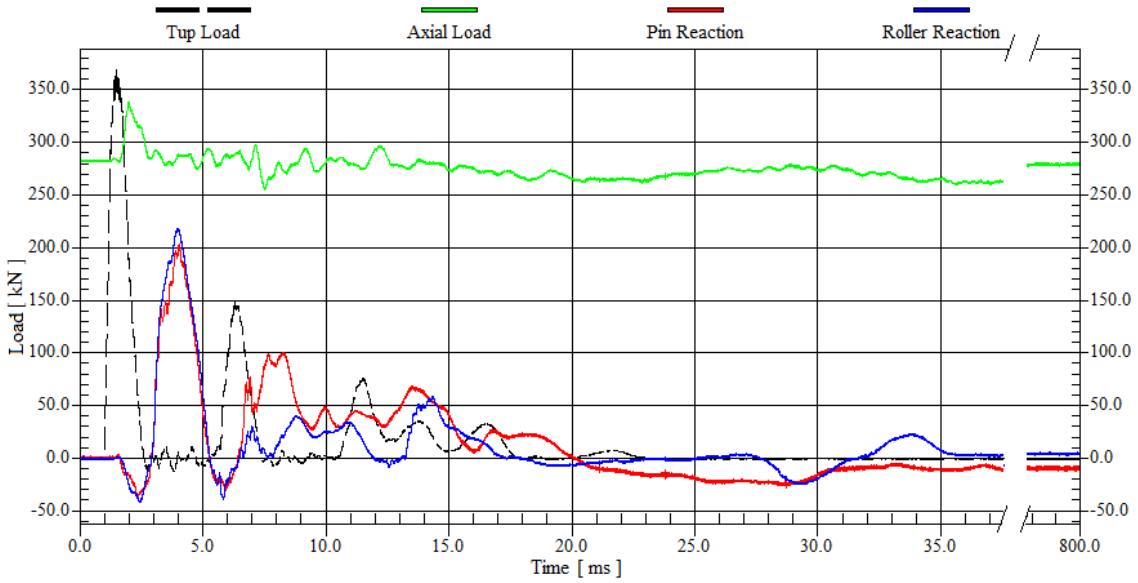

Figure 5-15: Axial load and support reactions for Imp-1

One modification was made to the axial loading system for the impact test on Imp-3: a shut-off valve was added in the system near the slave jacks. This valve was closed prior to impact when the desired axial load of 100 kN was reached, isolating the slave jacks from the master jack and MTS. Following impact on Imp-3, the axial load stabilized to 115 kN after reaching a maximum of 174 kN, 0.47 ms after peak impact force (Figure 5-16). This increase in load was reasonable since the specimen elongated slightly at the roller support as it deflected during the impact, compressing the fixed amount of hydraulic fluid in the system. There is also a secondary spike to 170 kN, 4.68 ms after peak tup load. It was found that the effect of the shut-off valve on the response of the specimen was negligible since both Imp-1 and Imp-3 present similar responses.

For the impact test on Imp-3, the high speed camera was used to film the roller support and the axial load transfer plates nearest the slave jacks. The video was captured at 2573 fps. The video indicates that the roller behaved as expected, allowing elongation of the specimen. However, it was evident from the full video, of which two frames are shown in Figure 5-17, that the axial loading system seemed to restrict the uplifting motion of the overhang, contrary to design intention. Most noticeable was that the post-tensioning rods were pushed upwards due to the roller of the axial system applying a vertical force on the intermediate transfer plate. The rods were not intended to move/deflect and were only designed to carry axial forces. That does not

seem to have been the case. As such, the performance of the axial loading system is deemed unsatisfactory as it most likely transfers load into the supports, increasing recorded values.

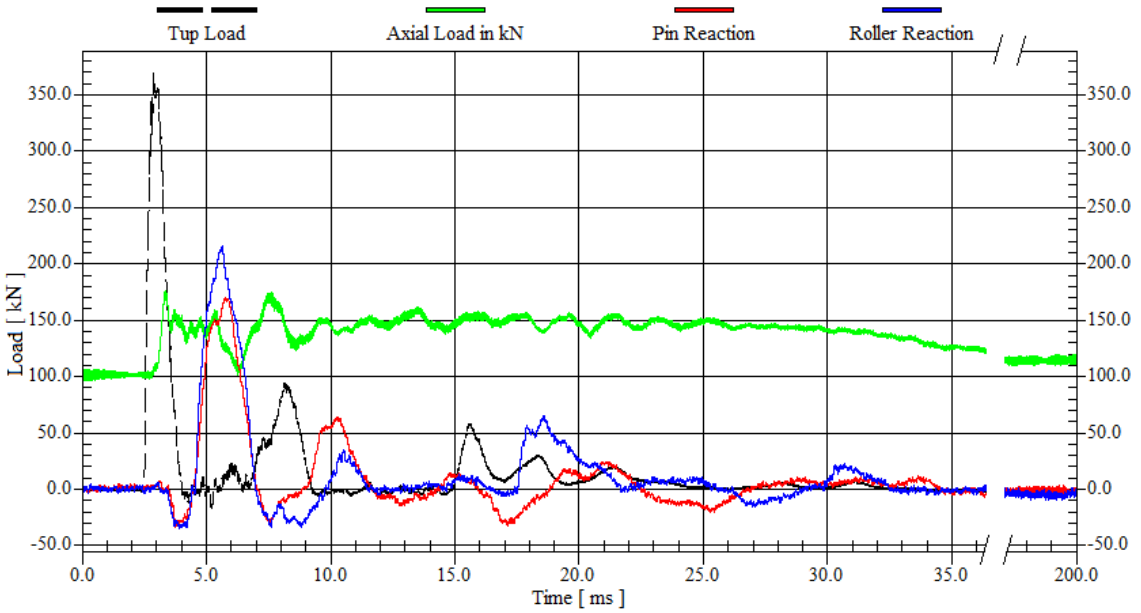

Figure 5-16: Axial load and support reactions for Imp-3

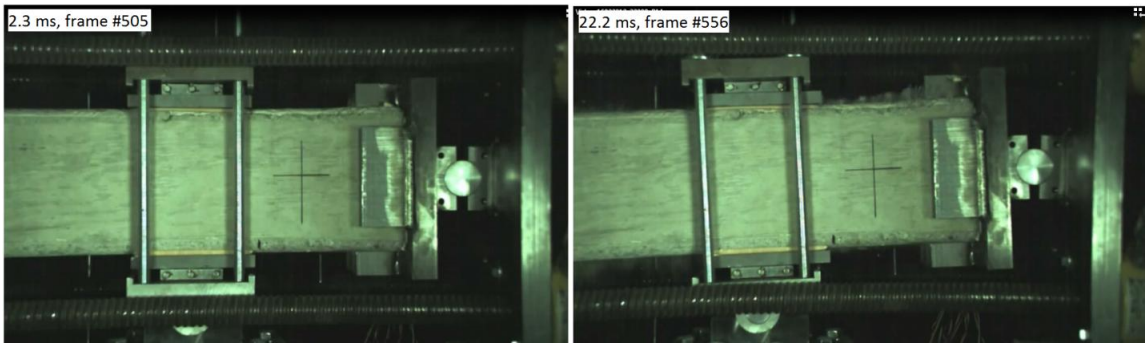

Figure 5-17: Frames from high speed video (2573 fps) of roller support and axial load transfer plates for Imp-3

5.4.2 Effect of Axial Load on Impact Response

The influence of axial load on the response of the impacted specimens was significant. The specimens discussed in this section are Imp-1 (283 kN axial load and 37.5 mm stirrup spacing), Imp-2 (no axial load and 75 mm stirrup spacing) and Imp-3 (100 kN axial load and 100 mm stirrup spacing). All specimens had the same unsupported length of 2000 mm. For the purpose of comparison, the stirrup spacing was considered inconsequential in the response. Also, all specimens discussed in this section were impacted with 70.6 kg at 7 m/s.

It was observed that the axially loaded specimens were laterally stiffer resulting in smaller deflections, quicker peak responses, and much greater damping (Figure 5-18). For both axially loaded specimens, midspan deflection stopped fluctuating after 100 ms while specimen Imp-2, with no axial load, continued to fluctuate for almost 1000 ms.

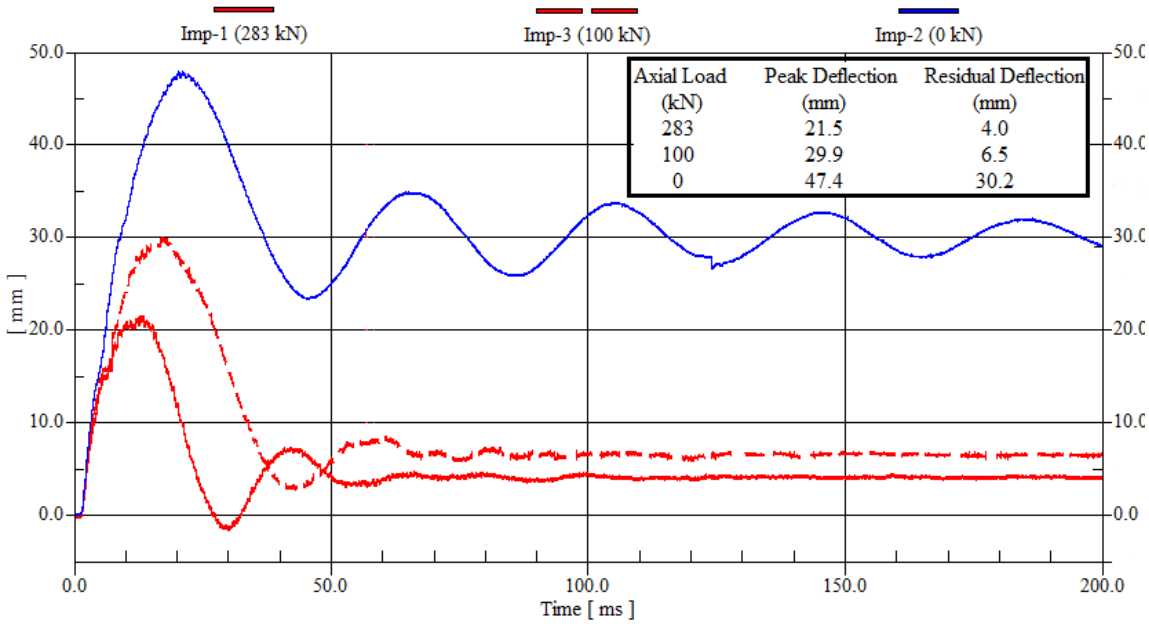

Figure 5-18: Deflection-time history with varying levels of axial load (Imp-1, Imp-2 and Imp-3)

The reaction load measurements for these three specimens presented interesting results (Figure 5-19). The variation of the axial load level for specimens Imp-1 and Imp-3 had minimal influence on the peak total reaction loads and their time of occurrence, both responses are nearly identical. What is very surprising is that the peak reaction load for Imp-2 without axial load is 101 kN, while it reaches 420 kN for Imp-1 and 386 kN for Imp-3. However, while the peak positive reaction loads between axially loaded specimens and those without vary considerably, the peak negative reaction loads are nearly identical.

It is known that the impact of beams/columns causes uplift from supports. The observed results indicate that these uplift forces were independent of axial load levels in these tests. It seems that, for the same impact, the axially loaded specimens transferred the impact load to the supports, while the same impact force did not transfer as large a force to the supports for the specimen with no axial load. For Imp-2 (no axial load), the energy of the impact force was absorbed by crushing and cracking of the concrete and yielding of the reinforcement, thus it did not translate to significant forces reaching the supports. Conversely, the columns of Imp-1 and Imp-3 remained

mainly elastic and displayed minimal damage, thus higher forces were transferred through the specimen and into the support. That, combined with the influence of the axial loading system, explain why reaction loads are over 250% higher for specimens loaded axially.

Additionally, simple calculations based on assumed deflected shape and the sum of dynamic moments about the centroid of inertial forces from Biggs (1964) were found to be inaccurate in predicting reaction loads for the current investigation. It is thought that higher frequency excitation modes are stimulated in the early impact response making these calculations inaccurate. Also, there is a need for further testing with different axial load systems to verify that the observed behaviour is attributable to the presence of axial load and not to the design of the system used that seems to limit the deflection of specimen overhangs which might cause the very high levels of support reactions that were observed.

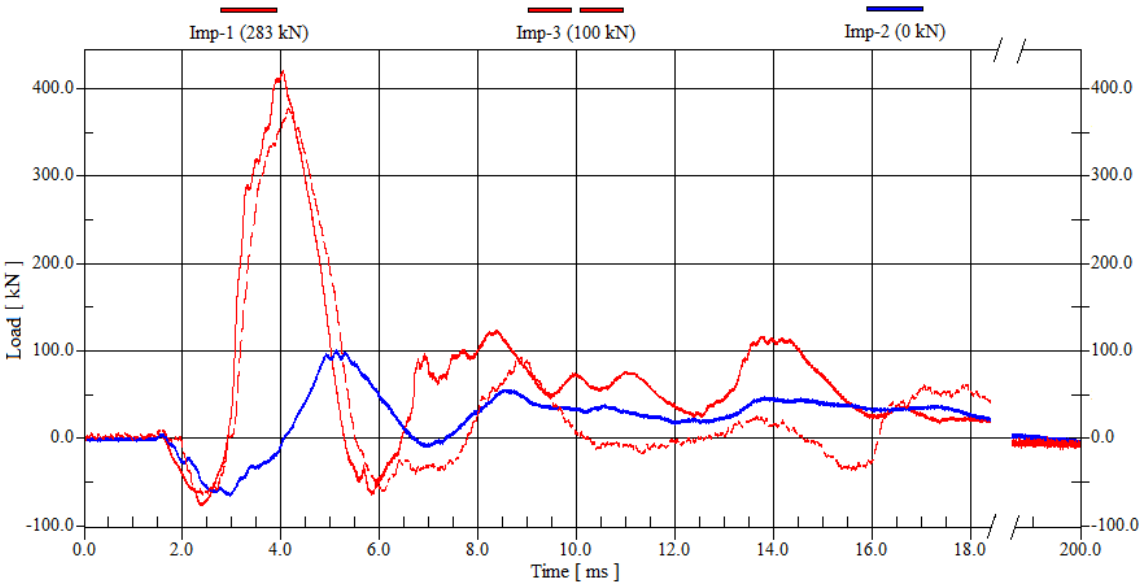

Figure 5-19: Reaction force-time history for Imp-1, Imp-2 and Imp-3

5.5 Effect of Retrofit on Impact Performance

Specimens Imp-4 and Imp-5 had the same geometry with the exception that Imp-5 was retrofitted with two layers of FRP in each of the longitudinal and lateral directions. The first impact on Imp-5 for which only deflection and reaction load data were obtained is compared to the impact test of Imp-4. Peak deflection was 63% lower for the retrofitted specimen (21.4 mm versus 57.3 mm) with minimal residual displacement (2.0 mm versus 37.3 mm for the control), as shown in Figure

5-20. Furthermore, peak deflection occurs more rapidly for the retrofitted specimen (10.4 ms rise time) than for the control (24.1 ms rise time).

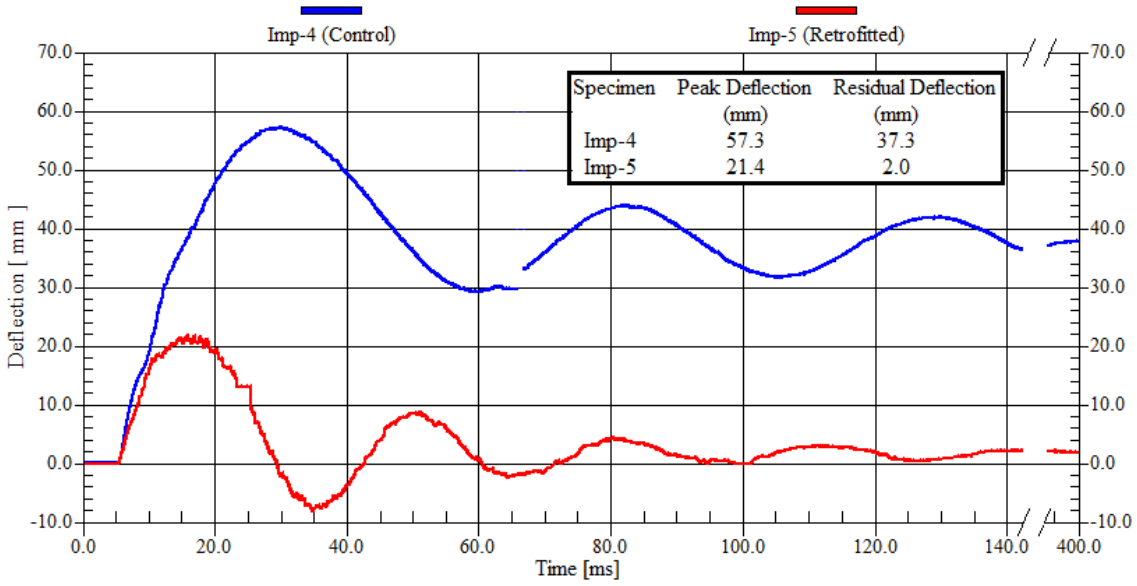

Figure 5-20: Deflection-time history with and without retrofit (Imp-4 and 1st impact of Imp-5)

As the retrofitted specimen was stiffer, its response was quicker. The peak reaction force occurred 0.90 ms earlier and, similar to the specimens loaded axially, the peak total reaction force was significantly higher than that of the control (254 kN versus 133 kN for the control), as shown in Figure 5-21. The difference in peak uplift forces was not as great with peak uplift forces reaching -115.6 and -93.7 for the retrofitted and control specimen, respectively. The higher peak total reaction load for the retrofitted specimen reinforces the notion that with limited damage and more elastic-dominated behaviour, the higher the reaction loads due to less energy being absorbed through damage of the specimen.

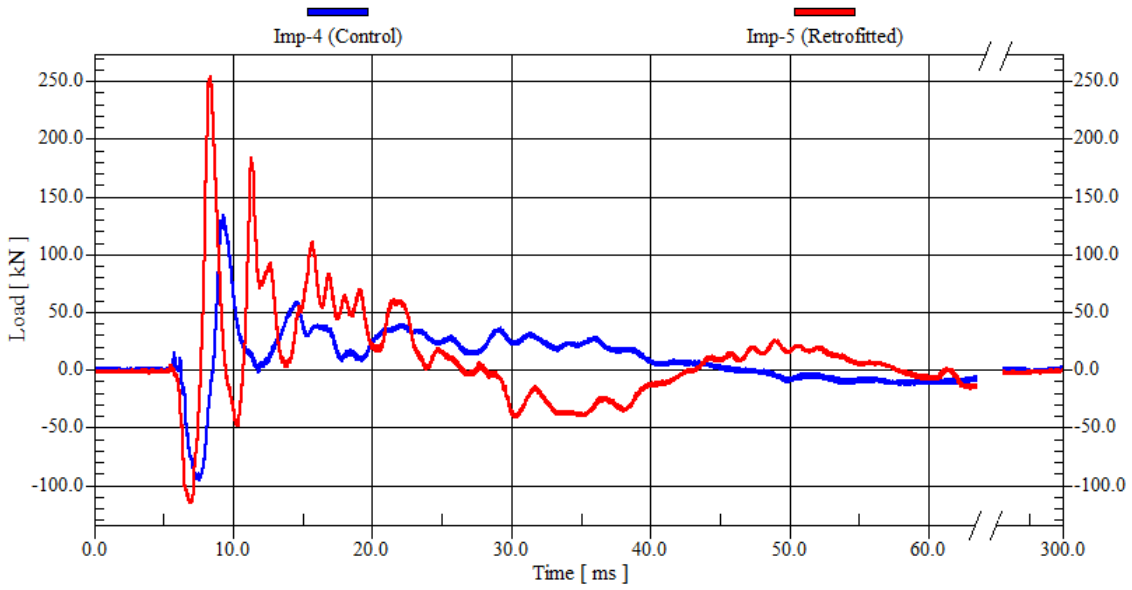

Figure 5-21: Reaction force-time history with and without retrofit (Imp-4 and Imp-5)

5.6 Compressive Rebar Strain Observations

During static loading, compression zone reinforcing bars are expected to remain in compression. These bars can experience tension at midspan, but only for very large load levels when the neutral axis rises above these bars. Additionally, further from midspan, where moments are typically smaller, no tensile strains should be observed. This was confirmed by the quasi-static testing of QS-1 and QS-2.

It was thus interesting to observe significant tensile strains along the compression bars for impact tests on Imp-3 and Imp-4 (Figure 5-22 and Figure 5-23, respectively). These very large tensile strains, resulting in yielding of the bar, occurred well before peak displacement was reached and were initiated very early in the response. These tensile strains in the upper half of the specimen could have been explained by the specimen experiencing negative bending moments near the support, as suggested by Saatci (2007) and Cotsovos et al. (2008). If this were the case, it would be expected that tension zone rebars undergo compressive strains. This was, however, not the case.

The tension experienced by the compression bars could be attributed to a pull-out effect as the compressive rebar is impacted at midspan, pulling in the lengths that extend from the impact zone. This is speculative and additional data is required to form a proper explanation of the observed tensile behaviour. From the current study, only compressive rebar strain data from specimens

Imp-3 and Imp-4 could be commented on as Imp-1 and Imp-2 did not have instrumented reinforcement while the strain data obtained from Imp-5 was erroneous due to a power surge.

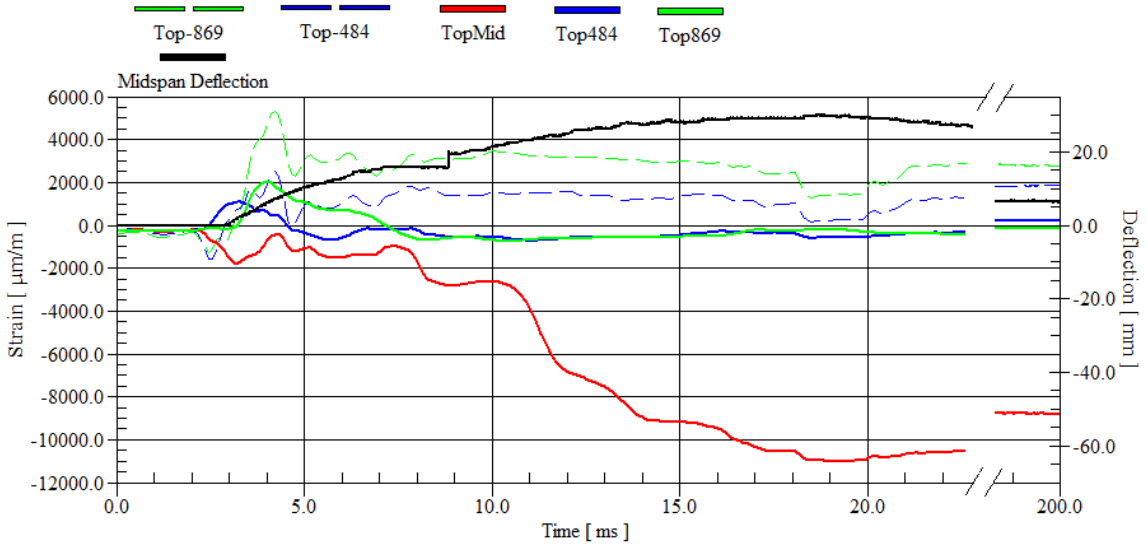

Figure 5-22: Compressive rebar strain-time history for Imp-3

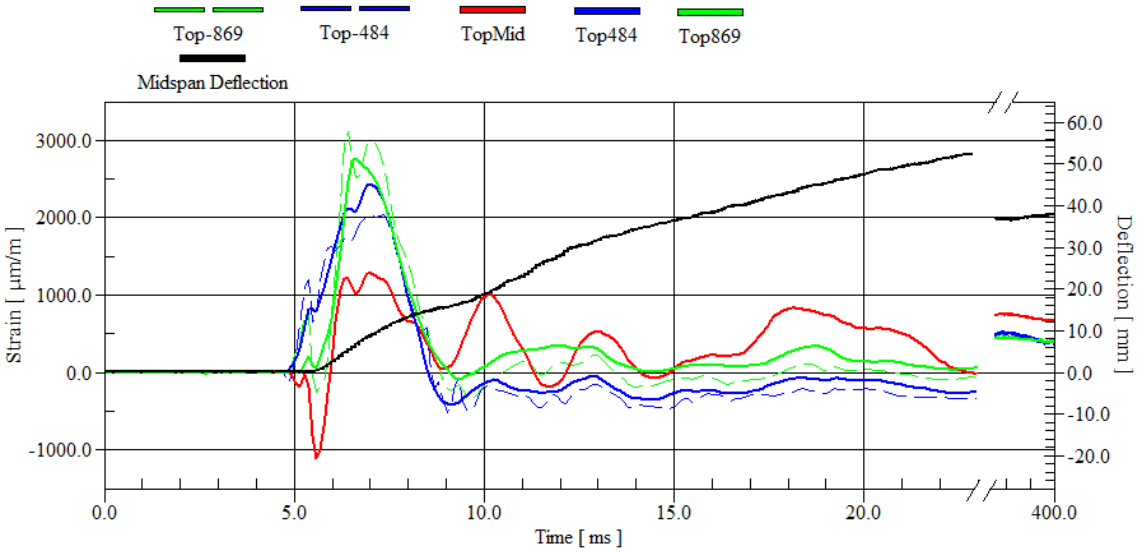

Figure 5-23: Compressive rebar strain-time history for Imp-4

Table 5-1 and Table 5-2 summarize the data from the above strain-time histories. For both specimen Imp-3 and Imp-4, the strain readings from the strain gauges located at midspan (TopMid) present responses different from what was seen for the other strain gauges located on the same rebar. For Imp-3, no tensile strain occurs with the peak (negative) value occurring simultaneously with peak deflection. For Imp-4, a very rapid negative spike occurs before peak

tup load is even reached, followed by a response that follows more closely the other strain gauges on the compression rebar. This inconsistent strain behaviour at midspan it thought to be due to localized buckling of the rebar, situated immediately beneath the impact surface.

Table 5-1: Peak strain for compressive rebar of Imp-3

Distance from Midspan (mm)*	Peak Strain (μm/m)	Time to Peak Strain (μm/m)**	Residual Strain (μm/m)
-869	5287	1.23	2798
-484	2495	1.25	1841
0 (Midspan)	-10990	16.23	-8788
484	1188	0.27	215
869	2020	1.02	-152

Note that time to peak deflection was 15.87 ms

*A negative distance indicates that the strain reading is on the pin ended side of midspan

**Time to peak strain is taken as the difference between time of peak strain and time of peak tup load

Table 5-2: Peak strain for compressive rebar of Imp-4

Distance from Midspan (mm)*	Peak Strain (μm/m)	Time to Peak Strain (μm/m)**	Residual Strain (μm/m)
-869	3087	0.66	446
-484	2024	1.63	430
0 (Midspan)	1278	1.26	707
484	2452	1.21	469
869	2754	0.97	414

Note that time to peak deflection was 22.41 ms

*A negative distance indicates that the strain reading is on the pin ended side of midspan

**Time to peak strain is taken as difference between the time of peak strain and time of peak tup load

5.7 Performance of Retrofit with Repeated Loading

The retrofitted specimen (Imp-5) was impacted twice due to recording inconsistencies during the first drop. To match its impacted counterpart, specimen QS-2 was loaded statically twice to match the peak midspan deflections reached by Imp-5 during its two impact tests. This allowed for observations into the multiple impact and cyclic performance of the retrofit installed on these specimens.

From the static test, it can be seen that there is a slight drop in stiffness during the first loading cycle at around 10 kN (from 3.89 kN/m to 2.45 kN/m) attributable to concrete cracking and a second, slighter decrease in stiffness at approximately 43 kN (from 2.45 kN/m to 1.71 kN/m). For the second loading cycle of QS-2, a reduction in stiffness (from 3.00 kN/m to 1.54 kN/m) occurs when the load reaches 50.5 kN, the peak value attained during the first static loading cycle, as shown in Figure 5-24. This would indicate that the response of the retrofitted beam is entirely dictated by the FRP which remains elastic until sudden failure. This was confirmed during the testing of retrofitted concrete cylinders tested in compression, which behaved generally elastic, with some observable reductions in stiffness, before failing suddenly due to debonding or rupturing of the FRP overlay. More details on this study are provided in Appendix B.

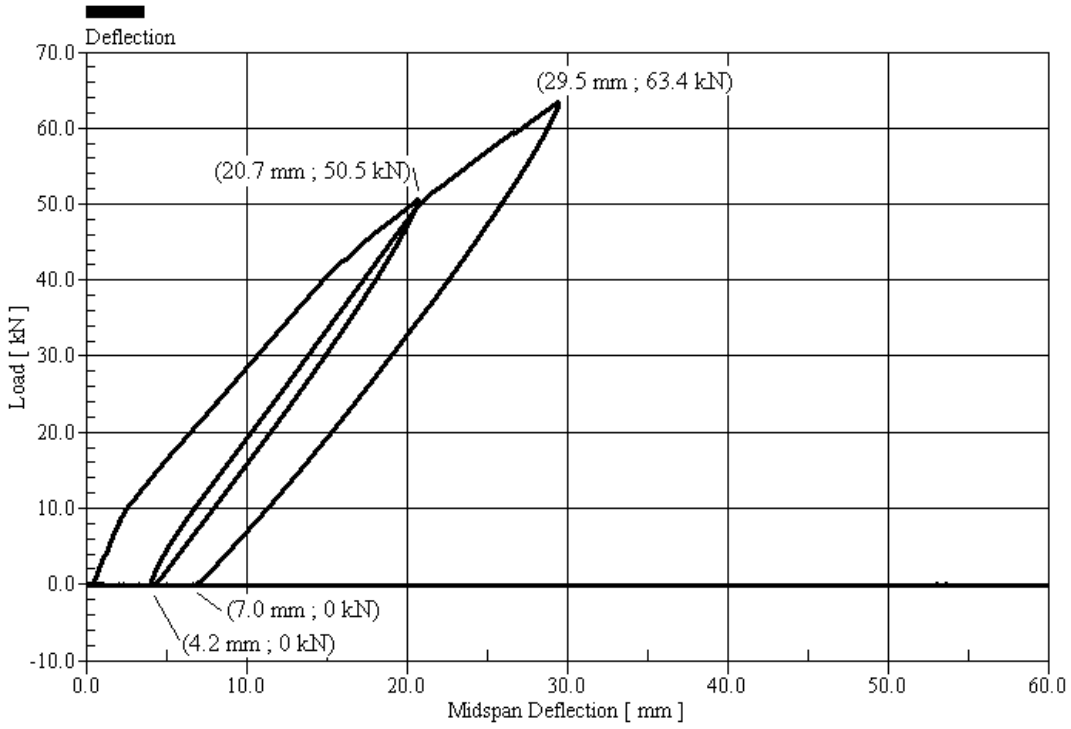

Figure 5-24: Load-deflection for QS-2

Concerning the dynamic performance of the retrofitted specimen under repeated impact, the retrofit behaved elastic as well. A verification of the striker velocity prior to impact (see Appendix A) reveals that the velocity of the first impact was 15% lower than for the second impact. This is most probably due to the generalized failure of all computerized equipment during the first impact. As such, the tup load versus time for the first impact was not recorded, making the comparison of the imparted force on Imp-5 for the first impact not possible. However, it can be assumed that the impact energy was not as great for the first drop, owing to the reduced striker velocity.

The first impact resulted in a peak deflection of 21.4 mm with a residual value of 2.0 mm. The second impact caused a greater peak deflection (28.9 mm), but the residual deflection remained essentially unchanged (Figure 5-25).

Similarly, the total reaction loads from each impact are similar in their response but with the second impact imposing larger values that were experienced more slowly, partly owing to reduced stiffness due to damage that was sustained from the first impact and partly attributable to the fact that the second impact was most likely larger than the first.

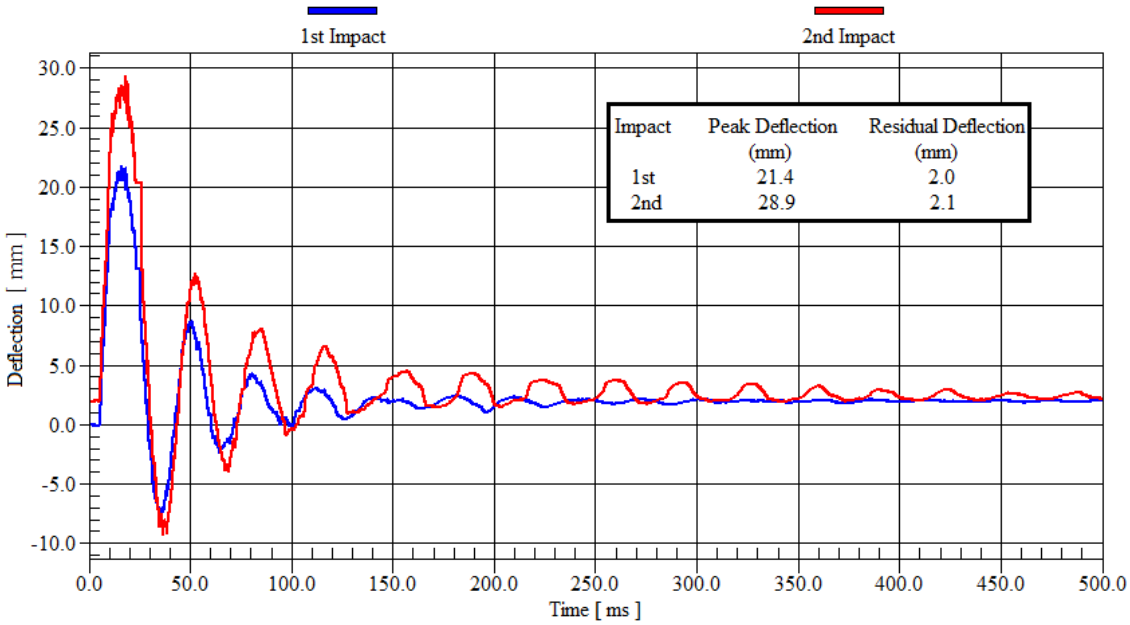

Figure 5-25: Deflection-time history for Imp-5 (impacted twice)

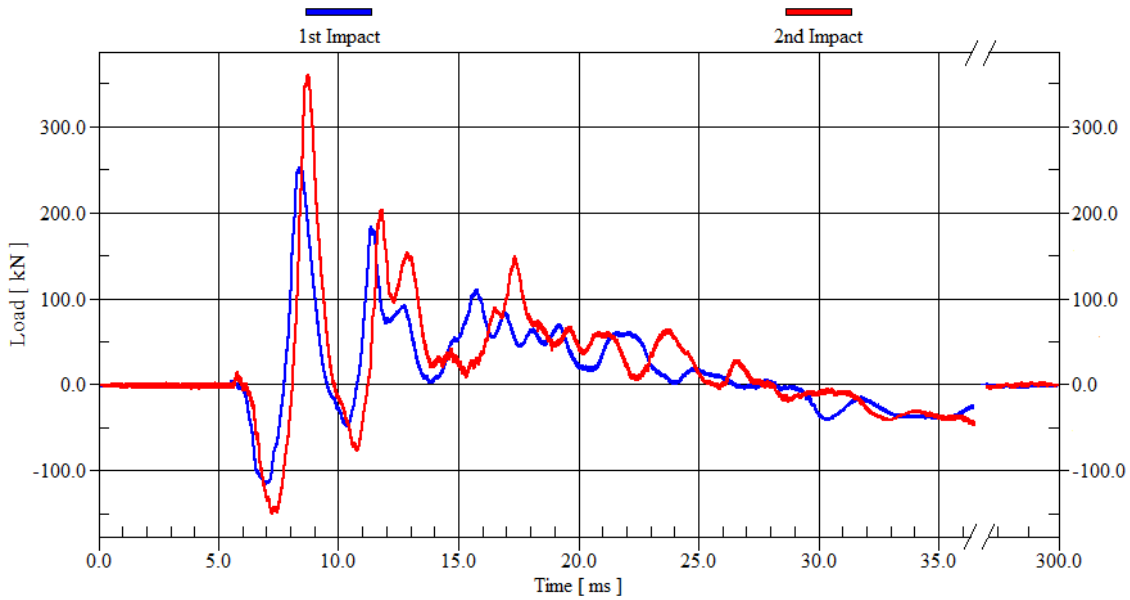

Figure 5-26: Reaction load-time for Imp-5 (impacted twice)

Furthermore, a simple verification regarding the consistency of the retrofitted specimen's stiffness can be made for both impacts. The following equation stated by Humar (2005) to obtain the fundamental period of vibration of a simply supported uniform beam was used:

$$T = 2\pi\sqrt{\frac{m^*}{k^*}} \qquad [5.1]$$

where T is the fundamental period of vibration, m* is the equivalent mass of the system and k* is the equivalent stiffness of the system. Both the equivalent mass and stiffness were obtained for the SDOF modeling of the second impact on Imp-5. The equivalent stiffness was 2.50 x 10 kN/mm while the equivalent mass was 57.7 kg. The equivalent stiffness was taken as the direct slope of the second loading cycle of the load-deflection curve for specimen QS-2. This was possible as the impact load is considered a point load applied at the location of the degree of freedom. Meanwhile, the equivalent mass was obtained by applying Equation 2.9. Using these values in Equation 5.1 provides a fundamental period of vibration of 30.1 ms. If the specimen remains elastic following impact as assumed, then its period of vibration (time between successive peaks on the deflection-time history graph) following impact should be its fundamental period of vibration, obtained above. The period of vibration following impact for Imp-5 is given in Table 5-3.

Table 5-3: Period of vibration for both impacts performed on Imp-5

	1st Mode Vibration Following Impact	1st Impact		2nd Impact	
		Positive Peaks	Negative Peaks	Positive Peaks	Negative Peaks
Period of Vibration, T (ms)	1st	34.5	30.4	35.9	31.8
	2nd	29.7	33.9	31.8	30.4
	3rd	30.4	27.6	32.5	30.4
	Average	**31.1**		**32.1**	

The results indicate that, while the periods of vibration are slightly longer than the fundamental period (30.1 ms), they are still reasonably close to the fundamental value and to each other. This would indicate that the specimen remained nearly elastic under repeated impact and also reinforces the equivalent stiffness used for the SDOF modeling of the second impact on Imp-5 (refer to Section 5.2).

5.8 Static and Dynamic Crack Pattern Comparison

Two identical RC beams with the same span and boundary conditions were tested under lateral load to the same midspan deflection. The peak midspan deflection sustained by Imp-4 under an impact of 70.6 kg at 7 m/s (57.3 mm) was the deflection at which the static load applied on QS-1 was terminated. Due to the deflection readings measured by the laser displacement sensors being slightly different than the displacement sensor built into the static actuator, the peak midspan deflection reached by QS-1 was 56.9 mm (0.7% lower than the target value). The peak impact force recorded was 355 kN while the peak static force was only 22.9 kN. Residual deflection for the static test was 43.3 mm, higher than the residual deflection recorded after the impact of 37.3 mm.

The cracking that surfaced for the static specimen (QS-1) is a typical flexural failure pattern with cracks spaced at approximately 100 mm extending vertically from the specimen underside to within 30 mm of the top face. The cracking sustained by the impacted specimen (Imp-4) is quite different, with the beginning of a shear plug, the punching out of the opposite face of the impacted surface, formed in the lower half of the specimen's height, beneath the location of impact. Figure 5-27 presents a map of the residual cracking at midspan following the impact test on Imp-4 and

the quasi-static test on QS-1. Note that only residual crack widths are reported but not maximum crack widths.

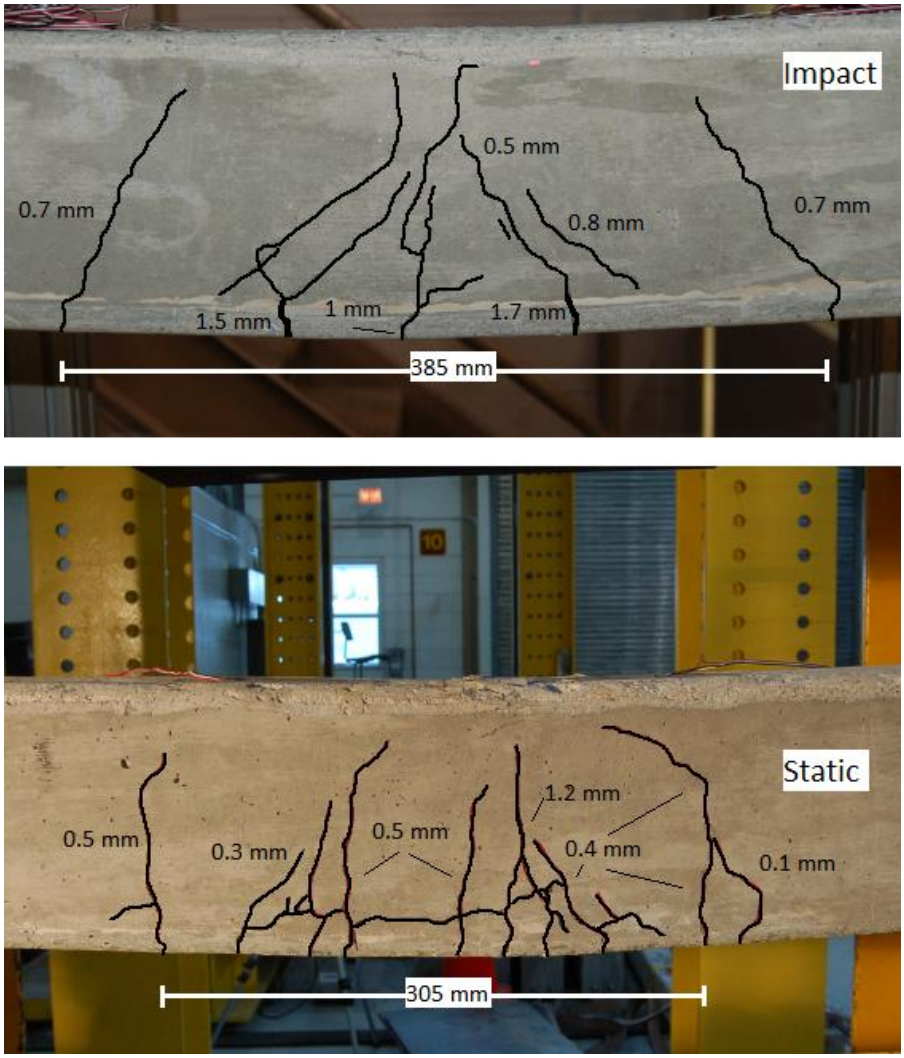

Figure 5-27: Comparison of cracking pattern for impact (top) and statically loaded (bottom) specimens

While researchers, such as Saatci (2007), Cotsovos (2008) and Ozbolt and Sharma (2011), have observed the formation of shear plugs in RC beams subjected to impact, their crack development during impact and an explanation into the influence that they might have on the specimen response has not been fully addressed.

The high speed video recording of the impact test on Imp-4 permits an in-depth look at how the cracks developed under impact. Unlike crack development for the static case where flexural cracks appear at around 12 mm deflection, the diagonal shear plug cracks appear as early as 1 ms

after tup-specimen contact at deflections below 1.5 mm. These shear plug cracks are present from almost the beginning of the response and widen as deflection increases, as shown in Figure 5-28.

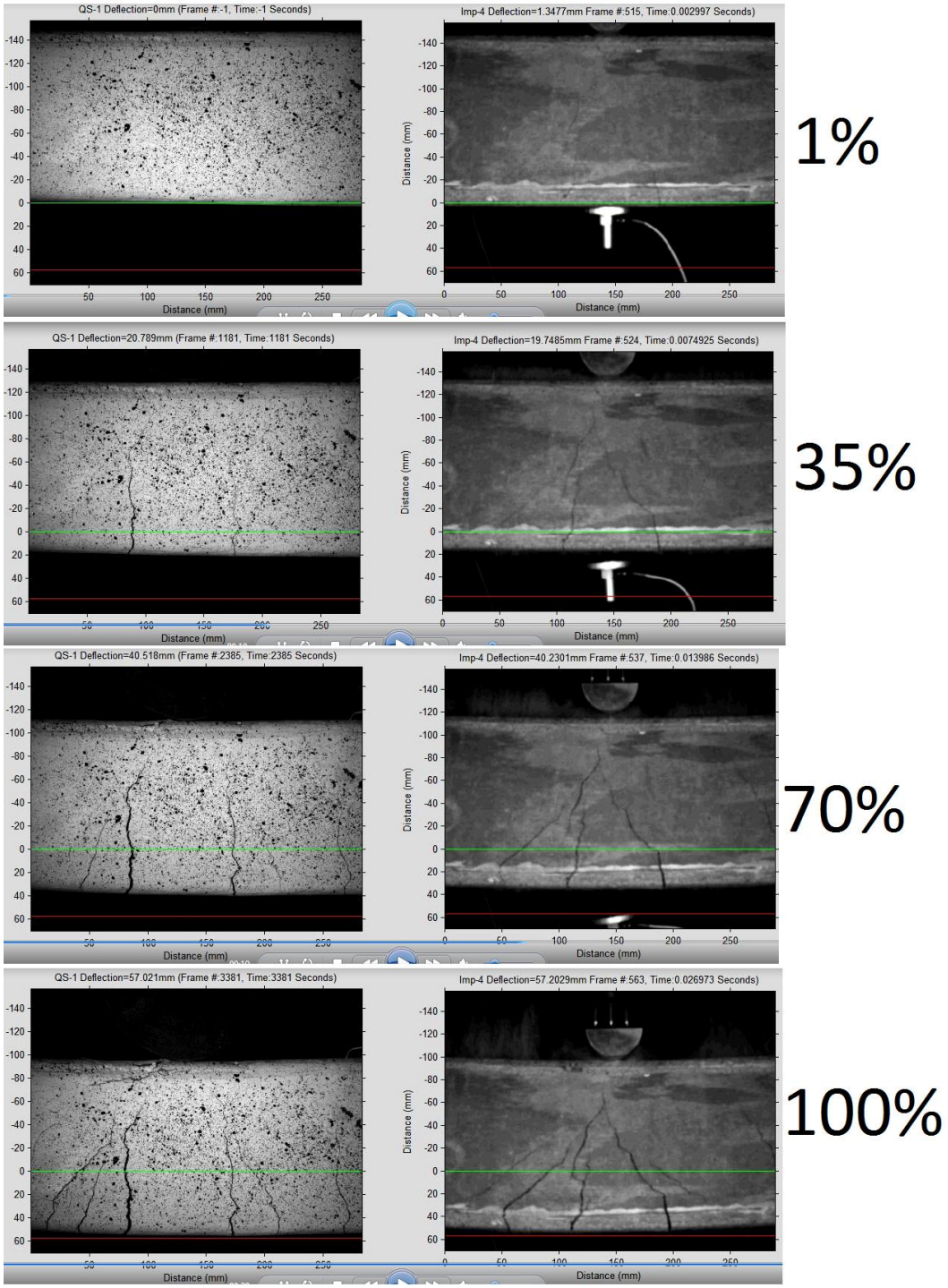

Figure 5-28: Comparative frames showing static (left) and dynamic (right) crack formation with the percentage indicating deflection relative to peak deflection (note that shear plug cracks are present in Imp-4 at 1% deflection)

The presence of the shear plug cracks from the onset of response for RC members subjected to impact is contrary to results obtained by Ozbolt and Sharma (2011). Although the impacts that they modeled were of lower velocity than the ones discussed herein (1m/s versus 7 m/s), their results indicate that the shear plug cracks appear when the member has reached 50% of its peak deflection. Before 50% of peak displacement, flexural cracks (similar to the ones observed for QS-1) were apparent in the bottom portion of the specimen (Figure 5-29).

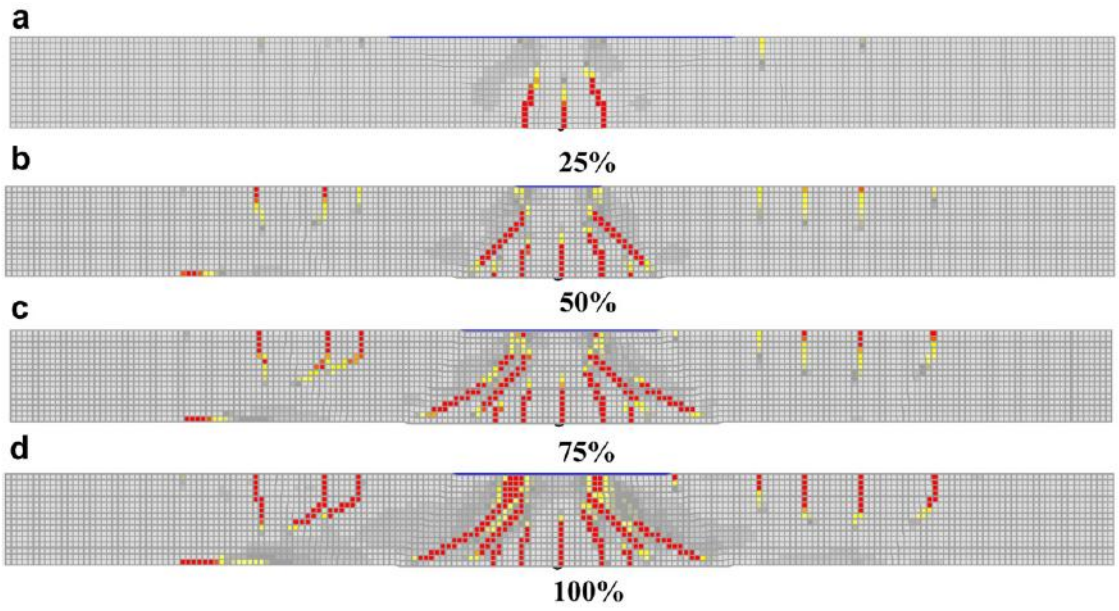

Figure 5-29: Analytical crack patterns corresponding to various percentages of peak displacement at the midspan of specimen SS2a, tested by Sharma (Ozbolt and Sharma, 2011)

Following observations made during the crack development of Imp-4, impact of RC members causes shear forces that fully develop prior to initiation of specimen deflection. The two shear planes where the shear plug cracking occurs create a semi-plastic response of the member portions located between the shear plug and supports. The shear plug acts as a hinge in effect. The rotation of the two specimens about this hinge explains the uplift forces that occur before reaction loads transfer the impact load to the ground. Furthermore, numerical simulations where the impact is represented as a dynamic increase in deflection may not be suitable for estimating crack development.

Additionally, flexural cracks that extend from the top face are visible (marked in blue) for Imp-4 (Figure 5-30). These cracks are most likely due to negative moments developing near the supports early in the response due to the impulsive loading as observed by several researches. No such cracking surfaced in QS-1.

The difference in observed cracking pattern at midspan, the presence of negative flexural cracks along the top of specimen Imp-4, and the differences in residual deflections would indicate that, for similar peak deflections, static and impact forces are resisted differently by the specimen. These observations also reinforce the notion that SDOF modeling may be inadequate to properly predict the response of RC members subjected to impact.

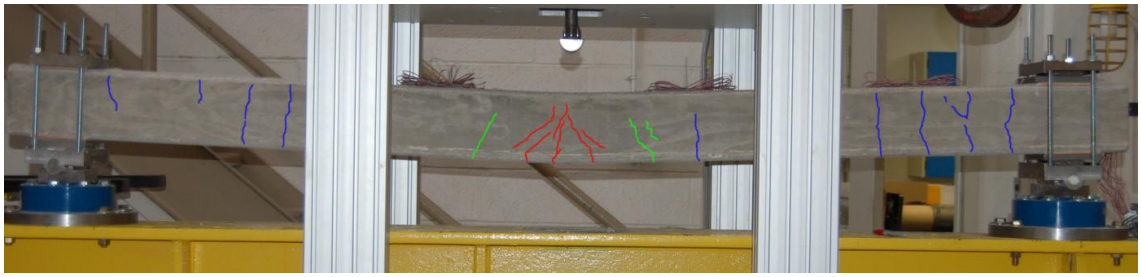

Figure 5-30: Flexural cracks in support region of Imp-4 (marked in blue)

5.9 Strain Rate

Strain rate is the measure of strain variation with time. For strain gauges located near the contact surface of the impacted specimens, this variation was calculated. Most of the strain data contained high frequency noise making the instantaneous variation of strain rate difficult to interpret. Thus, the average strain rate is presented here. The average strain rate was calculated as the variation of strain with time from its initial value up to the first peak reached during the initial response while the peak strain rate was taken as the maximum slope that occurred on the strain-time history plots. These values are provided in Table 5-4. No strain rate data is presented for Imp-5 as the recorded strain data was deemed corrupted.

Table 5-4: Strain rates for impacted specimens

Specimen	Strain Gauge	Average Strain Rate (s^{-1})	Peak Strain Rate (s^{-1})
Imp-1	Sur102 (Concrete)	1.36	1.36
Imp-2	Sur102 (Concrete)	0.09	0.54
Imp-3	Sur-102 (Concrete)	0.13	1.02
	Sur102 (Concrete)	0.31	1.02
	TopMid (Steel)	0.63	3.74
Imp-4	Sur-102 (Concrete)	0.15	1.16
	Sur102 (Concrete)	0.32	1.16
	TopMid (Steel)	2.16	
	BotMid (Steel)	4.40	

As expected the strain rate data for all specimens is of the order of 10^0, consistent with values reported in the literature. Strain rates measured within steel reinforcement were consistently observed to be higher than that for concrete. Furthermore, the influence that axial load has on measured strain rates cannot be commented on as no pattern is visible for the acquired data.

Chapter 6: Conclusions and Future Research

6.1 Summary

An extensive literature review that detailed strain rate sensitivity, impact testing of reinforced concrete beams and columns, the protection of RC infrastructure against impacts and SDOF modeling of RC members subjected to impact was conducted. An experimental investigation was then carried out to implement an impact testing protocol at the NRC (National Research Council) and to study the performance of half-scale reinforced concrete columns subjected to impact. Impact loads were applied by a drop-weight tower with a drop mass of 70.6 kg and impact velocity of 7 m/s. Three columns were impacted as part of a preliminary study to gain experience in impact testing of reinforced concrete members. Of these, two were tested with axial load applied by a custom built axial loading system. The second portion of the testing program compared the performance of control and retrofitted RC columns under impact and quasi-static loading conditions. All specimens were tested with the use of custom-built instrumented supports that provided a pin-roller configuration. Deflections and forces were recorded at a frequency of 1 000 000 Hz while reinforcing steel and concrete surface strains were recorded at a frequency of 9600 Hz. A parallel study was also conducted, which included the testing of concrete cylinders to better understand the material behaviour of concrete confined by externally applied FRP in the hoop direction. The FRP retrofit applied to these cylinders was consistent with that applied to the retrofitted specimens.

6.2 Conclusions

The following conclusions are drawn from the experimental and analytical research presented in this thesis:

6.2.1 Experimental

- The use of custom-built supports permitted the study of member behaviour under the theoretically idealized case of pin-roller boundary conditions and indicated that, under impact, longitudinal steel may experience slightly higher tensile forces on the pin-ended side owing to member elongation towards the roller.

- Impact loads on the RC specimens caused initial negative reactions that should be accounted for in design. Following these negative reaction loads, peak positive reaction loads were

experienced. It appears that these positive loads were heavily dependent on the stiffness of the impacted specimens; the stiffer the specimen, the larger the measured positive peak reaction loads. Also, the higher the damage sustained by the impacted specimen, the lower the peak positive reaction loads.

- The use of unidirectional FRP for the retrofit of the specimens was very effective at limiting deflections and promoting elastic response under impact. Furthermore, it seems possible to design such retrofits to remain elastic, even under repeated impact loading.

6.2.2 Analytical

- SDOF modeling was inadequate to capture the complexities of impact loading on RC specimens that responded in the inelastic range. However, SDOF modeling was adequate for predicting the impact response of retrofitted members that remained elastic even when exposed to extreme shocks.

- Modeling techniques were the impact of RC beams is simulated by incrementing midspan displacements at the rate observed experimentally is inadequate to properly predict crack formation under impact.

6.3 Recommendations for Future Research

The following recommendations are made for future research:

- An investigation into the effect that axial load levels have on the damage of RC columns under impact is suggested. It is hypothesized that below a certain axial load threshold, the axial load stiffens the structure, making it more resistant to impact. However, above this threshold, the addition of axial load may reduce the capacity of the member to withstand impact as a result of the pre-compressed concrete being close to material failure. The existence of this "axial load inflection point" could be of significance in the design of columns to withstand impact loads.

- The anchoring of reinforcing bars nearest the face of RC members vulnerable to impact should be analyzed to determine whether these bars are at the risk of pull-out failure. Furthermore, drop-weight impact tests could be performed on steel rebar lengths, solidly

anchored at the ends, to observe how the buckling of the middle portion of the steel affects strain distribution along the bar.

- The measurement of reaction forces during impulsive testing should always be performed with load cells capable of measuring tension to permit the evaluation of uplift forces on the reactions.

- A further investigation into the effect that axial load levels have on the reaction forces of RC members subjected to impact should be performed. It would seem that, for the same level of impact, the intensity of reaction forces varies when axial load is applied to the column. While the columns with and without axial load seem to experience initial negative reactions of similar magnitude, the subsequent positive reactions could be four times as high for the columns with axial load.

- Different retrofit configurations utilizing unidirectional FRP should be studied under impact to optimize the design of the retrofit.

- If the Ceast 9350 drop-weight impact tower is to be used for further testing in its current configuration, a thorough verification of the tup load-time history output should be conducted. It is suggested that numerous impacts of moderate magnitude (less than 7 m/s) be applied to a retrofitted specimen of known lateral stiffness in order to use simple SDOF analysis techniques to verify the recorded tup load.

- The use of accelerometers during impact testing is of utmost importance. Their use allows for precise calculations of inertia forces that provide valuable information regarding the response of the impacted specimen.

Bibliography

Alghamdi A. (2001). "Collapsible impact energy absorbers: An overview". *Thin-Walled Structures.*39(2).189-213.

Almansour H., Margeson R. and Smith R. (2012). "Protection of critical concrete infrastructure against extreme shocks using advanced composites - Innovative testing procedures for high-speed load application - Report #B5337-3". National Research Council. Ottawa, Canada.

Banthia N. (1987). "Impact resistance of concrete". Thesis (PhD). University of British Columbia.

Biggs J. (1964). "Introduction to structural dynamics". McGraw-Hill, United States

Bisby L and Ranger M. (2010). "Axial-flexural interaction in circular FRP confined RC columns". *Construction and building materials 24*: 1672-1681

Dixon D. (1990). "Spall failure in a carbon fibre reinforced thermoplastic composite". *J Mater SciLett.*9(5).606-8.

Cotsovos DM, Pavlović MN. (2008). "Numerical investigation of concrete subjected to compressive impact loading. part 1: A fundamental explanation for the apparent strength gain at high loading rates". *Comput Struct* 1;86(1-2):145-63.

Cotsovos DM, Pavlović MN. (2008). "Numerical investigation of concrete subjected to compressive impactloading. part 2: Parametric investigation of factors affecting behaviour at high loading rates". *Comput Struct* 1;86(1-2):164-80.

Cotsovos DM, Zeris CA, Stathopoulos,ND. (2008) "Behavior of RC beams subjected to high rates of concentrated loading". *Journal of structural engineering*: 134(12):1839-1851.

Cotsovos DM. (2010). "A simplified approach for assessing the load-carrying capacity of reinforced concrete beams under concentrated load applied at high rates". *Int J Impact Eng* 8;37(8):907-17.

Erki M, Meier U. (1999). "Impact loading of concrete beams externally strengthened with CFRP laminates". *J of composites for construction*.3(3).117-124.

Fujikake K, Li B, Soeun S. (2009). "Impact response of reinforced concrete beam and its analytical evaluation". *Journal of structural engineering*:135(8):938-950.

Grote DL, Park SW, Zhou M. (2001). "Dynamic behavior of concrete at high strain rates and pressures: I.experimental characterization". *Int J Impact Eng* 10;25(9):869-86.

Humar J. (2005). "Dynamics of structures". Taylor & Francis Group plc, London, UK

ISIS Canada. (2008). "*FRP rehabilitation of reinforced concrete structures Design manual No.4 Version 2"*. ISIS Canada Research Network. Winnipeg, Manitoba, Canada

Jacques E. (2011). "Blast Retrofit of Reinforced Concrete Walls and Slabs". Thesis (M. A. Sc). University of Ottawa.

Jacques E, Lloyd A, Saatcioglu M. (2012). "Predicting reinforced concrete response to blast loads". Canadian Journal of Civil Engineering. 10.1139/L2012-014.

Jerome, DM and Ross, CA. (1997). "Simulation of the dynamic response of concrete beams externally reinforced with carbon-fibre reinforced plastic". *ComputStruct*. 9;64(5-6). 1129-53.

Khalighi Y. (2009). "A study of bond between fibre reinforced polymer and concrete under quasi-static and impact loading". Thesis (PhD). University of British Columbia.

Krauthammer T, Shahriar S, Shanaa H. (1990). "Response of reinforced concrete elements to severe impulsive loads". *J of structural engineering*:116(4):1061-1079.

Lloyd A. (2012). "Performance of Reinforce Concrete Columns Under Shock Tube Induced Shock Wave Loading". Thesis (M. A. Sc). University of Ottawa.

Louw J, Maritz G, Loedolff M. (1992). "RC cantilever columns under lateral impact load: an experimental investigation". *Structures under shock and impact II*:308-319

Milke, J andVizzini, A. (1993). "The effects of simulated fire exposure on glass-reinforced thermoplastic materials". *J of fire protection engineering*.4(3).113-124.

Miyamoto A, King M, Fujii M. (1989). "Non-linear dynamic analysis and design concepts for RC beams under impulsive loads". Bulletin of the New Zealand national society for earthquake engineering:22(2):98-111.

Ngo T, Mendis P, Gupta A, Ramsay J. (2007). "Blast loading and blast effects on structures – an overview". Electronic journal of structural engineering 7: 76-91

Ozbolt J and Sharma A. (2011). "Numerical simulation of reinforced concrete beams with different shear reinforcements under dynamic impact loads". International Journal of Impact Engineering. V 38. 940-950

Paz M. (1991). "Structural Dynamics: theory and computation". Van Nostrand Reinhold, New York, United States

Rossi P. (1997). "Strain rate effects in concrete structures: the LCPC experience". Materiaux et constructions. V 30. N Suppl. 196. 54-62

Saatci S. 2007. "Behaviour and modelling of reinforced concrete structures subjected to impact loads". Thesis, (PhD). University of Toronto.

Sharma H, Hurlebaus S and Gardoni P. (2008). "Development of a bridge bumper to protect bridge girders from overheight vehicle impacts". *Computer aided civil and infrastructure engineering*.23(6). 415-426.

Suaris W, Shah S. (1983). "Properties of concrete subjected to impact". *J of structural engineering*: 109(7):1727-1741.

Tang T. (2002). "Behavior of composite beams retrofitted with composite laminates under impact loading". Thesis, (PhD).University of Arizona.

Tang, T and Saadatmanesh, H. (2003). "Behavior of concrete beams strengthened with fibre-reinforced polymer laminates under impact loading". *J of composites for construction*.7(3).209-218.

Uddin, N, Farhat, N, Vaidya, U and Serrano-Perez, J. (2005). "Vulnerability reduction for bridge piers". *University transportation center for Alabama (UTCA) report 03229* 2005.

Uddin, N, Purdue, J and Vaidya, U. (2008). "Feasibility of thermoplastic composite jackets for bridge impact protection". Journal of aerospace engineering. 21(4).259-265.

Yang M andQiao P. (2010). "Analysis of cushion systems for impact protection design of bridges against overheight vehicle collision". Int J Impact Eng. 12;37(12). 1220-8.

Zhang XX, Ruiz G, Yu RC, Tarifa M. (2009). "Fracture behaviour of high-strength concrete at a wide range of loading rates". *Int J Impact Eng* 200910/11;36(10-11):1204-9.

Zheng S., Haussler-Combe U., and Eibl, J. (1999). "New approach to strain rate sensitivity of concrete in compression", *J. Engrg. Mech.* 125, 1403, DOI:10.1061/(ASCE)0733-9399(1999)125:12(1403)

Appendix A: Additional Data for All Test Specimens

A.1. Imp-1

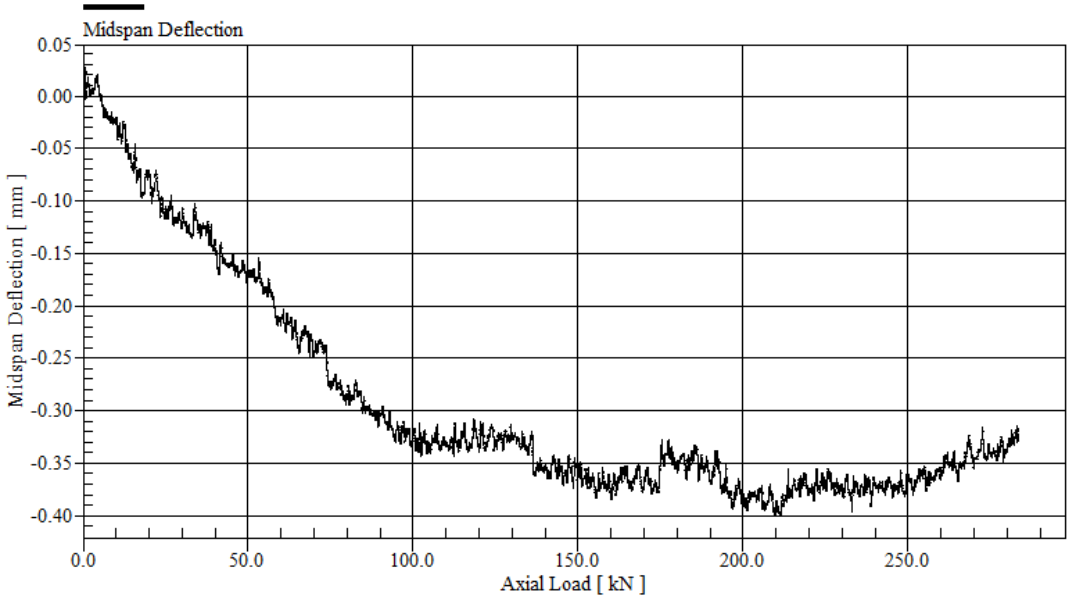

Figure A-1: Midspan deflection during quasi-static axial load application

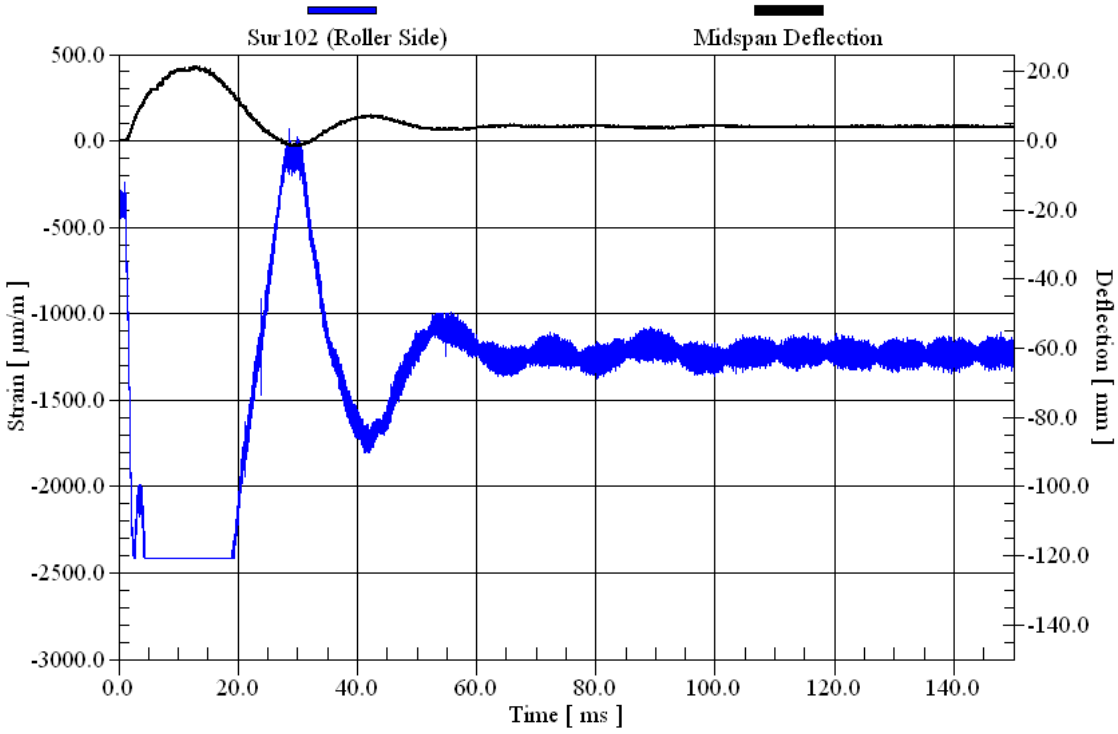

Figure A-2: Concrete surface strain-time history for Imp-1

Table A-1: Strain data for Imp-1

Strain Gauge	Peak Strain (μm/m)	Time to Peak Strain (ms)	Average Strain Rate (s^{-1})	Peak Strain Rate (s^{-1})	Residual Strain (μm/m)
Sur102	Unknown	Unknown	Unknown	1.36	-1223

A.2. Imp-2

Table A-2: Strain data for Imp-2

Strain Gauge	Peak Strain (μm/m)	Time to Peak Strain (ms)	Average Strain Rate (s^{-1})	Peak Strain Rate (s^{-1})	Residual Strain (μm/m)
Sur102	-1609	16.67	0.09	0.54	-116
Sur483	-1061	3.49	0.28	0.28	-363

A.3. Imp-3

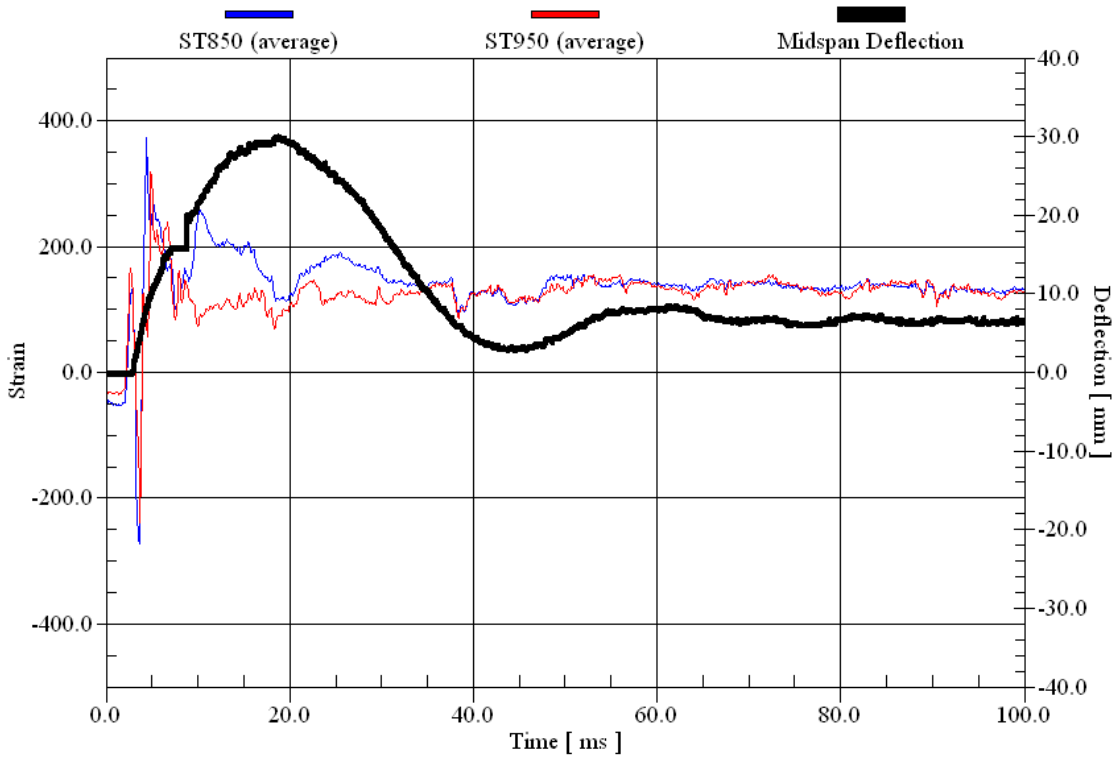

Figure A-3: Average stirrup strain-time history for Imp-3

For the above strain-time history plot and for others similar plots in the Appendix, when "(average)" is indicated beside a strain gauge identification, it means that, for every data point, the reported data is the averaged value for strain gauges that are located symmetrically about the specimen. For example, "ST850 (average)" refers to the average of strain gauge ST850_1 and ST850_2. Similarly, "Bot484 (average)" refers to the average of strain gauge Bot-484 and Bot484.

Table A-3: Strain data for Imp-3

Strain Gauge	Peak Strain (μm/m)	Time to Peak Strain (ms)	Average Strain Rate (s^{-1})	Peak Strain Rate (s^{-1})	Residual Strain (μm/m)
Top-869	5168	1.28	2.65	8.37	2811
Top-484	2495	1.28	1.28	4.40	1861
TopMid	-10930	16.40	0.64	5.29	-8776
Top484	1129	0.26	1.21	2.05	242
Top869	2079	1.08	1.19	3.35	-150
BotMid	Unknown	Unknown	Unknown	7.56	Unknown
Bot484	3092	8.31	0.36	1.67	322
Bot869	1123	7.37	0.16	1.32	-143
Sur-102	-2112	14.20	0.13	0.54	-501
Sur102	-2803	8.83	0.28	0.54	-815

A.4. Imp-4

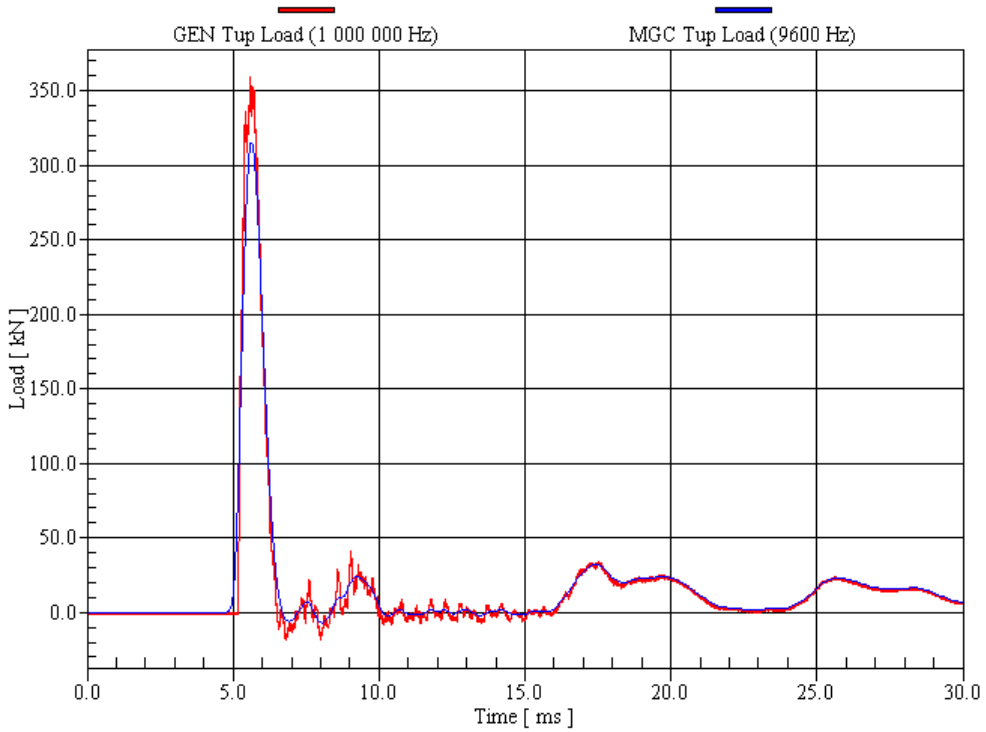

Figure A-4: Tup load comparison for Imp-4

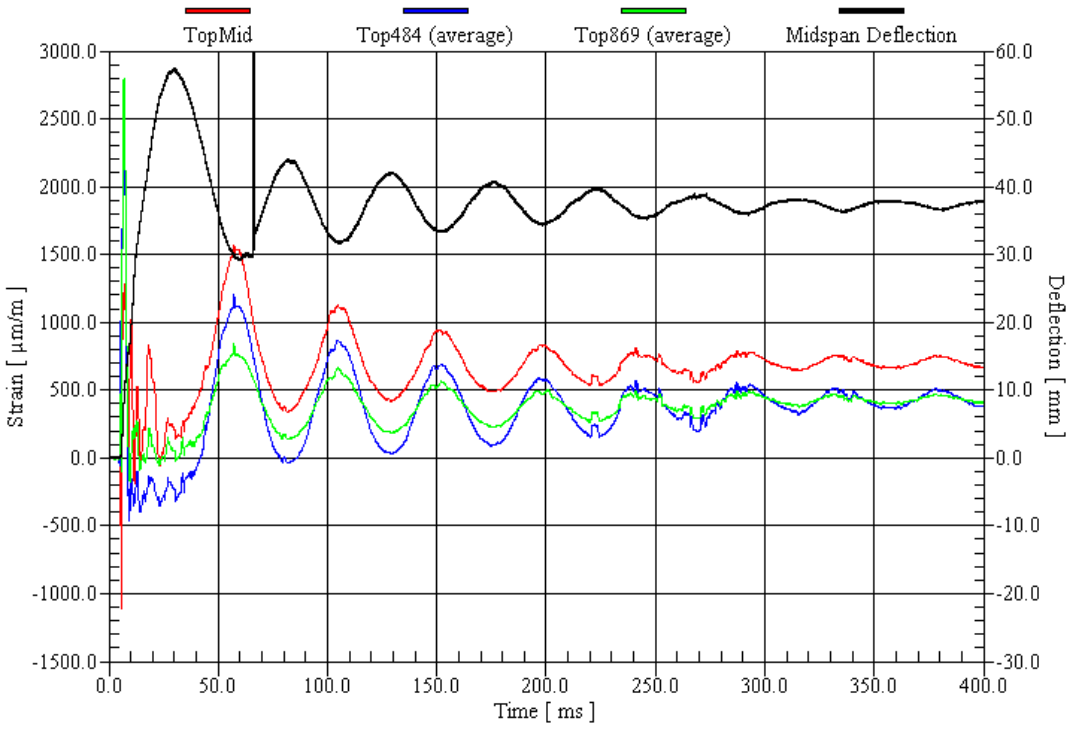

Figure A-5: Compression rebar strain-time history for Imp-4

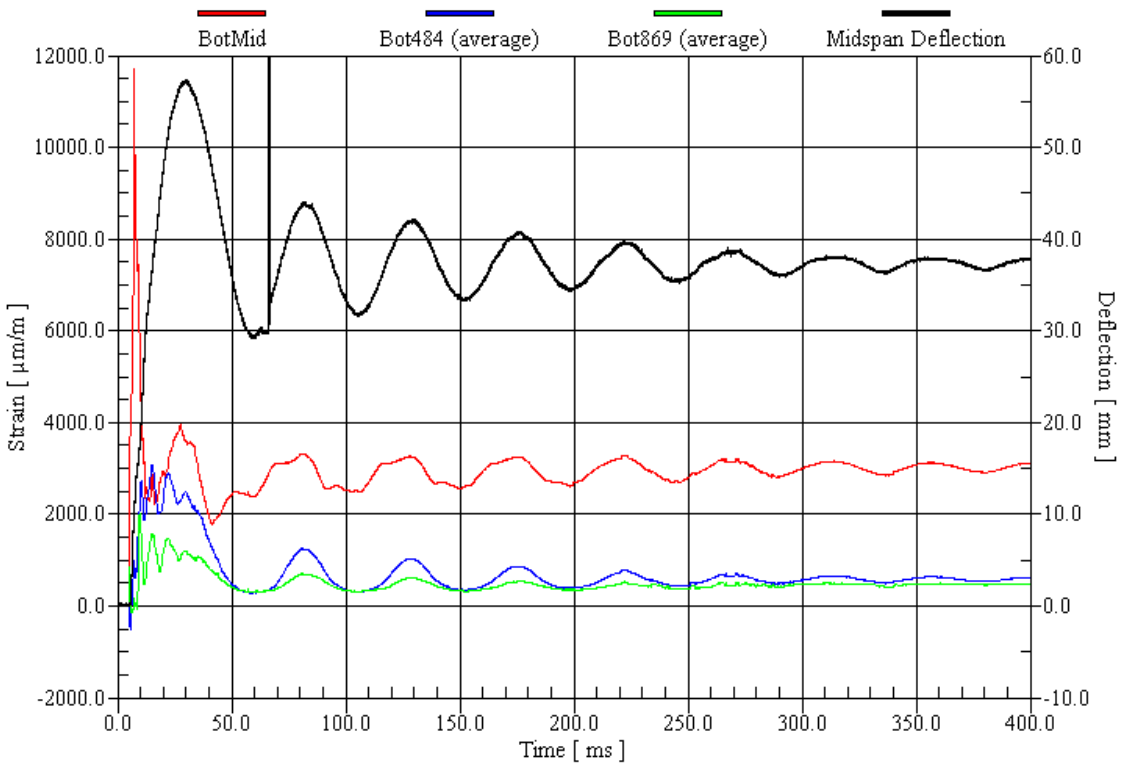

Figure A-6: Tension rebar strain-time history for Imp-4

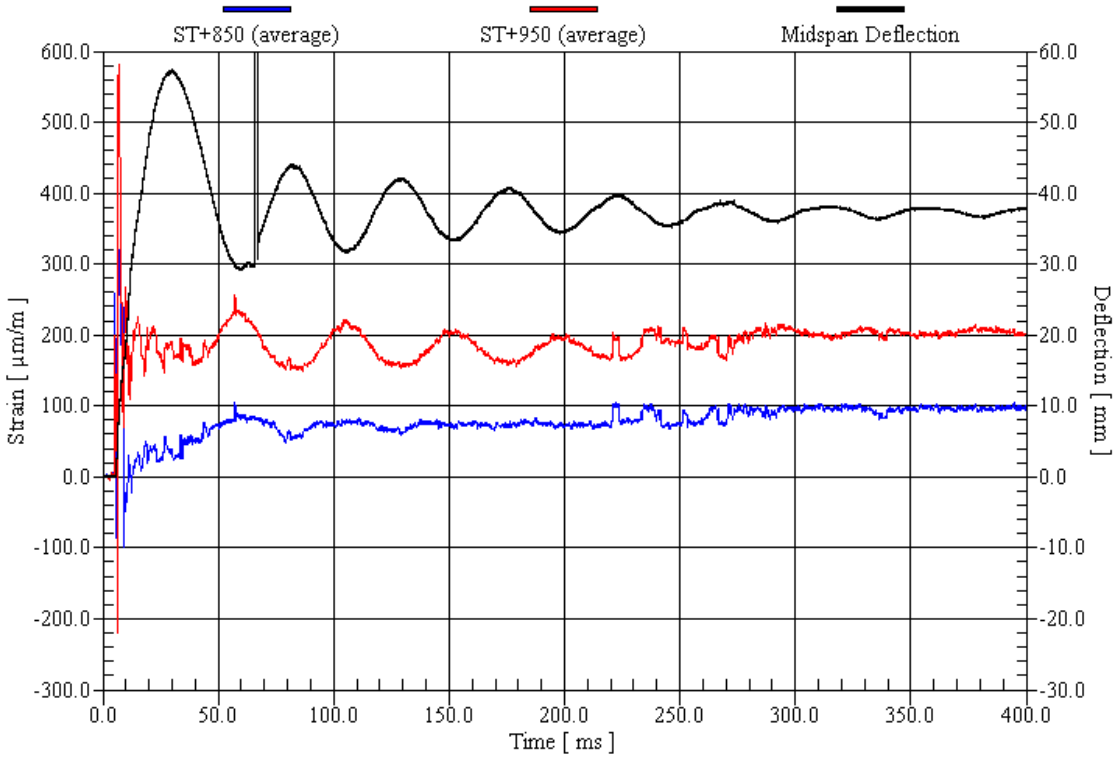

Figure A-7: Stirrup strain-time history for Imp-4

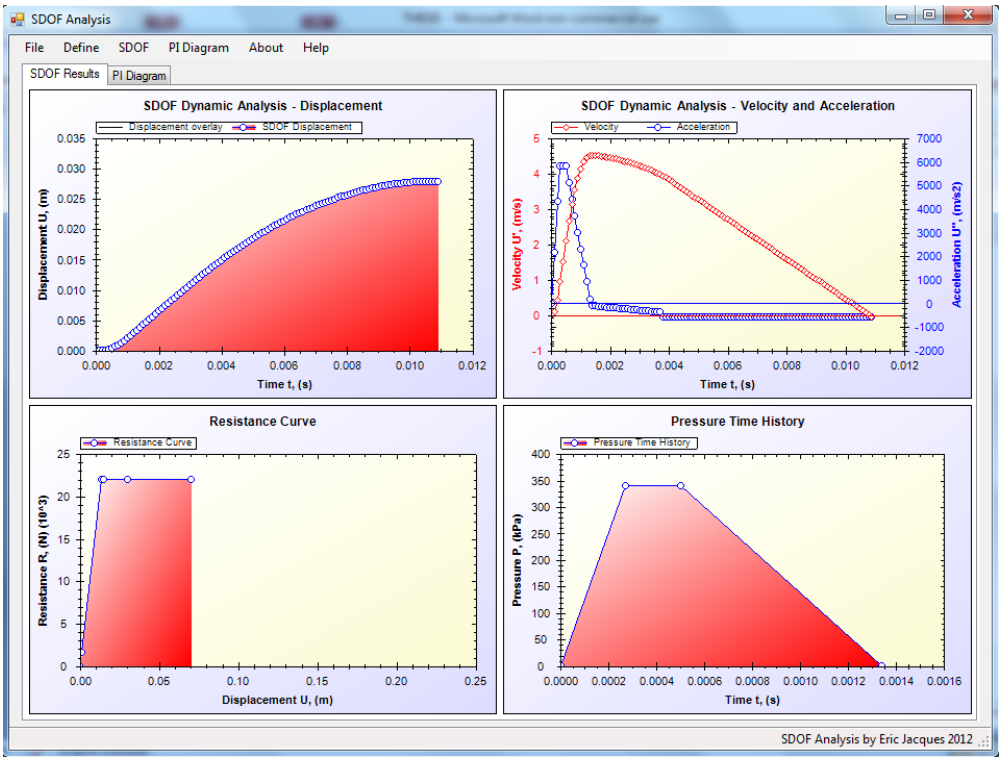

Figure A-8: Screenshot of SDOF analysis software used for response of Imp-4 (© Eric Jacques)

Table A-4: Strain data for Imp-4

Strain Gauge	Peak Strain (μm/m)	Time to Peak Strain (ms)	Average Strain Rate (s^{-1})	Peak Strain Rate (s^{-1})	Residual Strain (μm/m)
Top-869	3087	0.66	1.91	6.10	456
Top-484	2008	1.40	0.85	3.56	426
TopMid	1278	1.21	0.59	5.08	710
Top484	2437	1.35	1.05	3.07	466
Top869	2738	0.80	1.56	4.08	420
Bot-869	1625	Unknown	3.07	7.45	476
Bot-484	2419	4.66	0.44	3.38	571
BotMid	11557	1.55	4.70	7.74	3007
Bot484	3135	4.66	0.56	2.29	595
Bot869	2460	3.98	0.50	2.33	476
Sur-102	-3605	22.56	0.16	1.16	-1620
Sur102	-2342	11.66	0.32	1.16	-771

A.5. Imp-5

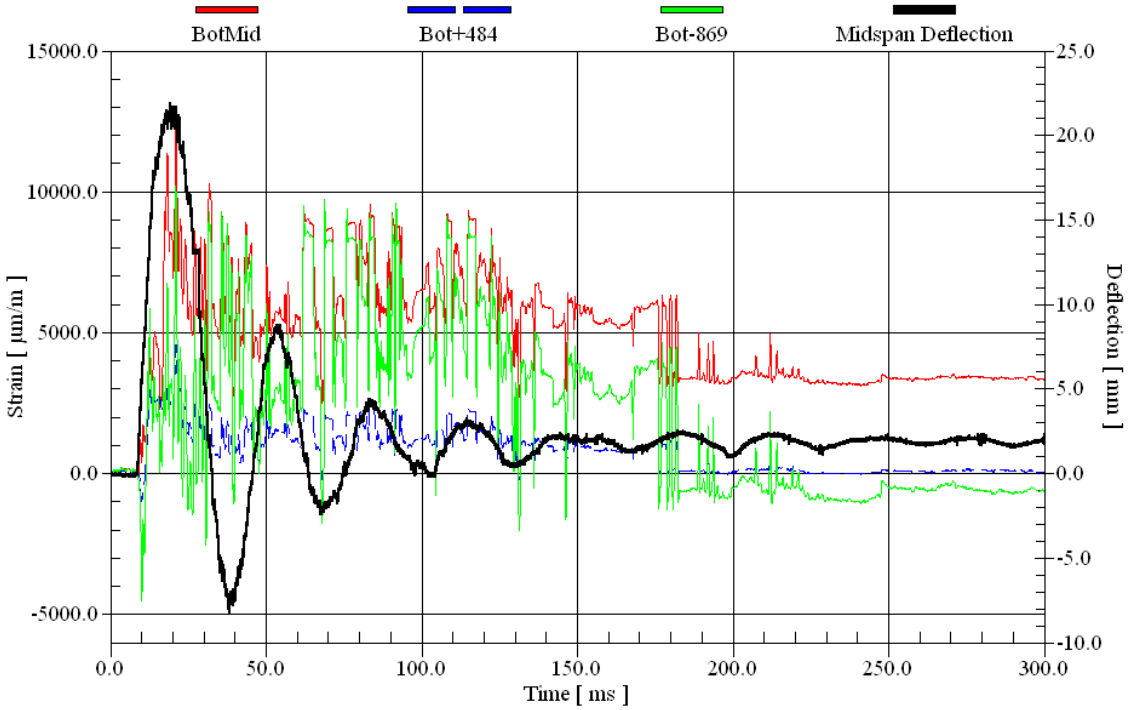

Figure A-9: Tension rebar strain-time history for 1st impact on Imp-5

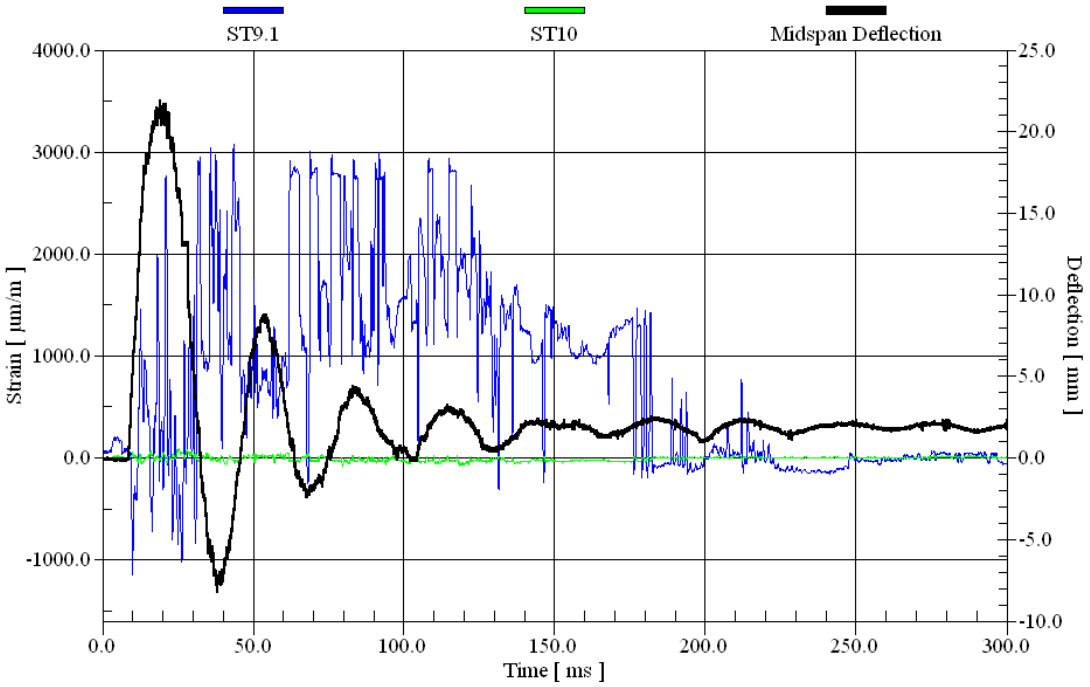

Figure A-10: Stirrup strain-time history for 1st impact of Imp-5

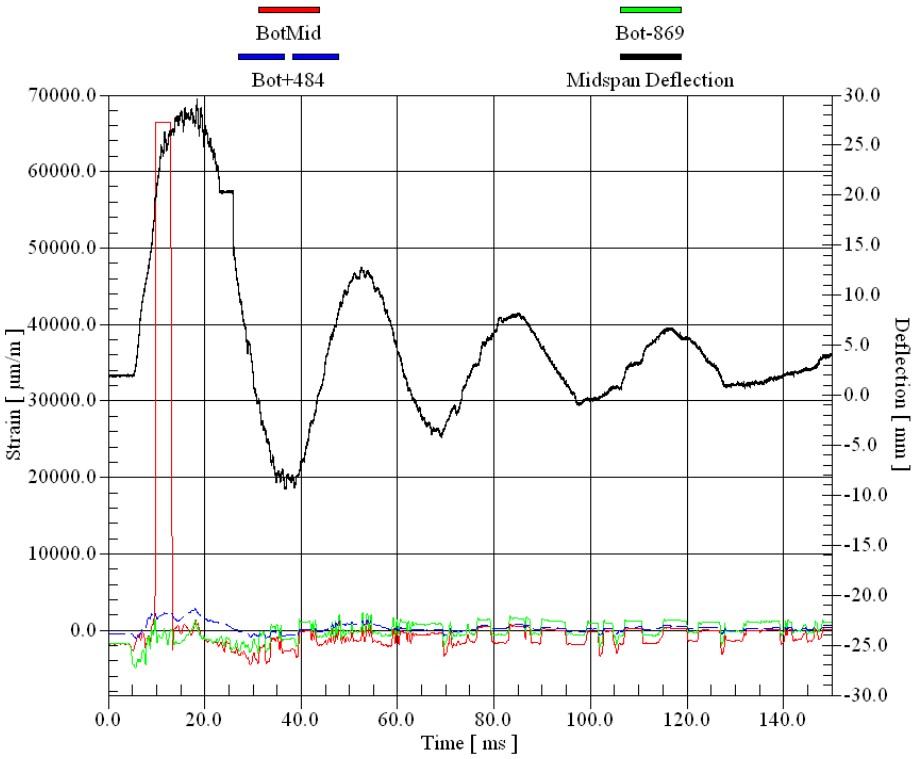

Figure A-11: Tension rebar strain-time history for 2nd impact on Imp-5

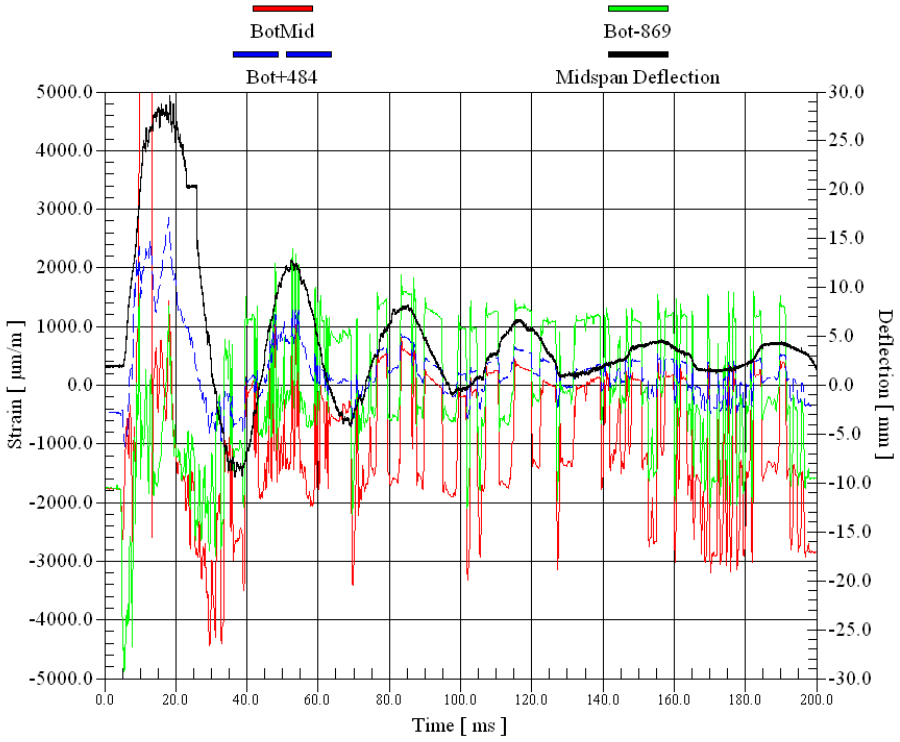

Figure A-12: Tension rebar strain-time history for 2nd impact on Imp-5 (smaller scale)

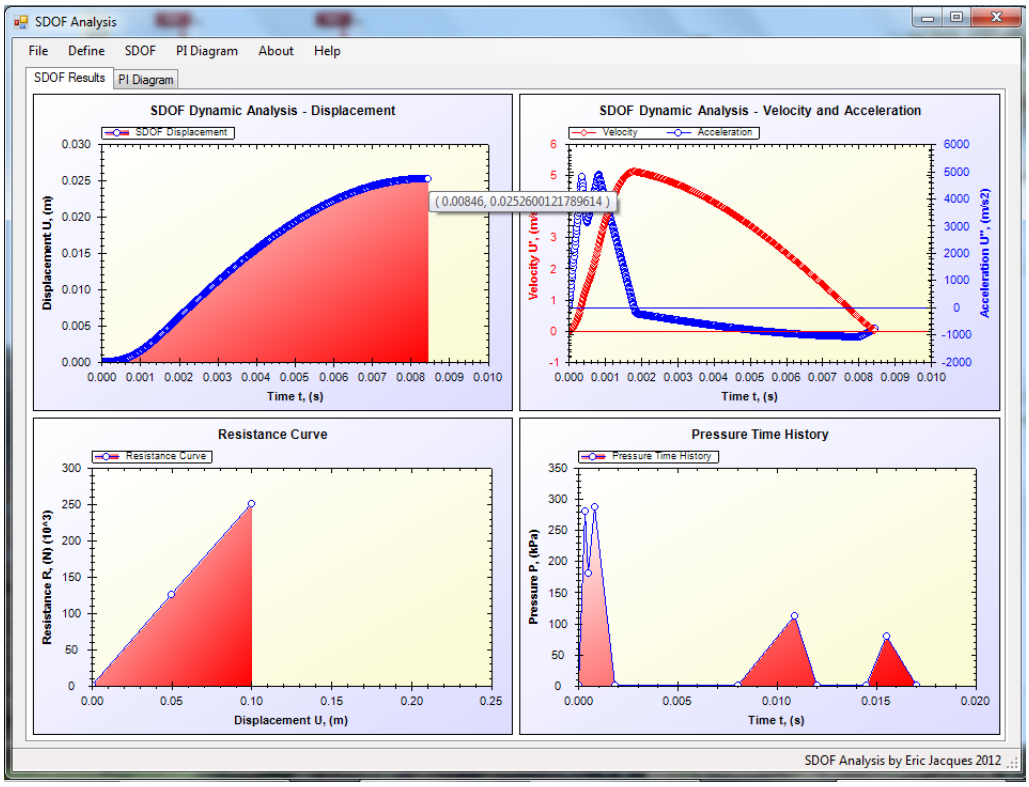

Figure A-13: Screenshot of SDOF analysis software used for response of Imp-5 (© Eric Jacques)

A.6. QS-1

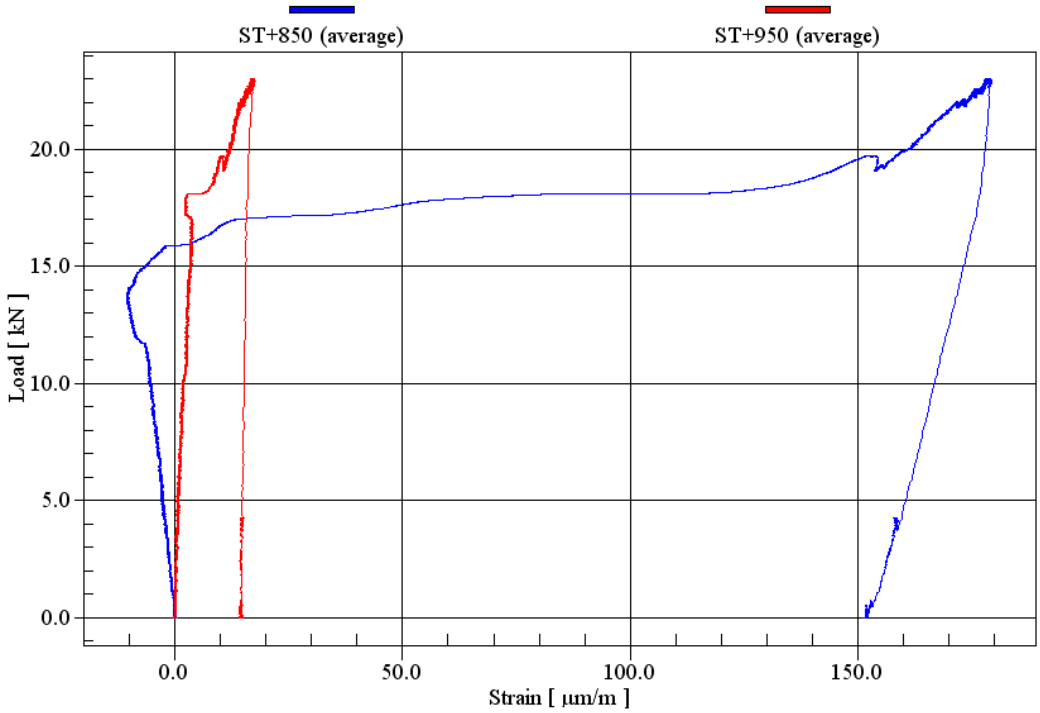

Figure A-14: Load-stirrup strain for QS-1

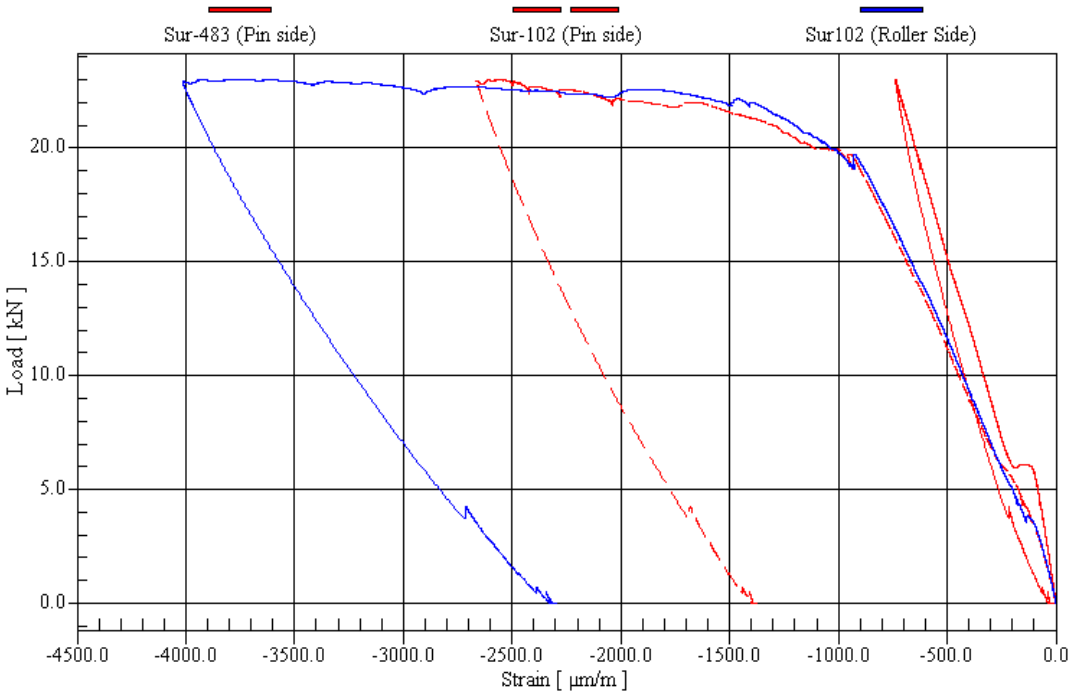

Figure A-15: Load-concrete surface strain for QS-1

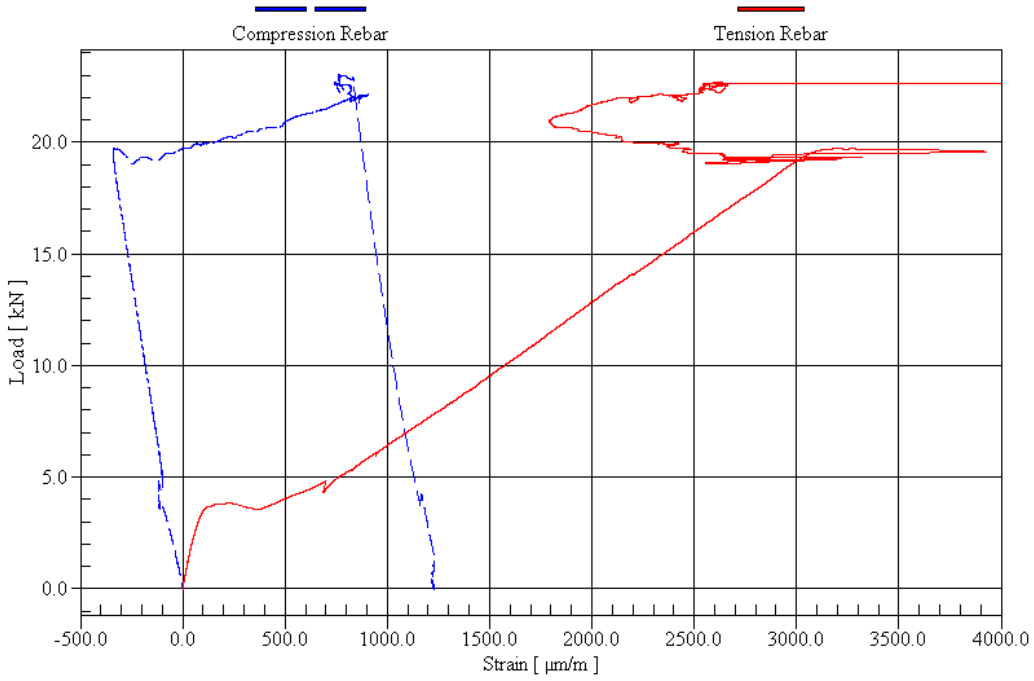

Figure A-16: Load-midspan strain for QS-1

Table A-5: Strain data for QS-1

Strain Gauge	Peak Strain (μm/m)	Residual Strain (μm/m)
Top-869	-138	92
Top-484	-238	91
Top-242	-454	234
TopMid	-339	1228
Top484	-229	82
Top869	-87	48
Bot-869	830	456
Bot-484	2026	618
Bot-242	2793	573
BotMid	Unknown	Unknown
Bot484	2217	618
Bot869	830	456
St850_1	249	203
St850_2	109	102
St950_1	22	16
St950_2	22	13
Sur-483	-730	-40
Sur-102	-2667	-1414
Sur102	-4024	-2336
Sur483	Unknown	Unknown

A.7. QS-2

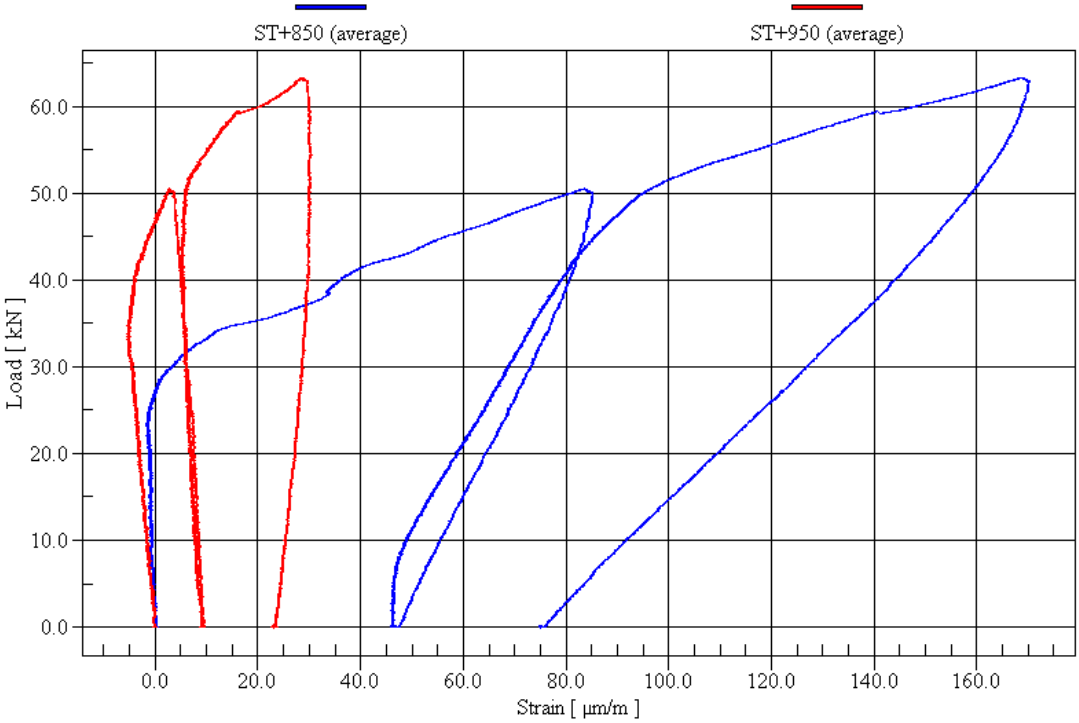

Figure A-17: Load-stirrup strain for QS-2

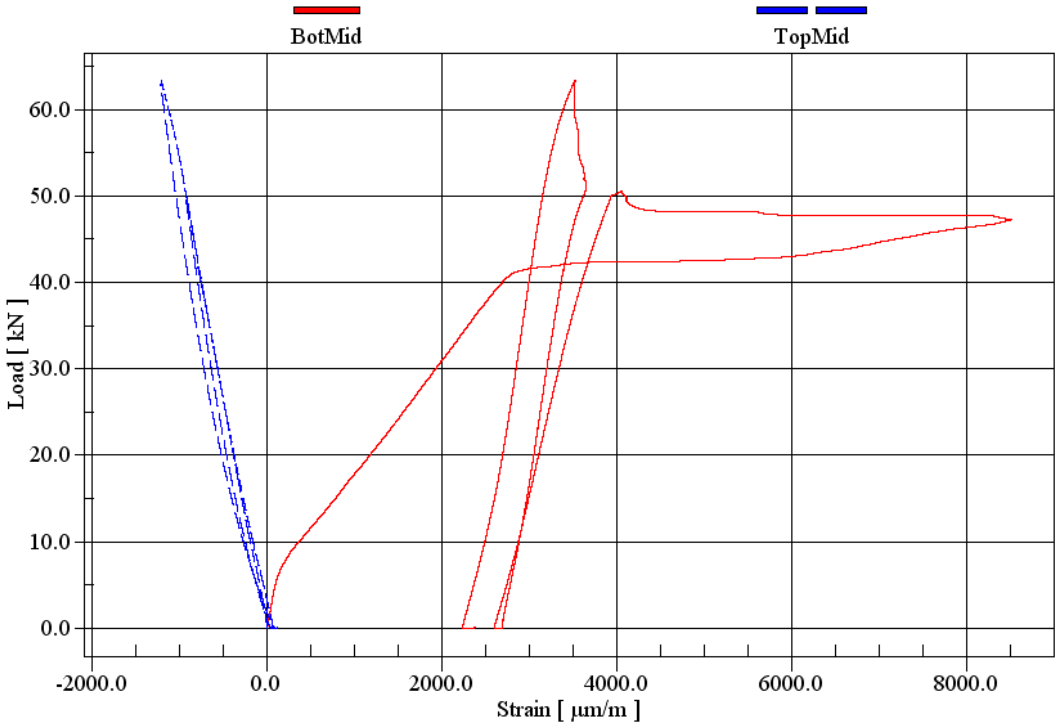

Figure A-18: Load-midspan strain for QS-2

Table A-6: Strain data for QS-2

Strain Gauge	1st Loading Cycle		2nd Loading Cycle	
	Peak Strain (µm/m)	**Residual Strain (µm/m)**	**Peak Strain (µm/m)**	**Residual Strain (µm/m)**
Top-869	204	-3	-246	4
Top-484	-563	21	-688	25
Top-242	-957	-41	-1176	-52
TopMid	-935	38	-1209	84
Top484	-511	12	-636	19
Top869	-171	2	-213	4
Bot-869	650	165	1004	253
Bot-484	2012	362	2640	412
Bot-242	2512	172	15507	11031
BotMid	Unknown	Unknown	Unknown	Unknown
Bot484	2184	362	2780	412
Bot869	586	165	876	231
St850_1	86	45	155	72
St850_2	83	50	183	81
St950_1	-3	8	16	20
St950_2	9	11	41	27

Appendix B: Cylinder Retrofit Study

To gain a better understanding of the effect that FRP retrofitting has on the material behaviour of concrete in compression, fifteen concrete cylinders, both wrapped and unwrapped, were tested in compression to failure. The objective of these tests was to record the stress-strain relationship of each specimen up to peak stress and then draw a comparison between the different retrofit configurations.

B.1. Test Specimens

The test specimens were casted in standard plastic moulds and had a nominal height of eight inches (203.2 mm) and a diameter of four inches (101.6 mm). To observe the influence of concrete strength on the behaviour of the retrofitted cylinders, two mixes with differing compressive strengths (45.6 and 57.6 MPa) were used. The 45.6 MPa concrete was from the same batch as that used to cast all test specimens discussed in the main body of this thesis. Beyond two unwrapped control specimens for each type of concrete, the remaining cylinders were wrapped with FRP applied in both the longitudinal (90°) and confinement (0°) directions. All retrofitted cylinders had two layers of longitudinal FRP applied as one continuous sheet with an overlap of approximately 70 mm. In addition to this two-ply bottom layer, confinement FRP was placed as the outer layerhaving one, two or three plies. Eleven specimens were considered normal strength (NS) with a concrete strength of 45.6 MPa and included four separate test sets: two controls, three cylinders with one outer confinement layer, three cylinders with two outer confinement layers and three cylinders with three outer confinement layers. The four remaining specimens were considered high strength (HS) with a lower than expected concrete strength of 57.6 MPa. These cylinders were separated into two test sets: two controls and two cylinders with two 90° plies and two 0° plies. Table B-1 provides an overview of the test specimen companion sets.

Table B-1: Cylinder Study Specimens

Specimen	f'c (MPa)	# of Longitudinal FRP Layers (90°)	# of Confinement FRP Layers (90°)
NS-Control-1 NS-Control-2	45.6	0	0
NS-1x0-1 NS-1x0-2 NS-1x0-3	45.6	2	1
NS-2x0-1 NS-2x0-2 NS-2x0-3	45.6	2	2
NS-3x0-1 NS-3x0-2 NS-3x0-3	45.6	2	3
HS-Control-1 HS-Control-2	57.6	0	0
HS-2x0-1 HS-2x0-2	57.6	2	2

Preliminary tests were conducted in advance of the current study to gain experience in the difficult task of wrapping these cylinders. The major lesson learned from these preliminary tests was that the layers of FRP had to extend as close as possible to the edge of the concrete cylinders to minimize the likelihood that the unconfined edges would fail prematurely (Figure B-1). It was also concluded that the number of seams should be limited. This was accomplished by only cutting two sheets of FRP for each cylinder. The first bottom sheet was 195 mm high (fibres oriented in this direction) and 700 mm long. The second, outer, sheet was also 195 mm high but varied in length from 350, 700 or 1000 mm (fibres oriented in this direction) as depicted in Figure B-2. Furthermore, great care was taken to ensure that the retrofitting was as tight as possible to the concrete cylinder (Figure B-3).

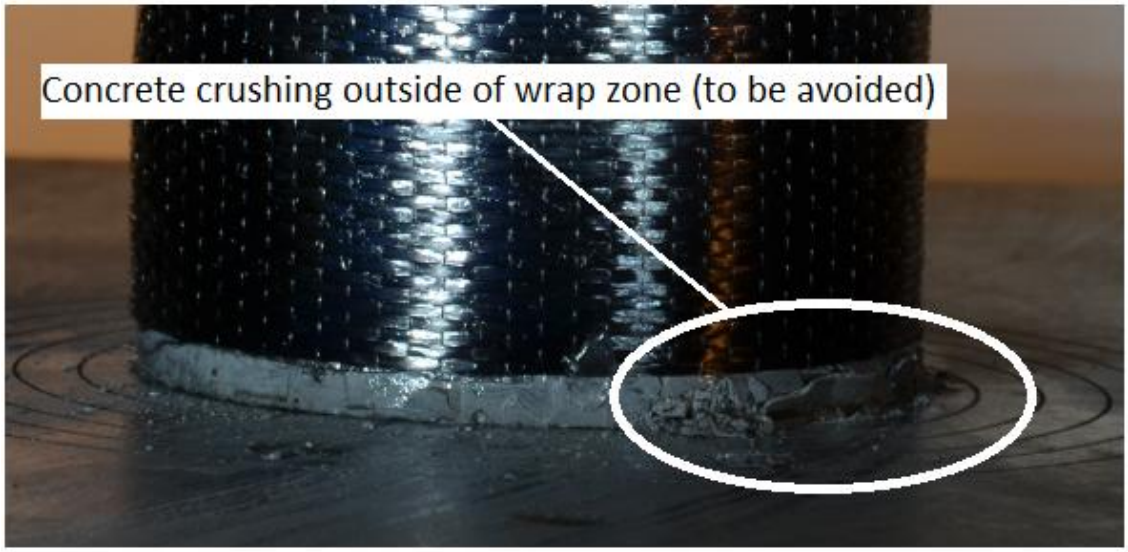

Figure B-1: Preliminary FRP wrapped concrete cylinder with inadequate FRP coverage

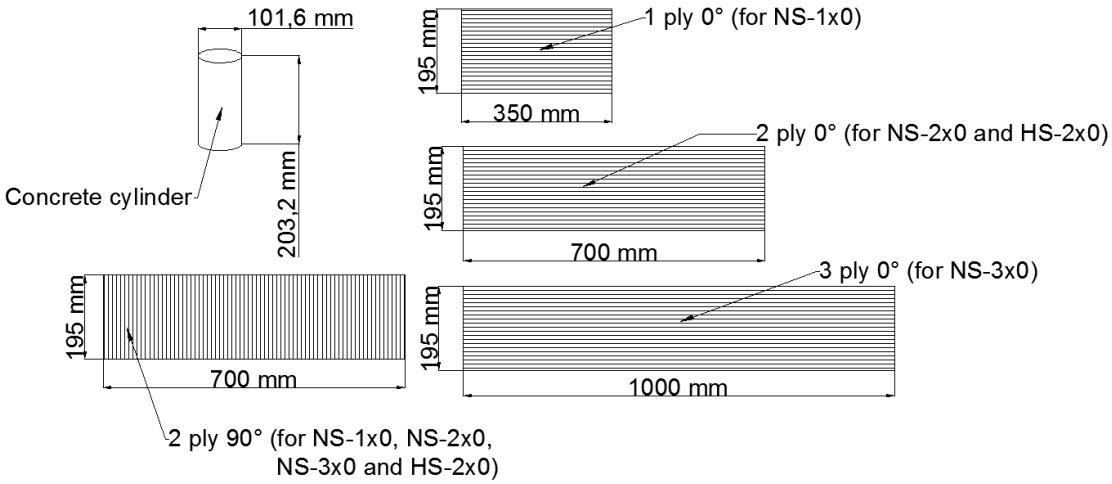

Figure B-2: Cylinder FRP wrapping scheme

Figure B-3: Application of inner 90° layer to concrete cylinder

B.2. Test Procedure

All specimens were tested in compression to failure in a Satec 2000 kN hydraulic testing frame in displacement controlled loading at a rate of 0.5 mm/min. The Satec frame is capable of recording load and displacement levels. However, the displacement readings recorded by a built-in wire gauge in the testing frame were a cause of concern for several reasons. The wire gauge had a limited resolution which resulted in a stepped displacement pattern with low precision - it was placed near the back of the hydraulic piston and not in its center near the specimen itself; and the accuracy of the readings were questionable given the fact that the expected displacement levels were below 1 mm for the control specimens, while the gauge was calibrated to a measuring range of up to two meters. For these reasons, displacement levels were also measured by two laser displacement sensors mounted to the hydraulic piston at the bottom of the frame. The sensors reflected their beam off the stationary crosshead at the top, thus recording the cross head displacement with the resolution of the lasers. These readings were recorded by an HBM MGC data acquisition system at a sampling rate of 50 Hz. The voltage outputs from the Satec loading frame for both displacement and load were also recorded by the MGC system. These readings were calibrated to fall within 1% accuracy. Thus, for each cylinder, the recorded data included:

time, load and three displacement readings (one from the Satec frame and one for each displacement laser). Also, for certain specimens, high speed video of the failure was recorded.

B.3. Test Results

It was clear from the results that the strain values calculated from the Satec internal displacement readings were inadequate for the study's purposes. The resulting stress-strain curves were not smooth and instead presented steps. However, while the Satec displacements/strains were not very precise, they were reasonably accurate, Figure B-4.

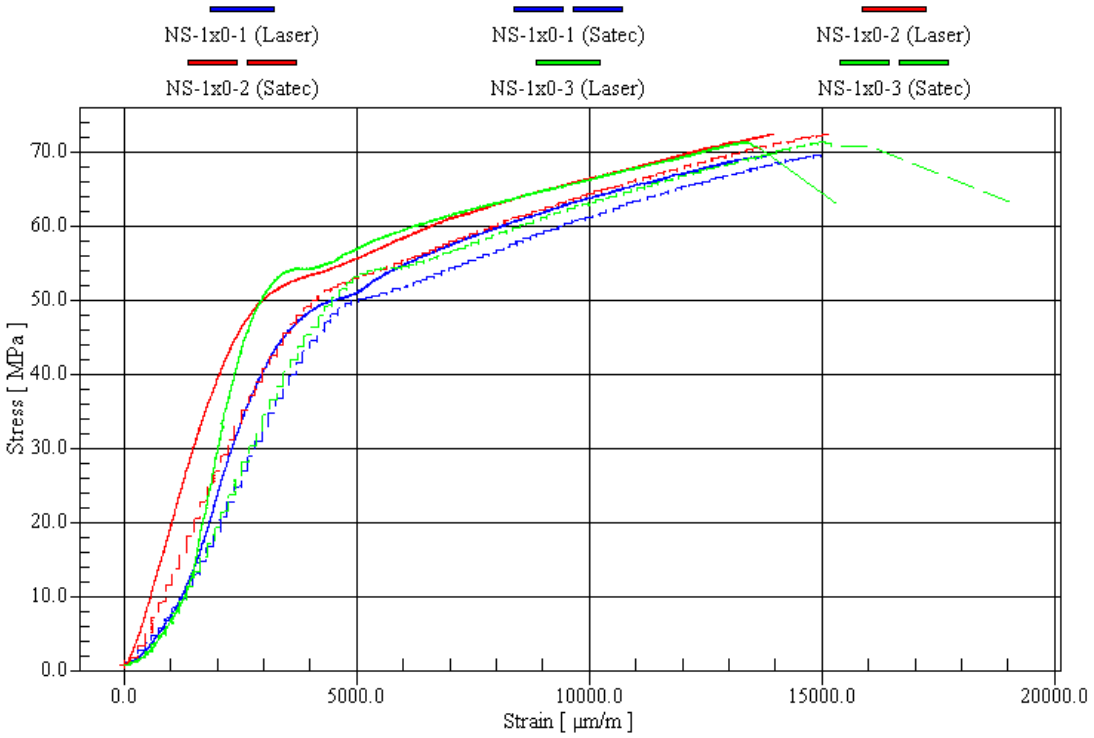

Figure B-4: Stress-strain curves for NS-1x0 samples (Satec and laser average based strain)

Stress results were obtained by dividing the load output from the Satec frame by the nominal concrete area of the specimens. For each specimen, the strain values were obtained by dividing the averaged laser displacement readings by the length of the specimen. Peak stress was the maximum stress value reached by the specimen during its loading. Table B-2 provides a summary of performance increase for each companion set.

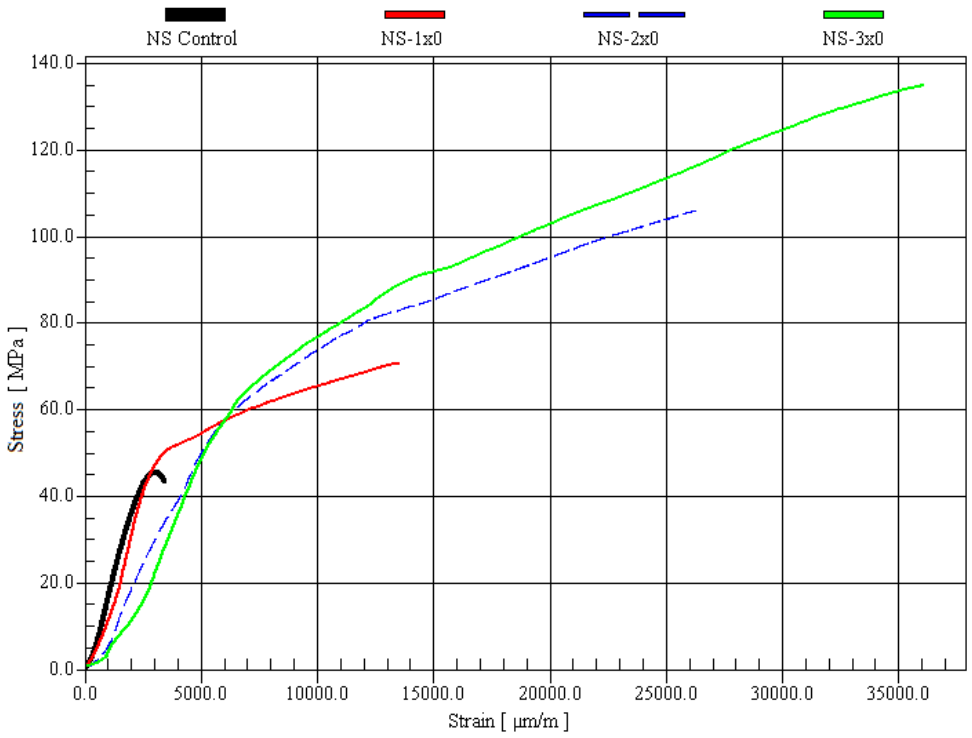

Figure B-5: Average stress-strain curves for NS samples

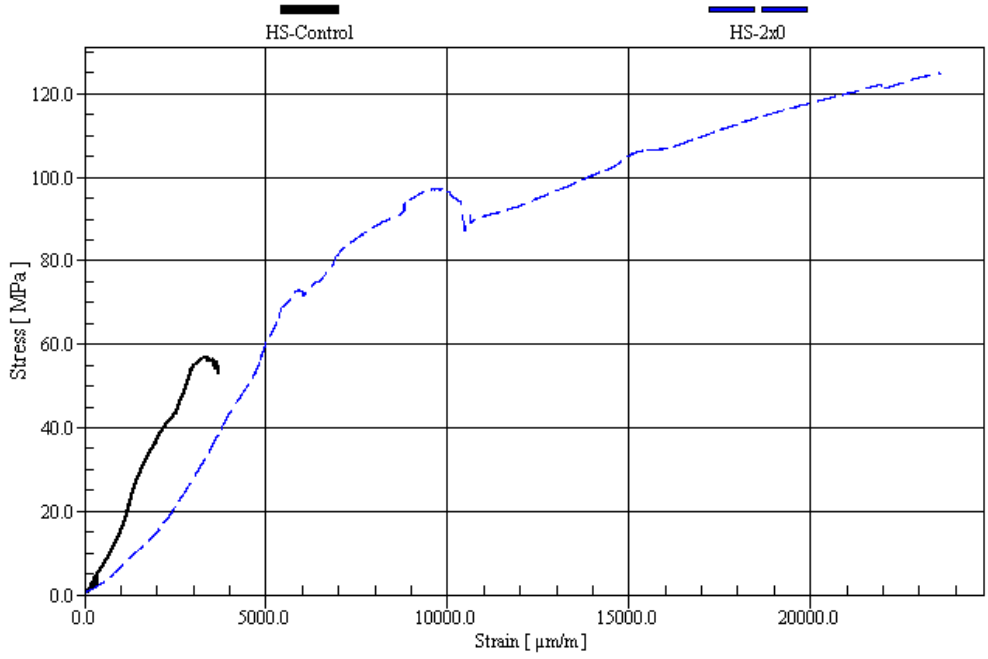

Figure B-6: Average stress-strain curves for HS samples

Table B-2: Summary of performance increase for each specimen set

Specimen Set	Average Peak Stress (MPa)	Peak Stress Increase (%)	Average Strain at Peak (μm/m)	Peak Strain Increase (%)
NS-Control	45.6	x	2988	x
NS-1x0	71.1	56	13695	358
NS-2x0	110.6	143	30048	906
NS-3x0	135.6	197	36462	1120
HS-Control	57.7	x	3368	X
HS-2x0	128.9	124	25661	662